Physical and Chemical Properties of Matrix in Primitive Chondrites

Thesis

Physical and chemical properties of matrix in primitive chondrites

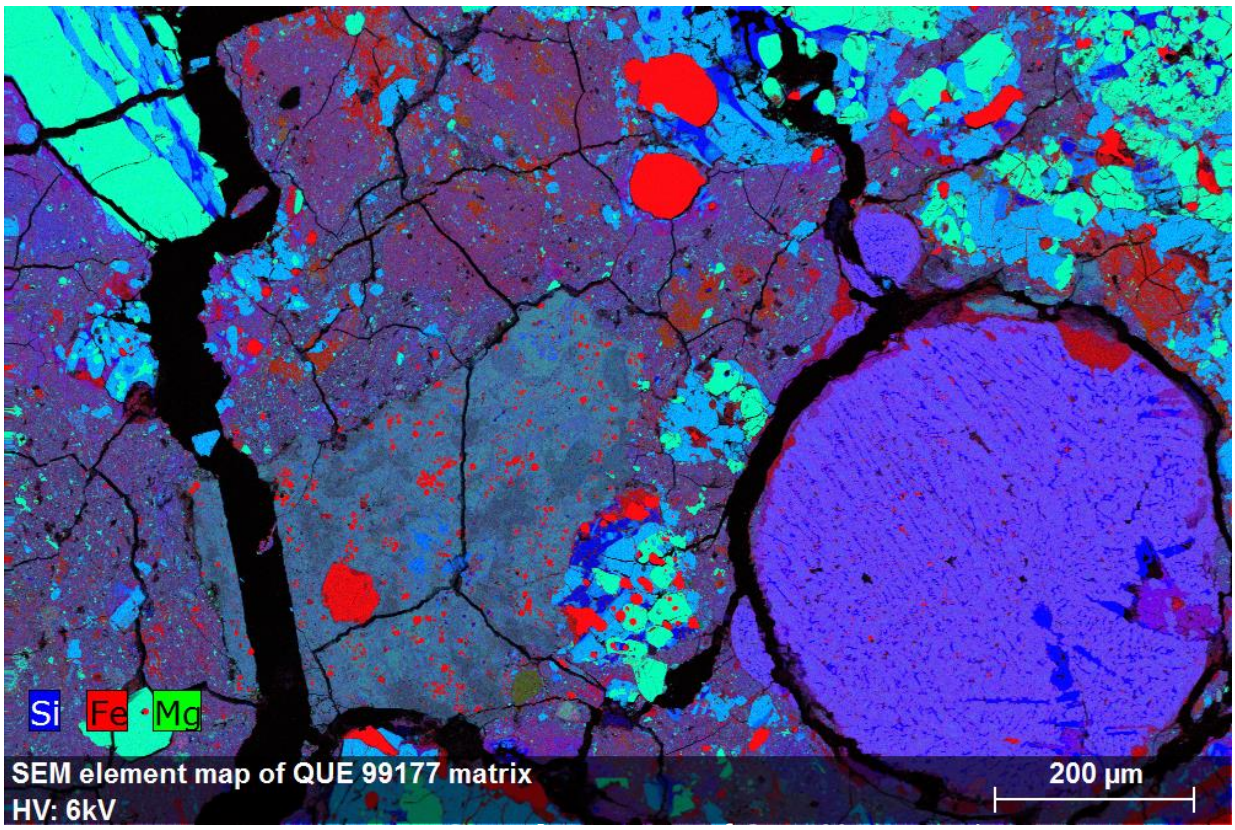

Epifanio Vaccaro

(MSc Hons. Geological Sciences, Palermo University)

The Open University & Natural History Museum, London
Supervisors: Natalie Starkey, Ian Franchi, Sara Russell

November 2017

This thesis was submitted to The Open University for the degree of Doctor of Philosophy

Abstract

The origin and formation of our Solar System is an open research question, which the scientific community is trying to address. In this work was specifically investigated the fine grained matrix which is a mixture of fine-grained materials composed largely of amorphous silicate and sub-micrometre crystals forsterite and enstatite. This is thought to be the remnants of the dust and gas of the protoplanetary disk that allows us to better understand chemical and physical properties of this precursor material. Four pristine primitive meteorites were selected: Acfer 094 (C2-ung.), ALHA77307 (CO3), MIL 07687 (C3-ung.) and QUE 99177 (CR2). The ability of a new generation of SEM-EDX detector was tested, in order to acquire high-resolution element maps of fine grained matrix. This allowed the calculation of abundances, and size distribution of discrete grains of different phases (silicate vs. opaque). Data acquired suggest that the four meteorites can be split into two groups, ALHA77307-MIL 07687 and QUE 99177 and Acfer 094, based on differences in relative abundances and sizes of discrete grains in their matrix. Micro X-ray diffraction was also used for mineralogical phase identification of the matrix constituents allowing the estimation of their modal mineralogy.

MIL 0768 and Acfer 094 were also investigated using Scanning Transmission X-ray Microscopy (STXM) which revealed predominantly oxidising conditions; some reducing conditions are also displayed by some grains, reflecting the mixed redox conditions of the solar nebula.

Measurements of O-isotopic composition of matrix regions were performed, and revealed similarities to values previously reported for IDPs (Starkey et al. 2013,2014 Nakashima et al., 2012, Aleon et al., 2009), rather than those of bulk meteorites (Clayton & Mayeda, 1999). I infer that the observed differences between these matrix components within the meteorite reflect the heterogeneity of the protoplanetary disk. Although these meteorites are pristine, parent body processes have also affected the small matrix grains.

Acknowledgements

I am very grateful to Sara, my NHM supervisor, for believing in me and giving me the life-changing opportunity that I always dreamed of. Thanks for her patience, motivation and knowledge shared. Thanks to my supervisors Ian and Natalie for their support and guidance during my time at the OU.

I would also like to thank the planetary group at the NHM. In particular, Caroline, who gave me my first opportunity at the NHM, introducing me to the world of meteoritics and inspiring me as a scientist. I'd also like to acknowledge my friends Penny, Ashley and Natasha for their invaluable help and encouragement.

In addition, I would like to thank Anton, Tomasz and Jens, for their support and assistance in the labs.

Last, but not least, I would like to thank my family: my parents, who devotedly supported me throughout my education, and my loving and caring wife, Mariko, whose patience and support was invaluable during the most difficult times. I could not have done this without them.

Statements of original authorship

The research contained in this thesis is original and has not been used for submission in any previous degree courses. Where previously published research is mentioned, the relevant publication is cited in both the text and in the reference list.

Table of contents

Abstract ii

Acknowledgements iii

Statement of original authorship iii

Table of contents iv

List of figures ix

List of Tables xix

Chapter 1 1

1. Introduction 1

1.1 - Star and Planet Formation 1

1.1.1 - Protoplanetary Disks and Chondritic Matrix 1
1.1.2 - Star Formation 2
1.1.3 - Cloud collapse and disk formation by conservation of angular momentum 4
1.1.4 - Early hot disk hypothesis 6
1.1.5 - Heating mechanisms of the disk 7
1.1.6 - Effect of gas drag on particles 8
1.1.7 - Settling to mid-plane 9
1.1.8 - Radial mixing mechanisms 10
1.1.9 - Grain growth 12
1.1.10 - Diagnostic tools to disk detection 13
1.1.11 - Accretion times 15
1.1.12 - Chemistry of the dust 16
1.1.13 - Comparison of dust disks to Solar System components 17
1.1.14 - Oxidation state of the solar nebula 19

1.2 -Chondrites **20**

1.2.1 - Introduction **20**
1.2.2 - Chondrite Classification **21**
1.2.2a - Chondrite groups **21**
1.2.2b - Chondrite types **21**
1.2.2.1 - Carbonaceous Chondrites **22**
1.2.3 - Chondritic Components **23**
1.2.3.1 - Chondrules **23**
1.2.3.2 - Refractory Inclusions **24**
1.2.3.3 - Metal and Troilite **26**
1.2.3.4 - Matrix Material **27**
1.2.3.4a - Chondrule Rims **28**
1.2.3.5 - Organic material in carbonaceous chondrites **29**
1.2.4 - Presolar Grains and Nucleosynthesis **30**

1.3 - Matrix-chondrule complementarity **34**

1.4 - Purpose of Study **35**

1.5 - Reason for choosing these samples **36**

Chapter 2 **39**

2. Methods **39**

2.1- Introduction **39**

2.2 - Scanning electron Microscopy (SEM) **42**

2.3 - Zeiss EVO 15LS SEM **43**

2.4 - Carl Zeiss Ultra Plus **45**

2.5 - FEI Quanta 650 FEG SEM **49**

2.6 - XRD diffraction **54**
2.6.1- GeniX Cu high flux X-ray source **58**
2.6. 2 - D/MAX-RAPID II **59**
2.6.2.1- Modal mineralogy profile-stripping method **62**
2.7 - Focused Ion Beam (FIB) **51**
2.7.1 - Focused Ion Beam (FIB) settings used for the project **63**

2.8 - Synchrotron **66**
2.8.1 - Diamond I08 beamline settings used for the project **68**

2.9 - Nano SIMS **72**

Chapter 3 **76**

3. Petrology of Fine Grained Matrix **76**

3.1 - CO3.0 carbonaceous chondrite ALHA77307 **76**

3.1.1 – Previous Studies **76**
3.1.1.1- Anhydrous Crystalline Phases in the Matrix **77**
3.1.1.2 – Amorphous Phases in the Matrix **78**
3.1.1.3 – Phyllosilicates in the Matrix **78**

3.1.2 - Study carried out in this project **78**
3.1.2a – Matrix abundance **78**
3.1.2b – Bulk Chemical Composition of Matrix **80**
3.1.2c – Modal Mineralogy of the Matrix **83**
3.1.2d – High Resolution Element Maps of Matrix **85**
3.1.2e - Enstatite whiskers **87**
3.1.2f – Mineralogy of the Matrix **90**

3.2 - Ungrouped Carbonaceous Chondrite MIL07687 **93**

3.2.1- Previous Studies **93**
3.2.1.1 - Anhydrous Crystalline Phases in the Matrix **93**

3.2.1.2 - Phyllosilicates in the Matrix 94

3.2.2 – Study carried out in this project 94
3.2.2a - Matrix abundance 94
3.2.2b – Bulk Chemical Composition of Matrix 96
3.2.2c – Modal Mineralogy of Matrix 98
3.2.2d – High Resolution Element Maps of Matrix 100
3.2.2e - Enstatite whiskers 101
3.2.2f – Mineralogy of the Matrix 103
3.2.2g – XANES Results 106

3.2.3- Reactive transport during fluid flow 111

3.2.4 - Discussion of petrological results for ALHA77307 and MIL 07687 113

3.2.5 - Enstatite whiskers in ALHA77307 and MIL 07687 117

3.3 - CR3.0 carbonaceous chondrite QUE 99177 119

3.3.1- Previous Studies 119
3.3.1.1 - Anhydrous Crystalline Phases in the Matrix 119
3.3.1.2 – Amorphous Phases in Matrix 120
3.3.1.3 - Phyllosilicates in the Matrix 120

3.3.2 – Study carried out in this project 121
3.3.2a - Matrix abundance 121
3.3.2b – Bulk Chemical Composition of Matrix 122
3.3.2c – Modal Mineralogy of Matrix 125
3.3.2d – High Resolution Element Maps of Matrix 128
3.3.2e – Mineralogy of the Matrix 129

3.4 - Ungrouped carbonaceous chondrite Acfer 094 132

3.4.1- Previous Studies 132
3.4.1.1 - Anhydrous Crystalline Phases in the Matrix 132

3.4.1.2 – Amorphous Phases in Matrix 133
3.4.1.3 - Phyllosilicates in the Matrix 133

3.4.2 – Study carried out in this project 134
3.4.2a - Matrix abundance 134
3.4.2b – Bulk Chemical Composition of Matrix 135
3.4.2c – Modal Mineralogy of Matrix 138
3.4.2d – High Resolution Element Maps of Matrix 140
3.4.2e – XANES Results 141

3.4.3 - Discussion of petrological results for QUE 99177 and Acfer 094 144

3.5 – Conclusions 150

Chapter 4 155

4. Grain Size distribution 155

4.1 – Introduction 155

4.2 – Methods 156
4.2a - Cumulative frequencies, geometric Mean and Standard deviations 160
4.2b - 2D-3D correction 162

4.3 - Result 163

4.4 – Discussion 170

4.5 - Comparing Acfer 094 size distribution data to literature data 182

4.6 - Summary and conclusions 185
4.6.1- Mobility of sulfides and their coarsening during metamorphism 187
4.6.2 - Crystal growth, during parent body aqueous alteration 187

Chapter 5 189

5. Oxygen & Hydrogen Isotopes 189

5.1 - Oxygen Isotopes in the Solar System 189

5.2 - Oxygen isotopic anomalies in the Solar System 190
5.2.1 - Nucleosynthetic effects 191
5.2.2 - Chemical mass-independent fractionation effect during solid formation 192
5.2.3 - Photochemical self-shielding effects 192

5.3 - Bulk oxygen isotopes in meteorites 193
5.3.1 - Oxygen Isotopic composition of chondrules and CAIs 195
5.3.2 - Oxygen Isotopic composition of matrix 197

5. 4 - Chondritic porous interplanetary dust particles (CP-IDPs) 198

5. 5 - Oxygen composition of presolar grains 199

5.6 - D/H variations 200

5.7 - Oxygen isotopes results 202
5.7.1 - Bulk matrix oxygen isotopes compositions 202

5.8 - D/H isotope results 204
5.8.1 - Bulk D/H isotope compositions 204

5. 9 – Discussion 204
5.9.1 – Comparison with bulk meteorites 204
5.9.2 – Comparison with IDPs 207
5.9.3 - Presolar grains 209
5.9.4 - D/H discussion 211

5.10 – Conclusions 213

Chapter 6 **215**

6. Conclusions and Future work **215**

6.1 - Enstatite whisker and grain transport in the protoplanetary disk **215**

6.2 - Size distribution **217**

6.3 - Matrix similarities with IDPs and protoplanetary dust **218**

6.4 - Parent body versus nebula processes **220**

6.5 - Accretion processes **221**

6.6 – Future work **222**

References **226**

Appendix on accompanying DVD

List of figures

Fig. 1.1.1 – ALMA composite image showing dust and gas disk around HD142527

Fig. 1.1.2 – Illustration showing snapshot of the collapsing of an un-magnetised non-rotating isothermal sphere and magnetised isothermal toroid, adapted from Allen, 2004.

Fig. 1.1.3 – Illustration showing snapshots of the collapse of an un-magnetised non-rotating isothermal toroid and magnetised isothermal toroid with uniform rotational velocity, adapted from Allen, 2004.

Fig. 1.1.4 – Illustration of a protoplanetary disk surrounding a young star

Fig. 1.1.5 – Illustration of proto-planetary disk and it's structure showing the effects of radial mixing transporting dust from inner disk to the comet forming region (Image credit: A. Mandell, NASA GSFC)

Fig. 1.1.6 - The protoplanetary disk of HL Tauri from ALMA showing large gaps in the disk created by forming planets (Brogan et al.,2015).

Fig.1.1.7 Diagram from from Natta and Testi, 2006 showing observed profiles of the 10 μm silicate feature for HAe stars

Fig.1.2.1 - Chart summarizing the grouping of carbonaceous chondrites into chemical and petrographic types

Fig. 1.2.2 – (a) Backscattered electron image of a chondrule in sample QUE 99177, (b) Element map of same chondrule

Fig.1.2.3 – Element map of one of a CAI in sample MIL 07687.

Fig.1.2.4 - Element map of sample QUE 99177 showing the presence of iron metal

Fig.1.2.5 - Backscattered electron image of sample ALHA77307 showing matrix filling the interstices between chondrules

Fig. 1.2.6- Scanning electron micrograph of a SiC grain from the Murchison meteorite

Fig. 2.3.1- Diagram showing thermionic tungsten electron source of the type used in EVO 15L SEM

Fig.2.3.2 Backscattered electron and X-ray element map montages of samples ALHA77307, Acfer 094, QUE 99177 and MIL 07687, acquired using Zeiss EVO 15LS SEM.

Fig. 2.4.1 - Gun configuration for field emission SEM

Fig. 2.4.2 - Schematic representation of FEG SEM Ultra Plus Showing principle of SE detection by an In-lens detector

Fig. 2.4.3 a & b - Schematic representation of FEG SEM Ultra Plus Showing principle of BSE signal detection, and Energy selective Backscattered (EsB) detection.

Fig. 2.4.4a - EsB image of matrix region of ALHA77307 showing composition differences of matrix constituents

Fig. 2.4.4b - In-Lens image of matrix region showing detailed information about the sample surface

Fig. 2.5.1 - Diagram FEI Quanta 650 FEG SEM showing the X-ray detector (EDS) Bruker Flat Quad 5060F

Fig. 2.5.2 - Picture (a) & diagram (b) of EDS XFlash QUAD 5040 fitted in the FEI Quanta 650 FEG SEM

Fig. 2.5.3a - Monte Carlo electron – trajectory simulation of the interaction volume of ~ 3.5×3.5μm generated in a forsterite crystal at 15kV

Fig. 2.5.3b - Element map of matrix region of ALHA77307 generated at 15kV, showing poorly defined edges of the matrix constituents, resulting in an overall blurred image

Fig. 2.5.4a - Monte Carlo electron – trajectory simulation of the interaction volume of ~0.4×0.4μm generated in a forsterite crystal at 5kV

Fig. 2.5.4b - Element map of matrix region of ALHA77307 generated at 5kV, showing well defined edges of the matrix constituents, resulting in an overall sharp image

Fig. 2.6.1 - Diagram showing the angular dispersion of the incident x-ray beam reduced by collimation as it goes through a slit placed between the x-ray source and the sample

Fig. 2.6.2 - Diagram of wave interacting with an object producing scattered spherical wave (Ewald's sphere) with its origin coinciding with the object, and Debye diffraction cones

Fig. 2.6.3a - Schematic representation of XRD linear detector

Fig. 2.6.3b – Schematic representation of photographic film showing Debye rings intersecting the direction of scan in a single point

Fig. 2.6.4 - Diagram of wave interacting with an object producing scattered spherical wave (Ewald's sphere) with its origin coinciding with the object, and Debye diffraction ring generated by the interception with an IP

Fig. 2.6.5 - Diffraction pattern in the standard format as relative intensity versus 2θ of matrix Area 4 of ALHA77307 showing identified mineralogical phases.

Fig. 2.6.6 - GeniX Cu high flux X-ray source equipped with INEL 120º position sensitive detector (PSD) linear detector

Fig. 2.6.7a - Optical camera image of sample ALHA77307 taken perpendicular to the polished thin section

Fig. 2.6.7b - Optical camera image of sample ALHA77307

Fig. 2.6.8a - Schematic representation of Rigaku D max Rapid II stage

Fig. 2.6.8b – Image of of Rigaku D max Rapid II at NHM

Fig. 2.6.8c - 2D diffraction pattern, collected on imaging plate detector, showing Debye-Scherrer rings originated by the incident beam scattered with a 2θ angle

Fig. 2.7.1a - SEM pictures of sample Acfer 094 showing a strip of Pt deposited above the area of interest in order to protect it from ablation and Ga-implantation during preparation

Fig. 2.7.1b - SEM pictures of sample Acfer 094 showing designated trenches to be milled on both sides on the Pt strip

Fig. 2.7.2a & b - SEM pictures of sample Acfer 094 showing at different angles a cross-sectional slice remaining between the two trenches milled capped by the Pt strip

Fig. 2.7.3a - SEM pictures of sample Acfer 094 showing FIB section welded to the needle of the micromanipulator and detached from the substrate while being lifted out

Fig. 2.7.3b - SEM pictures showing FIB sections of sample Acfer 094 welded to the copper grid

Fig. 2.8.1 - Schematic diagram of synchrotron facilities

Fig.2.8.1.1 - Graph showing correction applied to XANES spectra

Fig.2.8.1.2 - Graph showing L3 edges of XANES spectra from standards: San Carlos olivine (blue), Fe-oxyhydroxyde (orange), and Ferrihydrite (grey)

Fig. 2.8.1.3 - Calibration line obtained using our standard spectra

Fig. 2.8.1.4 - Calibration method used by Le Guillou et al., 2015 (a) Graph showing L3 and L2 edges of XANES spectra from QUE 99177

Fig. 2.9.1 - Diagram showing primary ion bean striking the sample surface

Fig. 2.9.2a – ^{18}O ion image of matrix Area 1of sample ALHA77307

Fig. 2.9.2b – ^{16}O ion image of matrix Area 1of sample ALHA77307

Fig. 2.9.2c – D/H ion image of matrix Area 1of sample ALHA77307

Fig. 3.1.1 - Element map of sample ALHA77307

Fig. 3.1.2 – Binarised image of ALHA77307 element map

Fig. 3.1.3- Binarised image of ALHA77307 element map showing micro fractures

Fig. 3.1.4 - Binarised image of ALHA77307 element map showing chondrules and CAIs

Fig. 3.1.5 - ALHA77307 Element map showing the 5 matrix Areas investigated

Fig. 3.1.6 – Compositional data from matrix regions of sample ALHA77307 plotted in a ternary Si-Fe-Mg (element wt %) diagram

Fig. 3.1.7 - Normalised element ratio diagram showing data of five different matrix regions in sample ALHA77307

Fig. 3.1.8 - Pie Charts of the different sample areas in sample ALHA77307

Fig. 3.1.9 – SE-element map of matrix ALHA77307 Area 1

Fig. 3.1.10 - Element map of matrix ALHA77307 Area 1

Fig. 3.1.11 - SE-element map of matrix ALHA 77307 Area 5

Fig. 3.1.12 - Element map of matrix ALHA77307 Area 5

Fig.3.1.13 - Secondary Electron images of whisker in the matrix of sample ALHA77307

Fig. 3.1.14 - SE Element map of whisker in the matrix of sample ALHA77307

Fig. 3.1.15 - Element map of whisker in the matrix of sample ALHA77307

Fig. 3.1.16 - X-ray diffraction pattern of the matrix areas investigated in ALHA77307

Fig. 3.1.17 - TEM investigations of matrix for sample ALHA77307

Fig. 3.1.18 - Bar chart reporting abundances of mineral phases in sample ALHA77307

Fig. 3.2.1 - Element map of sample MIL 07687

Fig. 3.2.2 - Binarised image of sample MIL 07687 element map

Fig. 3.2.3 - Binarised image of MIL 07687 element map showing micro fractures

Fig. 3.2.4 - Binarised image of MIL 07687 element map showing chondrules and CAI

Fig. 3.2.5 – MIL 07687 Element map showing the 5 matrix Areas investigated

Fig. 3.2.6 – Compositional data from matrix region plotted in a ternary Si-Fe- Mg (element wt %) diagram

Fig. 3.2.7 - Normalised element ratio diagram showing data of five different matrix regions in MIL 07687

Fig. 3.2.8 - Pie Charts of the different sample areas in MIL 07687

Fig. 3.2.9 - SE- element map of sample MIL 07687

Fig. 3.2.10 - SE-element map of matrix Area 5

Fig. 3.2.11 - Backscatter Electron images showing a whisker in the matrix of sample MIL 07687

Fig. 3.2.12 - SE Element map of whisker in the matrix of sample MIL 07687

Fig. 3.2.13 - Element map of whisker in the matrix of sample MIL 07687

Fig. 3.2.14 - Diffraction pattern of the matrix areas investigated in MIL 07687

Fig. 3.2.15 – X-ray diffraction pattern of the matrix area 5 investigated in MIL 07687

Fig. 3.2.16 – Bar chart reporting abundances of mineral phases in MIL 07687

Fig. 3.2.17a - SEM element maps of matrix in sample MIL 07687

Fig. 3.2.17b – Bulk Spectra of the foils in MIL 07687 consistent with Fe^{3+}

Fig. 3.2.18 – (a) SEM FIB section image of inner rim matrix in sample MIL 07687,
(b) X-ray Fluorescence map of FIB section image (red dashed box in a) of inner rim matrix in sample MIL 07687, (c) Spectra of different ROIs within the same foil all characterised by Fe^{3+} enrichments

Fig. 3.2.19 – (a) SEM FIB section image of rim matrix in sample MIL 07687,

(b) X-ray Fluorescence map of FIB section image (red dashed box in a) of inner rim matrix in sample MIL 07687, (c) Spectra of different ROIs within the same foil all characterised by Fe^{3+} enrichments

Fig. 3.2.20 – (a) SEM FIB section image of outer rim matrix in sample MIL 07687,

(b) X-ray Fluorescence map of FIB section image (red dashed box in a) of inner rim matrix in sample MIL 07687, (c) Spectra of different ROIs within the same foil with one spectra from ROI 1 (purple) is characterised by Fe^{2+} enrichments

Fig. 3.2.3.1 – Silicate grain in MIL 07687 surrounded by Fe-rich matrix suggesting that the source of water may have been the ice coating the grain and distributed outwards through capillary

Fig. 3.3.1 - Element map of sample QUE 99177

Fig. 3.3.2 - Binarised image of sample QUE 99177 element map

Fig. 3.3.3 - Binarised image of QUE 99177 element map showing micro fractures

Fig. 3.3.4 - Binarised image of QUE 99177 element map showing chondrules and CAIs.

Fig. 3.3.5 - QUE 99177 Element map showing the 5 matrix Areas investigated

Fig. 3.3.6 - Compositional data from matrix regions of sample QUE 99177 plotted in a ternary Si-Fe-Mg (element wt %) diagram

Fig. 3.3.7 - Normalised element ratio diagram showing data of five different matrix regions in sample QUE 99177

Fig. 3.3.8 - Pie Charts of the different sample areas in sample QUE 99177

Fig.3.3.9 - BSE of Area 4 in sample QUE 99177

Fig. 3.3.10 - BSE of Area 5 in sample QUE 99177

Fig. 3.3.11 - Element map of matrix Areas 4-5 in sample QUE 99177 red dotted line indicates the outline of the clast hosting Area 5, yellow boxes indicates Areas 4 & 5

Fig. 3.3.12 - Element map of matrix areas 4-5 in sample QUE 99177

Fig. 3.3.13 - Diffraction pattern of the matrix areas investigated in sample QUE 99177

Fig. 3.3.14 – Bar chart reporting abundances of mineral phases present in each individual area and sample QUE 99177 average values.

Fig. 3.4.1 - Element map of sample Acfer 094

Fig. 3.4.2 - Binarised image of Acfer 094 element map

Fig. 3.4.3 - Binarised image of Acfer 094 element map showing micro fractures.

Fig. 3.4.4 - Binarised image of Acfer 09407 element map showing chondrules and CAI.

Fig. 3.4.5 – Acfer 094 Element map showing the 5 matrix Areas investigated

Fig. 3.4.6 – Ternary Si-Fe- Mg (element wt %) diagram of compositional data from matrix regions of sample Acfer 094

Fig. 3.4.7 - Normalised element ratio diagram showing data of five different matrix regions in sample Acfer 094

Fig. 3.4.8 - Pie Charts of the different sample areas in sample Acfer 094

Fig. 3.4.9 - Element map of matrix Area 1

Fig. 3.4.10 - Element map of matrix Area 1- dotted yellow box outlines the Area 1in Fig. 3.4.8

Fig. 3.4.11 - SEM element maps of FIB section A, C and D of sample Acfer 094 matrix

Fig. 3.4.12 - SEM element maps of FIB sections of sample Acfer 094 matrix showing ROIs (in boxes) within the foils and related spectra

Fig. 3.4.13 - SE-element map of matrix Areas 4-5 in sample QUE 99177

Fig. 3.4.14 - Cartoon of model of chondrules redistribution in carbonaceous chondrites parent body

Fig. 3.5.1 - Pie Charts of samples ALHA77307, MIL 07687, QUE 99177 and Acfer 094

Fig. 3.5.2 - SE-element map of matrix in sample Acfer 094

Fig. 3.5.3 - Normalised element ratio diagram showing averaged data of matrix regions in ALHA77307, MIL 07687, QUE 99177 and Acfer 094

Fig. 3.5.4 - X-ray diffraction pattern of the matrix areas investigated in ALHA77307

Fig. 3.5.5 - X-ray diffraction pattern of the matrix areas investigated in MIL 07687

Fig. 3.5.6 - X-ray diffraction pattern of the matrix areas investigated in QUE 99177

Fig. 4.2.1a - Element Map of ALHA 77307 area 1acquired with FEI Quanta

Fig. 4.1b - Traced shapes around silicates phases, revealed by element map, in sample ALHA77307 matrix area

Fig. 4.2.2 - Threshold menu showing the Gaussian covering the whole range of pixels intensities

Fig. 4.2.3a - Image map of sample QUE99177 Area 2 acquired using the Ultra Plus.

Fig. 4.2.3b - Traced shapes around opaque phases thresholded within the dotted area of interest on Fig. 3.2.3a

Fig. 4.2.4 - Example of cumulative frequency plotted as a function of ln(*r*), using the modified geometric Folk & Ward (1957) equations of Blott & Pye

Fig. 4.2.5 - Diagram Mr-opaques versus Mr-silicates showing both corrected and uncorrected values of Mr-opaques and Mr-silicates

Fig. 4.3.1 - Diagram Mr-opaques versus Mr-silicates showing our data compared with CP IDPS data from Wozniakiewicz, 2012

Fig. 4.3.2a - Cumulative frequency curves plotted as a function of ln(*r*) of samples ALHA77307 using the modified geometric Folk & Ward (1957) equations of Blott & Pye

Fig. 4.3.2b - Cumulative frequency curves plotted as a function of ln(*r*) of samples MIL 07687 using the modified geometric Folk & Ward (1957) equations of Blott & Pye

Fig. 4.3.2c Cumulative frequency curves plotted as a function of ln(*r*) of sample QUE 99177 using the modified geometric Folk & Ward (1957) equations of Blott & Pye

Fig. 4.3.2d - Cumulative frequency curves plotted as a function of ln(*r*) of sample Acfer 094 using the modified geometric Folk & Ward (1957) equations of Blott & Pye

Fig. 4.3.3a - Histogram showing distribution of the radii for both the silicate and opaque phases for sample ALHA77307

Fig. 4.3.3b - Histograms showing distribution of the radii for both the silicate and opaque phases for sample MIL 07687

Fig. 4.3.3c - Histograms showing distribution of the radii for both the silicate and opaque phases for sample QUE 99177

Fig. 4.3.3d - Histograms showing distribution of the radii for both the silicate and opaque phases for sample Acfer 094

Fig. 4.4.1a - Image map of sample ALHA77307 area 1matrix aquired with Ultra Plus, showing the limited presence and relatively large size of opaque phases

Fig. 4.4.1b - Thresholding of the white phases using Image J emphasises the size and abundance of opaques

Fig. 4.4.1c - Thesholding of the grey pale phase using Image J emphasises the abundance of a Fe rich phase that seems to be the product of alteration of the opaques

Fig. 4.4.1d - Element map of sample ALHA77307 area 1matrix acquired with FEI Quanta, showing the Fe rich composition of the pale grey phase thresholded in Fig. 4.4.1c

Fig. 4.4.2a Element map of sample MIL 07687 acquired using FEI Quanta, showing particular of matrix region characterised by a clearly defined boundary between the two different type of matrix

Fig. 4.4.2b Element map of sample MIL 07687 acquired using EVO

Fig. 4.4.2c BSE image map of sample MIL 07687 aquired using EVO, showing the presence of Fe-rich (brighter), and Fe-poor (darker) matrix having different

Fig. 4.4.3a - BSE image map of sample MIL 07687 acquired using EVO

Fig. 4.4.3b Matrix image map of sample MIL 07687 area 1 acquired with Ultra Plus, showing evident aqueous alteration and limited presence and of relatively large size of opaque phases

Fig. 4.4.3c Thesholding of the white phases of same area using Image J emphasizing the size and abundance of opaques

Fig. 4.4.4a - BSE image map of sample MIL 07687 acquired using EVO.

Fig. 4.4.4b Matrix image map of sample MIL 07687 Area 5 acquired with Ultra Plus

Fig. 3.4.4c Thesholding of the white phases of same area using Image J

Fig. 4.4.5a - Image map of sample QUE 99177 Area 2 acquired with Ultra Plus

Fig. 4.4.5b - Thesholding of the white phases of same area using Image J

Fig. 4.4.6a - Image map of sample Acfer 094 area 1 acquired with Ultra Plus

Fig. 4.4.6b - Thesholding of the white phases of same area using Image J

Fig. 4.5.1a - Histogram showing distribution of the radii for the silicate phases for samples Acfer 094

Fig. 4.5.1b - Histograms showing distribution of the radii for the opaque phases for samples Acfer 094

Fig. 4.5.2 - Additive colour mixtures diagram showing the mixing of blue and green to produce cyan

Fig. 4.5.3 - Element map of Acfer 094 Area 1 matrix acquired using FEI Quanta

Fig. 5.1.1 - Meteorites of different classes plot in distinct fields on an oxygen isotope diagram from Wittke, 2008

Fig. 5.3.1.1 - Oxygen isotopic composition of chondrules from all classes of chondritic meteorites

Fig. 5.3.1.2 -3-isotopes diagram reporting meteorites and terrestrial planets data relative to the CAI slope =1 line

Fig 5.6.1a – Bulk composition of carbonaceous chondrites plotting on subparallel line

Fig 5.6.1b – Expanded scale of Fig 5.6.1a showing that Cm and CR lines pass through the compositions of the most primitive chondritic IOM

Fig. 5.7.1 - Oxygen three-isotope plot showing ALHA77307, MIL 07687, and QUE 99177 matrix date plotted with literature data for different compositions of major primary components of solar system matter

Fig. 5.9.1 - Oxygen three-isotope plot showing ALHA77307, MIL 07687, and QUE 99177 matrix data plotted with literature data for different groups meteorites

Fig. 5.9.2 - Oxygen three-isotope plot showing ALHA77307, MIL 07687, and QUE 99177 matrix date plotted with CP-IDPs literature data

Fig. 5.9.3 - Oxygen three-isotope plot of oxygen-rich presolar grain identified in ALHA77307 and QUE 99177

Fig. 5.9.4 - Histogram showing comparison between D/H ratios of QUE 99177, ALHA77307 matrices and distribution of D/H ratio in IDPs and carbonaceous chondrites

List of Tables

Table 3.1.1 – EVO 15L EDS analyses of selected matrix regions in ALHA77307

Table 3.1.2 - Table showing thresholding values of the different matrix regions in sample ALHA77307

Table 3.1.3 - Table showing abundances and average values of each individual gray scale unities and in different matrix regions in ALHA77307

Table 3.1.4 - Table showing abundances of the mineral phases calculated using micro-XRD in each area and sample average values of ALHA77307

Table 3.2.1 - EVO 15L EDS analyses of selected matrix regions in MIL 07687

Table - 3.2.2 - Table showing thresholding values of the different matrix regions in MIL 07687

Table 3.2.3 - Table showing abundances and average values of each individual grey scale unities and in different matrix regions in sample MIL 07687

Table 3.2.4 - showing abundances of the mineral phases calculated using micro-XRD in each area and sample average values in MIL 07687

Table 3.3.1 - EVO 15L analyses of selected matrix regions in QUE 99177

Table 3.3.2 – Table showing thresholding values of the different matrix regions in sample QUE 99177

Table 3.3.3 - Table showing abundances of the mineral phases calculated in each area and sample average values in QUE 99177

Table 3.3.4 - showing abundances of the mineral phases calculated using micro-XRD in each area and sample average values in QUE 99177

Table 3.4.1 - EVO 15L analyses of selected matrix regions in Acfer 094

Table 3.4.2 - Table showing abundances and average values of each individual grey scale unities and in different matrix regions in sample Acfer 094

Table 3.4.2 - Table showing thresholding values of the different matrix regions in sample Acfer 094

Table 4.1 - Geometric mean radii, standard deviation values on the mean for silicates and opaque phases for samples ALHA77307, MIL 07687, QUE 99177 and Acfer 094.

Table 5.7.1 – Bulk oxygen isotope data for ALHA77307, MIL 07687, and QUE 99177 matrix

Table 5.8.1 – Showing bulk D/H ratios measured on samples QUE 99177 and ALHA77307

Table 5.9.1- Showing $^{17}O/^{16}O$ and $^{18}O/^{16}O$ ratios, size, and abundances of presolar grains in QUE 99177 and ALHA77307

Chapter 1

1. Introduction

1.1 - Star and Planet Formation

1.1.1 - Protoplanetary Disks and Chondritic Matrix

The Solar System formed from a cloud of interstellar dust and gas that collapsed under its own gravity forming the Sun and a rotating disk that eventually coalesced into planets. Astronomical observations of ‘‘proto-planetary disks’’ surrounding young stars have provided a large amount of information about the disks surrounding young stars such as: the mineralogy of the dust particles (e.g. Natta and Testi, 2006), and the gas and dust distribution within the disk (e.g. Fukagawa et al., 2013) (Fig. 1.1.1). These observations at ultraviolet through near-infrared to millimetre wavelengths tell us about conditions throughout a disk from the hottest regions to the coolest. This allowed understanding how young stars and their surrounding circumstellar disk form and evolve.

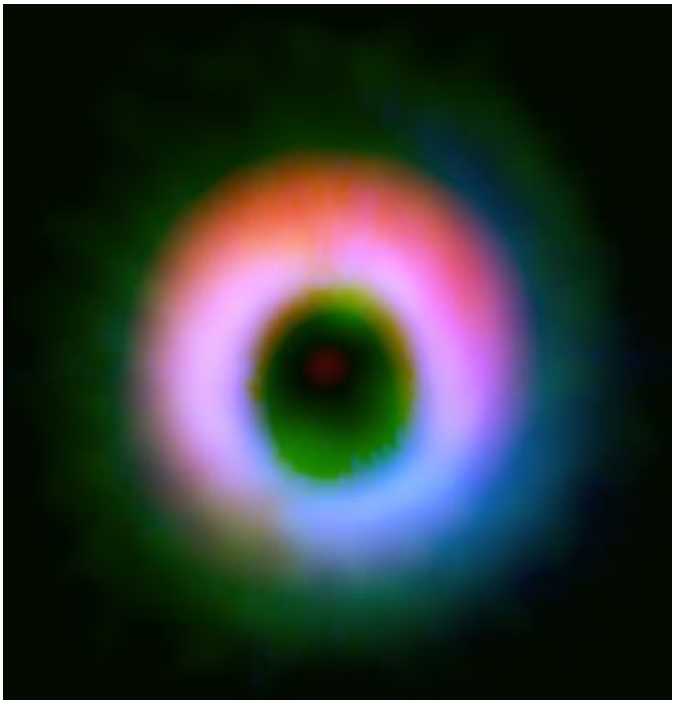

Fig. 1.1.1 – Composite image showing dust and gas disk around HD142527. The submillimeter emission from the dust and gas distributions observed by ALMA are shown in red and green, respectively. Near-infrared image taken by the NAOJ Subaru Telescope is shown in blue. The image shows that the dust is concentrated in the northern (upper) part indicated as the possible site for planet formation. Credit: ALMA (ESO/NAOJ/NRAO), NAOJ, Fukagawa et al., 2013.

Such disks originate by the conservation of angular momentum, as molecular cloud cores gravitationally collapse to stellar scales. The dust and gas that make up the disks are the materials from which planets form, and disks are the sites within which the planet originate. The mass of proto-planetary disks is dominated by gas (e.g. Natta and Testi, 2006) but dust grains, organics and ices, which make up the solid component of the disk is crucial for the formation of the planetesimals as these dust grains coalesce together and eventually form planets. Gas and dust in the disks are natural precursors of planetary systems, and while most of the earliest material has been extensively processed by geological events, some of it has remained relatively unchanged, and is preserved within primitive meteorites that originate in the asteroid belt. These primitive meteorites are remnants from the disk stage of Solar System evolution and they contain fine grained matrix that preserves primitive dust. The presence of amorphous silicates indicates that the matrix is primitive and has not experienced thermal metamorphism, as even a small increase of temperature would have converted the amorphous silicates into crystalline mineralogical phases (e.g. Brearley, 1993). Much of the information we have gathered about planet formation was obtained from astronomical observation. However, cosmochemical studies are also very important, complementing the astronomical observations with detailed knowledge obtained from the direct study of objects formed during the earliest stages of the formation of our Solar System. Understanding the physical and chemical evolution of the matrix in primitive meteorites provides a unique opportunity to help understand better the precursor material from which the Solar System formed and the processes operating on the fine dust.

1.1.2 - Star Formation

According to the current understanding of the processes leading to star formation, stars form in a disk galaxy when massive ($\sim 10^7$ $M_\odot$) (Vogel, Kulkarni & Scoville, 1988; Sakamoto et al., 1999). Molecular clouds condense out of the diffuse ISM owing to

gravitational instabilities, and this usually starts in the spiral arms regions (e.g. Elmegreen 1980; La Vigne, Vogel & Ostriker, 2006). The diffuse ISM passes high levels of internal turbulence onto the most massive structures, and this combined with self-gravity causes fragmentation into giant molecular clouds (GMCs), as well as clumps within the GMCs (e.g. McKee et al., 2007).

Some of the densest regions created by turbulence become self-gravitating cores, which, due to the turbulent flow, are frequently clustered. Dense cores undergo collapse, and the collapse of a core leads to the formation of a rotating disk. A combination of processes that transport angular momentum outward is responsible for the accretion. Processes that transport angular momentum in young stellar object (YSO) disks include: hydrodynamic, Magnetohydrodynamic (MHD), or self-gravitating mechanisms (e.g. McKee et al., 2007).

The hydrodynamic mechanism is the simplest transport mechanism that develops a velocity field through convection to transport angular momentum outward (e.g. McKee et al., 2007). In the MHD mechanism, weakly or moderately magnetized differentially rotating disks are subject to a powerful local instability (Balbus et al., 1991). MHD winds generated by this instability may remove angular momentum from disks, driving the matter remaining in the disk to accrete in order to maintain centrifugal balance (e.g. McKee et al., 2007). The self-gravitational mechanism is the gravitational force applied on the dust and gas particles making up the disk, by the particles themselves that allows them to be held together. Self-gravity is likely to be particularly important during the embedded stage of disk evolution, when disk masses are the largest significant mass transport owing to a self-gravitating rotational force (Mayer et al., 2004).

If the protostar is still accreting dust and gas from the surrounding cloud, the surface of circumstellar disks emits powerful winds. These are magnetocentrifugally driven, and the inner portion of the wind emerging nearest the central star, due to magnetic hoop stresses becomes collimated into a jet-like flow. Outflows become broader over time (Arce &

Sargent, 2006), and the impact of a wide-angle, stratified disk wind on the protostellar core sweeps up much of the ambient gas into a massive molecular outflow. The development of winds and outflows is very important, as they are a mechanism contributing to transport in disks. Winds during the main lifetime of the disk remove some of the dust and gas that make up the disk, and the remnant part accretes into planets or is removed by photoevaporation (McKee et al., 2007).

1.1.3 - Cloud collapse and disk formation by conservation of angular momentum

Stars are considered the "atoms" of the Universe (McKee et al., 2007). Understanding how stars and planetary systems form is the focus of modern astrophysics.

Star formation is important to unravel, as most of the elements we are made of are formed in stars, and the star forming process is intimately linked with the formation and early evolution of planetary systems.

Stars form from the agglomeration of lower-density material. It has long been suggested that the gravitational collapse of molecular clouds is a means of forming stars (e.g. Shu, Adams & Lizano, 1987). Star-forming regions are characterised by supersonic turbulent velocities (e.g. Allan, 2004) and as they impose density variations within the flow the density becomes strongly structured. This density structure is crucial to the star-formation process.

Allan (2004) has modelled the collapse of a molecular cloud assuming that the cloud must start very close to force balance. For simplification, the model involves only two forces always present in a finite temperature molecular cloud: gravity and gas pressure Fig. 1.1.2.

Interestingly, the collapse calculations reported a collapse wave that moves outward at the speed of sound causing an *inside-out* collapse and a constant accretion rate.

Clouds are seen to rotate, and so do planetary systems, suggesting that rotation plays an important role. The centrifugal force can combine with gas pressure to balance gravity,

tending to assume a toroidal (doughnut- shaped) configuration (Toomre, 1982; Hayashi, 1982) Fig. 1.1.3. The four forces of gravity, gas pressure, rotation, and magnetism can all interact to form the force-balanced configuration (Allen et al., 2003) undergoing inside-out collapse leading to growth of a pointmass, and accretion proceeds at a constant rate.

Conservation of angular momentum is a physical property of a spinning system such that its spin remains constant unless it is acted upon by an external torque. Due to the toroidal field generated from angular momentum conservation during the collapse; the angular momentum is transported upward and away from the pointmass.

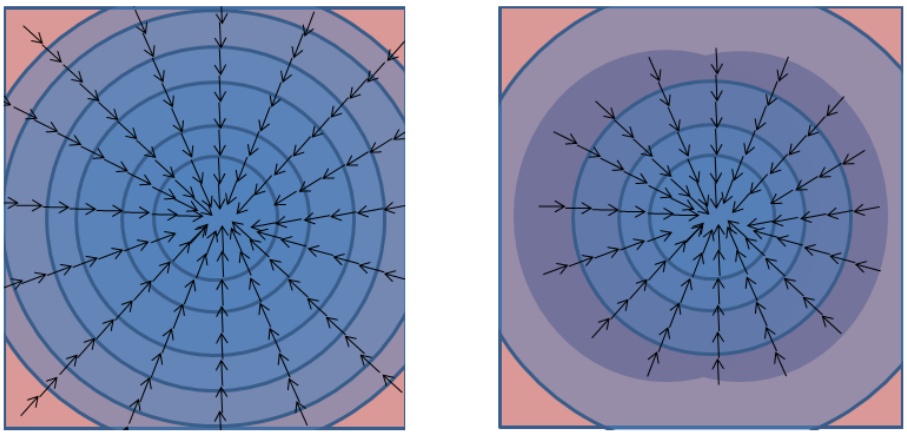

Fig. 1.1.2 – Illustration showing snapshot of the collapsing of an un-magnetised non-rotating isothermal sphere (right) and magnetised isothermal toroid with uniform rotational velocity (left). Shaded iso-density regions are shown I same colour; adapted from Allen, 2004.

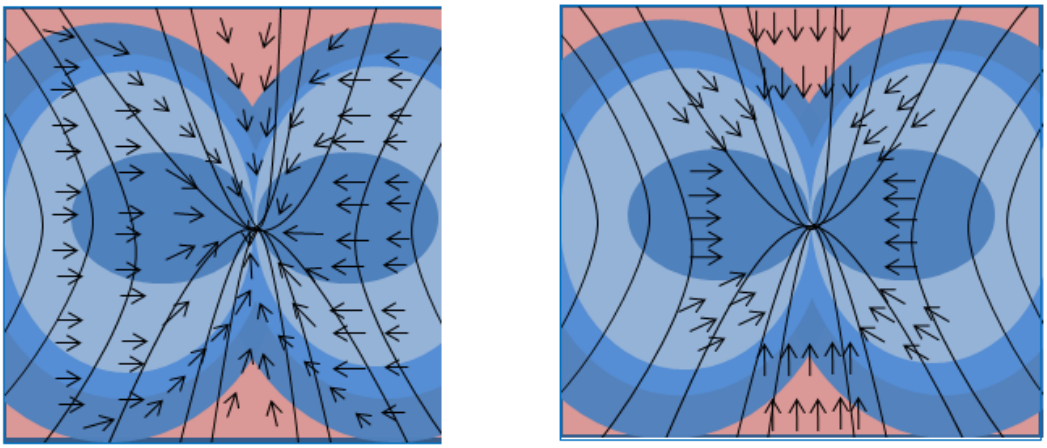

Fig. 1.1.3 – Illustration showing snapshots of the collapse of an un-magnetised non-rotating isothermal toroid (right) and magnetised isothermal toroid with uniform rotational velocity (left). Shaded iso-density regions are shown I same colour; 3D unit vectors show the direction of fluid flow, and solid lines show the magnetic field; adapted from Allen, 2004.

1.1.4 - Early hot disk hypothesis

The idea that the Solar System was born out of a protoplanetary disk originates back to 1755, when Kant, a German philosopher realized that all planets in the Solar System rotate around the Sun in the same plane and in the same direction which must mean that they all have a common origin in a flat rotating solar nebula. Forty years later, Laplace, a French mathematician created a model based on Kant's model, where the Sun was already formed and rotating, and according to the model the Sun had its atmosphere extending beyond the distance of the farthest planet. Laplace assumed that the Sun would start cooling down radiating away its heat, and as consequence of this cooling depressurised, and contracted. According to the law of conservation of angular momentum, the decrease in size would be followed by an increase in the Sun's rotational velocity. As a result, centrifugal forces would push the material in the Sun's atmosphere outward, while gravitational attraction would pull it toward the central mass. The balance of these forces would produce rings of material left behind in the plane of the Sun's equator, and each of these rings then would have coalesced to form a planet. The Kant-Laplace nebular hypothesis where the Sun is the only source of heat, was widely accepted for about 100 years (Owen, 2016). Developments have been made since then, and in the late1970s Scalo (1977) studied the heating of dense interstellar cloud by the drift between neutral gas and charged particles called magnetic ion slip. He constrained the cloud magnetic field strength derivating a semi-empirical upper limit, including in the equilibrium calculations: cooling by rotational transitions of CO, H_2 and inelastic gas-grain collisions. Today, it is well known that cosmic rays are an important source of heating in the interstellar medium, where they are a fundamental source of ionization influencing the chemical, thermal and dynamical evolution of the molecular cloud (Padovani et al., 2009). The matrix of primitive meteorites also, demonstrates that

the early hot disk hypothesis can't possibly be true. The matrix it is in fact characterised by the presence of low temperature constituents, such as amorphous silicates and organics, intimately associated with high temperature material, such as anhydrous silicates.

1.2.5 - Heating mechanisms of the disk

Protoplanetary disk heating and evolution is driven by spiral density waves (Rafikov, 2016). Recent high-resolution observations of protoplanetary disks using optical and near-IR bands have revealed the presence of remarkable non-axisymmetric structures such as spiral arms seen on scales of tens to hundreds of au and exhibit rather open morphology (Muto et al., 2012; Boccaletti et al., 2013; Grady et al., 2013; Wagner et al., 2015). Since the spirals in protoplanetary disks were first discovered it has been hypothesized that these structures are density waves excited, most likely by giant planets causing perturbances (Muto et al., 2012; Grady et al., 2013; Benisty et al., 2015). These spiral arms, not only reveal the possible presence of planets, but also have interesting heating effects on the disk itself. Energy is released and angular momentum transports across the disk. Density waves, in fact, carry momentum and energy in the form of heat, which is passed on to the disk. This exchange affects the global properties of the disk and leads to its evolution, as shown by Goodman & Rafikov (2001) and Rafikov (2002a). The increase of the velocity dispersion in the radial and azimuthal directions through scattering by spiral density waves can lead to anisotropy of the particle motions in the plane and in the vertical direction. As a result, bending instability can develop in the disk. Rafikov, (2016) confirmed the existence of bar bending instability that was first detected by Raha et al., (1991). The dispersal of the disk induced by the planet or spiral can provide an alternative mechanism for its removal, complementary to the photo-evaporation by the stellar UV and X-rays (Rafikov, 2016).

A radiation-hydrodynamic model of a protoplanetary disc irradiated with an X-ray extreme ultraviolet (X-EUV) spectrum was proposed by Owen et al., (2010). They find a photo-evaporation rate two orders of magnitude greater than the case of EUV photo-evaporation

alone when the total ionizing luminosity is divided equally between X-ray and EUV luminosity. This demonstrates that, it is clear that the X-rays are the dominant driving mechanism for photo-evaporation. X-rays in fact, are capable of penetrating much larger columns (∼1022 cm−2), and therefore heat-up denser regions and at larger radius than the EUV (Owen et al., 2010).

The heating of the upper surface of the accretion disk caused by X-rays from the inner disk, produces mass loss driven by the thermal expansion. The heating causes the disk to swell, and an equatorial thermally driven wind arises from the accretion disk producing this outflowing gas (Higginbottom et al., 2016).

1.1.6 - Effect of gas drag on particles

The effect of gas drag is the mechanism that facilitates accretion of proto-planets (Ormel et al., 2010). Planetary bodies around the stars form by accretion of smaller bodies, and a very efficient way to grow proto-planets is by accreting particles of size of chondrules, boulders, or fragments of larger bodies as they can be kept dynamically cold (Goldreich et al., 2004). However, these particles are travelling in a medium of gas, and the gas drag has some effects on the impact radii and the accretion rates of these particles.

In the early stages of planet formation, the gas affects the growth of dust to planetesimals by reducing the velocities of small particles. Initially, the (relative) velocities between particles are low allowing dust grains to accrete due to intermolecular forces (Dominik & Tielens, 1997; Blum & Wurm, 2000).

With increasing size (or, more correctly, increasing mass-to-surface area) particles couple less well to the gas and relative velocities increase, culminating in the so called meter size barrier, which, at our current level of understanding, can best be overcome by the combined efforts of turbulent concentration and gravitational collapse (Johansen et al., 2007, 2009; Cuzzi et al., 2010).

Gas drag affects also the collision rates between large bodies the size of planetesimals or protoplanets and small particles such as dust, chondrules, or boulders (Ormel et al., 2010). Bodies can accrete particles at a cross section larger than their geometrical cross section due to gravitational deflection (Safronov, 1969; Wetherill & Stewart, 1989; Greenzweig & Lissauer, 1990, 1992). However, this effect depends highly on the velocity at which the bodies approach, and if the velocity is too large, the accretion does not take place (Ormel et al., 2010). As a protoplanet grows, the random motion of the bodies it is accreting from is passed onto the growing body; and this slows down the growth (Ida & Makino 1993; Kokubo & Ida, 1998; Ormel et al., 2010a). Gas drag mitigates the effects of this by reducing random motions of the planetesimals. Moreover, the capture probability of planetesimals is also significantly increased when proto-planets are surrounded by atmospheres (Inaba & Ikoma, 2003; Tanigawa & Ohtsuki, 2010).

Ormel et al., 2010 concluded that small particles are very unlikely candidates to grow to planetesimals of $10 - 10^2$ km, since their trajectories are tightly coupled to the gas. However, if the protoplanet has reached a size of $\sim 10^3$ km it can very quickly accrete. Since these fragments do not suffer from the proto-planet gravitational scattering, accretion under such conditions favourite rapid growth, especially in the outer disk.

1.1.7 - Settling to mid-plane

In laminar discs, it is well known that gas drag causes the particles to sediment towards the disc mid-plane (e.g. Carballido et al., 2006). In the absence of turbulence, sedimentation takes place forming a very thin dust layer. As a result gravitational instability can occur, starting gravitationally bound clumps, leading to planetesimal formation (Goldreich & Ward, 1973).

The interaction of the sedimenting dust with the gas, however, may produce turbulence that inhibits gravitational instability (e.g. Gómez & Ostriker, 2005). Small particles are

strongly coupled to the fluid and essentially follow the gas whereas, larger particles, for which the coupling is weaker, start to settle despite the presence of turbulence (Turner et al., 2006) (Fig.1.1.4).

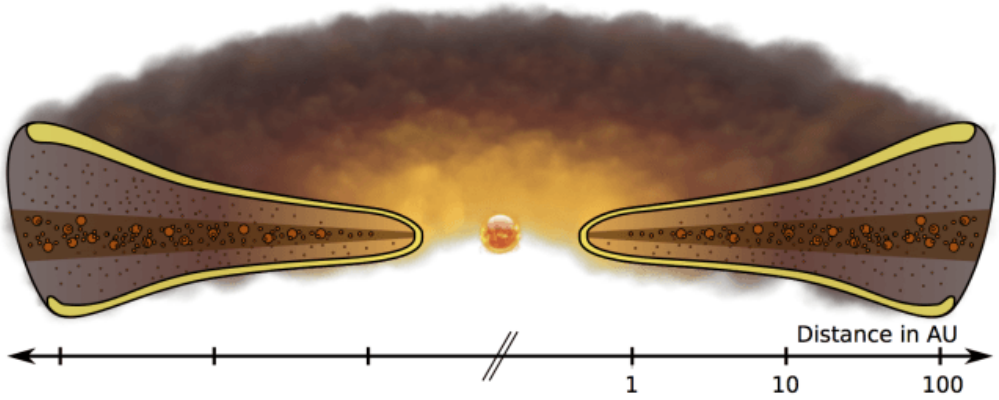

Fig. 1.1.4 – Illustration of a protoplanetary disk surrounding a young star showing larger dust particles concentrated near the disk mid-plane, while the small grains remain well-mixed vertically. Image from Wiersema, Iconset.

Turbulence is responsible for stirring the dust layer up to approximately 20 per cent of the disc scaleheight for particles of about 10 cm in radius at 5.2 AU (Fromang & Papaloizou, 2006). Therefore, dust particles of this size range cannot accrete, and as a consequence on a scale of 5 AU, the formation of planetesimals is obstracted until the particles have reached a much larger size (Fromang & Papaloizou, 2006). The conditions for gravitational instability in the outer regions of protoplanetary disk are such that bodies in the size range 50–600 m can accrete to form Kuiper belt-like objects with characteristic radii ranging from tens to hundreds of kilometres (Carballido et al., 2006).

1.1.8 - Radial mixing mechanisms

The outer regions of protoplanetary accretion discs are formed by material from the parent molecular cloud of the freshly forming stars, and the interstellar dust in this material is a mixture of unequilibrated grains. Mass accretion carries this material into the warm inner disc zones where it experiences chemical and thermal processing (e.g. Gail, 2004). Gail (2004) has modelled the processes responsible for the conversion of the interstellar dust

mixture into the chemically equilibrated dust mixture dominating the inner portions of protoplanetary discs, and the results of the model are in agreement with the composition of matrix material of primitive meteorites and dust in cometary nuclei.

Observations of dust from cometary nuclei have shown the presence of crystalline silicates in agreement with Gail, 2004 model (e.g. Zolensky et al., 2006). Since the formation of crystalline silicates requires high temperatures, in contrast to the amorphous silicates, it is surprising that comets have incorporated both high and low temperature materials, including ice, and this is also true for the matrix components.

Gail (1998) assuming that the nebula was already formed, studied the fate of amorphous silicates radially infalling onto the Sun. Using a stationary model of the nebula, he showed that the annealing of amorphous silicates was inefficient at heliocentric distances greater than 1.5 AU. This means that the temperature was too cold in the outer nebula in the comets forming region, for the interstellar silicate grains to be thermally processed prior to their incorporation to comets. The implications are that, either crystallization started at low temperature, as proposed for disks around evolved stars (Molster et al., 1999), or a considerable radial mixing was operating, and that mixed material from the hot parts of the solar nebula and the cold parts were combined in the comet forming region.

Evidence of concomitant presence of high and low temperature material in the same regions of the nebula is provided by the presence of chondrules and CAIs occurring associated with the matrix in meteorites. Moreover, the matrix itself is characterised by the presence of crystalline and amorphous silicates (e.g. Brearly, 1992), both having a completely different thermal history but occurring intimately associated with each other.

Bockelée-Morvan et al., (2002) investigated the formation of crystalline silicates in the inner hot regions of the solar nebula and their diffusive transport out to the comet formation zone, using a turbulent evolutionary model of the solar nebula. Fig. 1.1.5 illustrates the proto-planetary disk and its structure showing the effects of radial mixing

transporting dust from inner disk to the comet forming region. Bockelée-Morvan (2002) have shown that turbulent diffusion is an efficient process to carry crystalline silicates from inner to outer disk regions within timescales of a few 10^4 yr. This implies that all comets formed in the turbulent part of the solar nebula could have the same crystalline/amorphous silicates ratio. This is in agreement with available data on long-period comets.

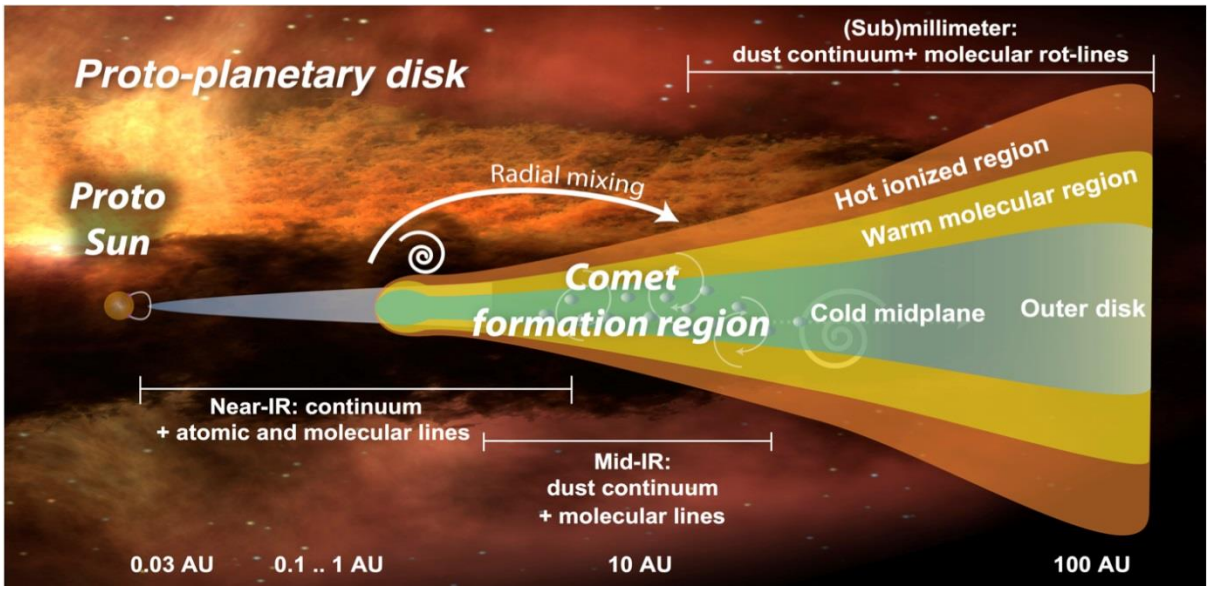

Fig. 1.1.5 – Illustration of proto-planetary disk and it's structure showing the effects of radial mixing transporting dust from inner disk to the comet forming region (Image credit: A. Mandell, NASA GSFC)

1.1.9 - Grain growth

The properties of dust in protoplanetary disks around optically visible pre-main sequence stars obtained have shown that grains in disks are on average much larger than in the diffuse interstellar medium (ISM) (Natta and Testi, 2006). In many disks, there is evidence that a large mass of dust is in grains with millimeter and centimeter sizes, more similar to "sand and pebbles" than to dust (Wilner et al., 2005). Smaller grains (with micron-sizes) exist closer to the disk surface, which also contain organic molecules, e.g. polycyclic aromatic hydrocarbons. There is some evidence of a vertical stratification, as in laminar disks it is well known that gas drag causes the particles to sediment towards the disc mid-plane (e.g. Carballido et al., 2006) leaving smaller grains closer to the surface.

Another difference between protoplanetary disks and the ISM is the higher fraction of crystalline relative to amorphous silicates found in disk surfaces (Natta and Testi, 2006).

Dust particles in the diffuse interstellar medium (ISM) are a mixture of silicates and carbonaceous grains, whose size distribution varies from about 100 °A to maximum radii of about $0.2 - 0.3$ μm, (e.g. Draine, 2003). Grains in protoplanetary disks are very different from grains in the diffuse interstellar medium; their properties change and evolve with time. In spite of the many uncertainties, the models suggest that grains can grow to very large sizes and settle under the effect of the stellar gravity, leaving a population of smaller grains closer to the disk surface and larger particles toward the mid-plane. Grain growth to centimetre and even metre-sizes is mainly driven by collisional aggregation, although gravitational instabilities may play a role in over-dense dust regions. Grain growth should be much slower in regions further away from the star than in regions closer to it, which should be completely depleted of small grains (Natta and Testi, 2006).

Grains experience major changes once the dust is incorporated into a protoplanetary disk, where the pristine interstellar grains may grow from sub-micron size, to kilometer-sized bodies like planetesimals, and eventually planets (Natta and Testi, 2006). The formation of dust grains provides solid surfaces important for chemical reactions and the freeze-out of molecular components such as CO and H_2O in the colder parts of disks. Finally, the solid mass of the disks is important because the dust grains are the building blocks, for the formation within the disk, of planetesimals and eventually planets.

1.1.10 - Diagnostic tools to disk detection

Gas and dust in disks are the precursor material of planetary bodies, and the mass of protoplanetary disks is dominated by gas. The dust grains which make up the solid component of the protoplanetary disk are fundamental for the evolution of the Solar System, and observations of light scattered on dust grains of protoplanetary disk and their

thermal emission are a key diagnostic tool to detect disks and to learn about their structure (Natta and Testi, 2006).

Protoplanetary disks around young stars are most readily detected through infrared observations. Their extremely high optical depth allows us to get information only on grains located at certain outer layer, which at optical and IR wavelengths detect a tiny fraction of the dust mass. The only way to measure the properties of the bulk of the dust mass is to go to longer wavelengths, where an increasing fraction of the disk becomes optically thin.

Emission from particles is not very efficient at wavelengths larger than their size, and particles much larger than the observing wavelength have a relatively small ratio of area to mass. Near infrared wavelength observations, therefore, tell us mainly about micron-sized dust grains, which represent the largest particles of the whole size spectrum of dust grains in the diffuse interstellar medium. Reviewed data from surveys of protoplanetary disks in clusters of different ages at millimeter, rather than micron, wavelengths (Williams, 2012) allow estimation the amount of dust throughout the disk, rather than simply the presence of warm dust close to the star. The data show that disks in young clusters have sufficient mass to form planets and solar systems of the scale of our own, but that the observed mass declines by over an order of magnitude within the next ~2 Myr (Williams, 2012). However, the rapid evolution of protoplanetary disks at millimeter wavelengths is not due to a decline in the disk mass but efficient agglomeration of dust grains from submicron to larger sizes within a few Myr (Williams, 2012). The low luminosities at millimeter wavelengths are due to the accretion of most of the dust in to relatively large particles with low surface area. These data are consistent with what observed in the disk around the star HL Tauri showing a rapid planetesimal formation (Brogan et al., 2015) (Fig. 1.1.6).

1.1.11 - Accretion times

Thanks to the new generation of telescopes, astronomers have been able to carry out large surveys in many regions of disks surrounding stars of different ages and measure their statistical lifetime. These infrared surveys show that disks are very common initially, found around about 90% of young stars with ages <1 Myr, but their occurrence decreases with star age such that <5% of stars have disks in clusters with ages >5 Myr (e.g. Williams, 2012, Haisch et al., 2001). The low disk frequency in stellar clusters over 5 Myr shows that the dust has been removed. The average disk lifetime was thought to be about 2 Myr (Williams, 2012). New images taken with the new Atacama Large Millimeter Array (ALMA) of telescopes in Chile, of the protoplanetary disk of HL Tauri (Fig.1.1.6) has shown that planets form earlier than previously thought, since the HL Tauri star system is only about one million years old, and the protoplanetary disk is characterised by large gaps within the disk formed by massive planets (Brogan et al., 2015). Evidence from meteorites are in good agreement with astronomical observations with the ^{182}Hf-^{182}W isotopic measurements of CAIs, metal-rich chondrites, and iron meteorites indicating that core formation in the parent asteroids of the magmatic iron meteorites occurred less than ~1.5 Myr after formation of CAIs (Kleine et al., 2005).

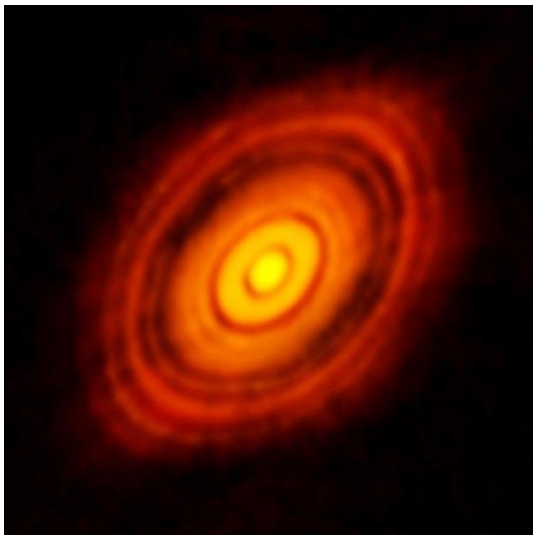

Fig. 1.1.6 - The protoplanetary disk of HL Tauri from ALMA showing large gaps in the disk created by forming planets (Brogan et al.,2015).

1.1.12 - Chemistry of the dust

The Infrared Space Observatory (ISO) and the latest generation of mid-infrared spectrographs on large ground based telescopes have revealed the presence of many new dust species, in addition to amorphous silicates, in the protoplanetary disks surrounding pre-main-sequence stars. The position and strength of the observed emission bands match well those of Mg-rich and Fe-poor crystalline silicates of olivine ($Mg_{2x}\,Fe_{2-2x}\,SiO_4$) and pyroxene ($Mg_x\,Fe_{1-x}\,SiO_3$), in particular their Mg-rich end members forsterite and enstatite respectively (x=1) (Natta and Testi, 2006) (Fig. 1.1.7).

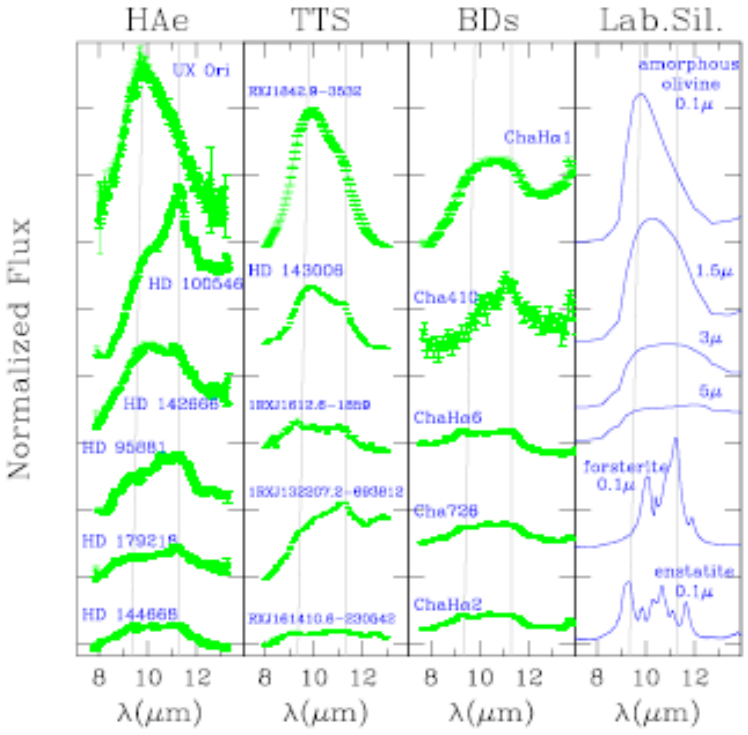

Fig.1.1.7 - Diagram from from Natta and Testi,2006 showing observed profiles of the 10 μm silicate feature for Herbig Ae stars (HAe) (van Boekel et al., 2004a), TTS (Bouwman et al., 2008), and BDs in Chamaleon (Apai et al., 2005). The dashed vertical lines show the location (at 9.8 μm) of the peak of small amorphous olivine (Mg_2SiO_4) and of the strongest crystalline feature of forsterite at 11.3 μm. The panel to the extreme right shows for comparison a selection of profiles of laboratory silicates. The top four curves shows amorphous olivine with different grain sizes (0.1 to 5 μm). The two bottom curves show the profile of small crystalline grains, forsterite (Mg_2SiO_4) and enstatite ($MgSiO_3$), respectively; larger crystalline grains have broader and weaker features (e.g., van Boekel et al., 2004b).

In addition to these components, evidence for FeS and SiO_2 has also been reported (Keller et al., 2002). The abundance of these dust species relative to amorphous silicates in protoplanetary disks is much higher than in the ISM and, therefore, indicates chemical and physical processing of the dust (e.g., Kemper et al., 2004). These dust species must be formed sometime during the collapse of the molecular cloud core or in the accretion disk surrounding the young star. There are several possible mechanisms that may be responsible for grain processing. In the innermost disk regions, where the dust temperature is above 1000 K, heat will induce a change of the grain lattice ordering leading to the transformation of amorphous silicates into crystalline phases such as olivines and pyroxenes. Above about 1200-1300 K, chemical equilibrium processes will lead to vaporisation and, upon subsequent cooling, gas-phase condensation of silicates, mostly in the form of crystalline forsterite. Local high-energy processes such as shocks and lightning as well as radial mixing may increase considerably the amount of crystalline silicates in the cool outer regions of the disk (Natta and Testi, 2006). Thermal annealing of amorphous, presumably Fe-rich silicates would lead to Fe-rich crystalline silicates (e.g. Brearley, 1993). Therefore, the Fe content of crystalline silicates may be used as an indication of the chemical processing that has occurred, however, the stoichiometry of interstellar amorphous silicates and in particular their Mg/Si and Fe/Si needs to be investigated further.

1.1.13 - Comparison of dust disks to Solar System components

The mineral composition of dust in protoplanetary disks can be compared directly to that of Solar System comets, asteroids and interplanetary dust particles (IDPs). The crystalline silicates in comet Hale-Bopp studied with ISO and from comet 81P/Wild 2 returned by the NASA Stardust mission are very Mg-rich and Fe-poor, similar to those in protoplanetary disks (e.g. Brucato et al., 1999 & Zolensky et al., 2006). Laboratory studies of IDPs of cometary origin also reveal the presence of Mg-rich crystalline silicates (e.g. Bradley,

1983). The situation for asteroids is much more diverse. Apart from Mg-rich crystalline silicates, many asteroids show Fe-containing silicates, probably related to parent body processing or to nebular processing in the inner solar nebula. Cosmochemical studies of extra-terrestrial material can complement the astronomical data observed to understand the physical and chemical properties of this precursor material from which our own Solar System formed. Primitive chondrites are particularly useful in this respect, since they come from asteroids (or at least part of asteroids) that never grew hot enough to melt, or indeed experienced high metamorphic temperatures. They are made up of millimetre-sized rocky beads called chondrules and millimetre to centimetre sized, irregularly shaped refractory inclusions surrounded by a fine grained, volatile-rich matrix. These primitive meteorite components all formed in the Sun's protoplanetary disk and did not experience significant changes since their formation. In this work the fine-grained matrix was specifically investigated to better understand chemical and physical properties of this precursor material.

Dust grains in protoplanetary disks are initially very small, typically around 1 μm or less in size. The existence of chondrules and refractory inclusions indicates that small grains were able to coalesce into much larger particles. Once solid bodies reached roughly 1km in size, gravitational forces became significant, therefore these planetesimals begin to interact between each other. The energy generated by impacts and the decay of radioactive isotopes increased temperatures in the interiors of planetary embryos (Tonks and Melosh, 1992), and when temperatures became high enough to cause partial melting, differentiation could begin. Some meteorites come from asteroids that have melted and differentiated, and many of which formed within the first 2Myr of the Solar System (Bizzarro et al., 2005; Schersten et al., 2006). This suggests that short-lived radioactive isotopes provided the heat needed to cause melting. Asteroids that formed later never grew hot enough to melt. However, primitive meteorites generally show signs of metamorphism and/or aqueous alteration at

temperatures between ~50 and 150 °C (e.g. Clayton and Mayeda, 1984; Zolensky et al., 1989) due to reactions involving water (Grossman et al., 2000).

1.1.14 - Oxidation state of the solar nebula

Primitive chondrites, being among the most pristine material available to us and preserving in the matrix the primordial dust of the protoplanetary disk, can give clues as to the oxidation state in the solar nebula where they formed. The solar nebula gas was very reducing (Krot et al., 2000), however, chondritic meteorites from which they formed show a wide range of oxidation states. They range from highly oxidizing conditions relative to the solar gas, responsible for the formation of the amorphous silicates in Acfer 094 (Hoppe et al., 2015), to highly reducing conditions relative to the solar gas; as shown by the lack of iron oxides in the minerals of enstatite chondrites. The state of Fe is a good petrographic indicator of oxidation state, and generally, in very reducing conditions only metallic iron is produced by condensation with almost no FeO in silicates or oxide condensates. In a gas of solar composition, forsterite (FeO-poor olivine) is the major phase to condense, with Fe condensing as metal. As the temperature decreases olivine is converted into enstatite. Conversely, oxidising conditions, which are associated with high oxygen fugacity (fO_2), are more easily recognisable in parent body processes. In these conditions, in the presence of water vapour, as the temperature decreases to 500K Fe-O bearing minerals become stable (Krot et al., 2000). Fayalitic olivine present in CAIs Allende for instance resulted from low-temperature alteration in the presence of aqueous solutions, and therefore does not reflect the redox conditions in the solar nebula (Krot et al., 1995, 1997, 1998 a,b, 1999). High contents of Si in Fe-Ni metal provide clear evidence for reducing nebula conditions in the region of enstatite chondrite formation (e.g., Keil, 1968), but there is also evidence of high-temperature oxidation in the solar nebula shown by the depletion of trace elements such as Mo and W in some CAIs (Fegley and Plame, 1985). All this evidence indicates considerable variation in the oxidation conditions of the solar nebula, the reasons for which

are still not fully understood. Highly oxidizing regions in the solar nebula might have been created by evaporation of icy presolar grains and highly reducing conditions might have been generated by the later condensation of these icy particles (Krot et al., 2000). Early accretion of reduced material in the inner solar nebula (e.g. Wänke, 1981) could also be responsible for the changes of oxygen fugacity in the solar nebula, leading to more oxidising conditions being established. Parent body processes and/or terrestrial weathering may also alter the primordial nebula signature, and it is challenging to discriminate between the effects of secondary processes and the original features. In this regard the investigation at the submicron scale of the matrix constituents using high resolution and high sensitivity techniques is essential.

1.2 - Chondrites

1.2.1 - Introduction

Chondrites are meteorites that provide the most detailed information about the origin of the Solar System. They are the oldest known rocks, their components formed during the birth of the Solar System ca. 4,568 Ma (e.g. Bouvier & Wadhwa, 2010), and their abundances of non-volatile elements are close to those in the solar photosphere (e.g. McKeegan et al., 2011). Studying chondrites helps us to understand environments and processes occurring at the birth of Solar System as they retain a wide range of components that record these processes. Chondrites are broadly ultramafic in composition, consisting largely of iron, magnesium, silicon, and oxygen. They are characterised by the presence of chondrules, which are igneous particles that crystallised rapidly in minutes to hours. Chondrites contain diverse proportions of three other components: refractory inclusions up to 3 %, metallic Fe-Ni (0.1–70%), and matrix material (1–80%) (Scott & Krot, 2007). Chondritic components formed at various locations within the protoplanetary disk over a period of several million years. Refractory inclusions probably formed close to the protosun at an

early stage when the disk was most active and accretion rates onto the protosun were highest (Wood, 2000, 2004). Chondrules probably formed over several million years in localised heating events near their accretion site with the youngest and oldest chondrules forming and accreting by different mechanisms (Kita et al., 2005; Scott and Krot, 2005b; Krot et al., 2005, Alexander et al., 2012).

1.2.2 - Chondrite Classification

1.2.2a - Chondrite groups

Chondrites have been classified into 15 groups: some meteorites do not fit comfortably into these groups and are called ungrouped, such as the unique meteorites Acfer 094 and MIL 07687. Thirteen of these groups form three classes: carbonaceous (CI, CM, CO, CV, CR, CH, CB, and CK), ordinary (H, L, and LL), and enstatite (EH and EL). The K and R chondrites do not belong to the three classes. Elemental ratios are commonly used for comparing chondrite compositions instead of concentrations, as some chondrites have excessive amounts of one component such as volatiles, in the form of inter-layer water and hydroxyl, organic carbonaceous material or metallic Fe-Ni, for example that dilute elements in other components. The elements silicon and magnesium are commonly used for normalising lithophiles and nickel is used for comparing siderophile elements. CI chondrites, which have the highest concentrations of volatile elements, are used as the reference standard because they provide the best match for the composition of the solar photosphere, neglecting the elements hydrogen, helium, carbon, nitrogen, oxygen, and the noble gases (e.g. Anders & Grevesse, 1989; Scott & Krot, 2007).

1.2.2b - Chondrite types

Chondrites are also classified into petrologic types 1–6, which indicate the extent of asteroidal processing, the degree to which they have been affected by secondary processes such as thermal metamorphism and aqueous alteration on the parent asteroid. Type 3 chondrites are the least metamorphosed and least aqueously altered; type 6 are the most metamorphosed. Type 1 chondrites, which lack chondrules, are composed almost entirely of minerals that formed during aqueous alteration. Type 2 chondrites are partly altered. Some of the type 3 groups has been subdivided into decimal subtypes, 3.0-3.9, of which 3.0 is the most primitive material that has suffered the least thermal processing.

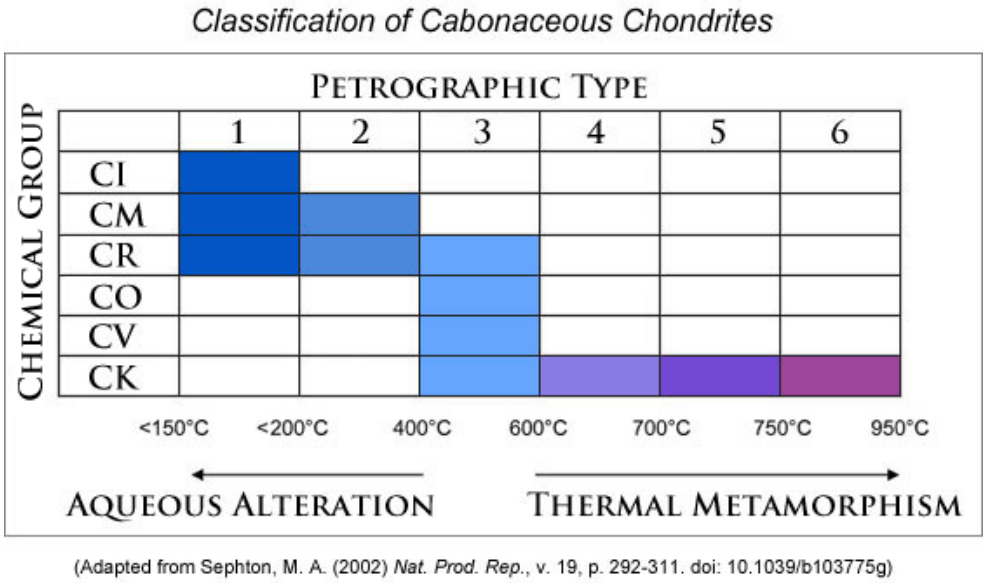

(Adapted from Sephton, M. A. (2002) *Nat. Prod. Rep.*, v. 19, p. 292-311. doi: 10.1039/b103775g)

Fig.1.2.1 - Chart summarizing the grouping of carbonaceous chondrites into chemical and petrographic types (by G. J. Taylor, 2011 PSRD). The chemical types are claimed to represent different asteroid parent bodies, while the petrographic types refer to various states of thermal metamorphism or aqueous alteration occurring on or within the parent bodies. Carbonaceous chondrites can be divided into those that show aqueous alteration and those that show thermal metamorphism. The blank boxes indicate the combinations that either do not exist or are very rare and have yet to be found.

1.2.2.1 - Carbonaceous Chondrites

Carbonaceous chondrites are grouped according to distinctive compositions thought to reflect the composition of the parent body from which they originated. Young et al. (1999) infer from oxygen-isotopic compositions that CI, CM, and CV chondrites could have been derived from different zones in a single, aqueously altered body. However, bulk chemical differences between these groups indicate fractionation during nebular processes. Most carbonaceous chondrites are thought to come from the low-albedo, C-type asteroids, which are the most abundant type between 2.7 and 3.4 AU (Bell et al., 1989). Lodders and Osborne (1999) suggest that CM and CI chondrites could be derived from a small fraction of comets that evolve into near- Earth objects after losing volatiles. More recently CM chondrites have been linked with a certain degree of confidence to the asteroid class known as Ch asteroid; these are defined by a 0.7-μm band, which indicates the presence of water and/or hydrated minerals on asteroids (Rivkin et al., 2015).

1.2.3 - Chondritic Components

1.2.3.1 - Chondrules

Chondrules are a major component of many primitive meteorites, accounting for up to 80% of their total mass (e.g. Jones et al., 2000). Chondrules are rounded beads composed mainly of silicates (Fig. 1.2.2) with textures that suggest they were heated to near the melting point and then cooled quickly within minutes to hours. Their short cooling times suggest that chondrules were heated in localised heating events that affected only a small portion of the solar nebula (Desch and Connolly, 2002).

They are composed largely of olivine and pyroxene, commonly contain metallic Fe,Ni and are 0.01–10mm in size. Some chondrules are rounded as they were once entirely molten

but many are irregular in shape because they were only partly melted or because they accreted other particles as they solidified.

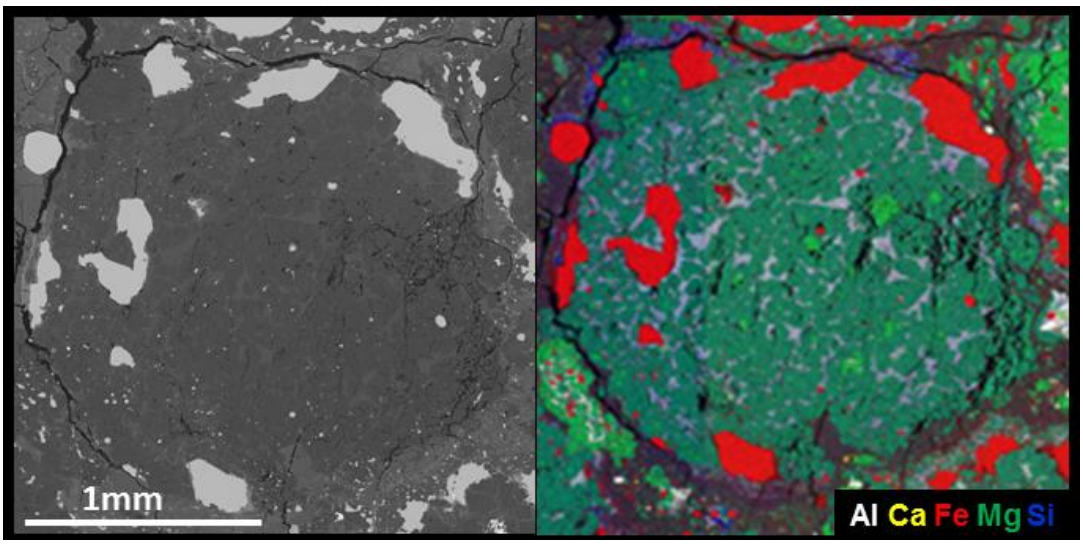

Fig. 1.2.2 – (a) Backscattered electron image of a chondrule in sample QUE 99177, (b) Element map of same chondrule.

1.2.3.2 - Refractory Inclusions

Refractory inclusions (Fig.1.2.3) are rarer than chondrules, and contain primarily refractory minerals (e.g. spinel ($MgAl_2O_4FeAl_2O_4$), melilite ($Ca_2Al_2SiO_7$), hibonite ($CaAl_{12}O_{19}$), Perovskite ($CaTiO_3$)) and appear to have been heated for longer than chondrules (Jones et al., 2000). Models suggest they formed under a narrower range of conditions than chondrules (Alexander, 2004), but it is unclear where they formed. Some models suggest they formed close to the Sun, since they show geochemical and petrological evidence that formed as fine-grained condensates from a gas of approximately solar composition in a high-temperature environment (>1300 K) at total pressure $\leq 10^{-4}$ bar. Some of them experienced subsequent re-melting to form distinct coarser igneous textures (Connelly et al., 2012).

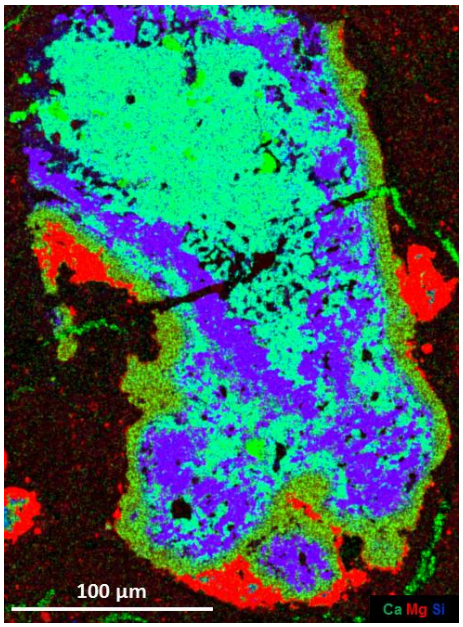

Fig.1.2.3 – Element map of one of a CAI in sample MIL 07687.

Radio-isotopes dating indicate that refractory inclusions are the oldest surviving materials that formed in the solar nebula (Connelly et al, 2012). They show signs of repeated heating episodes (Hsu et al., 2000; Huss et al., 2001), and their ages suggest they survived for several million years in the nebula before being incorporated into the parent bodies of primitive meteorites.

Refractory inclusions are tens of micrometers to centimetres in dimensions, lack primary volatile elements, and are the products of high-temperature processes including condensation, evaporation, and melting. Two types are recognized: calcium- and aluminium-rich inclusions or Ca–Al-rich inclusions (CAIs), and amoeboid olivine aggregates (AOA). CAIs are composed of minerals such as spinel, melilite, hibonite, perovskite, and Al–Ti-diopside, which are absent in other chondritic components (Scott & Krot, 2007).

1.2.3.3 - Metal and Troilite

Two kinds of metal are found in chondrites: Grains composed of refractory elements (iridium, osmium, ruthenium, molybdenum, tungsten, and rhenium), which condense along with the refractory oxides above ~1,600K from a solar gas at roughly 10^{-4} atm, and far more common grains composed predominantly of iron, cobalt, and nickel, which condense with forsterite and enstatite at ~1,350–1,450K (Campbell et al., 2005). The former are associated with CAIs (Palme and Wlotzka, 1976) and the latter with chondrules (Brearley & Jones, 1998) or found as isolated grains in matrix (e.g. Fig 1.2.4)

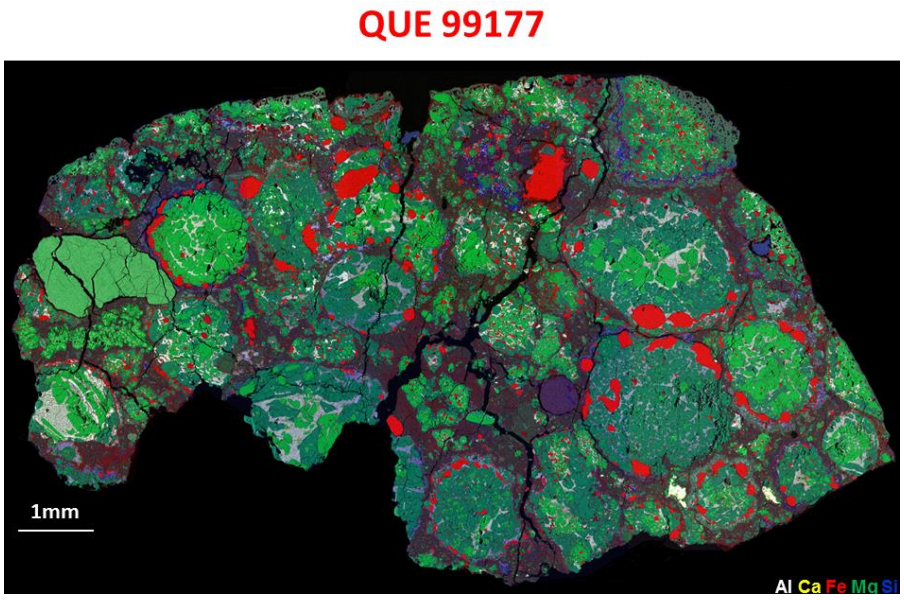

Fig.1.2.4 - Element map of sample QUE 99177 showing the presence of iron metal (in red).

Unfortunately, few chondrites preserve a good record of the formation history of their metal grains because subsequent low-temperature reactions formed oxides and sulfides and thermal metamorphism allowed kamacite to exsolve from taenite. Most grains of metallic Fe-Ni and troilite outside chondrules were probably lost from chondrules when they were molten. The size of metallic grains are roughly correlated with chondrule size (Skinner and Leenhouts, 1993; Kuebler et al., 1999; Schneider et al., 2003), but were probably modified by shock after compaction.

1.2.3.4 - Matrix Material

Matrix is fine-grained material made of sub-micron mineral grains that rims chondrules, CAIs, and other components and fills in the interstices between them (Scott et al., 1988) (Fig.1.2.5). Matrix grains are generally distinguished from fragments of chondrules, CAIs, and other components by their distinctive sizes, shapes, and textures. Minerals found in matrices include silicates, oxides, sulfides, metallic Fe, Ni, and especially in type 2 chondrites, phyllosilicates, and carbonates. Matrices are broadly chondritic in composition although richer in FeO than chondrules and have refractory abundances that deviate more from bulk chondrite values (McSween and Richardson, 1977; Bland et al., 2005; Huss et al., 2005).

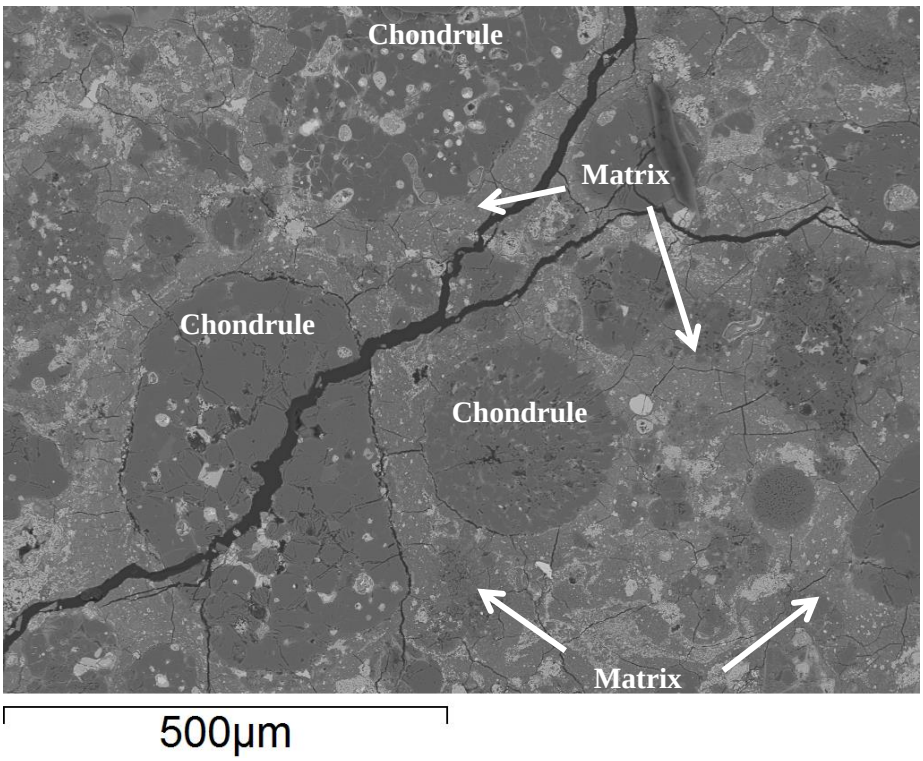

Fig.1.2.5 - Backscattered electron image of sample ALHA77307 showing matrix filling the interstices between chondrules.

Matrix typically accounts for 1–80 vol. % of the chondrite. Due to the small size of the grains, the study of the matrix is challenging, nevertheless progress has been made in identifying matrix components and understanding their origin. Since matrix is commonly

richer in volatiles than other components, it is commonly referred to as the ‘‘low-temperature component’’ of chondrites. But this strictly speaking is not correct as it is composed of diverse materials that formed under different conditions. Prior to detailed TEM studies and the acquisition of mineralogical and isotopic evidence for aqueous alteration on asteroids, all matrix minerals in carbonaceous chondrites including magnetite, carbonates, and phyllosilicates were thought to have condensed in the solar nebula (McSween, 1979). However, matrix minerals in most chondrites are now thought to be a complex mixture of presolar materials and nebular condensates that were mixed with fine chondrule fragments and experienced varying degrees of aqueous alteration and metamorphism depending on their parent body history (e.g., Scott et al., 1988). Matrix investigations are made difficult by the extremely fine grained nature of the constituents and the difficulty of distinguishing primary and secondary mineralogical features. The fine grain size (often as small as 50–100 nm), high porosity, and permeability of matrix cause it to be more susceptible to alteration by aqueous fluids and metamorphism in asteroids than other chondritic components.

There is evidence that matrix formation and chondrule formation are closely related (e.g., Brearley, 1993; Wasson, 2008), and Bland et al., (2005) highlighted the chemical complementarity between chondrules and matrix inferring that carbonaceous chondrite matrix formed from a material reservoir that was already depleted in volatile and moderately volatile elements.

1.2.3.4a - Chondrule Rims

Some chondrites show the presence of matrix material around chondrules called accretionary rims. In the least altered chondrites, chondrule rims are similar in chemical composition and mineralogy to the interstitial matrix material, although the rim material may be finer grained and lack clastic grains. The composition of rims on chondrules and on

CAIs appears indistinguishable. Rims are not uniform in width, but rim thickness is correlated with chondrule size within a chondrite group (Metzler et al., 1992; Paque and Cuzzi, 1997). However, matrix rims are absent in the CH, CB, and K chondrite groups. Clearly, matrix rims around chondritic components were acquired after the core components formed and before final lithification of these components into a rock.

Most authors believe that the chondritic components acquired their rims by accreting dust in the nebula (e.g., Morfill et al., 1998; Liffman and Toscano, 2000; Cuzzi et al., 2001; Cuzzi, 2004), although some argue that rims form in asteroidal regoliths (e.g., Symes et al., 1998; Tomeoka and Tanimura, 2000; Trigo-Rodriguez et al., 2006). A study of the Mokoia CV3 meteorite has shown that the mineralogical and petrographic characteristics of the chondrules and associated rims suggest that the alteration and metamorphism occurred within the meteorite parent body. However, the surrounding matrix does not show evidence of such alteration and metamorphism. This indicates that the alteration and metamorphism of the chondrules and their rims did not occur in situ. Based on this evidence the authors concluded that chondrules and rims are actually clasts transported from regions in the parent body different from the location where the host meteorite was finally lithified. A model has been proposed according to which chondrules and their rims experienced metamorphism and/or alteration elsewhere in the parent body and are actually clasts transported to the location where the host meteorite was finally lithified (Tomeoka, 2015).

1.2.3.5 - Organic material in carbonaceous chondrites

The carbonaceous chondrites contain up to 5% carbon in a variety of forms, including organic matter and, apart from some terrestrial contamination, these organic species were produced by non-biological methods of synthesis (Gilmour, 2003). Circumstellar space, the solar nebula, and asteroidal meteorite parent bodies have all been suggested as

environments where organic matter may have been formed and it is likely that all contributed to the final inventory.

Stable isotope studies have established that meteoritic organic matter contained material of probable interstellar origin (Yang and Epstein, 1985). Significant enrichments in ^{13}C, ^{15}N, and D detected in Murchison confirmed that a significant proportion of the solvent-extractable organic matter was indigenous to meteorites. The deuterium enrichments also provided strong evidence for the role of interstellar processes in the origin of meteoritic organic matter. Pearson et al., (2002) used an organic labelling technique to map the distribution of organic matter in the Murchison (CM2), Ivuna (CI1), Orgueil (CI1), and Tagish Lake chondrites. A strong association was observed between the distribution of organic matter and hydrous clay minerals, suggesting that the production of clays by aqueous processes influenced the distribution of organic matter in meteorites.

1.2.4 - Presolar Grains and Nucleosynthesis

It is known that the Solar System formed from pre-existing (presolar) interstellar dust grains (e.g. Fig. 1.2.6) and gas. Many grains originally formed in the circumstellar outflows of other stars. They were modified to various degrees, ranging from negligible modification to complete destruction in the interstellar medium (ISM) (Seab, 1987; Mathis, 1993). Finally, they were incorporated into the forming Solar System. Submicron-sized silicates and carbonaceous material are believed to be the most common grains in the ISM (Mathis, 1993; Sandford, 1996).

To better understand the process of Solar System formation, it is important to identify and analyse these presolar grains. These solid grains can be found in small primitive bodies like comets and asteroids that have undergone little, if any, parent-body alteration. Trace quantities of refractory presolar grains (e.g., SiC and Al_2O_3) survive in the matrices of the most primitive carbon-rich chondritic meteorites (Anders and Zinner, 1993; Bernatowicz and Zinner, 1996a; Bernatowicz and Walker, 1997; Hoppe and Zinner, 2000).

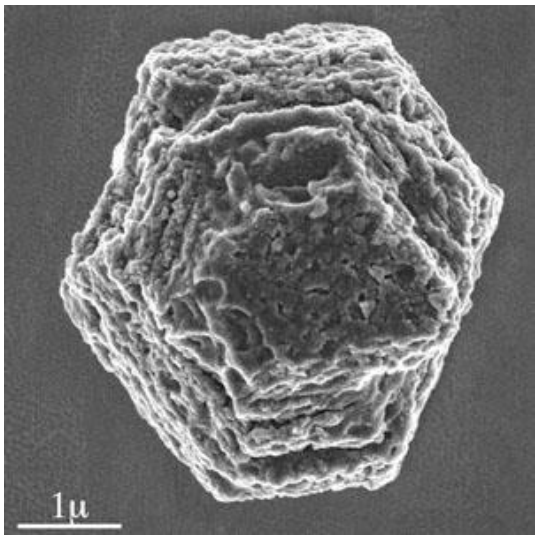

Fig. 1.2.6- Scanning electron micrograph of a SiC grain from the Murchison meteorite; the grain is about 2 microns in diameter. (Bernatowicz et al., 2003)

The stellar origin of presolar grains is recognised by their peculiar isotopic compositions, which are completely different from those of the Solar System and indicative of specific nucleosynthetic processes or events. Carbon and heavier elements are produced by nuclear reactions in stars and Burbidge et al. (1957) and Cameron (1957) provided a theoretical explanation for stellar nucleosynthesis. Nuclear processes produce elements with very different isotopic compositions, depending on the specific stellar source. The newly produced elements are injected into the interstellar medium (ISM) by stellar winds or as supernova (SN) ejecta, enriching the galaxy in ‘‘metals’’ (all elements heavier than helium) and after a long galactic history the Solar System is believed to have formed from a mix of this material.

Many different stellar sources must have contributed to the material that formed the Solar System (Burbidge et al., 1957) and (Cameron, 1957) and although astronomical observations indicate that some of this material was in the form of interstellar (IS) grains (e.g., Mathis, 1990), it was generally believed that it had been thoroughly homogenised in a hot solar nebula (Cameron, 1962). Presolar grains were discovered by tracking the carriers of anomalous noble gas components in density and size separated acid dissolution residues in carbonaceous chondrites. Primitive meteorites experienced varying degrees of

metamorphism on their parent bodies and these metamorphic processes affected different types of presolar grains in different ways. The abundance of different grain types can therefore give information about conditions in the solar nebula and about parent body processes (Huss and Lewis, 1995; Mendybaev et al., 2002). Davidson et al., (2014) for instance used SiC presolar grains to understand nebula/parent body processes, and found that the abundance in pristine meteorites such as ALHA77307 and QUE 99177 was: 11^{+4}_{-3} ppm and 44^{+24}_{-17}ppm respectively.

Several types of presolar grains have been identified, the most abundant being:

Silicon carbide

Silicon carbide (Fig. 1.2.6) is the most studied presolar grain type. It has been found in carbonaceous, unequilibrated ordinary, and enstatite chondrites. Many SiC grains show euhedral crystal features but there are large variations. Morphological studies by high-resolution SEM (Bernatowicz et al., 2003; Stroud and Bernatowicz, 2005) reveal detailed crystallographic features that give information about growth conditions. Such information is also obtained from TEM studies (Stroud et al., 2003, 2004b; Stroud and Bernatowicz, 2005; Hynes et al., 2006).

Diamond

Although diamond is the most abundant presolar grain species (~1,400 ppm) and was the first to be isolated (Lewis et al., 1987), it remains the least understood. The carbon isotopic composition of bulk diamonds is essentially the same as that in typical Solar System material (Russell et al., 1991, 1996) and diamonds are too small (the average size is ~ 2.6nm - hence nanodiamonds) to be analysed as single grains. Indeed a large percentage of the nanodiamonds presents in primitive meteorites may in fact originate in the solar nebula.

Graphite

Graphite is the third type of carbonaceous presolar grain and was isolated because it is the carrier of Ne-E(L) (Amari et al., 1990, 1995). SEM studies revealed two basic morphologies (Hoppe et al., 1995): dense aggregates of small scale ‘‘cauliflowers’’ and grains with smooth or shell-like platy surfaces ‘‘onions’’. TEM analysis of microtomed sections of graphite spherules (Bernatowicz et al., 1991, 1996b) found the surface morphology and chemical compositions provide information about physical properties such as pressure, temperature, and C/O ratio in the gas from which the grains condensed (Bernatowicz et al., 1996b, 2005; Croat et al., 2003, 2005).

Presolar silicates

Presolar silicate grains are the most abundant presolar grains and only relatively recently found in primitive meteorites using new technologies and well-chosen primitive samples. Messenger and colleagues have found silicates in IDPs (Keller and Messenger, 1999) K. Nagashima, H. Yurimoto and A. Krot have reported in situ discovery of presolar silicate grains in the matrices of Acfer 094 (Messenger, S. & Bernatowicz, 2000). These grains are usually, but not always, highly enriched in ^{17}O ($\delta^{17}O_{SMOW} > 100– 2000‰$), but have solar silicon isotopic compositions within analytical uncertainties, suggesting an origin in an oxygen-rich red giant or an asymptotic giant branch star (Nittler, et al., 1997, Lugaro et al., 1999). The estimated abundance of these presolar silicates (e.g. 52 ± 10 ppm in the matrix of CR chondrite Elephant Moraine 92161) is higher than reported for other types of presolar grains in meteorites (Leitner et al., 2016), consistent with their ubiquity in the early Solar System, but is about two orders of magnitude lower than their abundance in anhydrous interplanetary dust particles (Busemann et al., 2009) This result might be due to the destruction of silicates during high-temperature processing in the solar nebula.

1.3 –Matrix-chondrule complementarity

Chondrules and matrix are the two major components of carbonaceous chondrites (CC), and there is evidence that matrix formation and chondrule formation are closely related (e.g., Brearley, 1993; Wasson, 2008). The Mg/Si ratios of chondrules and matrices are complementary: chondrules have super CI chondritic Mg/Si ratios and matrices sub CI chondritic Mg/Si ratios (Hezel et al., 2010). Bland et al., (2005) also highlighted the chemical complementarity between chondrules and matrix inferring that carbonaceous chondrite matrix formed from a material reservoir that was already depleted in volatile and moderately volatile elements. This chemical relationship implies a common origins, thus must have formed from the same chemical reservoir, and later mixing. This constrains the chondrule formation process and the evolution of the protoplanetary disk. This interpretation is in contradiction with the X-wind model of chondrule forming processes according to which, chondrules and matrix have separate origin.

This complementarity can be explained in four different scenarios:

- Chondrules and matrix formed in a separate nebula region and mechanically mixed. This two-component model was proposed by e.g. Anders (1964), Larimer and Anders (1967, 1970), Grossman and Wasson (1982, 1983), Shu et al. (1996) and Alexander (2005), and the multi-component mixing model was proposed by Zanda et al. (2006).
- Exchange and redistribution of elements during metamorphism. These secondary processes must have happened after accretion into the parent body.
- Evaporation and re-condensation of e.g. Si from chondrules onto the matrix in the solar nebula. In this scenario, chondrules and matrix formed in the same reservoir.

- Predominant formation of Mg-rich grains from a CI chondritic reservoir. In this scenario, these Mg-rich grains were the starting material for chondrules. Whereas the Mg-depleted residue formed the matrix. In this case, chondrules and matrix again formed in the same reservoir.

1.4 - Purpose of Study

The types of meteorites that did not undergo significant thermal metamorphism and/or aqueous alteration to modify the mineralogy, petrology and texture of the overall meteorite, but that instead remained relatively pristine since their accretion, without experiencing significant changes, are known as "primitive meteorites". These extra-terrestrial materials are a particularly important type of meteorite as they preserve the closest physical and chemical properties of the solid component of the protoplanetary disk that was surrounding our young Sun at the very early stages of formation of our Solar System, and from which the planets and other celestial bodies eventually evolved. In particular the fine grained matrix material found among the coarser parts of the meteorites, such as chondrules and CAIs that act as a "glue" holding the rock together, is considered the most pristine remnants of this solid component of the disk.

Results from the study of samples of comet Wild2 returned by NASA Sturdust mission show that high temperature minerals were transported several AU from the inner regions of the solar nebula where they crystallised to the comet forming region in the outer disk (e.g. Zolensky et al., 2006). This means that a very efficient horizontal transport mechanism was operating prior to accretion and such a mechanism may also have affected a wider range of dust particles in the disk other than the restricted range of particles observed in the Sturdust samples. In that respect fine grained IDPs, to which matrix is often compared, have shown evidence of some aerodynamic sorting in the protoplanetary

disk (Wozniakiewicz et al., 2013). Similar aerodynamic sorting may also have affected the dust that eventually accreted into the parent bodies of the primitive meteorites. This has two important implications:

a) The matrix might be composed from constituents that formed in different regions of the solar nebula, from small heliocentric distances to the Kuiper belt, throughout the entire protoplanetary disk.

b) The matrix might have experienced aerodynamic sorting prior to accretion, with implications for mineralogical, chemical, and isotopic fractionation effects.

Isotopic studies of IDPs have revealed that, despite the turbulence and the horizontal transport, the protoplanetary disk was not isotopically homogeneous and shows evidence of discrete isotopic reservoirs within it (Starkey et. al, 2014). Considering that the matrix might have sampled different regions of the disk, similar to that shown by IDPs, the fingerprint of the different isotopic reservoirs might be still preserved in the matrix. Therefore the scientific questions addressed in this thesis are:

- How similar is the matrix to astronomical dust and to IDPs?
- Did the particles making up the matrix experience aerodynamic sorting prior to accretion?
- Considering the horizontal transport mechanism does, do the matrix constituents form at different AU within the protoplanetary disk. If so, are there differences between grains, and within matrix regions of the same meteorite?
- In terms of isotopic composition, does the matrix sample different reservoirs within the disk?
- Did parent body processes made significant changes into the physical and chemical properties of the dust particles after to accretion?

1.5 - Reason for choosing these samples

The aim of this project is to characterise the mineralogical diversity of primitive matrix (morphology, grain size and mineralogy) of pristine chondritic meteorites, to learn about its origins and any thermal and chemical processing it may have experienced.

For the purpose of this study The Open University meteorite collection provided:

- Un-grouped carbonaceous chondrite Acfer 094.

And the Antarctic Meteorite Working Group also provided the following three samples:

- CR2 chondrite QUE 99177
- CO3.0 ALHA77307
- Ungrouped MIL 07687

The unique carbonaceous chondrite Acfer 094 is among the most pristine meteorites known; it's fine-grained matrix comprises a highly unequilibrated assemblage of largely amorphous material, basically unaffected by secondary processes, with only minor amounts of serpentine and ferrihydrite present, as products of hydrous alteration (Greshake, 1997). The texture and chemical composition of the amorphous material are consistent with an origin by disequilibrium condensation in either the cooling solar nebula or a circumstellar environment (Greshake, 1997).

CR chondrites are particularly primitive meteorites, and QUE 99177 appears to be significantly less altered than most members of this group (Abreu and Brearley 2010).

ALHA77307 is largely unaltered, with abundant amorphous silicates and primitive carbonaceous matter (Abreu and Brearley 2010, Busemann et al. 2007). The recommended classification for ALHA77307 in the Meteoritical bulletin database is CO3.0.

ALHA77307 and QUE 99177 along with the ungrouped meteorite Acfer 094 were chosen for this project since they are among the most primitive meteorites that have been

minimally affected by low-temperature aqueous alteration (e.g. Brearley, 1993; Abreu and Brearley 2010; Greshake, 1997).

The ungrouped chondrite MIL 07687, has previously been classified as a CO3 chondrite, but has unique properties such as: an unusually high abundance of matrix, absent fine grained rims, and low abundances of refractory inclusions, that make it distinct from typical CO chondrites (Brearley, 2013). This unique meteorite shows evidence of a partial and localized aqueous alteration featuring FeO-rich regions of matrix characterised by a high abundance of ferrihydrite or akaganéite, and Fe-poor regions of matrix much finer-grained, homogeneous and, in the SEM, more closely resembling the matrices of low petrologic type CO3 chondrites such as ALHA77307 (Brearley, 2013). Despite showing effects of localised aqueous alteration, it is still to be considered pristine, since its matrix is characterised by the presence of amorphous silicates and presolar grains (Brearley, 2013; Davidson et al., 2014).

Acfer 094, QUE 99177 and ALHA77307, are among the most pristine meteorites known, and MIL 07687 is pristine with some evidence of partial aqueous alteration. Therefore these samples are good candidates in which to search for unequilibrated assemblages of matrix grains relatively unaffected by secondary processes, but also useful to investigate the extent and effects of aqueous alteration of these minute particles in the parent body.

Chapter 2

2. Methods

2.1 – Introduction

Samples, preparations and analyses

The aim of this project is to investigate the mineralogical heterogeneity of pristine chondritic matrix grains. Their morphology, size and mineralogy were observed, in order to learn about their origin and any thermal and chemical processing they may have experienced.

Four samples were chosen for being among the most pristine meteorites known: Acfer 094, QUE 99177, ALHA77307, and MIL 07687. All the samples were provided as polished thin sections, except for Acfer 094 which was provided as a polished resin block.

The use of a tiny fragment of the whole meteorite, prepared as a polished thin section or polished resin block, and interpretations of data obtained from them, are made by taking into consideration the bias that could have been produced by using a small fragment instead of the whole sample. In order to minimize the bias, five different regions of each sample have been investigated, in order to have the most representative possible results. Besides being potentially unrepresentative of the whole sample, thin sections are also offering only a 2D view of the sample, and this can induce errors especially when determining crystal size distributions. In this study, in order to eliminate the bias occurring in the size distribution (see chapter 4) a 2D-3D conversion was carried out to ensure the validity of the data.

All four samples were analysed using three different scanning electron microscopy (SEM) techniques: Zeiss EVO 15LS SEM, Carl Zeiss Ultra Plus, and FEI Quanta 650 FEG SEM.

Zeiss EVO 15LS SEM, due to its thermionic tungsten electron source is most suitable for low magnification investigations and microanalysis, and therefore is not capable of resolving the fine grained matrix. It was used to carry out an initial examination of samples and to select 5 regions of interest; the most representative areas of matrix and the most pristine areas away from form areas of alteration.

Carl Zeiss Ultra Plus, featuring a field emission gun, and its ultra-high resolution secondary and backscatter electron detectors, allowed high resolution imaging acquisition. This SEM was used to collect image maps resolving the discrete matrix grains within the matrix regions of interest. However, this technique is not suitable of providing chemical composition information of the individual grain, and therefore the selected matrix regions were subsequently investigated using the FEI Quanta 650 FEG SEM.

FEI Quanta 650 FEG SEM, equipped with the new design of the EDS XFlash QUAD 5040, which provides high resolution at high count rates due to the multi-channel nature of the Silicon Drift (SD) detector. This allowed the acquisition of the chemical element distribution, and it has been used to acquire element maps at high spatial resolution of the matrix regions of interest.

The samples QUE 99177, ALHA77307, and MIL 07687 were also investigated by X-ray diffraction. *In-situ μXRD* technique was used in order to identify the mineralogical phases making up the matrix and calculate their modal mineralogy. Due to the small sample surface area exhibited by the sample Acfer 094, which was provided as polished resin block, the application of the in-situ μXRD technique was not possible on this sample.

The samples Acfer 094 and MIL 07687, owing to the fact that both show peculiar styles of aqueous alteration: dry desert for Acfer 094, wet Antarctic and localised asteroidal for MIL 07687 were chosen to investigate the Fe oxidation state of the mineralogical phases making up their matrix using synchrotron techniques. In order to carry out these investigations, a FIB sample preparation technique was used.

Unaltered carbonaceous chondrite (CC) matrix is a mixture of fine-grained materials, composed largely of amorphous silicate, sub-micrometre forsterite and enstatite grains and micrometre sized aggregates of such crystals (Scott & Krot, 2007). Conventional scanning electron microscope (SEM) equipped with tungsten hairpin electron gun are not capable of resolving the individual grains due to a limitation of the spatial resolution achievable, which is related to the electron beam diameter. Two of the main limits on the beam diameter are the type of electron source and probe current used. Typical beam diameters at 0.1 nA probe current and 20 kV accelerating voltage are 2 nm for a field emission gun (FEG) W-source. The spatial resolution achieved in practice will depend on the sample, SEM operating conditions and electron source used. The new generation of SEMs improved considerably the spatial resolution, and are capable of resolving individual matrix grains at accelerating voltages as low as 3 kV. However, obtaining compositional information at these operating conditions is still very challenging. Transmission electron microscopy (TEM), in contrast, can provide microstructural, crystallographic, compositional and electronic information from micrometre to sub-nanometre sized regions of thin samples. Despite this technique being very useful for the investigation of fine-grained samples, it requires complicated and time consuming sample preparation. Observations are in fact undertaken on very small areas where it can be difficult to take into consideration the surroundings that can compromise understanding.

2.2 - Scanning electron Microscopy (SEM)

An electron microscope uses electron beam interaction with the sample to provide images. In the SEM the signals produced when the electron beam interacts with the specimen include backscattered electrons and secondary electrons and x-rays. Backscattered electrons are a significant fraction of the incident beam current that is scattered out of the specimen and depends primarily on the atomic number as well as the topography of the sample. They are an important signal collected for imaging that provides information related to the composition of the sample. Secondary electrons are electrons of the specimen ejected during inelastic scattering of the energetic beam electrons with atoms in the specimen. The secondary-electron emission is confined to a volume near the point of interaction between the beam and the sample's surface. After undergoing additional scattering events while traveling through the specimen, some of these ejected electrons emerge from the surface of the specimen. Secondary electrons are the main source of electrons for viewing images in the scanning electron microscope (SEM).

Energy Dispersive X-Ray Analysis (EDX) is a technique that identifies elements and provides quantitative compositional information. It relies on an interaction of some source of X-ray excitation and a sample. Its characterization, depend on the fundamental principle that each element has a unique atomic structure allowing a unique set of peaks on its electromagnetic emission spectrum. The data acquired by EDX analysis are energy spectra characterised by peaks corresponding to different elements present in the sample. Spectra can be acquired while the microscope is in imaging mode, producing maps of the distribution of chemical elements in the sample. The different types of measurements cannot always be optimised on one instrument and therefore for the purpose of this project a combination of the following different SEMs, all having different specifications, were used:

- Zeiss EVO 15LS SEM
- Carl Zeiss Ultra Plus
- FEI Quanta 650 FEG SEM

2.3 - Zeiss EVO 15LS SEM

Zeiss EVO 15LS SEM is a thermionic tungsten electron source SEM (Fig.2.3.1) suitable for applications where high brightness (defined as the current density per solid angle) is not necessary, such as low magnification, or where stable high currents are required as in x-ray microanalysis.

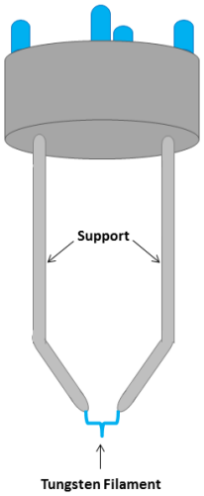

Fig. 2.3.1- Diagram showing thermionic tungsten electron source of the type used in EVO 15L SEM (adapted from Hat'nCoat, 2008)

The Zeiss EVO 15LS SEM was used to carry out an initial examination of samples. Elemental analysis were acquired with an electron beam at an acceleration voltage of 20 kV, beam current of 3.0 nA, spot size 593, magnification ×300 and image dimension of 512×512 pixels; X-ray detection limit ~ 0.1- 0.3 mass % depending on the element. The samples were imaged through automated analyses using Oxford Instruments INCA software's feature mode. The entire specimen area was: ~ 80 mm^2 for ALHA77307, ~24 mm^2 for MIL 07687, ~70 mm^2 for QUE 99177 and ~25 mm^2 for Acfer 094. Backscattered

electron and X-ray element map montages (Fig.2.3.2) acquired for ~ 50 hours were also obtained automatically stitched together using Oxford Instruments INCA software's montage mode. The element maps were primarily used to carry out a preliminary survey of the samples in order select the matrix regions of interest to investigate further using SEMs capable of achieving much higher spatial resolution more suitable to investigate fine grained material, such as the Carl Zeiss Ultra Plus Field Emission SEM for ultra-high resolution image maps and the FEI Quanta 650 FEG SEM for elemental analyses.

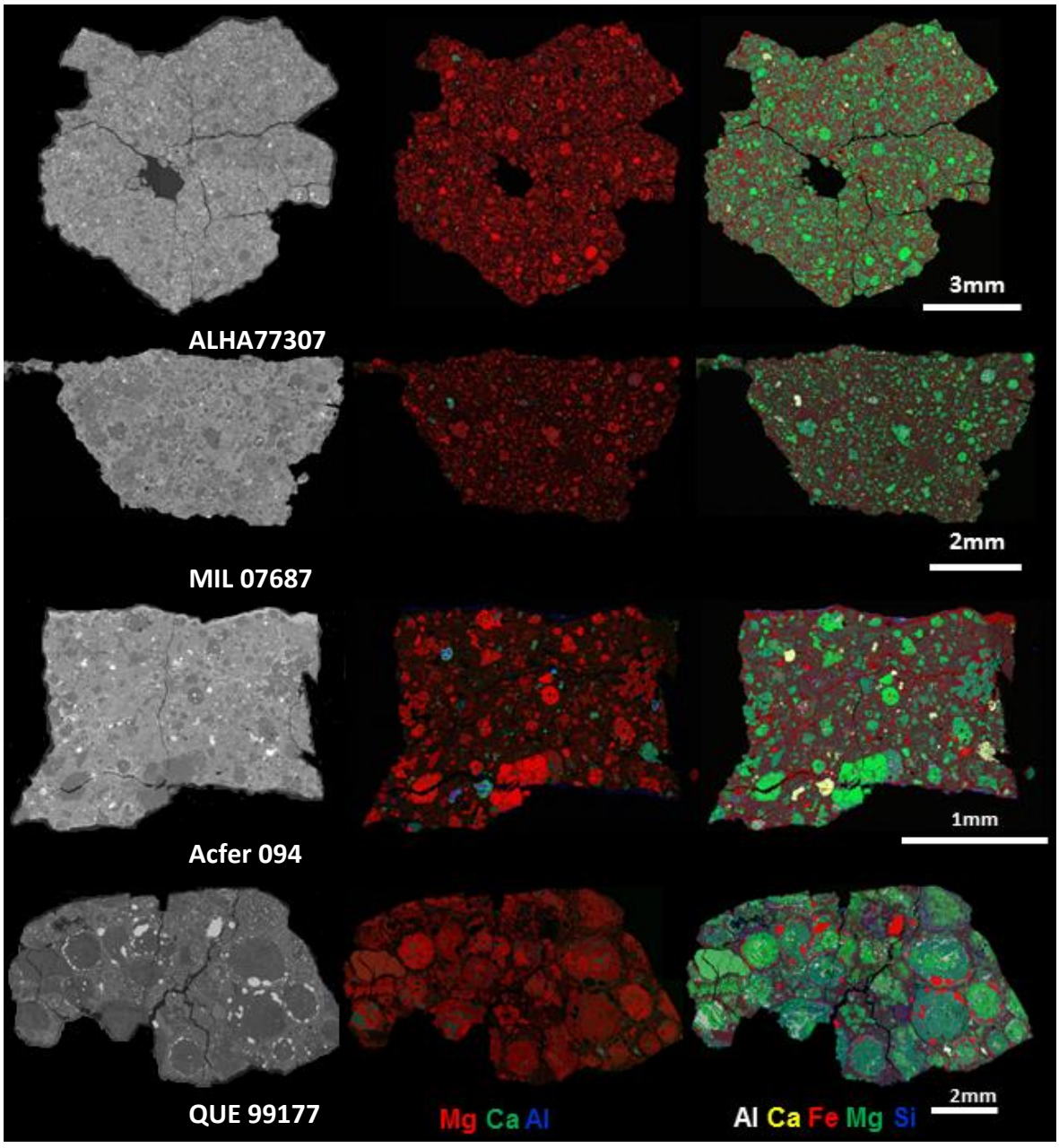

Fig.2.3.2 Backscattered electron and X-ray element map montages of ALHA77307, MIL 07687, Acfer 094 and QUE 99177 acquired using Zeiss EVO 15LS SEM

2.4 - Carl Zeiss Ultra Plus

Carl Zeiss Ultra Plus is a FEG (Field Emission Gun) SEM capable of achieving ultra-high resolution images. A field emission gun, such as the one fitted on this microscope, is a brighter source of electrons compared to the typical thermionic tungsten filament in the EVO 15L discussed above. The field emission cathode is usually a wire of a single-crystal of tungsten shaped into a sharp point and spot welded into a tungsten hairpin (Fig.2.4.1). The advantages of having a small tip, usually 100 nm, is that by applying a large potential gradient between the tip and the closely spaced first anode field emission from the tip is achieved, producing high current from a very small area, hence high brightness. A second anode is used to accelerate the electrons to the operating voltage.

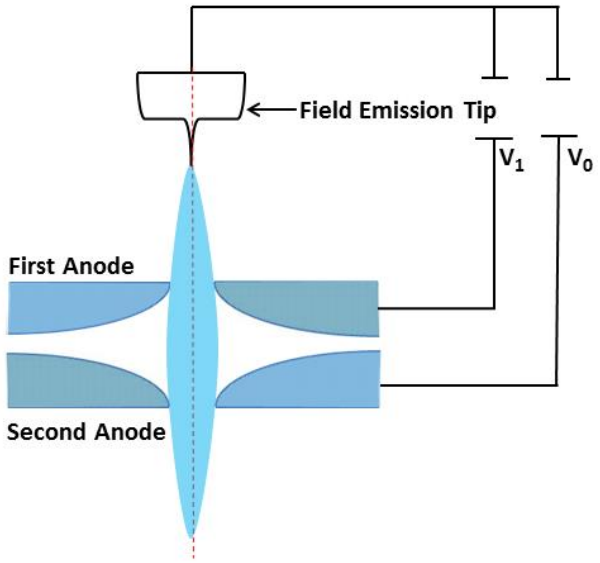

Fig. 2.4.1 - Gun configuration for field emission SEM, (Adapted from Goldstein et al., 1992)

The Ultra Plus scanning electron microscope is suitable for high-resolution imaging as it features ultra-high resolution secondary and backscatter electron imaging, using:

- In-lens SE detector.
- Energy selective Backscattered detector (EsB).

The In-lens SE detector is positioned on top of the pole piece inside the SEM column. During the in-lens secondary detection process a field is applied to an electrostatic lens to decelerate the primary beam, the field used to decelerated the beam also accelerates the

scattered electrons directing them back into the lens. The in-lens detector is particularly efficient in detecting SE1 electrons, which are generated in the superficial part of the interaction volume and contain information about the sample surface.

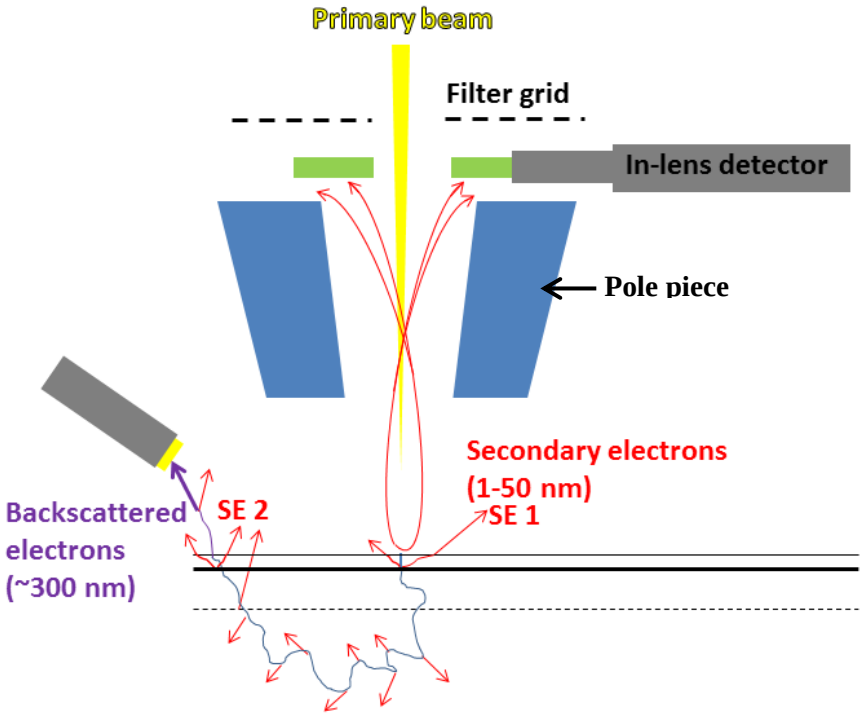

Fig. 2.4.2 - Schematic representation of the FEG SEM Ultra Plus Showing principle of SE detection by an In-lens detector, (adapted from Kuo et al., 2014)

The Energy selective Backscatter detector (EsB), also known as an in-lens backscattered detector, is located above the In-lens SE detector (Fig. 2.4.3a & b). It is equipped with an integrated filter grid which has a small negative voltage applied to it which is sufficient to reject the low energy SE reaching the EsB detector, enhancing image quality, providing a good signal to noise ratio and good contrast

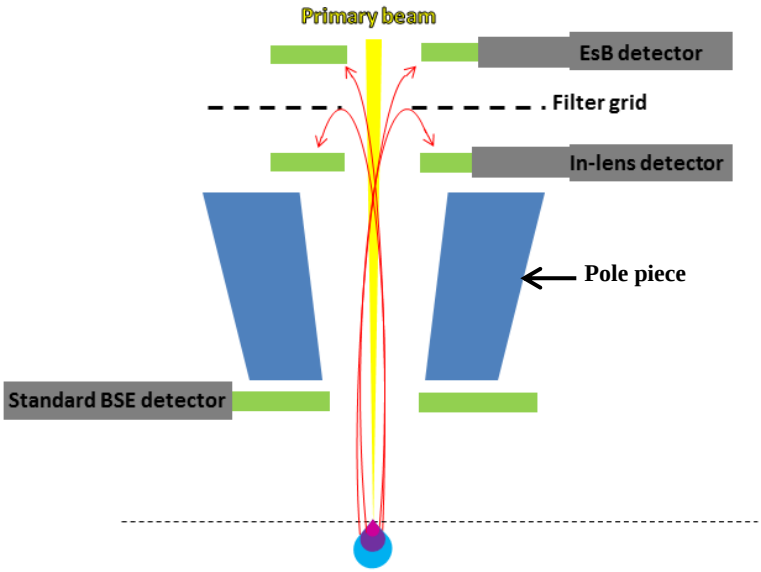

Fig. 2.4.3a - Schematic representation of the FEG SEM Ultra Plus showing the principle of BSE signal detection, and Energy selective Backscattered (EsB) detection

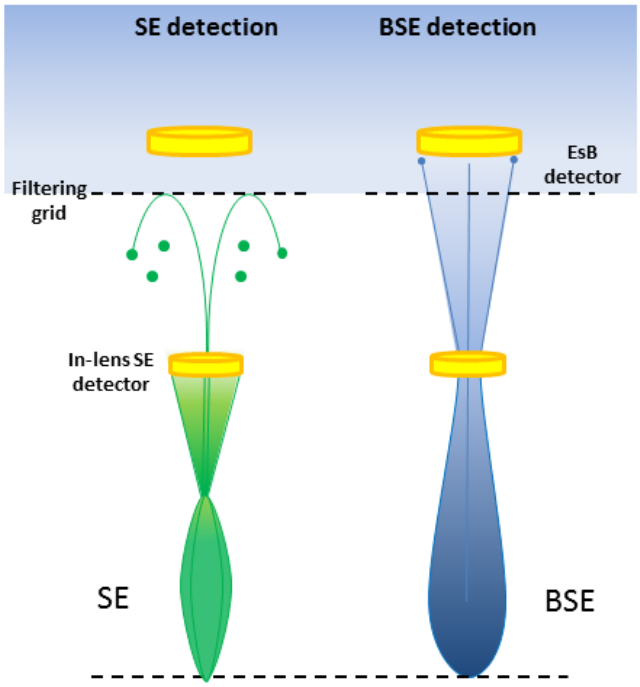

Fig. 2.4.3b - Schematic representation of the FEG SEM Ultra Plus showing the filtering grid voltage located in front of the EsB detector. The filtering grid voltage prevent detection of SEs, rejects the SEs allowing the detection of BSEs only,(Adapted from Kuo et al., 2014)

Using the Carl Zeiss Ultra Plus, ultra-high resolution images maps of matrix regions were acquire at magnification of ~×35k and a low accelerating voltage of 3.00 kV, aperture 30μm, and ~2.5mm working distance (WD). Each individual image was acquired in dual mode, using the EsB signal (e.g. Fig. 2.4.4a) and the In-Lens signal (e.g. Fig.2.4.4b). The individual images were stitched together, using Photoshop software, to generate an image map of the entire matrix area investigated.

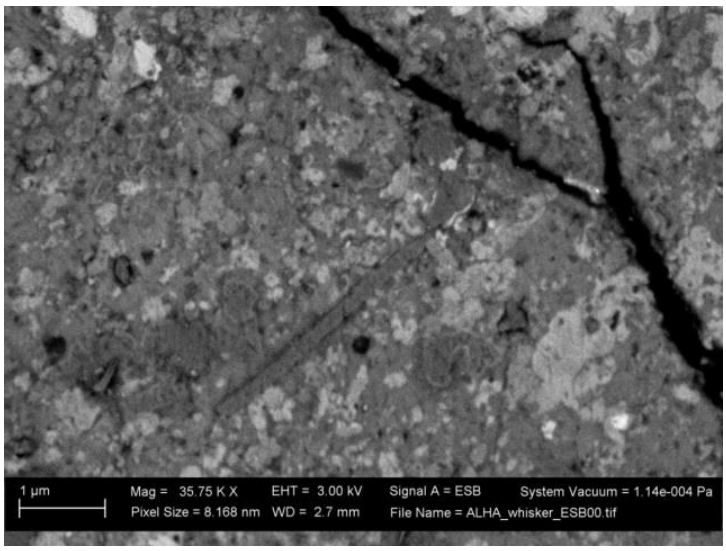

Fig. 2.4.4a

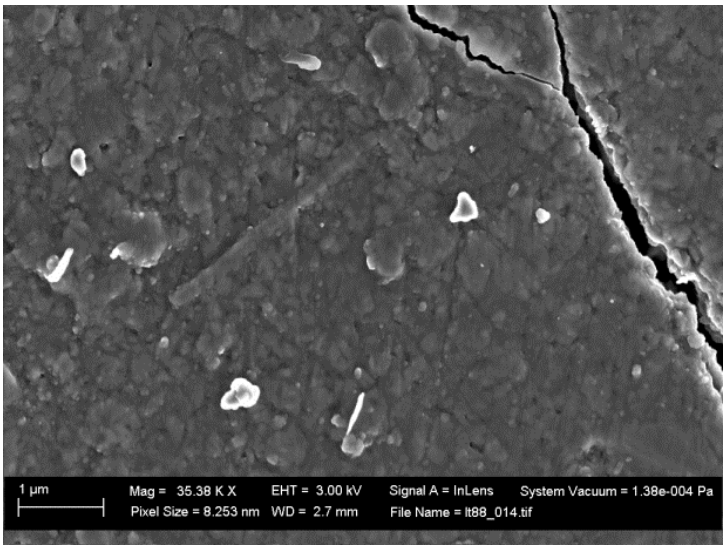

Fig. 2.4.4b

Fig. 2.4.4a - EsB image of matrix region of ALHA77307 showing composition differences of matrix constituents. Given the exceptionally high magnification, the focus of the image is the best achievable
Fig. 2.4.4 b - In-Lens image of matrix region showing detailed information about the sample surface

2.5 - FEI Quanta 650 FEG SEM

The FEI Quanta 650 FEG SEM is another microscope used to investigate the matrix; the speciality of this SEM is that it is equipped with a newly designed retractable energy dispersive X-ray detector (EDS) (Bruker Flat Quad 5060F). The detector is positioned between the microscope pole piece and the sample, which gives high count rates from high take-off angles providing the capability for low kV, high spatial resolution mapping. (Fig. 2.5.1)

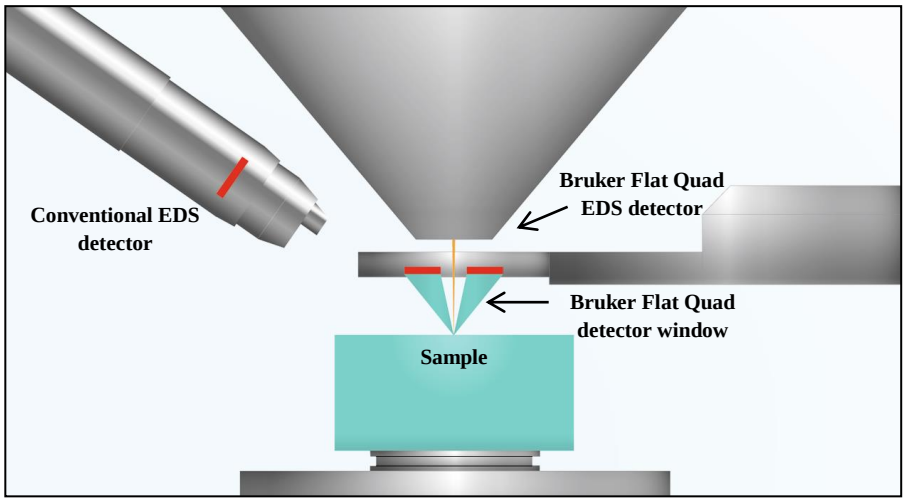

Fig. 2.5.1 - Diagram of FEI Quanta 650 FEG SEM showing the X-ray detector (EDS) Bruker Flat Quad 5060F positioned below the microscope pole piece and, the sample solid angle (Max solid angle achieved Ω >1.1sr at d 2.5mm.) This allows analyse at low beam currents and low accelerating voltages

The new design of the EDS XFlash QUAD 5040 provides high resolution at highest count rates due to the multi-channel nature of the Silicon Drift (SD) detector. A Silicon Drift Detector (SDD) is characterised by a transversal field generated by a series of ring electrodes that causes charge carriers to 'drift' to a small collection electrode that allows significantly higher count rates. Almost all of the EDS detectors available at present are single-channel detectors which means that one detector is associated to one set of processors, whereas EDS XFlash QUAD 5040 is equipped with four channel silicon drift detectors (SDD), where four independent sensors are associated with 4 sets of processors. In this annular four-channel detector the electron beam passes through a hole in the centre

of the detector, and it is surrounded by 4 sensors with an active area of 15mm^2 (Fig. 2.5.2). Using multiple detectors has a number of advantages including the increase of solid angle (Max solid angle achieved Ω >1.1sr at d 2.5mm) compared to traditional EDS detectors that are at a much greater distance from the sample and much smaller solid angle. Therefore, the counting rates can be much higher for a given probe current with the FlatQuad, offering the potential for much faster acquisition than a single channel SDD. In addition, the spectral resolution of the detector is 123eV proving sufficient resolution to identify the major rock forming elements. These key features permit use of low beam currents and low accelerating voltages, operating conditions that are crucial for high resolution image mapping.

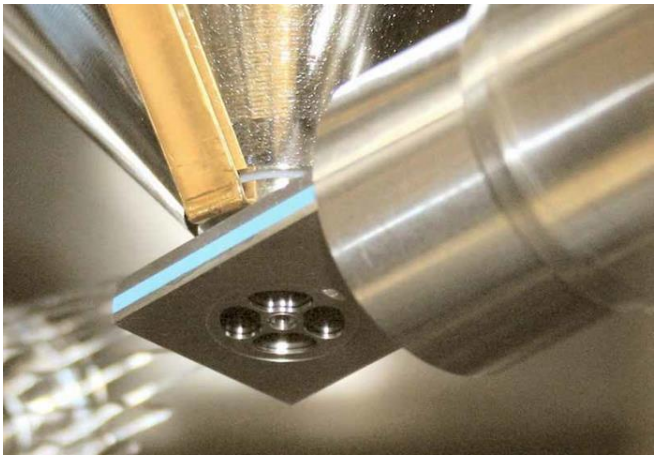

Fig. 2.5.2a

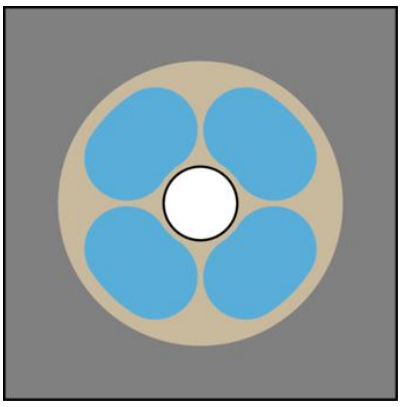

Fig. 2.5.2b

Fig. 2.5.2a - Picture of EDS XFlash QUAD 5040 fitted in the FEI Quanta 650 FEG SEM capable of providing high resolution images at highest count rates due to the multi-channel nature of the Silicon Drift (SD) detector (Scheller et al., 2010)
Fig. 2.5.2b - Diagram (b) of EDS XFlash QUAD 5040 fitted in the FEI Quanta 650 FEG SEM

Element maps were initially acquired with an accelerating voltage of 15kV. However, the spatial resolution of the EDS maps was larger than the grain size of the matrix, and therefore, in order to improve the spatial resolution and image quality of the map it was necessary to further reduce the electron beam accelerating voltage to 5-6 kV. This allowed to achieve considerably better definition of the map by defining better the edges of the matrix constituents (Fig. 2.5.3b & 2.5.4b). The element maps were acquired at magnification of (~×9k - ×900k), and provided chemical information at spatial resolution down to a volume of 200 nm in depth by 100 nm in radius at 5kV.

Typical SEM operating conditions range between 10-20kV; at these conditions large interaction volumes are generated that make those operating conditions unsuitable for high resolution microscopy. In order to achieve high-resolution imaging it is necessary to operate at low beam energies. When the electron beam produced by the source meets the specimen, energy is transferred into the sample, displacing the electrons and, producing the forms of secondary radiation which are measured; this generates in the sample an interaction volume (Fig. 2.5.3 a, Fig. 2.5.4 a). Understanding the size and the shape of the interaction volume in the sample investigated is very important for the interpretation of features of SEM images and spatial resolution of x-ray microanalysis, especially when the features investigated are at the nanometre scale like those in the matrix.

Monte Carlo electron-trajectory simulation software provides indirect method detection the interaction of the beam with the sample (Berger, 1963; Shimizu and Murata, 1971; Heinrich et al., 1976; Newbury et al., 1986; Heinrich and Newbury, 1991). The size of the interaction volume depends strongly on the energy of the electron beam that interacts with the sample, higher energy levels allow deeper penetration and lateral scatter of the electrons into the specimen. The Monte Carlo simulation shown in Fig. 2.5.3a for an electron beam with energy of 15kV entering a forsterite crystal target reveals the interaction volume is

~3.5×3.5µm, that is much larger than the typical matrix grains (<<1µm). These operating conditions are therefore not suitable for this project as the overall quality of the image generated was too low resolution to clearly identify individual components (Fig. 2.5.3b), hence compromising understanding of the feature observed in the matrix regions investigated. A similar simulation run at 5kV shows that the interaction volume is much smaller, ~0.4×0.4 µm, which is much more appropriate for this study (Fig. 2.5.4 a & b).

Monte Carlo electron - trajectory simulation

Monte Carlo electron - trajectory simulation provides an indirect method to visualise the interaction volume generated by the electron beam hitting the surface of the sample.

The effects of elastic and inelastic scattering are calculated based on appropriate models determining scattering angles, distances between scattering sites, and energy loss rates. Knowing this parameters and using geometric equations, the electron trajectory can be simulates from the exact point at which it enters the specimen to its final destination when it either escapes the specimen or loses all its energy and it is captured by the specimen.

Examples of individual trajectory calculated are shown in fig. 2.5.3a and 2.5.4a

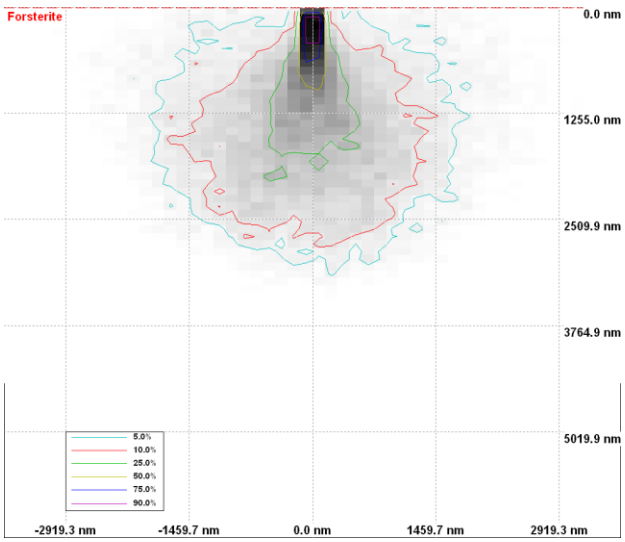

Fig. 2.5.3a - Monte Carlo electron distribution map of the interaction volume of ~ 3.5×3.5µm generated in a forsterite crystal at 15kV By Dr. Tobias Salge. – Grey scale indicates the electrons energy distribution and the contours outline their energy distribution boundary

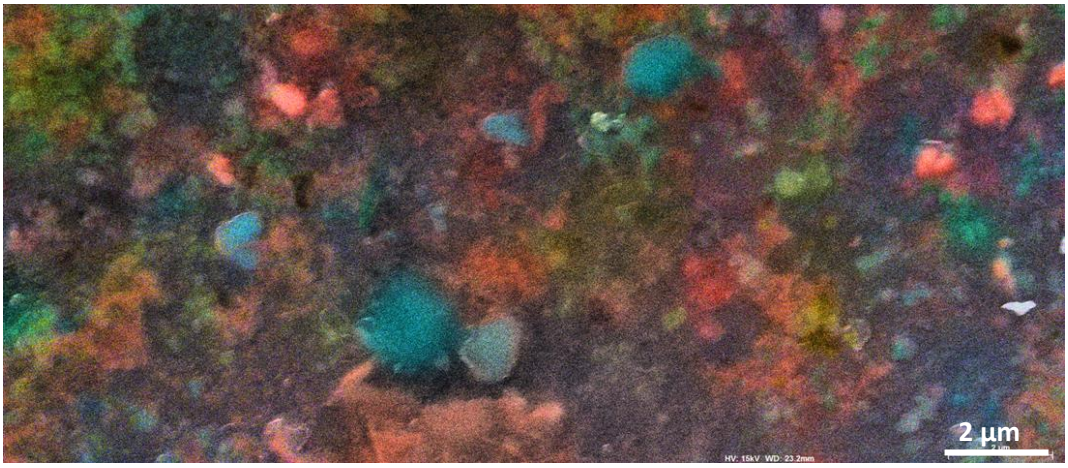

Fig. 2.5.3b - Element map of matrix region of ALHA77307 generated at 15kV, showing poorly defined edges of the matrix constituents, resulting in an overall blurred image

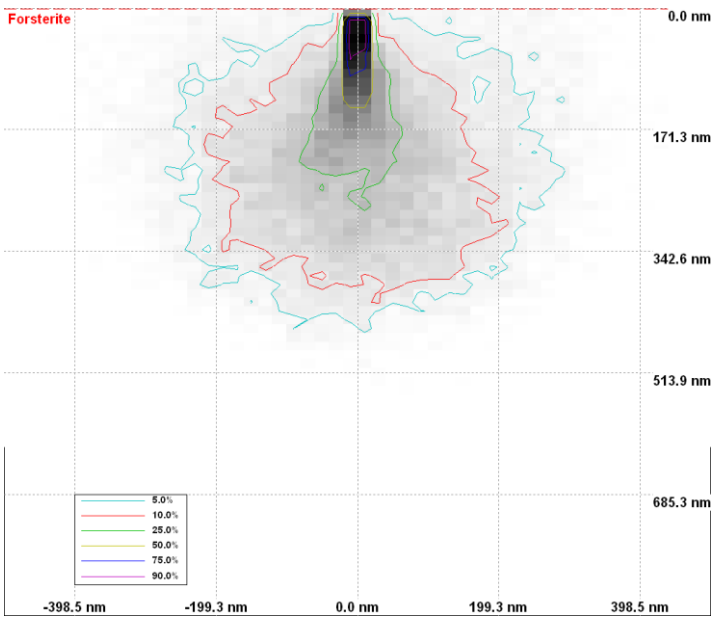

Fig. 2.5.4a - Monte Carlo electron distribution map of the interaction volume of ~0.4×0.4µm generated in a forsterite crystal at 15kV By Dr. Tobias Salge. – Grey scale indicates the electrons energy distribution and the contours outline their energy distribution boundary

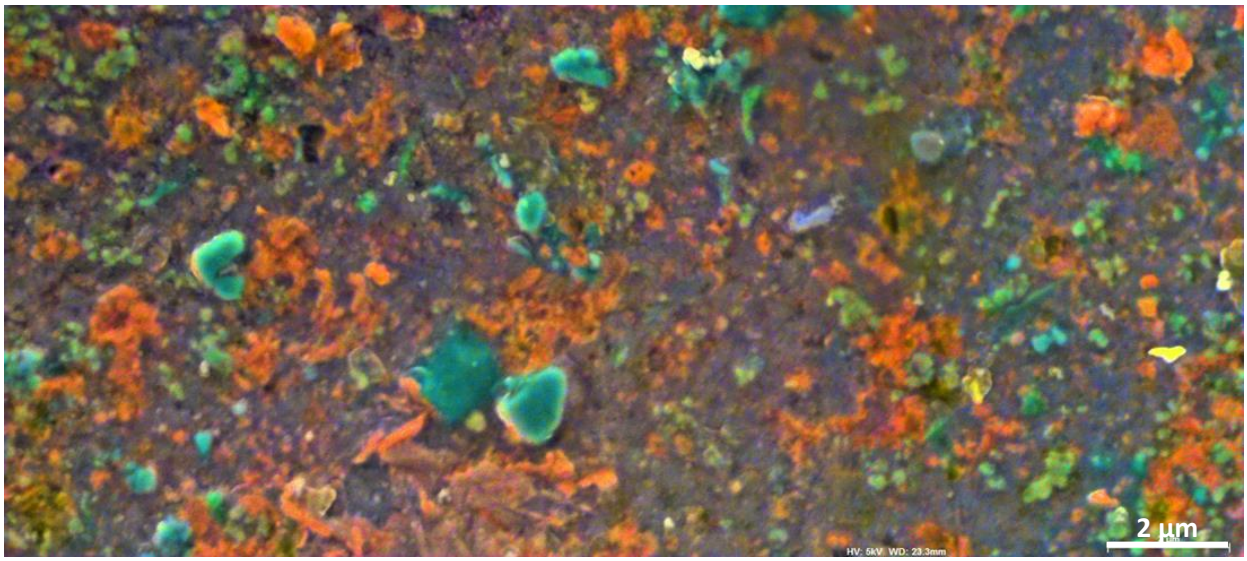

Fig. 2.5.4b - Element map of matrix region of ALHA77307 generated at 5kV, showing well defined edges of the matrix constituents, resulting in an overall sharp image

2.6 - XRD diffraction

Micro X-ray diffraction (micro-XRD) was used for data acquisition on matrix regions previously investigated using SEMs. Micro-XRD is a structural analysis technique which is used to obtain information about the structure of crystalline materials. The X-rays are generated using a conventional X-ray source, which is an X-ray tube, where electromagnetic waves are generated from impacts of high-energy electrons with a metal target. The angular dispersion of the incident X-ray beam produced is then reduced by collimation. This is achieved by placing a slit between the X-ray source and the sample as shown in Fig. 2.6.1

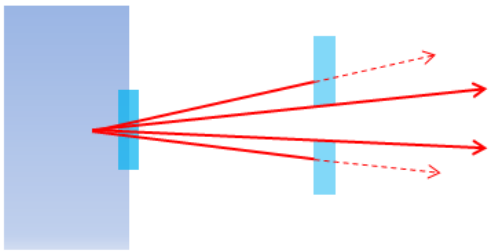

Fig. 2.6.1 - Diagram showing the angular dispersion of the incident X-ray beam reduced by collimation as it goes through a slit placed between the X-ray source and the sample, (Adapted from Goldstein et al. 1992)

The interaction of the incident rays with the sample produces constructive interference and there is strong reflection of electromagnetic radiation when conditions satisfy Bragg's Law ($n\lambda=2d\ \sin\theta$). This law relates the wavelength (λ) of the incident x-rays (θ) to the diffraction angle and the lattice spacing (d) in a crystalline sample. Usually this technique is used on powdered samples, as the ideal "powder" sample contains tens of thousands of randomly oriented crystallites, some of which diffract the incident beam and the scattering of x-rays from atoms in the crystallites, producing a diffraction pattern, which contains information about the atomic arrangement within the crystal. Given that each mineral has a set of unique d-spacings, the identification of the mineral phase is done by converting the diffraction peaks to d-spacings.

When a wave interacts with an object the wave is scattered, as a consequence a new wave is created, which spreads in all directions. The scattered spherical wave with its origin coinciding with the object is called Ewald's sphere. A cone along the sphere corresponds to a Bragg angle 2θ, and the infinite amount of crystallites in an ideal powder randomly oriented produce Debye diffraction cones.

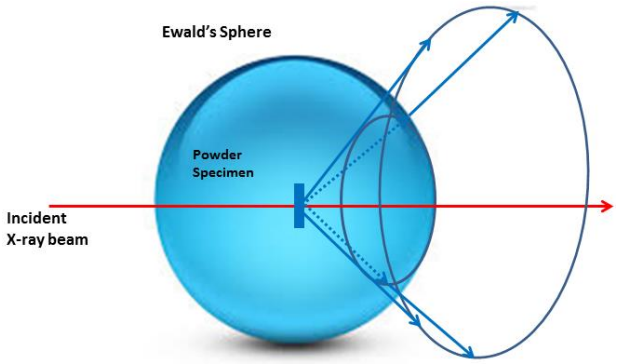

Fig. 2.6.2 - Diagram of wave interacting with an object producing scattered spherical wave (Ewald's sphere) with its origin coinciding with the object, and Debye diffraction cones, (adapted from Goldstein et al., 1992)

If the micro-XRD machine is fitted with a linear detector like the one shown in Fig. 2.6.3a, then the linear diffraction pattern is formed as the detector scans through an arc that intersects each Debye cone at a single point (Fig.2.6.3b).

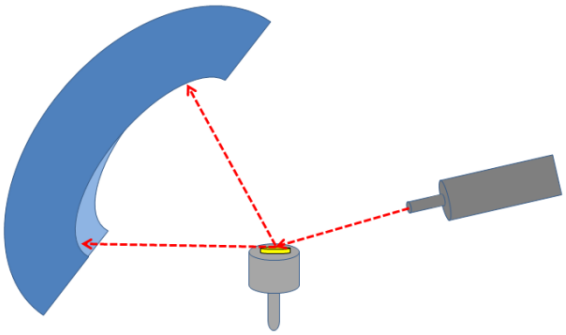

Fig. 2.6.3a - Schematic representation of XRD linear detector

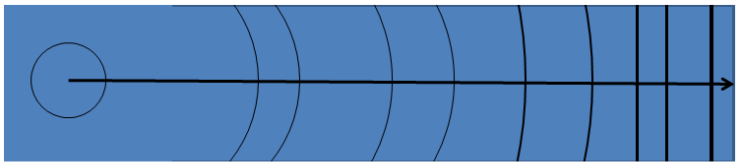

Fig. 2.6.3b – Schematic representation of photographic film showing Debye rings intersecting the direction of scan in a single point (adapted from Pecharsky et. al., 2003)

The interception of the Debye diffraction rings with detectors characterised by larger surface areas compared to the liner detectors such us Image Plane detectors (IP) allow the observation of a 2-D diffraction image over a broad range (Fig. 2.6.4).

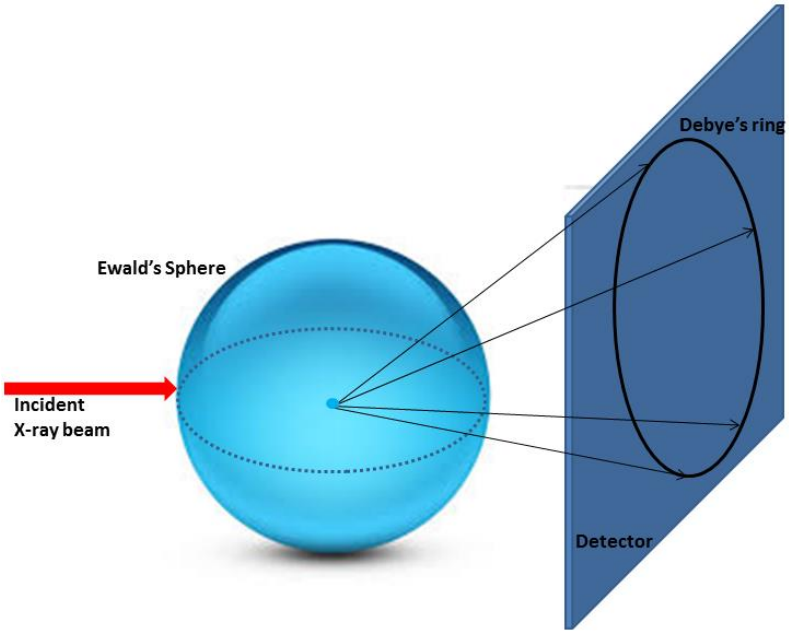

Fig. 2.6.4 - Diagram of wave interacting with an object producing scattered spherical wave (Ewald's sphere) with its origin coinciding with the object, and Debye diffraction ring generated by the interception with an IP (adapted from Goldstein et al., 1992)

The X-ray detected intensity is processed, counted, then generally represented as a function of Bragg angle 2θ, and is reported as counts per second (cps). In a typical powder diffractometer the resultant diffraction pattern is shown in the standard format as counts versus 2θ in Fig. 2.6.5. Detection limits depend on the crystallinity of the sample, for well crystallised mineral and high symmetry the detection limits is ~1vol%, whilst for minerals with low symmetry and poor crystallinity the detection limit is ~ 5vol%.

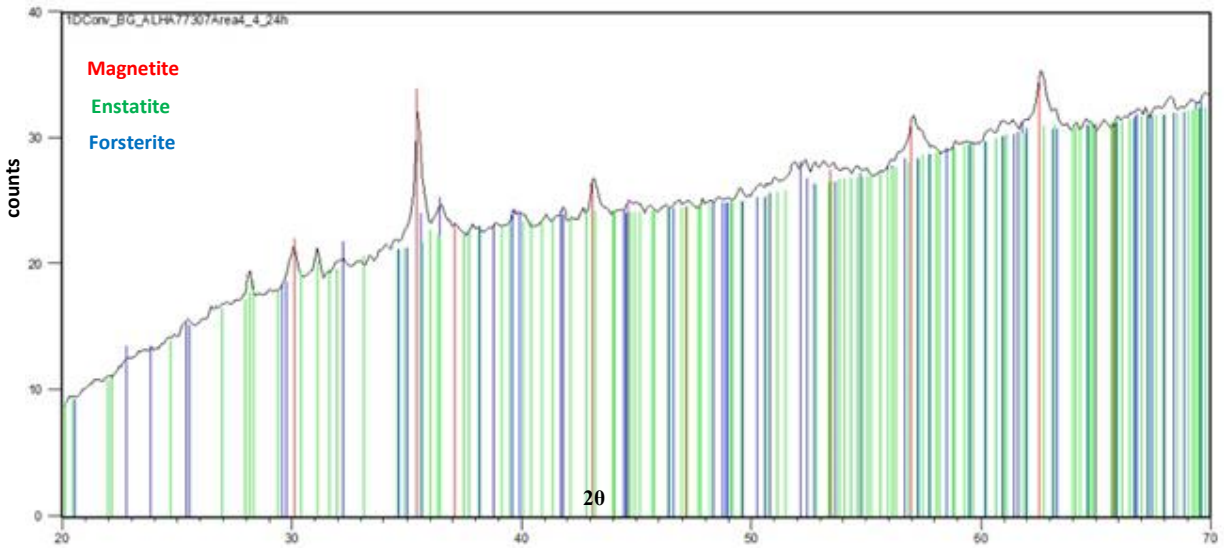

Fig. 2.6.5 - Diffraction pattern in the standard format as relative intensity versus 2θ of matrix Area 4 of ALHA77307 showing identified mineralogical phases

Micro-XRD analyses are conventionally collected on powdered samples, this requires crushing the meteorite in an agate mortar, hence this is usually a destructive technique. The technique was applied here in an unconventional way. Considering that the matrix of meteorites is constituted of very fine grains (≤ 1μm) it can be assumed that the matrix is already a powder, and therefore the XRD diffraction patterns, can be obtained directly from the thin sections without crushing the meteorites. This has great potential as the minute quantities or particle size of samples returned from future space missions makes it vital to develop non-invasive diagnostic research methods to study these precious materials.

The mineralogy of such samples is a key parameter to determine, but presents many challenges when material is limited or high spatial resolution is required.

2.6.1- GeniX Cu high flux X-ray source

The GeniX Cu high flux X-ray source (Fig. 2.6.6) was used for the acquisition of the first sets of data equipped with a FOX 2D 10_30P mirror that focusses the X-ray beam to 230 μm in size, at X-ray source operation conditions of 50kV and 1mA. The X-ray beam was further reduced through a collimator with a pinhole diameter of 30 μm. The instrument uses an INEL 120º position sensitive detector (PSD) that enables rapid data collection simultaneously over 120º 2θ. The angle of the X-ray beam between the sample and X-ray source was ~6°, and the angular linearity of the PSD was calibrated with silver behenate and silicon as external standards. No angular movement of tube, sample and detector position are allowed with this machine, and more importantly the GeniX Cu high flux X-ray source used to acquire the first set of data is equipped with a linear detector allowing only a narrow range of Debye diffraction rings collection.

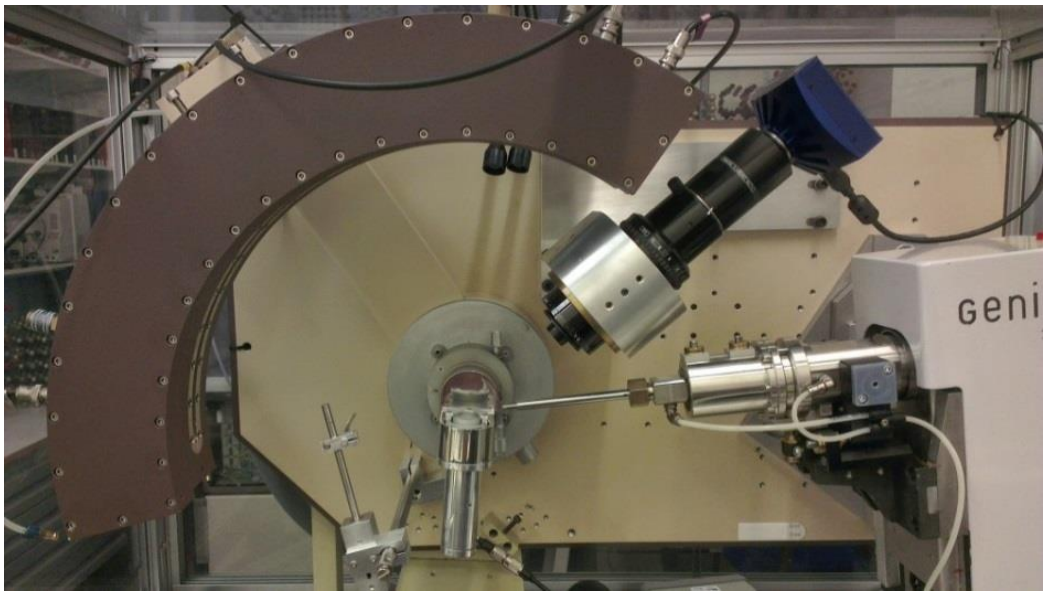

Fig. 2.6.6 - GeniX Cu high flux X-ray source equipped with INEL 120º position sensitive detector (PSD) linear detector

Preferred orientation issues using GeniX Cu high flux X-ray source

The theory of powder diffraction assumes that the "ideal powder" used to produce a diffraction pattern contains an infinite amount of crystallites randomly orientated, and for each and every Bragg reflection there should be the same fraction of the specimen volume that should be in the reflecting position. Most of the minerals are anisotropic as a result of natural preferences in packing, and therefore the powder shows distinctly non-random crystallite orientations known as preferred orientation which might generate non-negligible distortions of the intensity. During the data acquisition process some issues were experienced with preferred orientations in the patterns acquired that produced very high intensity peaks. This is most likely due to the fact that for the first acquired preliminary data an older instrument was used which lacks the sample positioning in X and Y axis, constraining the coordinates of the point to irradiate. Another possible cause, perhaps more important, is that the linear detector allows the detection of limited fraction of the Debye's rings. Integrating on small segments of the diffraction rings might compromise the statistics of the collected diffractions, and this might play a significant role in the production of preferred orientations effects.

2.6. 2 - D/MAX-RAPID II

In order to improve the quality of the mineralogy data acquired, a new set of data were collected using a new generation of micro-XRD diffraction system called the D/MAX-RAPID II. In this instrument the stage is mounted on a goniometer characterised by the following axes: a vertical ω–axis defining the angle between the beam and the sample (fixed at ω=20°), and a ϕ-axis allowing stage rotation (with a driving range of 360°); the χ (azimuth) angle is fixed at 45°. The sample adjusting range X and Y axis of: ±5 mm and: ±10 mm allows to carefully select the area and accurately specify the point to measure Fig. 2.6.7a & b.

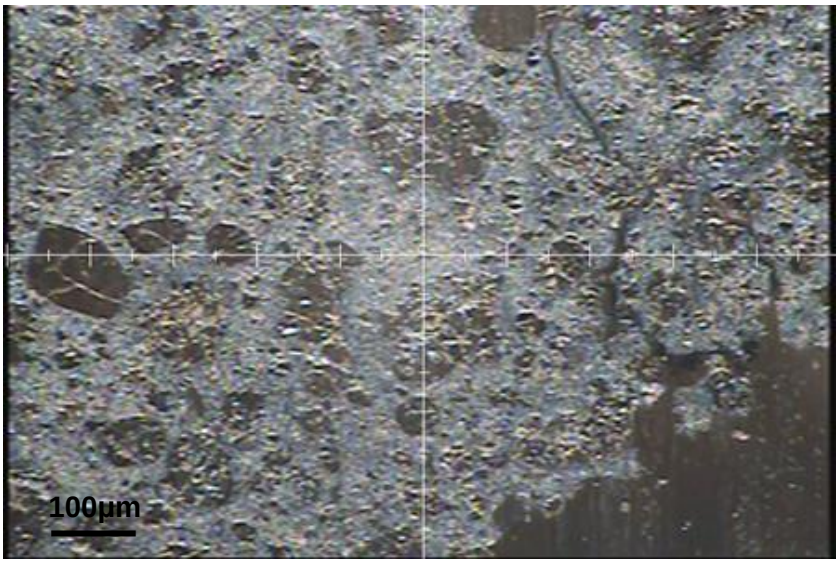

Fig. 2.6.7a

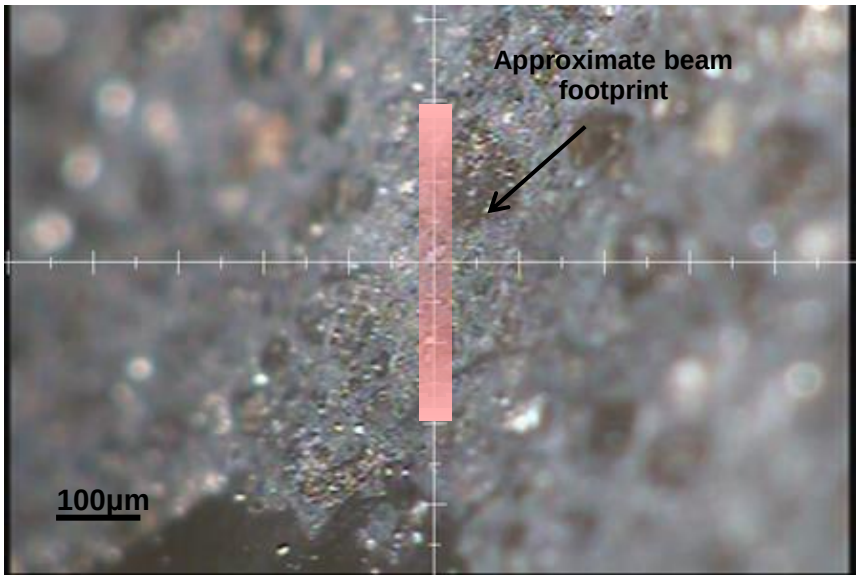

Fig. 2.6.7b

Fig. 2.6.7a - Optical camera image of sample ALHA77307 taken perpendicular to the polished thin section

Fig. 2.6.7b - Optical camera image of sample ALHA77307. The thin section is at a measurement angle ω=20° relative to the beam. Shaded area shows the approximate beam footprint on the sample ~50 × 500 µm

This detector is configured as a semi-cylindrical imaging plate (IP), which is placed in the inner part of a cylinder surrounding the ω-axis at the centre. This is a novel design and allows rapid measurement of 2-D X-ray diffraction images over a broad range Fig. 2.6.8a, b, c.

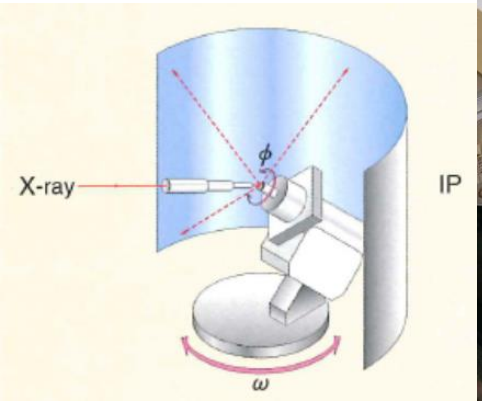

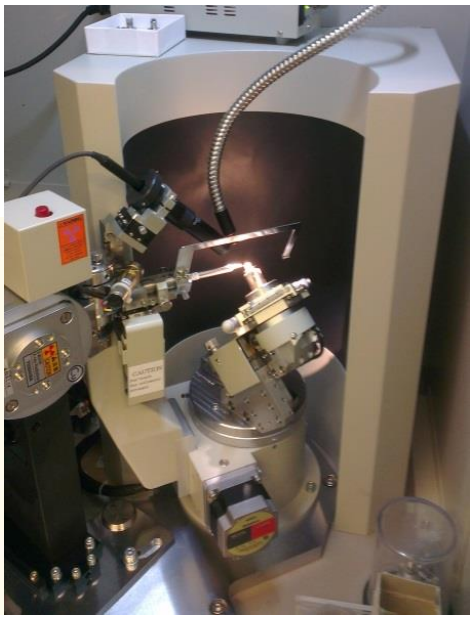

Fig. 2.6.8a Fig. 2.6.8b

Fig. 2.6.8a - Schematic representation of Rigaku D max Rapid II stage, characterised by an image plate (IP) placed on the inner surface of a cylinder. The IP surrounds the ω-axis, and a Φ spinning angle, allowing the collection of a 2D diffraction image over a broad range
Fig. 2.6.8b – Image of Rigaku D max Rapid II at NHM

The 2-D curved IP is 470×256mm in size, with 100×100μm pixel size, allowing for the detection of a wider range of Debye rings, and hence integration of more statistically significant diffractions that can mitigate against the effect of preferred orientations.

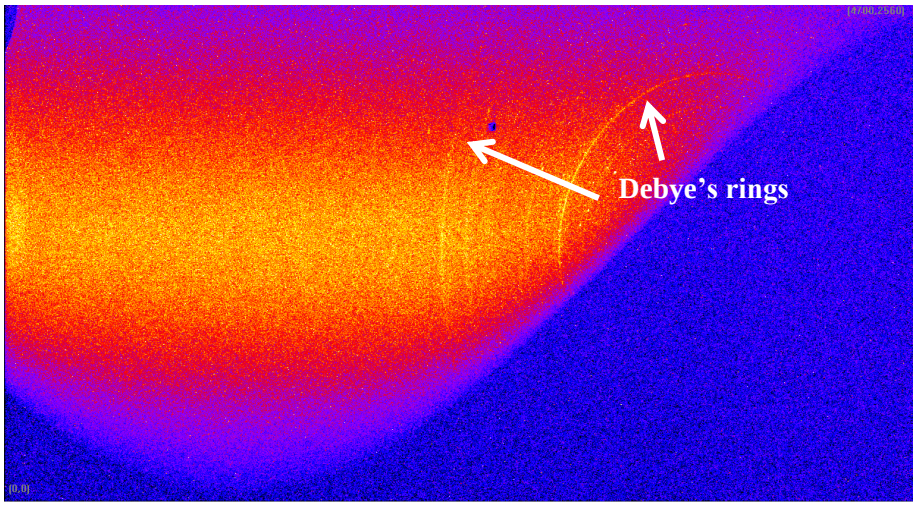

Fig. 2.6.8c - 2D diffraction pattern, collected on imaging plate detector, on sample ALHA77307 for this project. The image shows Debye-Scherrer rings generated by the incident beam scattered with a 2θ angle

2.6.2.1- Modal mineralogy profile-stripping method

Selected matrix areas of the sample ALHA77307, MIL 07687 and QUE 99177 previously investigated with SEM were subsequently studied with in-situ micro-XRD. Diffraction patterns were directly collected from the thin sections using Rigaku D/Max Rapid II XRD instrument. Cu $K\alpha_1$ radiation and a pin-hole of 30 μm and ω angle of 20˚ were used to achieve an X-ray beam footprint on the sample of ~50 × 500 μm. Based on mineralogical phases identified on the samples, standards were choosen and compared to the patterns acquired from the thin sections. Phase quantification of the minerals making up the matrix was obtained based on the peak intensity of the mineral phases present in the diffraction patters. A profile-stripping method developed at the NHM and fully described by Cressey and Schofield (1996) was used. Meteorite sample patterns were acquired for ~24hours, whereas mineral standard were acquired for 6 hours. Therefore, the diffraction pattern of a mineral standard was first scaled to the same measurement time as the meteorite sample (e.g. ×4 for a 24 h measurement). Subsequently the standard pattern was reduced in intensity to fit the meteorite pattern by a factor of 4 (e.g. 24/6 = 4) until it matched its intensity in the diffraction pattern of the sample. Once the standard peak intensity matched the peak intensity in the sample pattern it was subtracted to leave a residual meteorite pattern. The process was repeated for each mineral standard until the residual pattern was left with zero counts and the sum of the fit factors was one. This indicated that all phases present in the matrix region investigated were accounted for. The fit factors for the mineral standards were then corrected for relative differences in X-ray absorption to give their final volume fractions in the meteorite (e.g. see King et al., 2015 and Howard et al., 2009). Modal abundances were determined for each phase present (at ≥ ~1 vol%) in each of the five areas investigated.

2.7 - Focused Ion Beam (FIB)

Focused Ion beam (FIB) is a sample preparation technique that employs a beam of Ga^+ ions to sputter specific and well defined volumes of a sample, which can produce a thin foil for further examinations. Prior to FIB-ing, in order to protect the region of interest from unwanted sputtering and Ga-implantation during milling, a strip of Pt was deposited above the area of interest (Fig. 2. 7.1a & b). An organic Pt-gas was injected immediately above the sample area, while the Ga-ion beam was scanned over the preselected pattern. The beam decomposes the organic Pt cloud, depositing a platinum-rich strip.

Fig. 2.7.1a

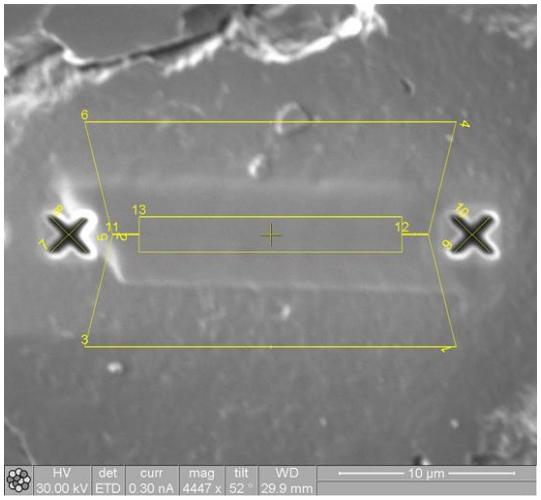

Fig. 2.7.1b

Fig. 2.7 a - SEM pictures of sample Acfer 094 showing a strip of Pt deposited above the area of interest in order to protect it from ablation and Ga-implantation during preparation. Fig. 2.7 b - SEM pictures of sample Acfer 094 showing designated trenches to be milled on both sides on the Pt strip

The FIB then automatically performs the milling of material from both sides, front and back of the area of interest producing a cross-sectional slice left standing topped by the Pt strip (Fig. 2.7.2 a & b).

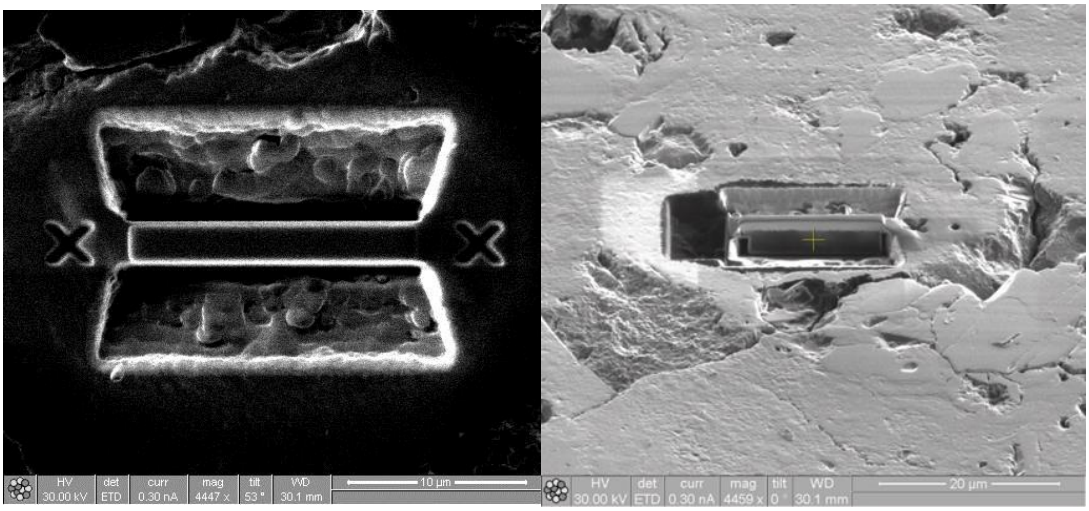

Fig. 2.7.2a **Fig. 2.7.2b**

Fig. 2.7.2 a & b - SEM pictures of sample Acfer 094 showing at different angles a cross-sectional slice remaining between the two trenches milled capped by the Pt strip

Secondary electrons are created during the sputtering process due to the interaction of Ga-ions with atoms and electrons of the sample. These secondary electron produced were used for imaging allowing to monitor the milling process. In order to regulate and minimize the milling time, the depths and widths of the trenches were optimized using the computer software. To extract a sample, the ion beam was used to weld a needle on the end of a mechanical lift–out device to the FIB section by depositing a small amount of Pt overlapping both. Once the needle was securely welded to the section, the section was detached from the substrate and lifted out of the trench and, subsequently welded on copper grid (Fig. 2.7.3a & b). The slice was then further reduced in thickness for X-ray absorption near edge structure (XANES) studies. This FIB sample preparation technique was necessary to investigate the samples using the synchrotron.

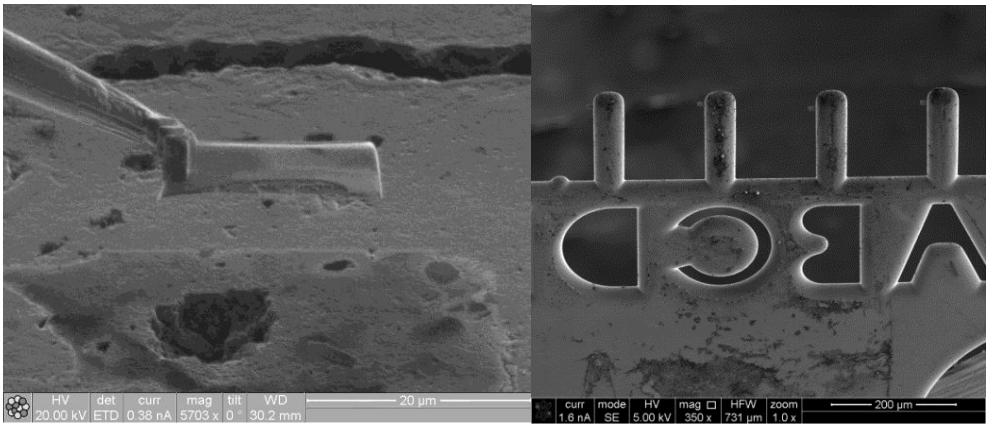

Fig. 2.7.3a **Fig. 2.7.3b**

Fig. 2.7.3a - SEM pictures of sample Acfer 094 showing FIB section welded to the needle of the micromanipulator and detached from the substrate while being lifted out
Fig. 2.7.3b - SEM pictures showing FIB sections of sample Acfer 094 welded to the copper grid

A FEI 200TEM FIB at Glasgow University was used to prepare electron transparent foils of matrix regions of ~15µm wide, 5µm high and about 100nm thick. The samples FIBed, Acfer 094 and MIL 07687, were previously examined using high resolution SEMs and µXRD, and were chosen among the others for their peculiar styles of aqueous alteration: dry desert for Acfer 094, wet Antarctic and localised for MIL 07687.

During the sample preparation a strip of Pt 17 µm long by 2 µm wide by 1 µm thick was deposited above the area of interest, with Pt deposition, operated at 30 kV. Following Pt deposition script, operated at high ion current (2.7 nA) was used to perform the milling to produce a cross-sectional slice left standing of ~0.2 µm thick by 15 mm long and 5 µm deep, topped by the Pt strip. Once the foil was lifted and attached to the copper grid the foil was then thinned down to a thickness of ~100 nm with a reduced beam current (350 pA) manually positioned on the FIB-ed foil attached to the copper grid. The samples prepared with this technique were then loaded directly into the Diamond I08 beamline for the soft X-ray spectro-microscopy data acquisition.

2.8 - Synchrotron

FIB sections were prepared for two of the samples investigated as part of this study (Acfer 094 and MIL 07687), to investigate the Fe oxidation state of the mineralogical phases making up the matrix of these samples. X-ray absorption fluorescence spectroscopy and X-ray absorption near edge structure (XANES) measurements were made. These investigations were carried out using the synchrotron radiation at the Diamond Light Source, located at the Harwell Science and Innovation Campus in Oxfordshire. Synchrotron radiation is the most powerful X-ray radiation source currently available, capable of producing an exceptionally bright beam and with very high coherence. Each synchrotron is optimised to produce light with a particular energy for specific applications – Diamond produces a 3 GeV (Giga-electron-volt) electron beam, and is classed as a medium energy synchrotron. The Diamond machine is the assemblage of a series of components utilised to generate a high energy electron beam, which is then confined in storage rings and kept for several hours in a closed orbit in order for the electron to produce synchrotron light.

The main assembled components that constitute the synchrotron (Fig. 2.8.1) are: an electron gun to produce a stream of low energy electrons; a linear accelerator to increase the electron's energy; a booster synchrotron to further accelerate the electron beam to its final energy; the storage ring of the size of hundreds of meters in diameter, where beams of accelerated electrons or positrons are moving in a circular orbit, controlled by a magnetic field, to near light speeds ; here the electron beam maintains the energy and is confined while it produces synchrotron light. Due to the acceleration of charged particles towards the centre of the ring the electromagnetic radiation produced rangs from radiofrequency (3 kHz to 300 GHz) to short wavelength x-ray region (3×1016 Hz to 3×1019 Hz). The high intensity observed in a broad range of photon energies allows users to select the desired wavelength. Moreover, considering the dimension of the storage ring, the beam, is weakly

divergent, generating the high instrumental resolution compared to that typically used in standard laboratory powder X-ray diffraction instruments.

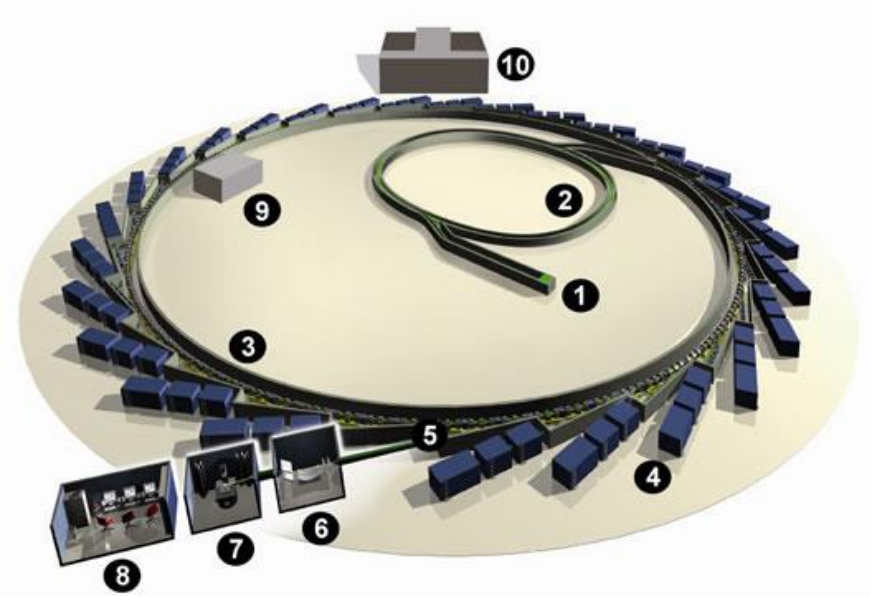

Fig. 2.8.1 - Schematic diagram of a synchrotron facilities illustrating location of: 1 Electron gun, 2 Booster Synchrotron where electron are accelerated, 3 Storage Ring synchrotron light is generated; large electromagnets are used to curve the electron beam kept under vacuum, 4 Beamlines research stations, 5 Front Ends where synchrotron light is chanelled into a beamline, 6 Optics Hutch where the beam is filtered and focused, 7 Experimental Hutch, 8 Control Cabin where the scientific team is monitoring the experiment, 9 Radiofrequency (RF) Cavity where electromagnetic fields oscillating at radio frequencies allows the beam to maintain a fixed orbit around the storage ring, 10 Diamond House. Courtesy of Diamond Light Source

Diamond I08 beamline

I08 is the Diamond Scanning X-ray Microscopy beamline that has the ability to obtain morphological and chemically-specific information under real conditions. X-rays are photons of electromagnetic radiations which can experience photoelectric absorption when interacting with an atom. At specific wavelengths the X-ray absorption of a chemical element jumps dramatically, these sharp variations are called absorption edges. The spectra observed near the absorption edge of a chemical element may contain a fine structure that reveals the electronic and geometrical environment of the absorbing atom. This technique is known as X-ray absorption near edge structure (XANES). The high intensity of synchrotron X-rays allow the detection of chemical elements present in very low

concentrations. Very high spatial resolution data acquisitions are made possible by combining the high brightness of the beam generated with a small spot size. The technique besides allowing the detection all major K- and L- absorption edges is complemented with imaging and spectroscopic techniques. This enabled characterisation of the matrix mineralogy, chemistry, and $Fe^{3+}/\sum Fe$ at the grain scale within the samples.

2.8.1 - Diamond I08 beamline settings used for the project

In order to identify the mineralogical, chemical and chemical-state variations both within and between individual grains whilst maintaining the spatial integrity of the sample high-resolution chemical and chemical-state maps were collected. These were acquired using soft X-ray absorption spectra (XAS) of matrix regions of Acfer 094 and MIL 07687 using Diamond I08 beamline soft X-ray spectro-microscopy. In particular soft X-ray spectro-microscopy and, Scanning Transmission X-ray Microscopy (STXM) were used, employing radiation in the 250 to 4200 eV photon energy range. This method allowed to image chemical distributions and simultaneously perform accurate mineral identifications at the 10s of nm scale, whilst maintaining the spatial integrity of the sample. It was integrated the bulk information from in-house diffraction, spectroscopy and chemistry techniques with that from spectromicroscopy methods at progressively decreasing lengthscales (from the μm to the nm). Large scale (~100 μm × 100 μm), high resolution (30-50 nm) chemical maps were collected for major elements (e.g. Si, Mg, Fe, S and O) and minor elements (including, Al, Ni, Ti, Ca and C) taking ~8 hours to collect.

In order to determine the mineralogy of the sub-micron grains, and to be able to measure the $Fe^{3+}/\sum Fe$ ratios some of these grains spectra were extracted from small regions within the large scale maps. Image stacks were acquired over approximately 1 hour for each of 7 elements (Si, Mg, Fe, S, O, Al, and Ca). Calibration spectra were obtained from 3 standard minerals (San Carlos olivine, Fe-oxyhydroxyde and Ferrihydrate. These samples were

prepared as grain mounts on standard TEM grids within a glove box in order to avoid oxidation of the Fe. Approximately 2 hours were required for the analysis of each standard. During the experiment X-ray fluorescence maps (XRF) of MIL 07687 were acquired. XRF maps are produced by the emission of characteristic fluorescent X-rays from a material excited by bombarding with high-energy X-rays; these maps were used to identify the element distribution in the sample. STXM was performed on samples Acfer 094 and MIL 07687.

Scanning transmission X-ray microscopy

STXM provides imaging at the 30 nm scale with speciation sensitivity using XANES to investigate the Fe-oxidation state of MIL 07687 and Acfer 094. The sample is irradiated with a focused X-ray beam, and at fixed photon energy an image is collected on the image plate, the operation is repeated at different energy steps and each individual image acquired is stacked-up to make the final total image. The image produced is characterised by a different contrast due to different X-rays absorption, which at the Fe-L edge is linked to the oxidation state of the Fe. All the images collected over the energy range of 702-730eV are stacked up to produce a XANES spectra. The energy resolution used in this work is 0. 5 eV for the energy range from 702 -708 eV, 0.1 eV from 708 – 715 eV (L_3 edge), 0.5 eV from 715 – 718 eV, 0.1 eV from 718 – 725 eV (L_2 edge), and 0.5 eV from 725 – 730 eV. Dwell time/pixel was 5ms.

This method uses changes in the position, shape and intensity of the Fe-L edge related to 2p→3d electron transitions. Both L edges characterised by different energy values (708-715 eV for the L_3 and 718-725 eV for the L_2) show two main absorption peaks and the intensity of these peaks is related to the contribution of Fe^{3+} and Fe^{2+} (e.g. Le Guillou et al., 2015). The acquisition of spectra across the full range of energy (702-730eV) permits both L_3 and L_2 edges. However, in this work due to poor quality of the spectra acquired from the standards only the L_3 edge was used to determine Fe^{3+}/Σ Fe ratio.

In order to determine the Fe^{3+}/Σ Fe ratio we adapted the method developed by Bourdelle et al. (2013) and Le Guillou et al. (2015). First a linear background fitted in the energy range of 702-705 eV was applied to the spectra to bring the lower energy region to an optical density of 0. (Chen et al., 1995; van Aken and Liebscher 2002; Brotton et al., 2007). An arctangent function **(Eqn. 2.8)** was fitted at each edge centred at 708.65 eV and 721.65 eV Fig.2.8.1.1

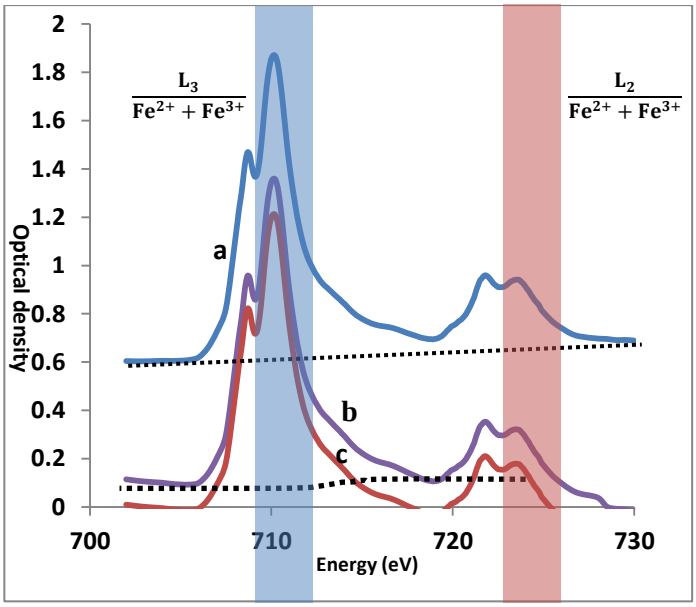

Fig. 2.8.1.1 - Graph showing correction applied to XANES spectra: (a) subtraction of background from spectra at Fe-L_3 and L_2–edges from sample MIL 07687 using a linear background (dashed line). (b) Application of two arctangent functions fitted at each edge (dashed curve) on Normalised background spectrum. (c) Edge normalised spectrum

$$\mathbf{f(\Delta E) = \frac{h_1}{\pi}\left(\arctan\left[\frac{\pi}{w_1}(\Delta E - E_1)\right] + \frac{\pi}{2}\right) + \frac{h_2}{\pi}\left(\arctan\left[\frac{\pi}{w_1}(\Delta E - E_2)\right] + \frac{\pi}{2}\right)} \quad \textbf{(2.8)}$$

Where h_1 and h_2 are the step heights of the two arctan functions, whilst w_1 and w_2 are the fixed peaks width and E_1 and E_2 are the positions of the inflection points resulting in a energy near the edge onset. Here w_1 and w_2 are fixed to 1eV. (e.g. Bourdelle et al., 2013). The calibration method described by Le Guillou et al. (2015) was applied, and the energy value at which Fe^{3+} peak intensity was more intense than the Fe^{2+} peak tail was taken in the energy range of 709.1-712 eV (Fig.2.8.1.2). The calibration method applied in this experiment was defined comparing a series of standards characterised by different Fe^{3+}/Σ

Fe ratios: San Carlos Olivine (Fe^{2+}), synthesized Ferrihydrite (Fe^{3+}), Fe-oxyhydroxyde (B.M.40039) (Fe^{3+}).

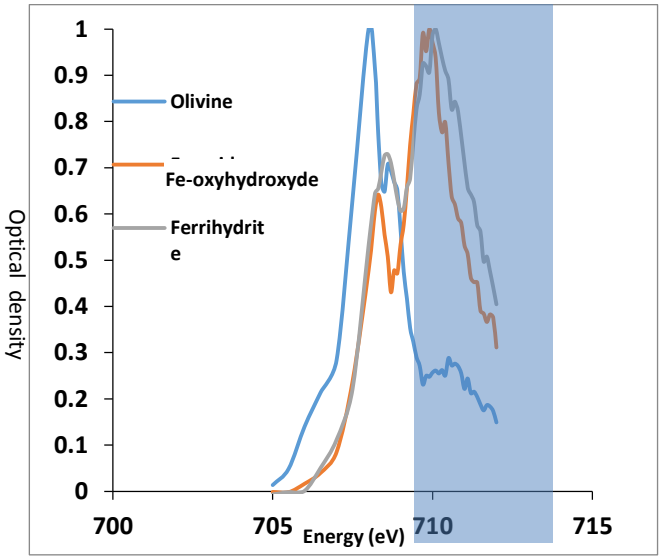

Fig. 2.8.1.2 - Graph showing L3 edges of XANES spectra from standards: San Carlos olivine (blue), Fe-oxyhydroxyde (orange), and Ferrihydrite (grey). The shaded area displays the energy range of the spectra at which the Fe^{3+} peak intensity was more intense than the Fe^{2+} peak tail. In the energy range of 709.1-712 eV

The area ratio for the Fe-L_3 edge was then linearly correlated to the known Fe^{3+}/Σ Fe as described by Bourdelle et al. (2013) and Le Guillou et al. (2015). In order to generate an accurate calibration line, several standards are required. The calibration line Fig. 2.8.1.3 used in this work was obtained using only 3 standards due to the unavailability of other standards. However, due to acquisition problems, two of the standard data almost coincided therefore the regression line was fitted to three points, two of which very close together. This is not statistically precise and therefore is to be considered very preliminary.

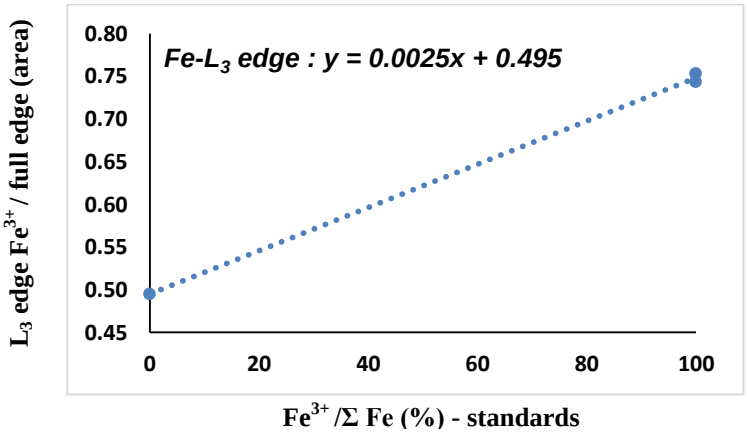

Fig. 2.8.1.3 - Calibration line obtained using our standard spectra. The equation of the linear regression is given for the Fe-L_3 edge only

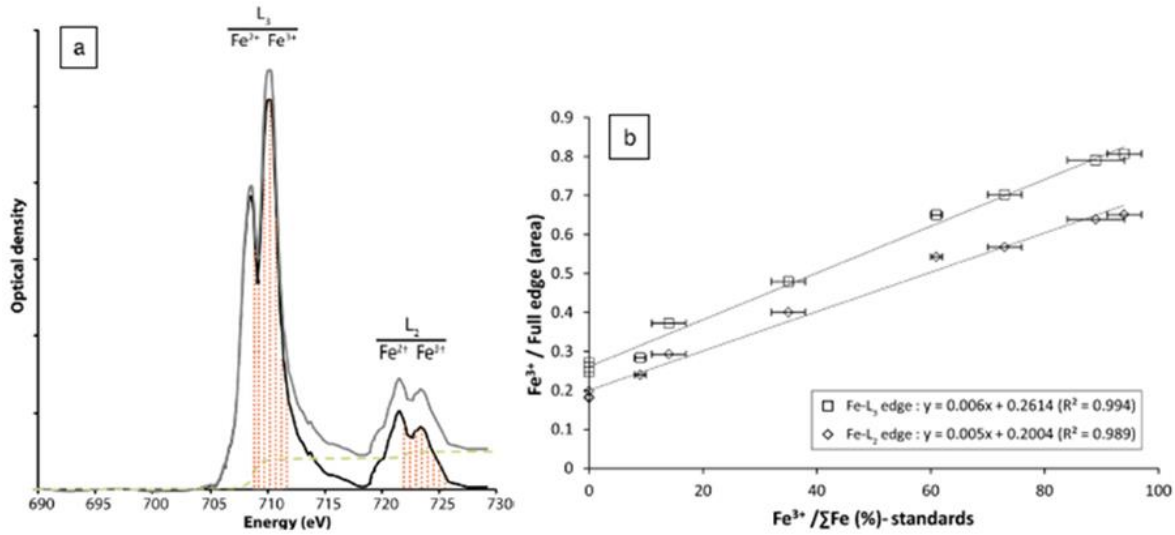

Fig. 2.8.1.4 - Calibration method used by Le Guillou et al. (2015). (a) Graph showing L3 and L2 edges of XANES spectra from QUE 99177. (b) Calibration lines obtained using Le Guillou et al. (2015) standards. The equations of the linear regression are given for both the Fe-L_2 edge and Fe-L_3

2.9 – NanoSIMS

Secondary ion mass spectrometry (SIMS), using the Cameca NanoSIMS 50L at the Open University, was used to determine the H and O isotopic composition of some of the matrix regions previously investigated using SEMs and XRD. SIMS measurements involve sputtering the surface of the specimen with a focused primary ion beam (in this case Cs^+) and collecting and analysing ejected secondary ions in a high transmission, high mass resolving power mass spectrometer. The NanoSIMS is optimised for high spatial resolution imaging, combining focus and fine control of the raster of the primary ion beam on to the sample surface, enabling the acquisition of data at the submicron scale. The primary ion beam in fact can be focused to achieve high sensitivity measurements at a spatial resolution of down 50 nm. Secondary ions produced were then extracted by applying an accelerating voltage between the sample and an extraction plate then passed through a mass spectrometer for mass separation (Fig. 2.9.1).

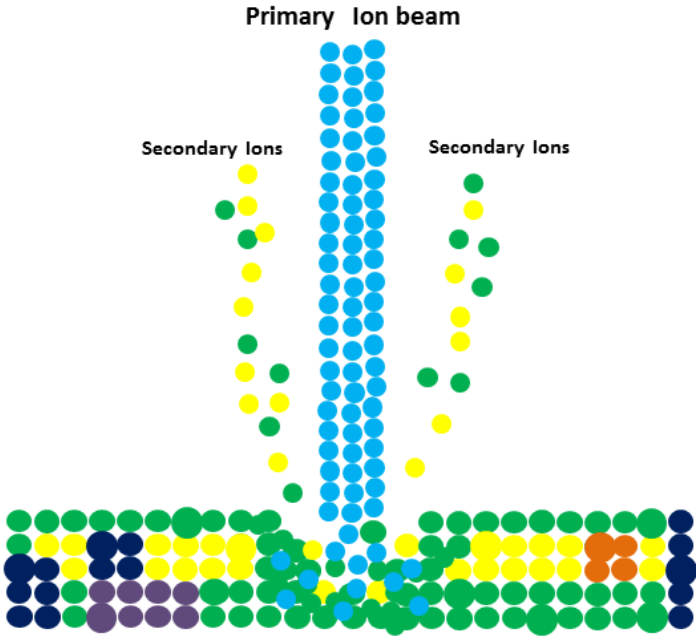

Fig. 2.9.1 - Diagram showing primary ion bean striking the sample surface producing: primary ions, along with electrons and photons containing information useful for identifying molecular species (adapted from Jiang et al., 2014).

NanoSIMS measurements were performed following procedures described in Starkey et al. (2014). Each area was extensively pre-sputtered over an area ~ 35×35 μm with a defocussed 300pA probe for ~15 minutes prior to analysis to remove the carbon coat, surface contamination and establish sputter equilibrium. Isotope ratio measurements were performed on 25×25 μm areas with a ≈ 1.6pA primary probe current providing a spatial resolution of ≤ 150 nm and the raster were conducted with a pixel step of ≤ 100 nm and a dwell time of 1000 μs per pixel. Data were collected in planes with total analysis times of ~2 hr. Charge compensation was applied with an electron gun with the same settings on both sample and standard. Negative secondary ions were collected on electron multipliers. For oxygen isotope measurements the detectors were set to collect ^{16}O, ^{17}O, ^{18}O, as well as ^{28}Si, $^{24}Mg^{16}O$, and $^{56}Fe^{16}O$ simultaneously. For hydrogen isotope measurements ^{1}H, ^{2}H, ^{12}C, and ^{18}O were measured simultaneously. Analyses involved collecting multiple image planes, typically 100 planes for oxygen, 40 planes for hydrogen. Each plane consists of 256×256 pixels. Automatic peak centring was performed regularly throughout each

measurement. Planes of images data were corrected for detector deadtime (44 ns), the quasi-simultaneous arrival (QSA) effects (for ^{16}O only) sample drift, combined and processed using the L'image software (L. Nittler, Carnegie Institute of Washington) to provide bulk $\delta^{17}O$, $\delta^{18}O$ and D/H ratios for each area (e.g. Fig. 2.9.2).

The finely focused primary ion beam scans the sample in a raster pattern and software saves secondary ion intensities as a function of beam position, in order to provide a secondary ion image of the area analysed. Standard analyses in imaging mode for the H measurements were performed on hydroxyl, whilst standard analyses in imaging mode for the O measurements were performed on flat, polished San Carlos olivine crystals on comparably-sized areas to the matrix areas analysed. Oxygen isotope ratios were normalised to Standard Mean Ocean Water (SMOW) using a San Carlos olivine standard that bracketed the sample analyses in order to generate $\delta^{17}O$ and $\delta^{18}O$ values and to provide corrections for instrumental mass fractionation. The best precision that can be achieved for isotope ratio measurements depends on the number of counts measured on the least abundant isotope which in this case is ^{17}O. To achieve a precision of 1‰ (1 sigma) requires at least 1 million counts (Kilburn et al., 2015). Errors for the isotope ratios reported in this work are given as 2 sigma, and combine the internal error for each analysis with the standard deviation of the mean of the associated standard. Errors are large due to the acquisition method; a smaller probe size was in fact required to measure ^{16}O of bulk regions produced poorer counting statistics. Typical reproducibility for the measurements estimated on the analysis of the standards ±2.8‰ for $\delta^{17}O$, ±1.7‰ for $\delta^{18}O$, and ±1.4‰ for δD.

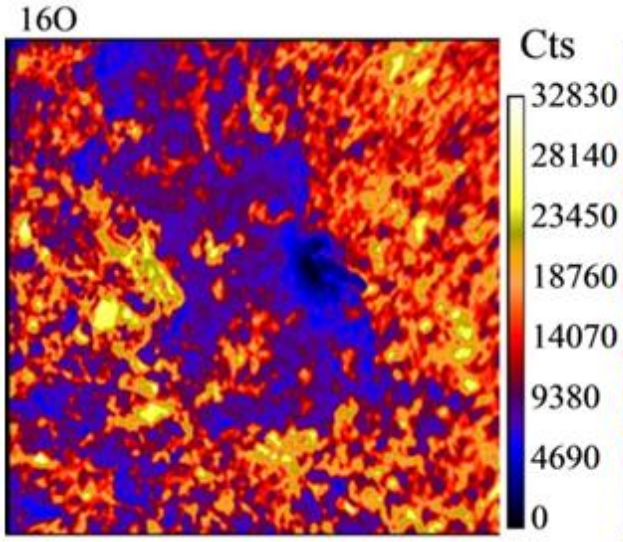

Fig. 2.9.2a

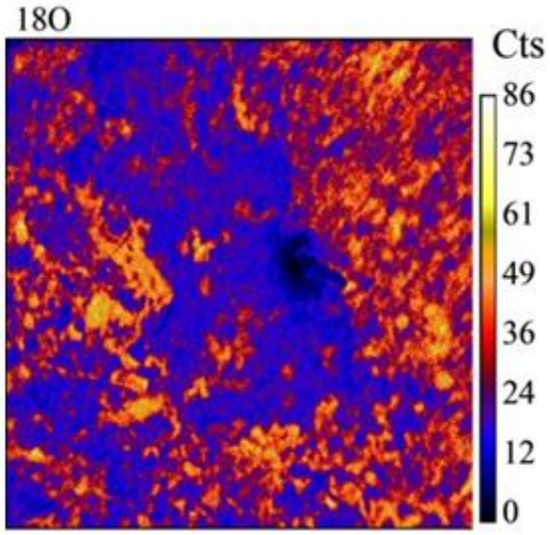

Fig. 2.9.2b

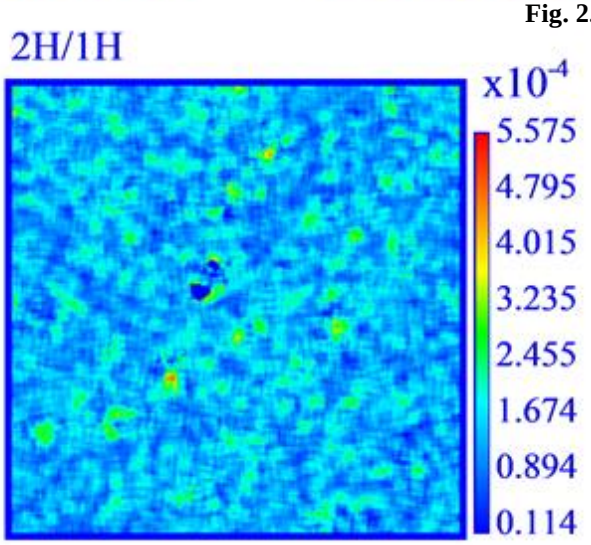

Fig. 2.9.2c

Fig. 2.9.2a – ^{18}O ion image of matrix Area 1of sample ALHA77307
Fig. 2.9.2b – ^{16}O ion image of matrix Area 1of sample ALHA77307
Fig. 2.9.2c – D/H ion image of matrix Area 1of sample ALHA77307

Chapter 3

3. Petrology of Fine Grained Matrix

The petrology of the fine grained matrix can give important clues about the physical and chemical processes experienced by the meteorite matrix constituents. The petrologic aspect is therefore important to consider as it may highlight processes that took place in the protoplanetary disk or in the parent body, and can help explain peculiar features or geochemical signatures observed. In this work a combination of high resolution SEM techniques are used. These have the advantage of studying wider regions of matrix, compared to narrower areas investigated using TEM foils. This can prove useful to contextualise observations and identify better the effects of aqueous alteration and thermal metamorphism, plus more representative sample of grains.

3.1 - CO3.0 carbonaceous chondrite ALHA77307

3.1.1 - Previous studies

ALHA77307 is a CO3.0 chondrite, characterised by fine-grained matrix consisting of abundant amorphous dust and unequilibrated assemblages of Fe and Si-rich material (Scott and Jones, 1990). This sample seems to have experienced minimal aqueous alteration (e.g. Scott and Jones, 1990; Brearley, 1993; Grossman and Brearley, 2005; Bonal et al., 2007), although Ikeda (1983) described some evidence for aqueous alteration which had affected the matrix and chondrules of ALHA77307 and suggested that alteration occurred prior to accretion of the meteorite. This meteorite shows evidence of minimal thermal metamorphism (e.g., Scott and Jones, 1990; Brearley, 1993; Grossman and Brearley, 2005; Bonal et al., 2007). On the basis of the absence of metamorphic effects in the silicates such as Cr content in the olivine and, abundances of noble gases in presolar grains Huss et al. (2006) determined a peak metamorphic temperature of just over 200 °C. One of the lowest

values they determined in contrast, Raman analyses indicate that the insoluble organic matter (IOM) present is less disordered than that of many CR (Busemann et al., 2007), suggesting some thermal processing of the organics.

3.1.1.1 – Anhydrous Crystalline Phases in the Matrix

ALHA77307 contains a very high abundance of opaque, fine-grained matrix, (~ 30 Vol.% McSween, 1977 & 40-50 Vol.% Scott, 1984) which occurs throughout the meteorite. After the amorphous component, olivine is the most abundant phase within the chondrule rims and matrix of ALHA77307. Pyroxene is much less abundant than olivine in the matrix and rims of ALHA77307, but also occurs in a number of different morphological types. Although the compositional data reported by (Brearley,1993) show that the matrix is relatively homogeneous, the TEM studies (Brearley, 1993) have revealed that mineralogically, the matrix and rims of ALHA77307 are extremely heterogeneous and complex, and have a highly unequilibrated mineral assemblage. The TEM studies also show that mineralogically there are no differences between matrix and rims, indicating that the two have a common origin. The matrix of ALHA77307 is dominated by amorphous silicates that occurs throughout rim and matrix material, and is often closely associated with olivine. Sulfides are comparatively abundant within the matrix of ALHA77307 and, like kamacite, appear to occur exclusively as fine-grained crystals within regions of the amorphous/microcrystalline material (Brearley, 1993).

3.1.1.2 – Amorphous Phases in the Matrix

The matrix of ALHA77307 is dominated by amorphous material which acts as a groundmass in which fine-grained crystalline phases occur. The proportions of crystalline phases vary from one region to another, with Brearley (1993) suggesting that these different regions represent distinct clusters of nebular grains or presolar dust that have experienced different degrees of annealing and probably formed under different conditions. If this is the case then the crystalline phases present within the amorphous component should have crystallized from the amorphous matrix, and have a composition which is closely related to it. Brearley (1993) provided support for a genetic relationship between the olivine and amorphous component. Olivines associated with the amorphous component according to Brearley (1993) formed as a result of low-temperature annealing due to the fact that they appear to be poorly crystalline, with abundant defects and poorly defined outlines.

3.1.1.3 – Phyllosilicates in the Matrix

Ikeda (1983) reported phyllosilicates in ALHA77307 occurring as grains embedded within the amorphous component of the matrix. Brearley (1993) also described isolated aggregates or single crystals of highly disordered, mixed layer phyllosilicates ranging in size from 0.3 μm up to over 1 μm, and have an extremely Fe-rich composition that closely resembles Fe-rich serpentine compositions found in CM meteorites.

3.1.2 - Study carried out in this project

3.1.2a - Matrix abundance

The element maps acquired using the EVO 15L SEM (Fig. 3.1.1) were used to estimate the abundance of matrix measured on an approximately 9.5 × 9.5 mm thin section. The Ornans (CO) chemical group of carbonaceous chondrites is distinguished by small chondrules and refractory inclusions (< 0.2 mm) occupying about half the volume of the rock, whilst the other half is the matrix, and they generally show a low degree of aqueous alteration (Weisberg et al., 2006). In order to estimate the matrix percentage of the sample, the element map was thresholded to create a binary image in order to measure the total sample area using Image J® (as described in chapter 3) which was set as 100% (Fig. 4.1.2).

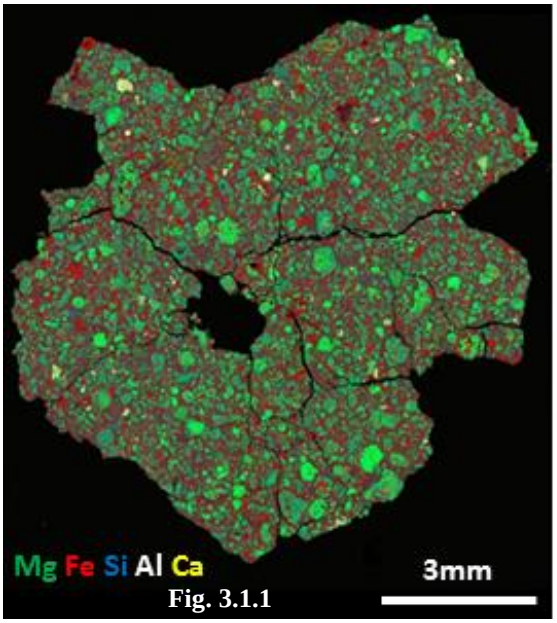

Fig. 3.1.1

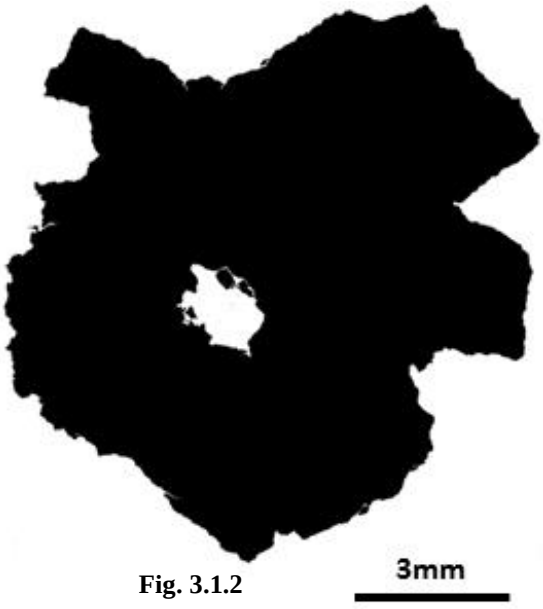

Fig. 3.1.2

Fig. 3.1.1 - Element map of sample ALHA77307
Fig. 3.1.2 - Binarised image of ALHA77307 element map

From the total sample area the surface area occupied by the micro fractures was calculated as 2% (Fig. 3.1.3). This subtracted from the total sample area, to obtain a real sample area of 98%. Segmentation of the chondrules and CAI in the element maps was then performed, separating them out from the background by thresholding the pixels with lowest intensity (black) (Fig. 3.1.4). The chondrules and CAI abundance accounted for 51%, which is

consistent with the meteoritic bulletin classification (Weisber et al., 2006). The matrix abundance in the sample ALHA77307 was then obtained by subtracting from the real sample area of 98% the chondrules and CAIs value of 51% that gave us the Matrix value of 47%. This value is consistent with previous studies (~ 30% McSween, 1977 and 40-50% Scott, 1984) for the same sample.

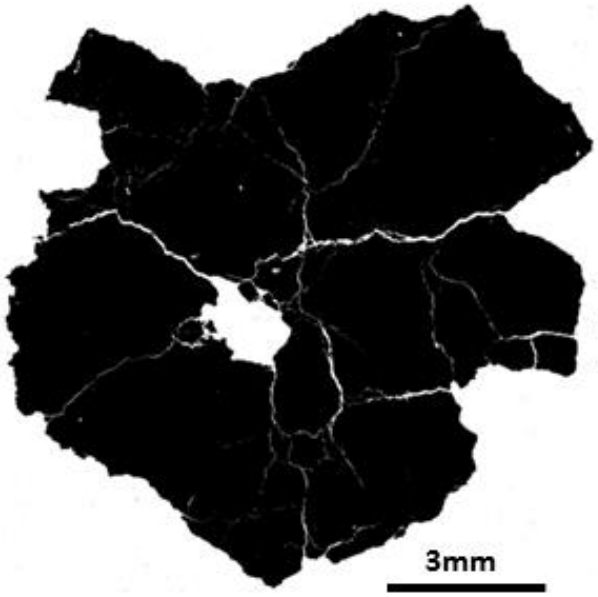

Fig. 3.1.3

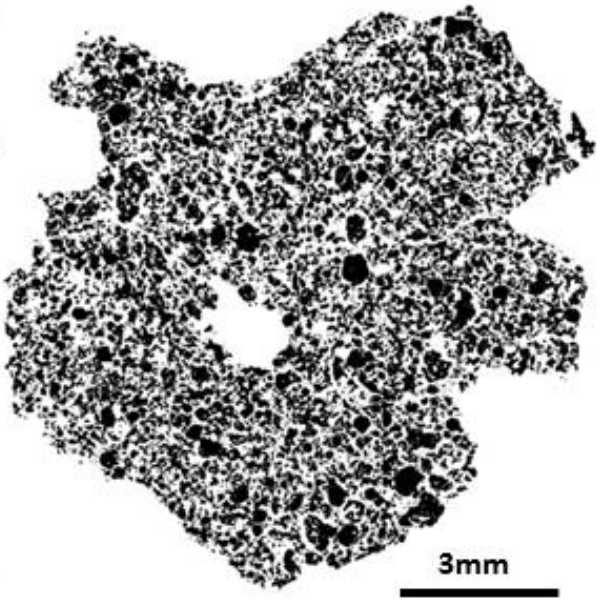

Fig. 3.1.4

Fig. 3.1.3- Binarised image of ALHA77307 element map showing micro fractures.
Fig. 3.1.4 - Binarised image of ALHA77307 element map showing chondrules and CAIs.

3.1.2b – Bulk Chemical Composition of Matrix

The compositions of matrix material in ALHA77307 have been obtained by extracting the spectrum from the montage map of 5 different matrix regions of approximately 1 mm^2 acquired with EVO 15L SEM (Fig. 3.1.5). Data are plotted on a ternary Si-Fe-Mg (element wt %) diagram in Fig. 3.1.6 and values of the extracted spectra are reported in Table 3.1.1. Fe has a negative trend with Si and Mg. It shows a narrow range of compositions, defining a trend from the Fe apex at roughly constant Mg/(Si + Mg) ~ 40, a result consistent with that reported by Brearley (1993).

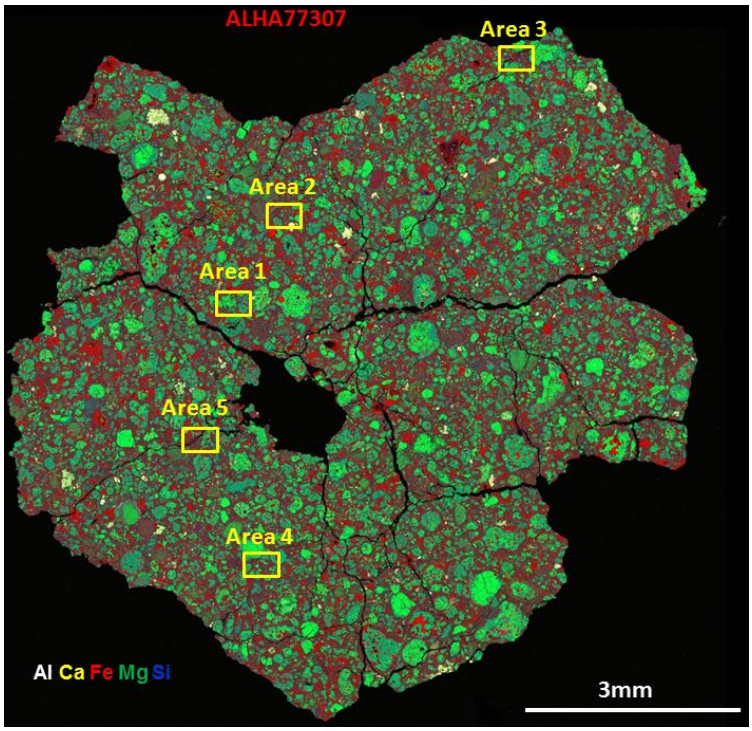

Fig. 3.1.5 – ALHA77307 Element map showing the 5 matrix Areas investigated

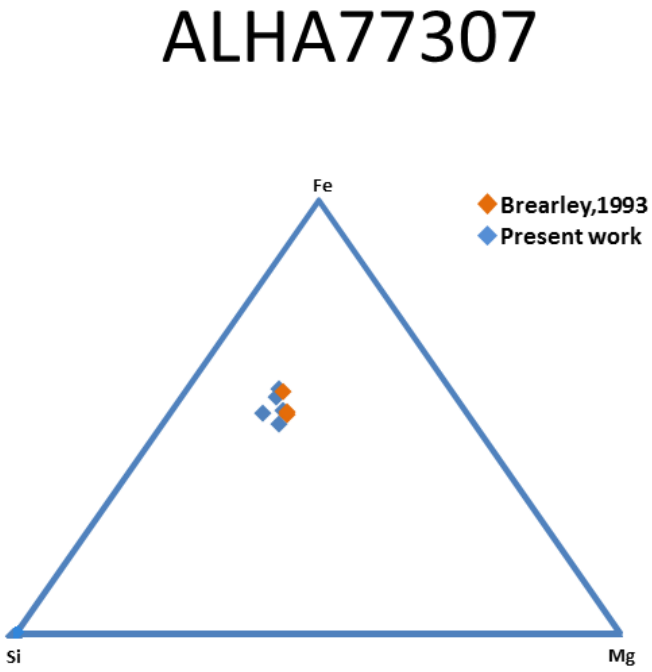

Fig. 3.1.6 – Plot showing the Fe:Mg:Si ratio of matrix regions in ALHA77307 plotted in a ternary (element wt %) diagram. Although there is a narrow range of compositions a trend of changing Fe content at constant Si; Mg ratio is apparent. Data are consistent with Brearley, 1993.

ALHA77307 (wt%)	AREA 1	AREA 2	AREA 3	AREA 4	AREA 5
O	40.1	36.0	37.8	38.2	40.4
Na	0.2	0.5	0.5	0.3	0.4
Mg	8.7	8.6	7.1	7.1	7.1
Al	2.2	2.0	2.7	2.0	2.3
Si	14.4	13.8	15.5	12.8	13.3
S	1.9	2.4	1.8	1.6	2.1
K	0.2	0.2	0.0	0.2	0.1
Ca	0.5	0.5	0.3	0.6	0.6
Ti	0.0	0.0	0.0	0.0	0.0
Cr	0.2	0.1	0.4	0.2	0.0
Mn	0.0	0.1	0.1	0.2	0.0
Fe	21.8	24.0	23.6	26.2	25.0
Co	0.0	0.9	0.2	0.0	0.0
Ni	1.6	1.8	1.2	2.4	2.4
Total	91.7	90.9	91.0	91.9	93.8

Table 3.1.1 – Chemical compositions (element %) determined by the Evo 15L analyses on selected matrix regions in ALHA77307

Major elements from the five different matrix regions, normalized to CI chondrite values and Si (from Anders & Grevesse, 1989) are shown in Fig. 3.1.7. All five regions analysed are similar showing only minor differences between them. In all the matrix regions the elements Al, K, and S appear to be significantly fractionated relative to CI abundances. The other elements are generally depleted with respect to CI displaying a relatively wide scatter between the five analysed regions. Ni shows the widest variation ranging from slightly depleted (Area 3 in Fig. 3.1.7) to slightly enriched (Areas 1, 2, 4, 5).

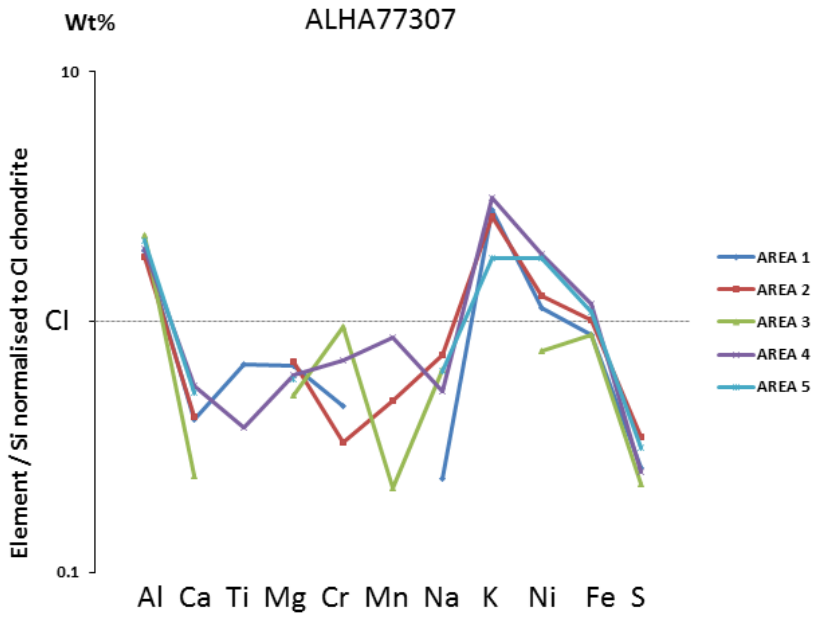

Fig. 3.1.7 - Normalised element ratio diagram showing data of five different matrix regions in ALHA77307. The data are normalised to Si and CI chondrite values from (Anders & Grevesse, 1989). There are no compositional differences between the different matrix regions. X-ray detection limit ~ 0.1- 0.3 mass % depending on the element

These analyses are in partial agreement with Brearley (1993) whose data also show a general fractionation relative to CI with Ca, S, Na showing the heaviest depletion. Ni, K, Al show enrichment compared to solar values and a slight enrichment is also exhibited by Fe (Brearley, 1993).

3.1.2c – Modal Mineralogy of the Matrix

High definition EsB image maps acquired using the FEG SEM Ultra Plus were used to estimate the abundance of the different matrix constituents on the basis of their different grey scale value using Image J (Fig. 3.1.8) and reported in Table 3.1.2. A similar approach as described in Chapter 2 was used, to threshold and carefully discriminate the different features present in the matrix characterised by different grey scale values. Each mineral phase displays a different intensity of BSE that depends on the average atomic density in the sample. The brighter phases in the BSE image indicate which contain the highest mass atoms, and these generally relate to the most Fe-rich, with the very brightest being Fe-Ni metal, whereas the lowest intensity (black) corresponds to most likely to interstitial pores.

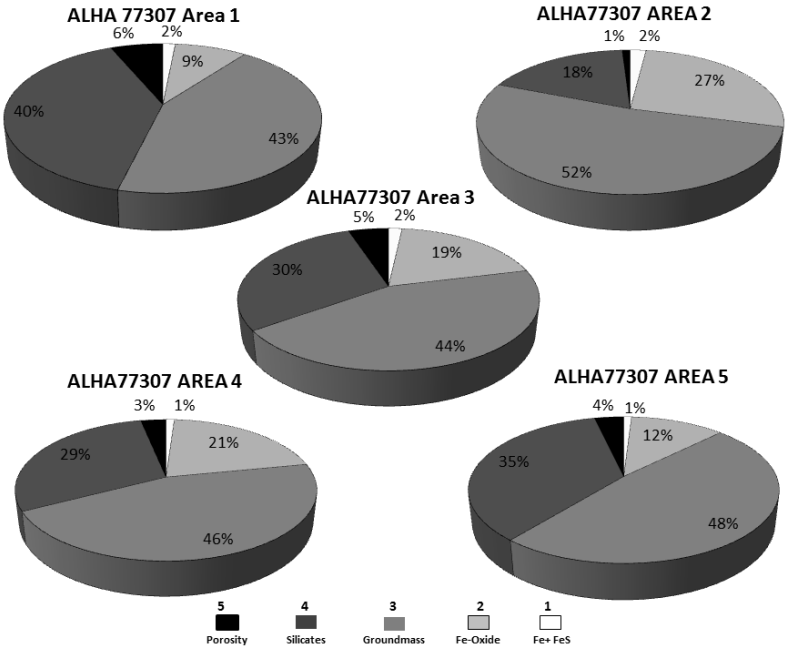

Fig. 3.1.8 - Pie Charts of the different sample areas in ALHA77307 showing abundances of the grayscale unities present in the matrix

The five image maps (each map having an area of ~ 20 x10 μm) of the matrix regions investigated show the average abundance of metal grains is 2±0.5% (shaded white=1 in Fig. 3.1.8), the average porosity is 4±1.9% (shaded black =5), and the average abundance of crystalline silicates is 30±8.2% (dark grey region = 4) . The light grey phase is characterised by relatively high intensity pixels suggesting that is a Fe-rich phase, most likely Fe-oxides, and accounts for 18±6.4% (shaded pale grey =2), whilst the groundmass of amorphous material accounts for 47±3.6%(mid grey areas = 3). Values of the thresholding and average values are reported in Table 4.1.3.

ALHA77307		Threshold	%Area
Area 1	Fe+ FeS	255-170	2
Area 1	Fe-Oxide	169-130	9
Area 1	Groundmass	129-90	43
Area 1	Silicates	89-50	40
Area 1	Porosity	49-0	6
			100

ALHA77307		Threshold	%Area
Area 2	Fe+ FeS	255-205	2
Area 2	Fe-Oxide	204-145	27
Area 2	Groundmass	144-100	52
Area 2	Silicates	99-50	18
Area 2	Porosity	49-0	1
			100

ALHA77307		Threshold	%Area
Area 3	Fe+ FeS	255-165	2
Area 3	Fe-Oxide	164-95	19
Area 3	Groundmass	94-55	44
Area 3	Silicates	54-25	30
Area 3	Porosity	24-0	5
			100

ALHA77307		Threshold	%Area
Area 4	Fe+ FeS	255-195	1
Area 4	Fe-Oxide	194-141	21
Area 4	Groundmass	140-100	46
Area 4	Silicates	99-50	29
Area 4	Porosity	49-0	3
			100

ALHA77307		Threshold	%Area
Area 5	Fe+ FeS	255-225	1
Area 5	Fe-Oxide	224-160	12
Area 5	Groundmass	159-100	48
Area 5	Silicates	99-45	35
Area 5	Porosity	44-0	4
			100

Table 3.1.2 – Table showing thresholding values of the different matrix regions in ALHA77307

ALHA77307	Porosity	Silicates	Groundmass	Opaques	Fe-Oxides
Area 1	6	40	43	2	9
Area 2	1	18	52	2	27
Area 3	5	30	44	2	19
Area 4	3	29	46	1	21
Area 5	4	35	48	1	12
Average (1σ)	4	30	47	2	18
STDV	1.9	8.2	3.6	0.5	6.4

Table 3.1.3 - Table showing abundances and average values of each individual grey scale unities and in different matrix regions in ALHA77307

3.1.2d – High Resolution Element Maps of Matrix

Element maps of the same matrix regions were acquired at 5kV (Fig. 3.1.9 & 3.1.10, Fig.3.1.11 & 3.1.12,) using a FEI Quanta 650 SEM with an innovative XFlash QUAD 5060F Bruker detector capable of providing chemical information at spatial resolution down to a volume of ~200 nm in depth by ~100 nm in radius at 5kV. Presented here are Areas 1 and 5, other map areas are reported in Appendix. Element maps show that the most abundant cations of the amorphous groundmass are Al, Si and Fe, consistent with previous works (e.g. Brearley, 1993, and Abreu & Brearley, 2010), and that Mg-rich crystalline silicates dominate the larger grain size.

Almost all the silicate crystals present in the matrix do not show well developed external crystal faces (anhedral), apart from the few whiskers observed which are euhedral (fully crystal-faced). The presence of anhedral isolated grains, suggest either collisional processing or indicate partial removal of crystalline material by reaction with gaseous fluids.

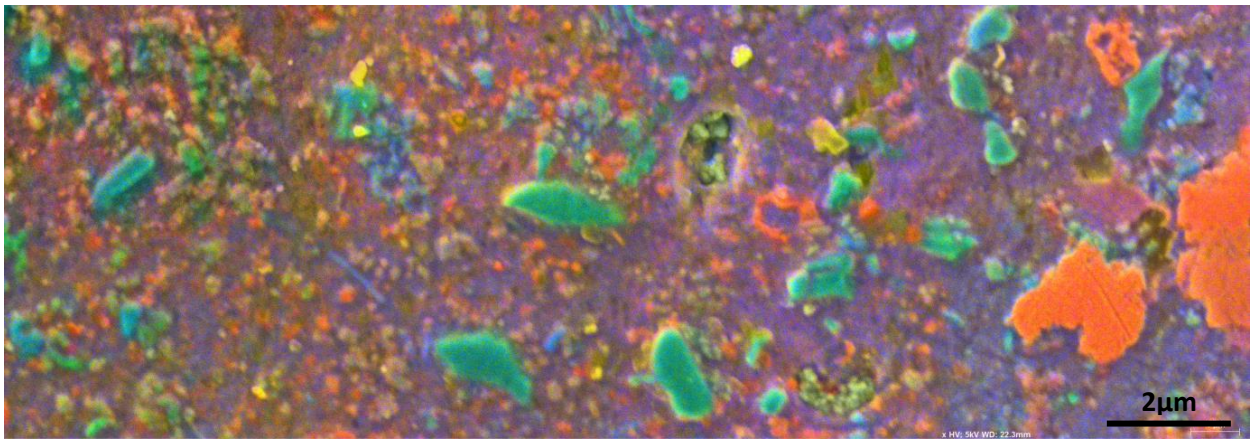

Fig. 3.1.9 – Combined SE-Element map of matrix ALHA77307 Area 1 **Fe Mg Si**

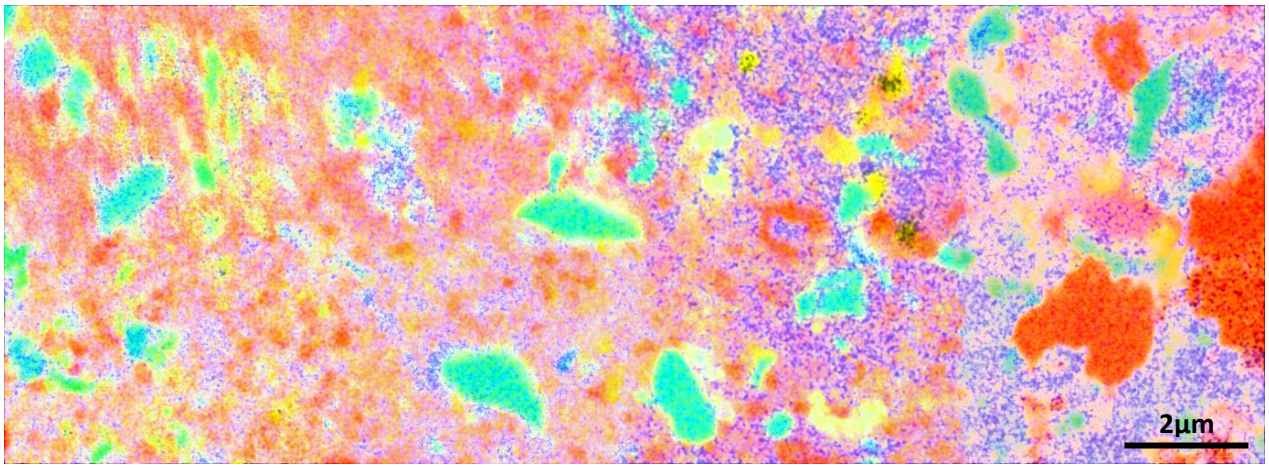

Fig. 3.1.10 - Element map of matrix ALHA77307 Area 1 **Fe Mg Si**

Fig.3.1.10 and Fig. 3.1.12 also display a zonation in the chemical composition of the matrix with the finer material enriched in Fe in the left hand area of Fig.3.1.9, similarly in Fig. 3.1.12 left part of the map displays enrichments in Fe. Some anhedral crystals, especially the Fe-rich phases, with variable brightness in back-scattered alectrons, exhibit lobate margins. This could indicate chemical reaction with fluid percolating and deposition of secondary phases by in-situ alteration.

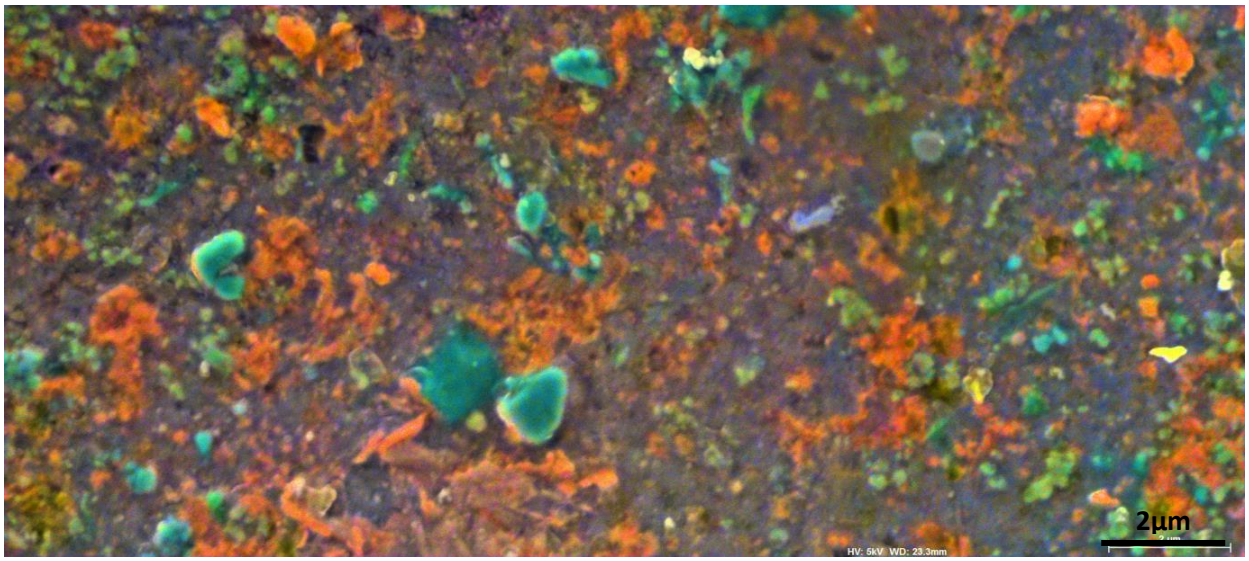

Fig. 3.1.11 – Combined SE-Element map of matrix ALHA 77307 Area 5 Fe Mg Si

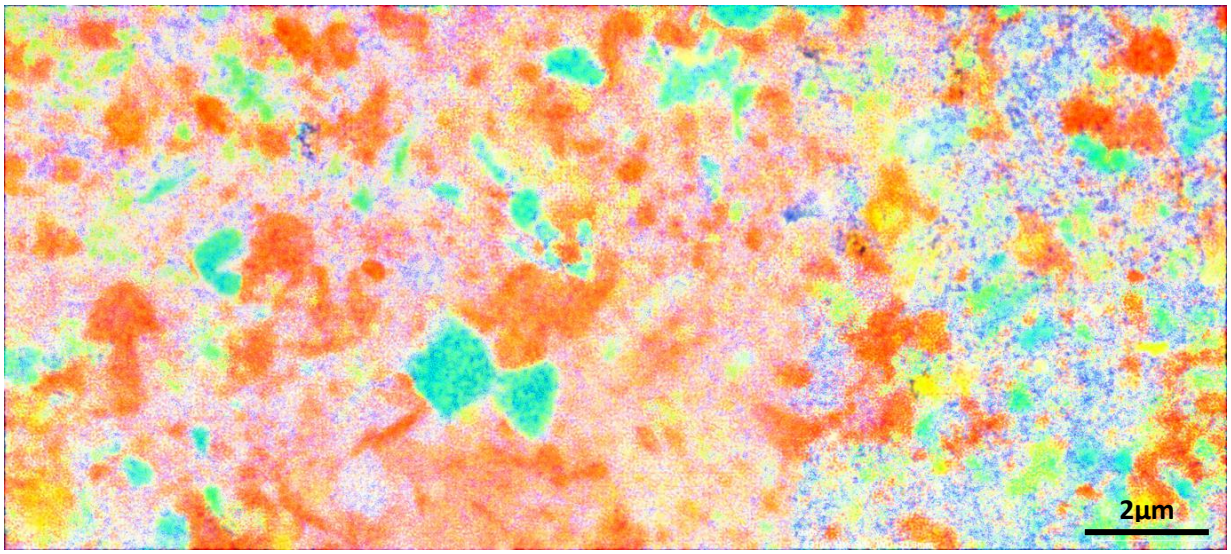

Fig. 3.1.12 - Element map of matrix ALHA77307 Area 5 Fe Mg Si

3.1.2e – Enstatite whiskers

The SEM observation of the matrix of ALHA77307 has revealed the presence of features compatible with enstatite whiskers. This type of solar nebula condensate are typically <10

μm in length and <200 nm width. Their distinctive features are the axis of elongation [100] and their axial screw dislocations which discriminates them from terrestrial grains usually elongated along [001]. This unique crystal morphology and microstructure are consistent with nebular or circumstellar gas condensation at low-pressure, and temperatures >~1300 K (Bradley, Brownlee & Veblen, 1983). Acicular crystals in the matrix of ALHA77307 were first observed in the ultra-high resolution maps acquired using Ultra Plus FEG SEM. Crystals are typically 2-3 μm in length and <200 nm in width (Fig. 3.1.13).

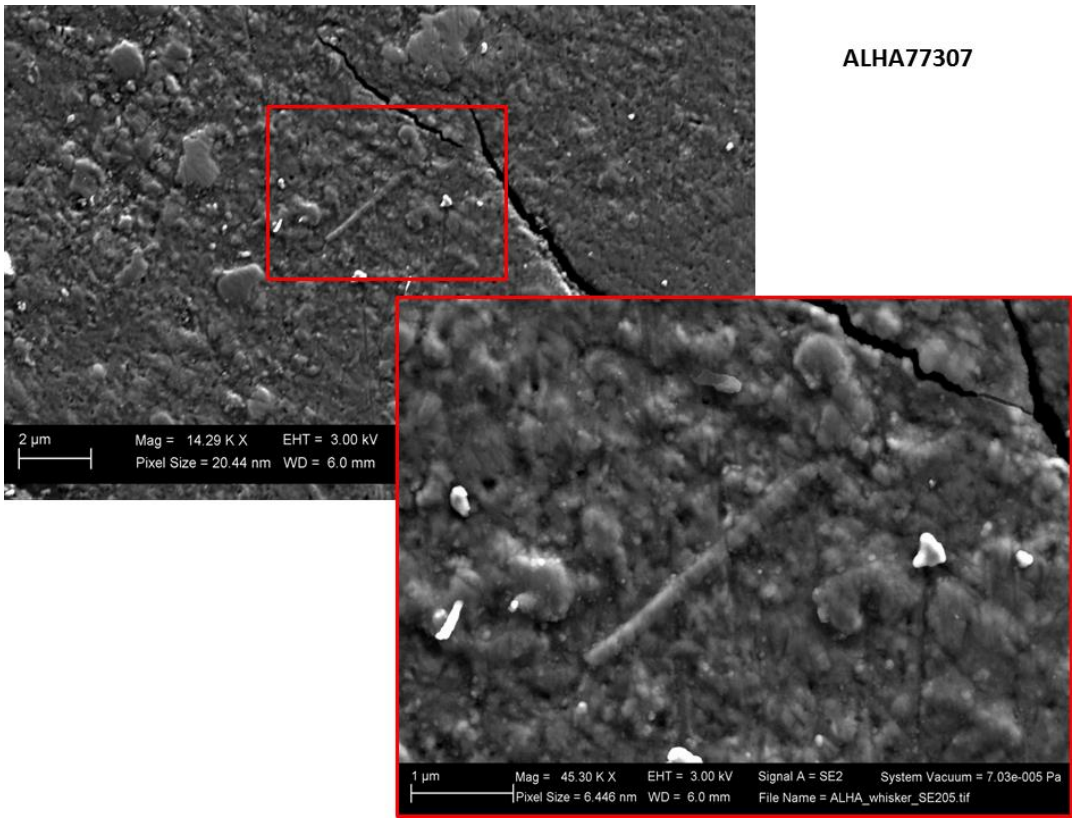

Fig. 3.1.13 - Secondary Electron images of whisker in the matrix of ALHA77307

Element maps were acquired using FEI Quanta at 3.5 kV in order to minimise the volume of interaction of the electron beam to provide chemical information with the same spatial resolution as the 5 kV maps, but reducing the depth of the interaction volume to ~ 100 nm. The chemical composition of the whisker is confirmed as Mg-rich silicates, consistent with the composition of the enstatites Fig. 3.1.14 & 3.1.15.

Fig. 3.1.14 - SE Element map of whisker in the matrix of ALHA77307

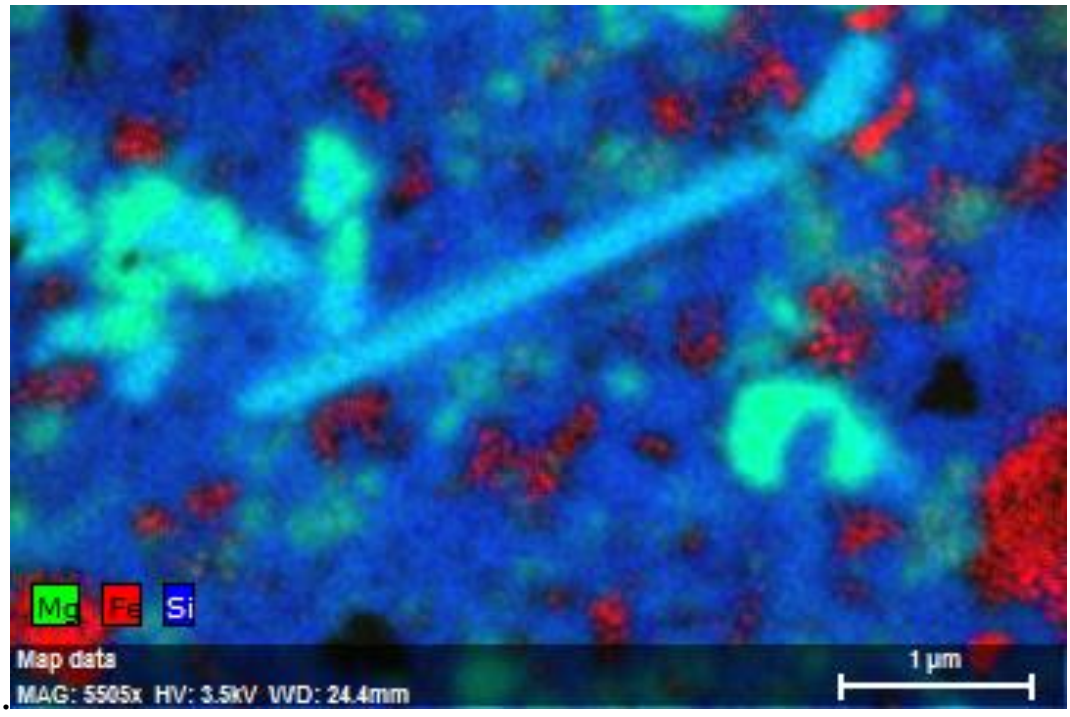

Fig. 3.1.15 - Element map of whisker in the matrix of ALHA77307

3.1.2f – Mineralogy of the Matrix

The micro-XRD patterns of the matrix for the 5 areas selected for study in sample ALHA77307 (Fig. 3.1.16) indicate the presence of olivine, enstatite, metal, iron sulfide, and magnetite. In previous TEM investigations also poorly ordered phyllosilicates were observed embedded in a groundmass of amorphous material (Vaccaro et al., 2014) (Fig. 3.1.17) but these were not detected by the micro-XRD due to the collection angle limits (ω angle fixed at 20°). The average abundance volumes for ALHA77307 obtained using a profile-stripping method are: 26% olivine $(Mg, Fe)_2SiO_4$, 20% enstatite ($MgSiO_3$), 7% magnetite $Fe^{2+}Fe^{3+}{}_2O_4$, 1% pyrrhotite $Fe_{1-x}S$ (x = 0 to 0.2), 1% Fe-metal. The remaining 45% contribution which is not accounted for is likely to be the poorly crystalline phases e.g. ferrihydrite $(Fe^{3+})_2O_3\ 0.5H_2O$ and/or amorphous silicates, which most likely are also contributing to the overall pattern background. The absence of strong peaks and a lack of amorphous silicate standards make it difficult to quantify the amorphous phase. Phase quantification values for each individual area are reported in Table 3.1. 4 and Fig. 3.1.18.

ALHA77307	1	2	3	4	5	Average
Olivine	26	13	41	15	36	26
Enstatite	18	13	22	27	19	20
Magnetite	5	12	3	7	7	7
Pyrrhotite	0	4	0	0	0	1
Fe-metal	0	0	0	2	4	1
Amorphous phases	51	58	34	49	35	45

Table - 3.1.4 - showing abundances of the mineral phases calculated in each area and sample average values. 1-5 columns represent the 5 areas selected to study, and amorphous phase was determined by difference. Phyllosilicates were not detected due to analytical limitations.

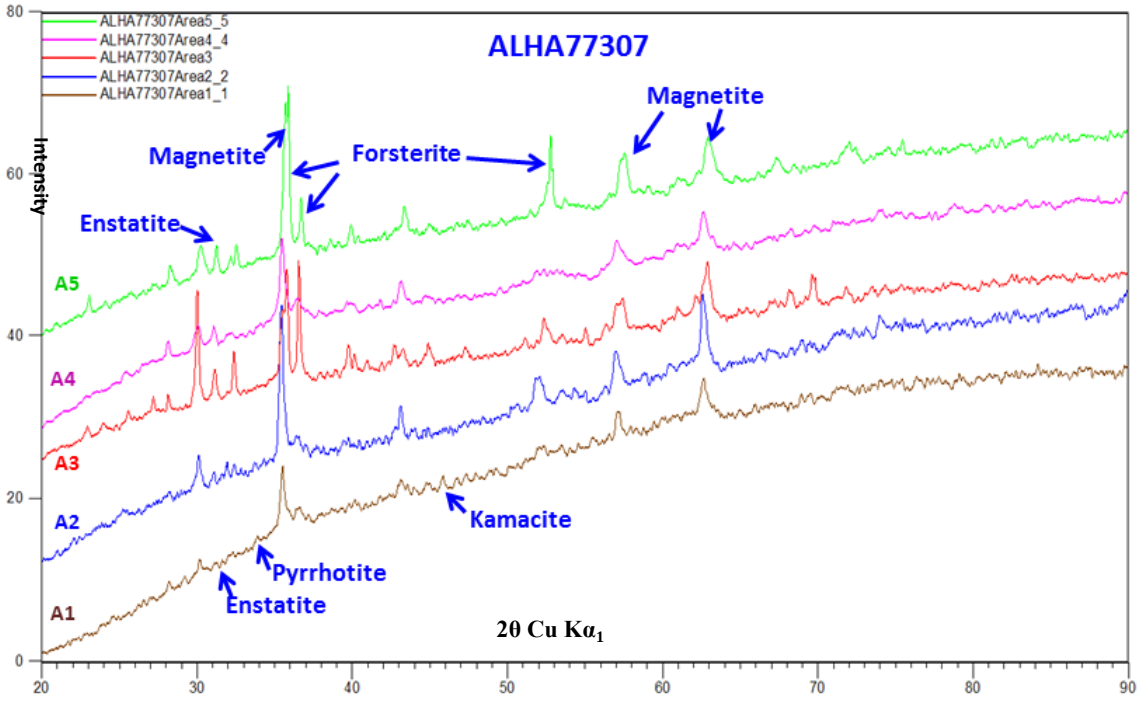

Fig. 3.1.16 – X-ray diffraction pattern of the matrix areas investigated in ALHA77307

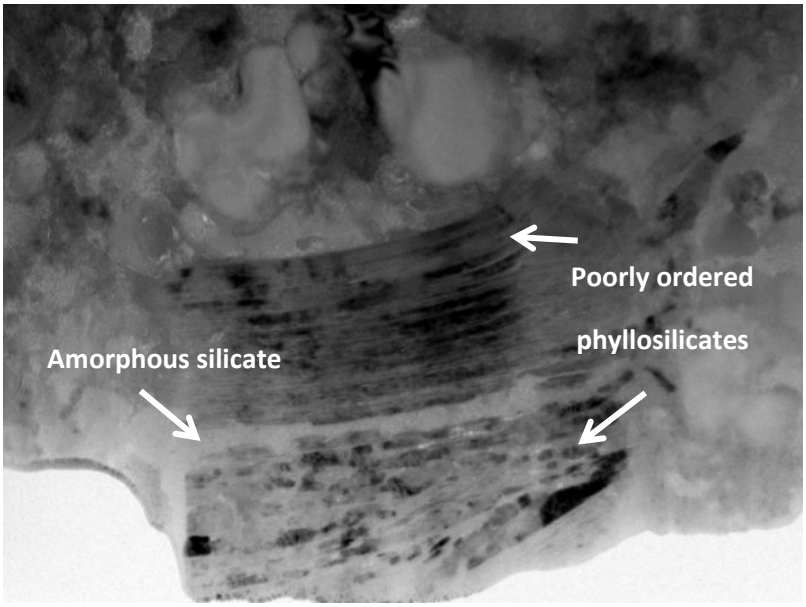

Fig. 3.1.17 - TEM investigations of matrix for ALHA77307 showing poorly ordered phyllosilicates embedded in a groundmass of amorphous material Vaccaro et al., 2014

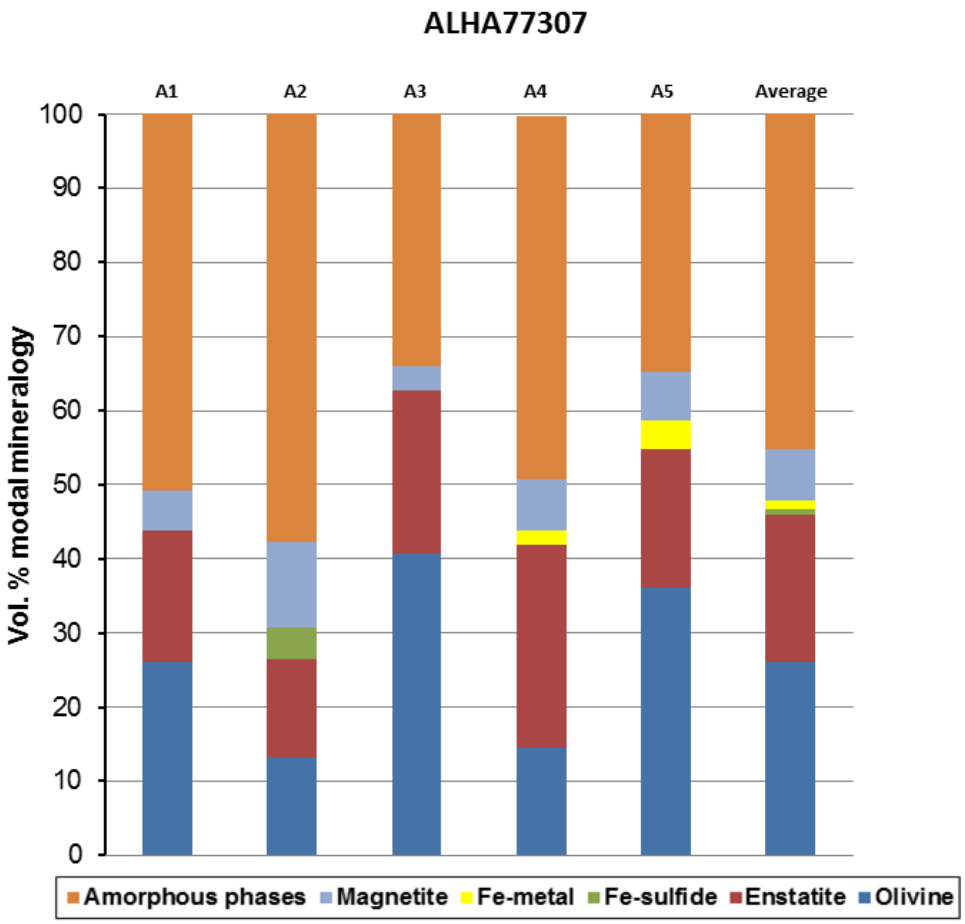

Fig. 3.1.18 – Bar chart reporting abundances of mineral phases present in each individual area and sample average values vol % in ALHA77307

3.2 - Ungrouped Carbonaceous Chondrite MIL07687

3.2.1 - Previous studies

The ungrouped carbonaceous chondrite MIL 07687 has been previously classified as a CO3 chondrite, but shows unique properties that make this meteorite different from typical CO chondrites (Brearley, 2013). This meteorite appears to be a rare example of a chondrite showing evidence of partial alteration of fine grained matrix, providing important insights on the diversity of processes that occurred in the early Solar System (Brearley, 2013). The matrix of MIL 07687 is characterised by a high abundance of presolar grains (231 grains, Davidson et al., 2014) whose isotopic compositions are consistent with those observed in other meteorites, with most grains indicating minimal evidence of thermal metamorphism experienced by the meteorite (Floss and Brearley, 2014). Carbon K-edge XANES spectra of the carbonaceous material present in the sample is chemically variable and appears to be similar to IOM from other primitive carbonaceous chondrites, and is present as abundant, isolated, sub-micron inclusions but also as larger veins of material (Davidson et al., 2015). The presence of carbonate is consistent with the aqueously altered nature of MIL 07687. Thus, MIL 07687 should be considered to be a type 2 carbonaceous chondrite (Davidson et al., 2015).

3.2.1.1 – Anhydrous Crystalline Phases in the Matrix

MIL 07687 features a texturally complex matrix consisting of irregularly shaped-regions with high and low contrast in BSE images indicating high Z of the components suggesting it is rich in Fe. Generally, FeO-rich matrix regions are separated from FeO-poor matrix regions and the boundary between the two matrix types is defined by a distinct, very Fe-enriched front of alteration. The FeO-rich regions of matrix are characterised by a high abundance of a fibrous phase which occurs as randomly oriented crystallites or radiating sets of fibres (Brearley, 2013). TEM EDS analyses show that the fibrous phase is very

FeO-rich (74-92 wt%), but also contains variable concentrations of SiO_2 MgO, Al_2O_3, and NiO (Brearley, 2013). The Fe-poor regions of matrix consist of much finer grained crystals, and are more homogeneous. Electron images of these FeO-poor regions closely resemble the matrix of low petrologic type CO3 chondrites such as ALHA77307 (Brearley, 1993).

3.2.1.2 – Phyllosilicates in the Matrix

The matrix of MIL 07687 shows unique features due to an unusual style of alteration. Phyllosilicate phases, very common products of aqueous alteration of silicates, are not present in the matrix, which is instead dominated by needle shaped Fe-oxyhydroxides. High resolution TEM analysis of these acicular phases indicate that the fibres consist of randomly oriented nanocrystallites, whose electron diffraction data are most consistent with either ferrihydrite ($(Fe^{3+})_2O_30.5H_2O$) or akaganéite ($Fe^{3+}O(OH,Cl)$) (Brearley, 2013). FeO-rich regions of matrix appear to be due to aqueous alteration of matrix, whilst the Fe-poor matrix regions represent the relatively unaltered protolith that escaped aqueous alteration (Brearley, 2013).

3.2.2- Study carried out in this project

3.2.2a - Matrix abundance

MIL 07687 was previously classified as a CO3, but its unusually high abundance of matrix of 68 vol% is one characteristic among others that makes this sample different from typical COs (Brearley, 2013). A new value for the matrix abundance in MIL 07687 was obtained by subtracting the total sample area measured by binarising, then thresholding the whole sample (Fig. 3.2.1 & 3.2.2) the chondrules and CAIs abundance in the sample which accounted for 37% vol. (Fig. 3.2.4). The surface area occupied by the micro fractures (Fig. 3.2.3) was neglected as it accounted for < 1 %vol. This provides a matrix abundance of

63%, similar to that determined previously and confirming the exceptionally high matrix abundance of this meteorite.

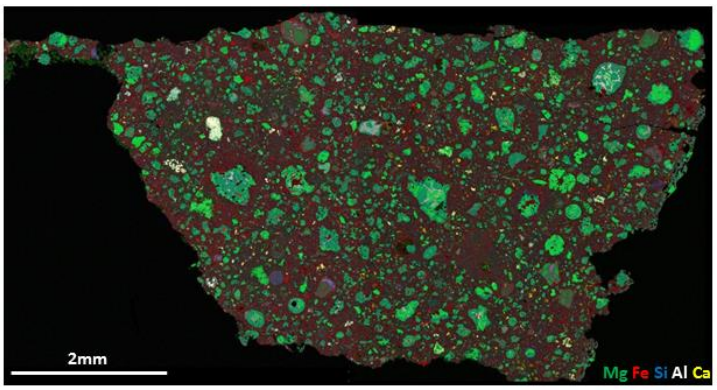

Fig. 3.2.1

Fig. 3.2.2

Fig. 3.2.1 - Element map of sample MIL 07687.
Fig. 3.2.2 - Binarised image of sample MIL 07687 element map.

Fig. 3.2.3

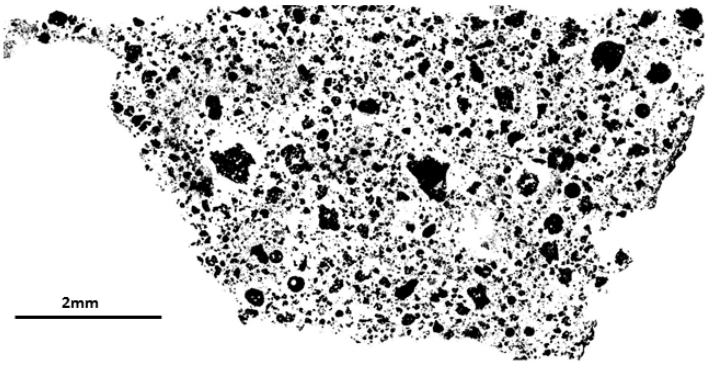

Fig. 3.2.4

Fig. 3.2.3 - Binarised image of MIL 07687 element map showing micro fractures.
Fig. 3.2.4 - Binarised image of MIL 07687 element map showing chondrules and CAI.

3.2.2b – Bulk Chemical Composition of the Matrix

Spectra extracted from the sample MIL 07687 montage map acquired using the EVO 15L SEM are reported in Table 3.2.1. Data were extracted from five different matrix regions across the sample (Fig. 3.2.5) of approximately 1 mm^2 and plotted on a ternary Si-Fe-Mg (element wt %) diagram in Fig. 3.2.6. Similarly to observations of ALHA77307, Fe shows variations, although somewhat greater than that displayed by ALHA77307, but still with more or less constant Mg/(Si+Mg)~40.

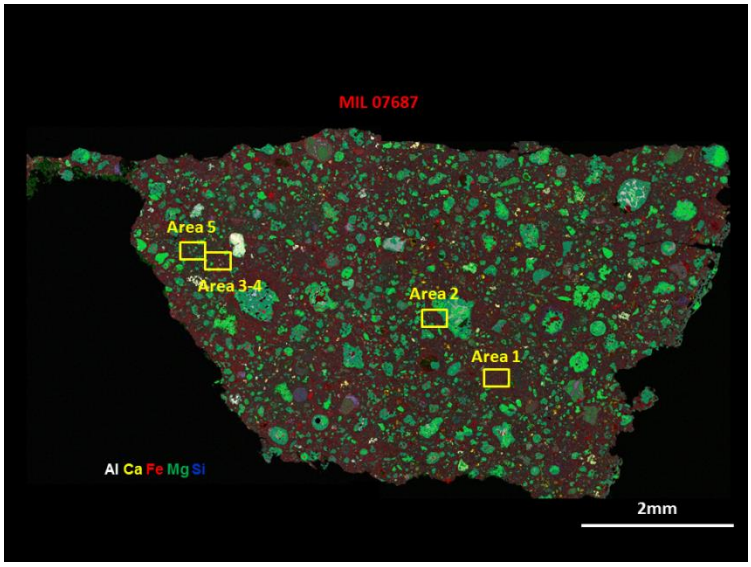

Fig. 3.2.5 – MIL 07687 Element map showing the 5 matrix Areas investigated.

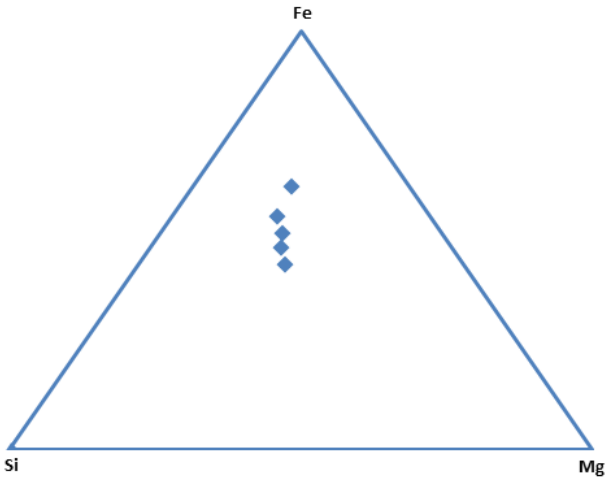

Fig. 3.2.6 – Plot showing the Fe:Mg:Si ratio of matrix regions in MIL 07687 plotted in a ternary (element wt %) diagram. Although there is a narrow range of compositions, Fe variations are greater than in ALHA77307, and a trend of changing Fe content at constant Si; Mg ratio is apparent.

MIL07687(wt%)	AREA 1	AREA 2	AREA 3	AREA 4	AREA 5
O	35.0	34.1	33.1	30.3	32.5
Na	0.4	0.3	0.4	0.5	0.2
Mg	8.7	9.8	8.3	8.8	10.3
Al	1.1	0.8	0.8	0.5	0.8
Si	12.4	12.5	9.7	11.4	12.4
S	3.7	3.4	4.3	3.2	3.2
K	0.1	0.1	0.1	0.0	0.1
Ca	0.5	0.4	0.5	0.5	0.6
Ti	0.0	0.1	0.0	0.2	0.1
Cr	0.4	0.1	0.1	0.2	0.1
Mn	0.1	0.2	0.1	0.2	0.2
Fe	26.5	23.6	30.3	18.7	17.9
Co	0.4	0.2	0.3	0.0	0.2
Ni	1.7	1.2	1.5	1.6	1.3
Totals	90.8	86.8	88.8	75.7	79.7

Table 3.2.1 – Chemical compositions (element %) determined by the Evo 15L analyses on selected matrix regions in MIL 07687. Areas A1 and A2 are FeO-rich, Area A3 is on the front of alteration (very FeO-rich), Areas A4 and A5 are FeO-poor.

Major elements from the five different matrix regions are shown in Fig. 3.2.7, normalized to CI chondrite values and Si (from Anders & Grevesse, 1989). All the five regions analysed show little variations between them. Each matrix region is fractionated in almost all the major elements (except Fe and Ni) relative to CI abundances. Area 2 exhibits Ti and K enrichment. Areas 3 and 4 show enrichments in Fe and pronounced depletion in Mn.

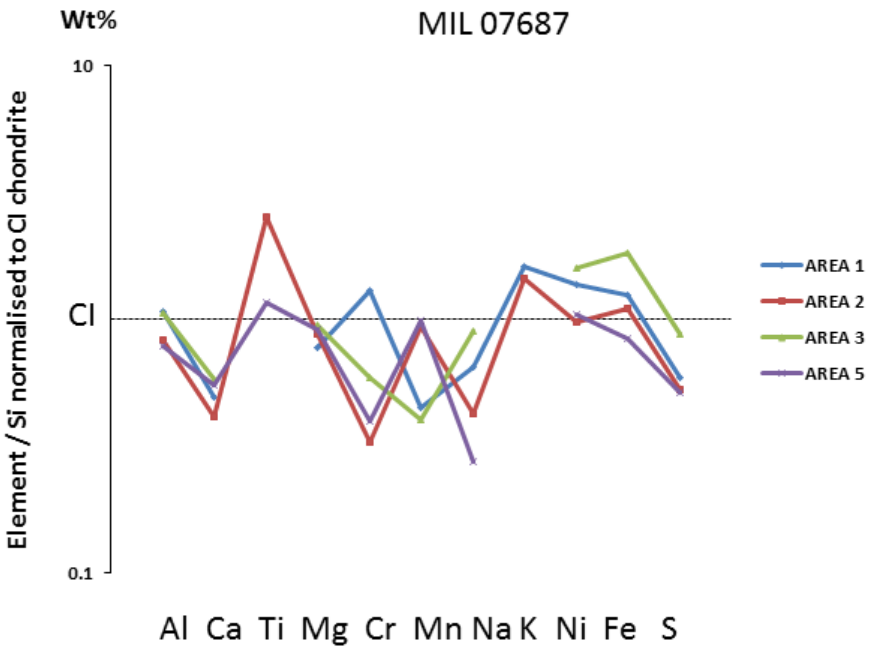

Fig. 3.2.7 - Normalised element ratio diagram showing data of five different matrix regions in MIL 07687. The data are normalised to Si and CI chondrite values from Anders & Grevesse 1989. There are no significant differences in composition between the regions. X-ray detection limit ~ 0.1- 0.3 mass % depending on the element.

These results are compatible with results from sample ALHA77307 which also show a general fractionation of almost all the major elements relative to CI except for Fe which exhibits a slight enrichment. In this case Ca, Cr, and Na show the heaviest depletion. Similar to Brearley (1993) for ALHA77307, these data show Ni enrichment relative to solar values.

3.2.2c – Modal Mineralogy of Matrix

Following the same method as for ALHA77307 and described in Chapter 2, high definition EsB maps acquired using the FEG SEM Ultra Plus, were used to estimate the percentage abundance of the different matrix constituent on the base is of their EsB intensity using Image J®. Abundances are reported in Table 3.2.2 and in Fig. 3.2.8.

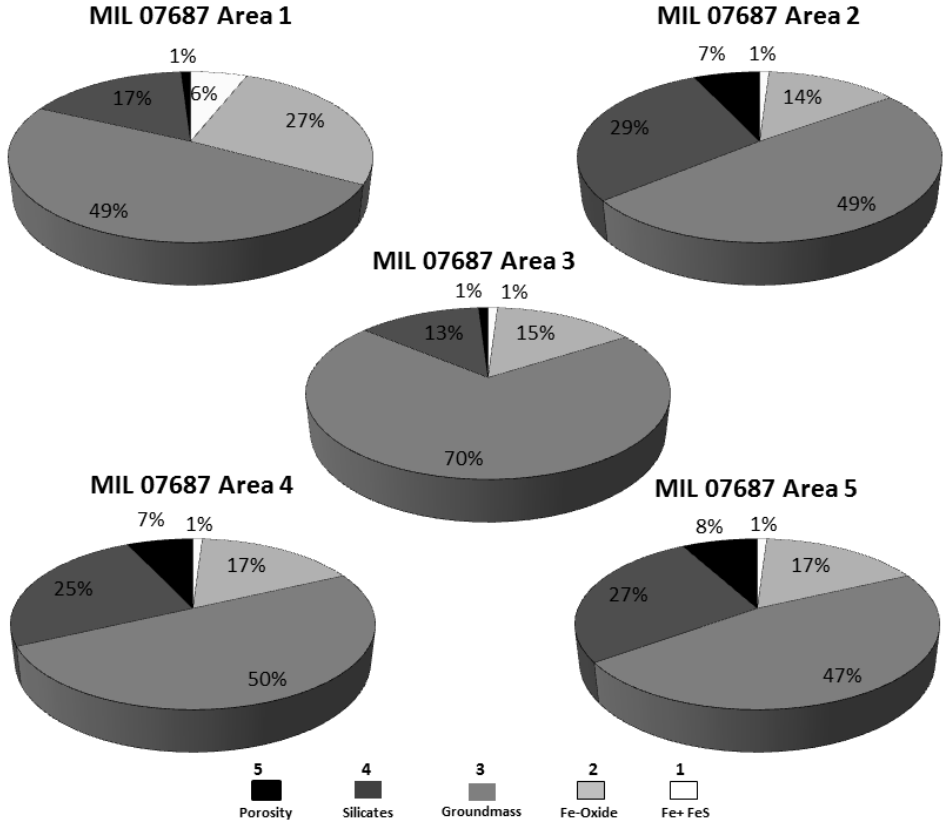

Fig. 3.2.8 - Pie Charts of the different sample areas in MIL 07687 showing abundances of the grayscale unities present in the matrix. Area A3 is on the front of alteration, Areas A4 and A5 are FeO-poor.

The five image maps (each map having an area of ~ 20 × 15 μm) of the matrix regions investigated show an average abundance of metal grains of 2±2% (white in Fig.3.2.8, and similarly for all the different components), the average porosity is 5±4%, and the average abundance of crystalline silicates is 22±7%. The light grey phase assumed Fe-oxides accounts for 18±5% and the groundmass accounts for 53±10%. Thresholding values and average values are reported in Table 3.2.2 & 3.2.3.

MIL 07687		Threshold	%Area
Area 1	Fe+ FeS	255-195	6
Area 1	Fe-Oxide	194-154	27
Area 1	Groundmass	153-89	49
Area 1	Silicates	88-40	17
Area 1	Porosity	39-0	1
			100

MIL 07687		Threshold	%Area
Area 2	Fe+ FeS	255-215	1
Area 2	Fe-Oxide	214-150	14
Area 2	Groundmass	149-90	49
Area 2	Silicates	89-50	29
Area 2	Porosity	49-0	7
			100

MIL 07687		Threshold	%Area
Area 3	Fe+ FeS	255-209	1
Area 3	Fe-Oxide	208-155	15
Area 3	Groundmass	154-75	70
Area 3	Silicates	74-30	13
Area 3	Porosity	29-0	1
			100

MIL 07687		Threshold	%Area
Area 4	Fe+ FeS	255-190	1
Area 4	Fe-Oxide	189-130	17
Area 4	Groundmass	129-70	50
Area 4	Silicates	69-35	25
Area 4	Porosity	34-0	7
			100

MIL 07687		Threshold	%Area
Area 5	Fe+ FeS	255-175	1
Area 5	Fe-Oxide	174-125	17
Area 5	Groundmass	124-76	47
Area 5	Silicates	75-45	27
Area 5	Porosity	44-0	8
			100

Table - 3.2.2 - Table showing thresholding values of the different matrix regions in MIL 07687.

MIL 07687	Porosity	Silicates	Groundmass	Opaques	Fe-Oxides
Area 1	1	17	49	6	27
Area 2	7	29	49	1	14
Area 3	1	13	70	1	15
Area 4	7	25	50	1	17
Area 5	8	27	47	1	17
Average	5	22	53	2	18
STDV (1σ)	3.5	6.9	9.6	2.2	4.6

Table 3.2.3 - Table showing abundances and average values of each individual grey scale unities and in different matrix regions in MIL 07687. Area A3 is on the front of alteration, Areas A4 and A5 are FeO-poor.

3.2.2d- High Resolution Element Maps of Matrix

Element maps acquired at 6kV using a FEI Quanta 650 SEM show that matrix is texturally and mineralogically complex in MIL 07687 and is characterised by regions with highly variable Fe-content (Fig. 3.2.9 & 3.2.10), which is consistent with TEM observations (Brearley, 2013).

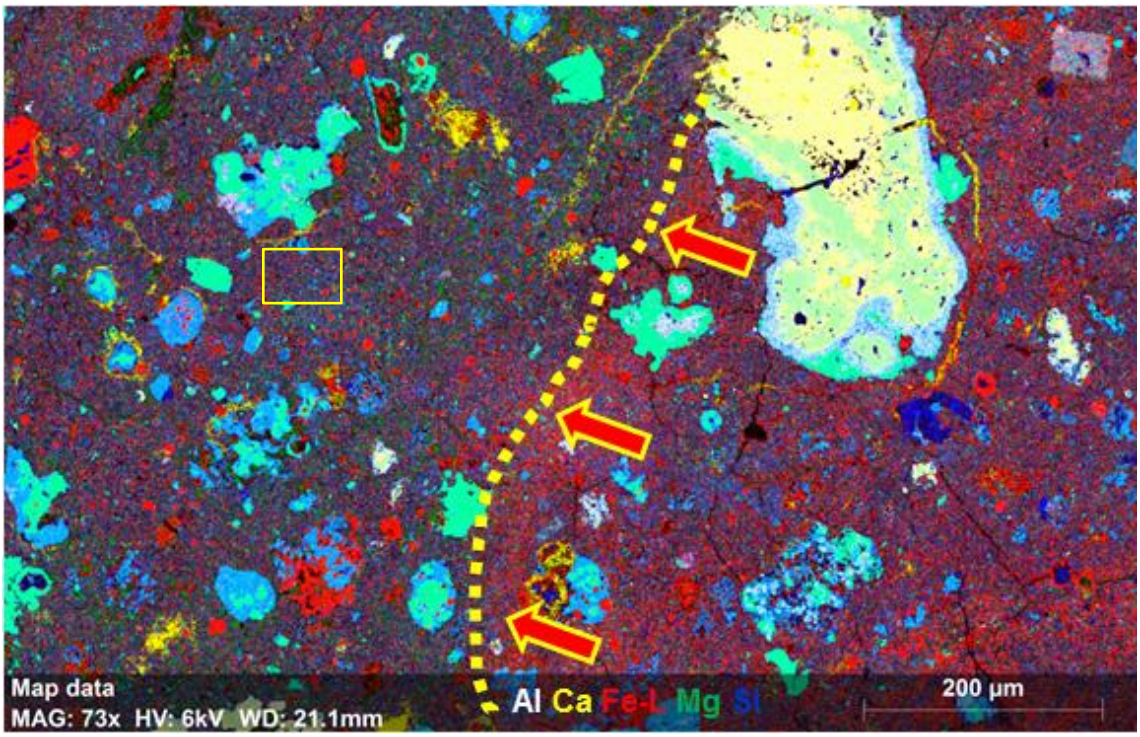

Fig. 3.2.9 - SE- element map of sample MIL 07687 showing a variable Fe concentration in the matrix. The front of alteration is highlighted by the dotted yellow line and red arrows. Yellow box indicated where higher magnification map Fig. 3.2.10 was acquired.

Fig. 3.2.10 - SE-element map of matrix Area 5 which appears to be less rich in Fe compared to other areas within the same sample

Similarly to what is observed in ALHA77307, the silicate crystals present in the matrix of MIL 07687 are anhedral, with the exception of the whiskers, which are euhedral. The presence of anhedral, isolated grains suggests either collisional processing or indicates reaction with gaseous fluids. Anhedral crystals, mainly the Fe-rich phases, present lobate margins. This could indicate deposition of secondary phases by in-situ alteration.

3.2.2e – Enstatite whiskers

Silicate crystals with elongated acicular habitat similar to those seen in the matrix of ALHA77307 have been observed also in the Fe-poor matrix of MIL 07687 (Fig. 3.2.11). So far 4 such crystals have been observed in ALHA77307 and 3 in MIL 07607.

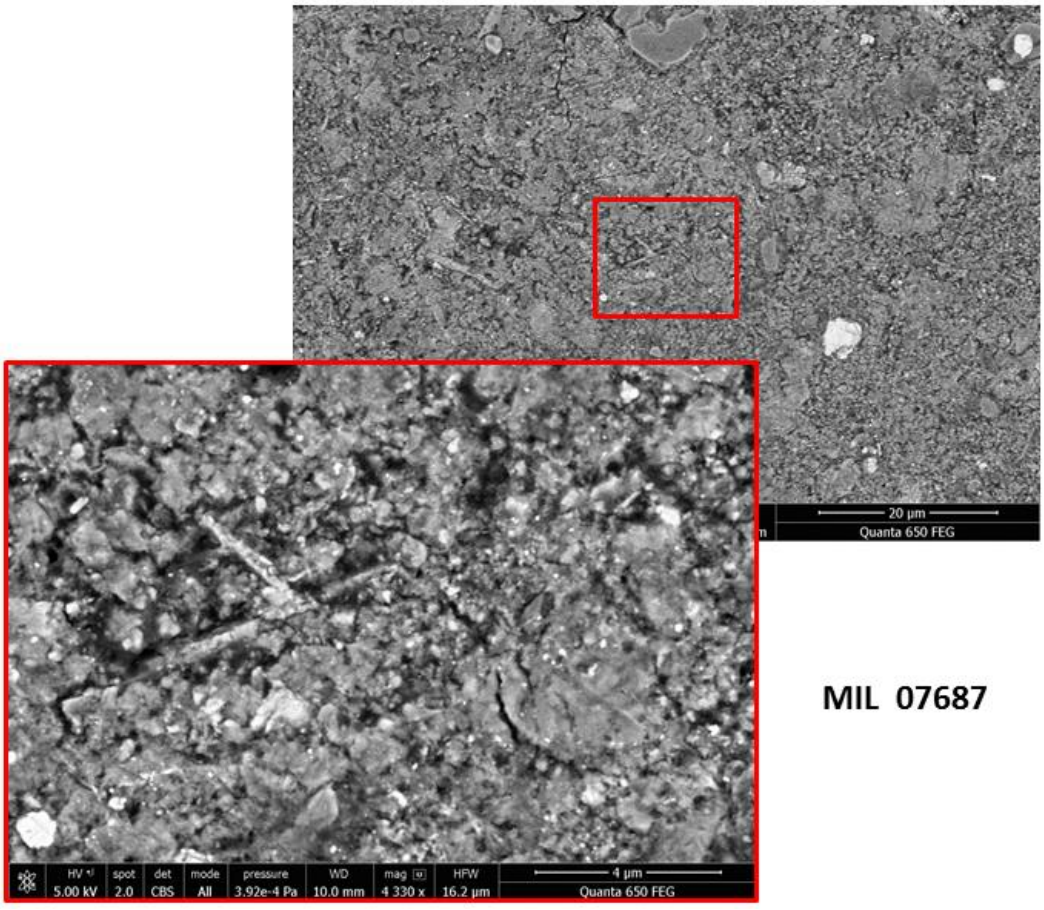

Fig. 3.2.11 - Backscatter Electron images showing a whisker in the Fe-poor matrix of sample MIL 07687

Element maps of these acicular shaped crystals also confirmed that their chemical composition is compatible with enstatite. However TEM investigations are necessary to

establish the orientation of the elongation axis of these phases and the presence of axial screw dislocations to definitely confirm their nature as solid condensates from the solar nebula. The whisker in MIL 07687 in Fig. 3.2.12 and Fig. 3.2.13 shows a peculiar morphology resembling two individual crystals joint together. This is an observation made purely based on the SEM element map investigation and need to be verified by TEM and possibly by CT imaging prior to FIB-ing. If this is confirmed, the crystal morphology gives important indications of the environmental conditions where it formed, suggesting a relatively high density of whiskers in the region of the protoplanetary disk where they condensed.

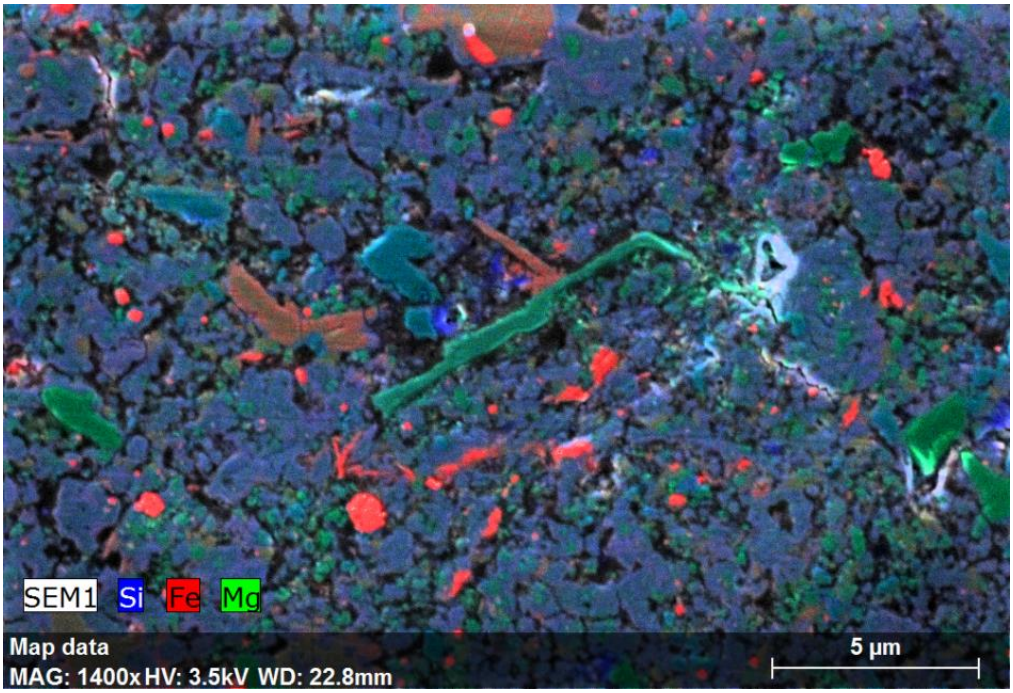

Fig. 3.2.12 - SE Element map of whisker in the Fe-poor matrix of sample MIL 07687.

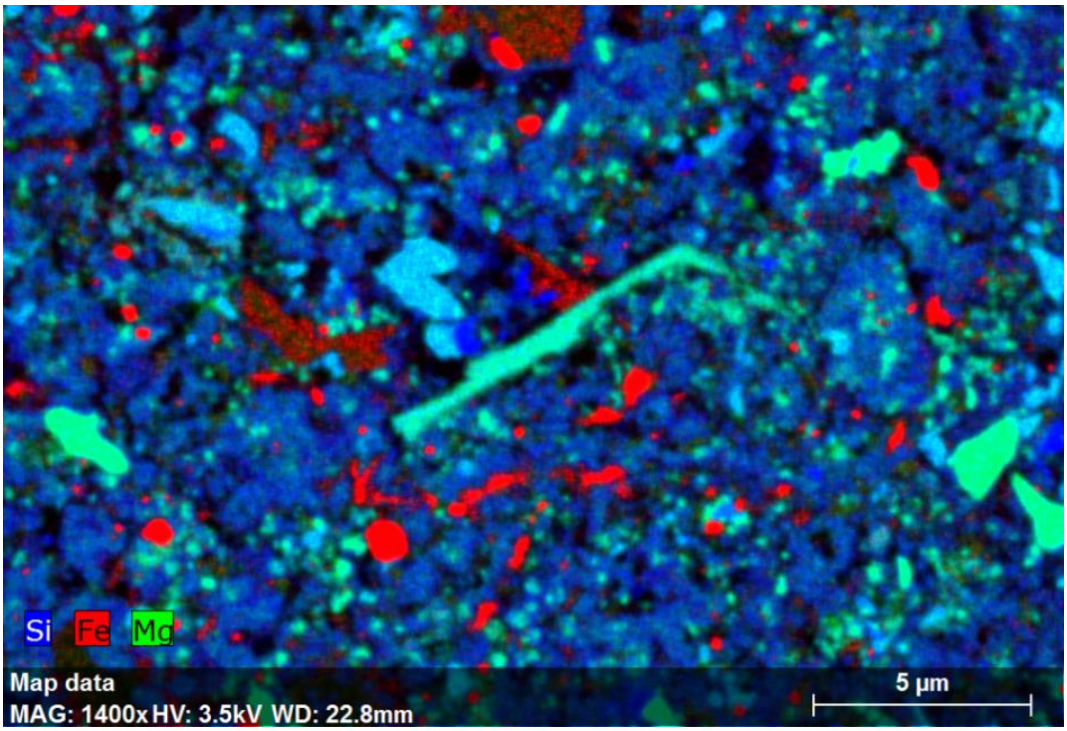

Fig. 3.2.13 - Element map of whisker in the Fe-poor matrix of sample MIL 07687.

3.2.2f – Mineralogy of the Matrix

In the micro-XRD patterns of the matrix of sample MIL 07687 the following crystalline phases have been identified: olivine, enstatite, iron sulfide and metal. Despite being collected on areas with different degrees of alteration all areas are characterised by remarkably similar diffraction patterns showing no significant differences between the areas (Fig. 3.2.14). In particular the XRD pattern for Area 5, which from the SEM observations appears to be the least altered matrix, is surprisingly similar to pattern from the more altered areas. The overall shape of the diffraction patterns obtained from Area 5 was compared to the diffraction pattern of the poorly crystalline ferrihydrite standards and only small variations were observed (Fig. 3.2.15).

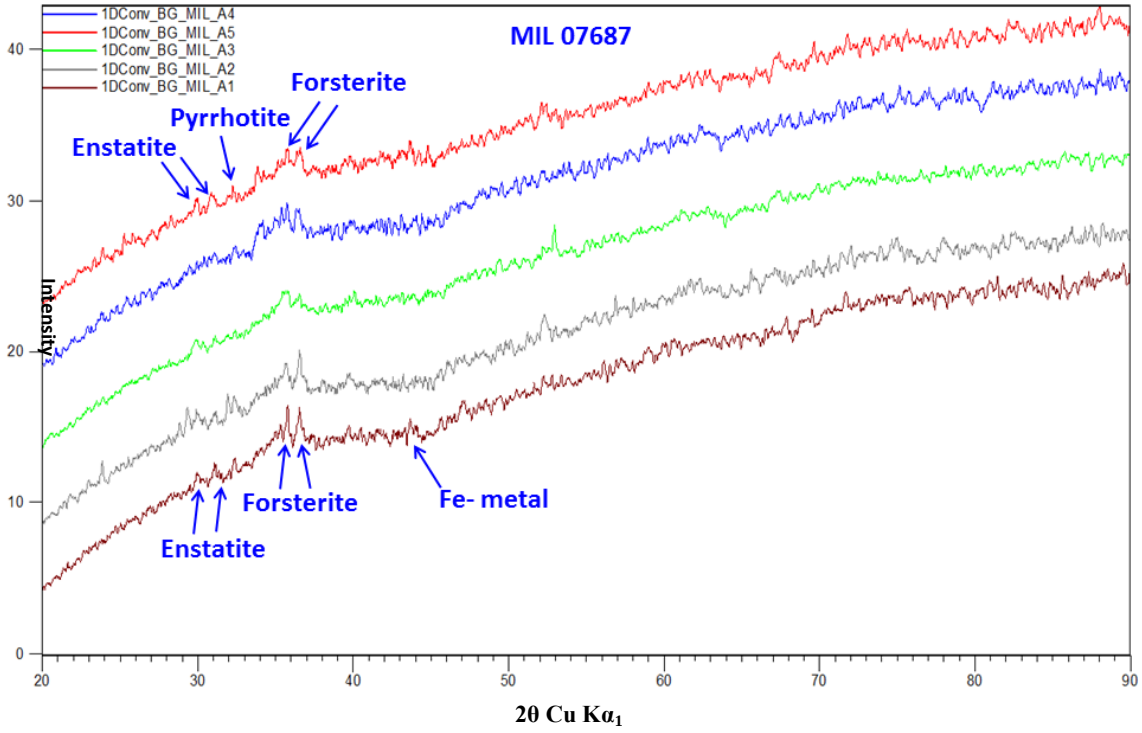

Fig. 3.2.14 - Diffraction pattern of the matrix areas investigated in MIL 07687.

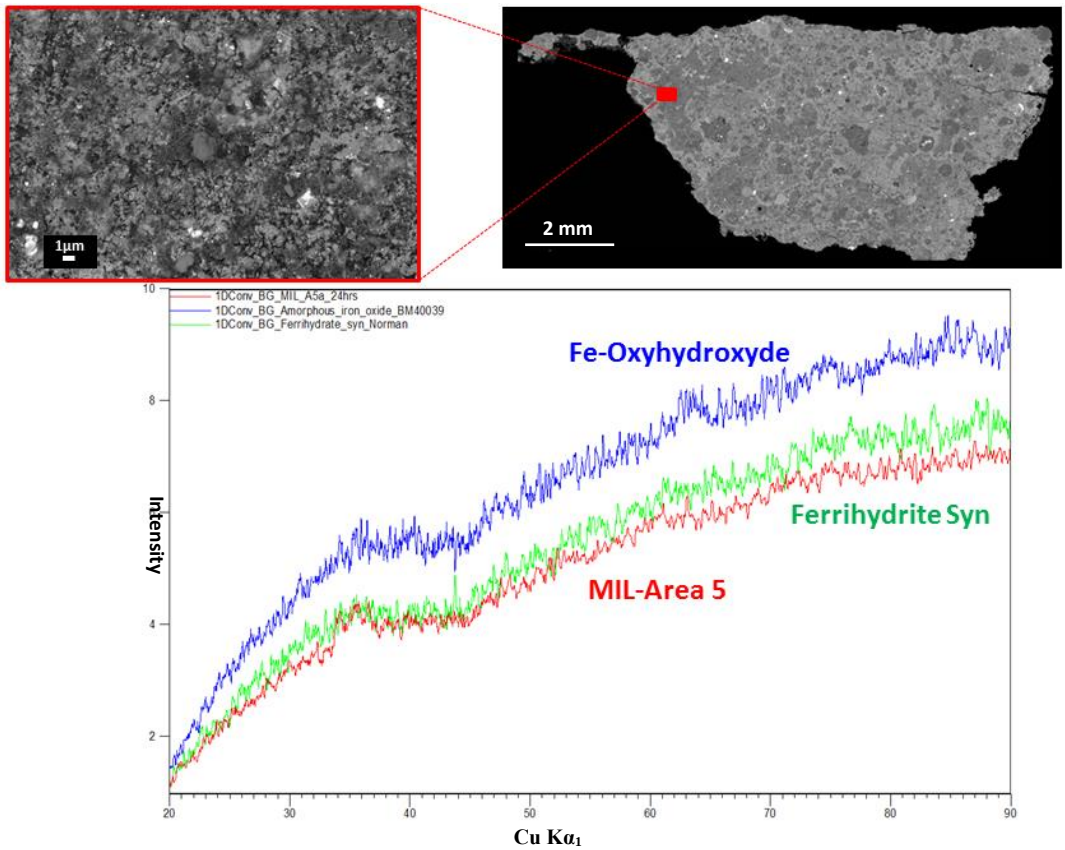

Fig. 3.2.15 – X-ray diffraction pattern of the matrix Area 5 investigated in MIL 07687 compared to X-ray diffraction patterns of the standards Fe-Oxyhydroxyde and synthetic Ferrihydrite.

The average abundance volumes for MIL 07687 obtained using a profile-stripping method are: olivine 18vol%, enstatite 18vol%, 1vol% Fe-sulfide, metal is only present in Area 1. Phase quantification values for each individual area are reported in Table 3.2.4 and (Fig. 3.2.16). The remaining 63% contribution, of which no strong peaks are present is likely to be attributed to the poorly crystalline phases e.g. ferrihydrite and/or amorphous silicates.

MIL 07687	1	2	3	4	5	Average
Olivine	25	25	14	14	14	18
Enstatite	17	17	18	18	18	18
Fe-sulphide	3	0	0	0	0	1
Fe-metal	1	0	0	0	0	0
Amorphous phases	54	58	68	68	68	63

Table 3. 2. 4 - Table showing abundances of the mineral phases calculated in each area and sample average values.

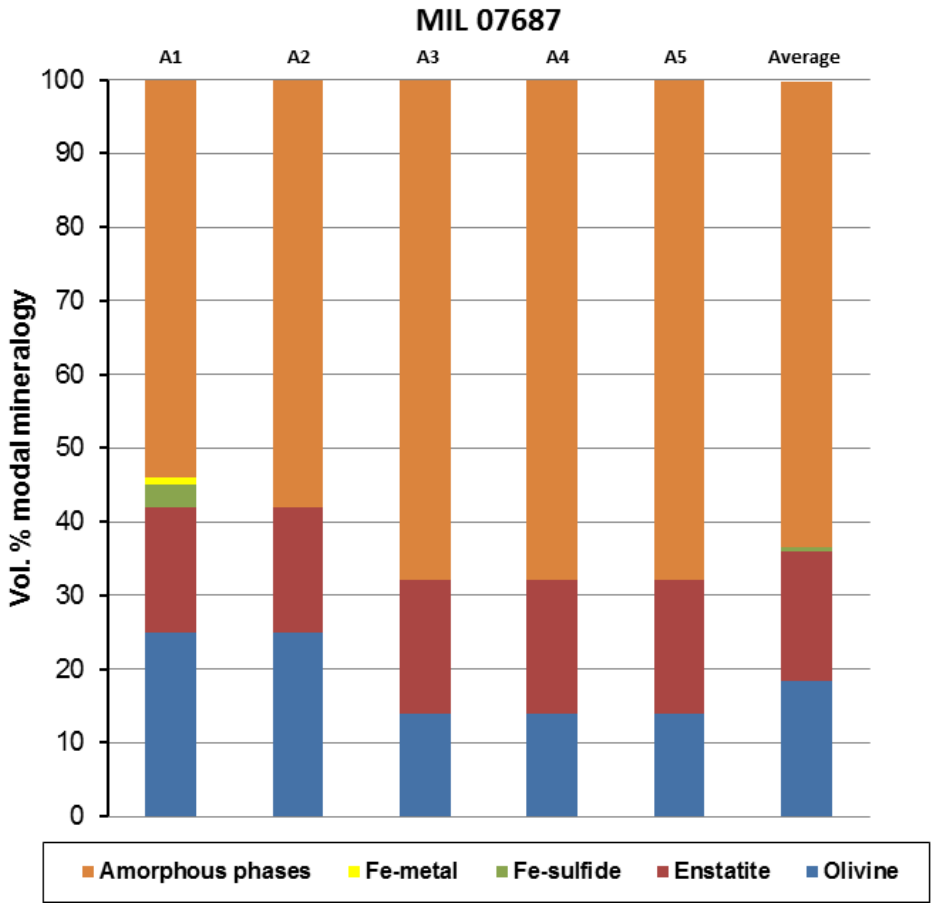

Fig. 3.2.16 – Bar chart reporting abundances of mineral phases present in each individual area and sample average values in MIL 07687. Areas 1 and 2 are Fe-rich, Area A3 is on the front of alteration, Areas A4 and A5 are FeO-poor.

3.2.2g - XANES Results

STXM observations were carried out on MIL 07687 and X-ray fluorescence maps (XRF) were also acquired to highlight the elemental distribution within the areas studied. The element maps acquired on MIL 07687 have revealed that matrix is complex and is characterised by regions with different degree of aqueous alteration resulting in variable in Fe-content. Therefore, three FIB foils were cut in matrix regions characterised by different degrees of aqueous alteration defined by variable Fe-content (Fig. 3.2.16 a & b). However, micro-XRD analyses despite being collected on areas with different degrees of alteration do not show significant variations.

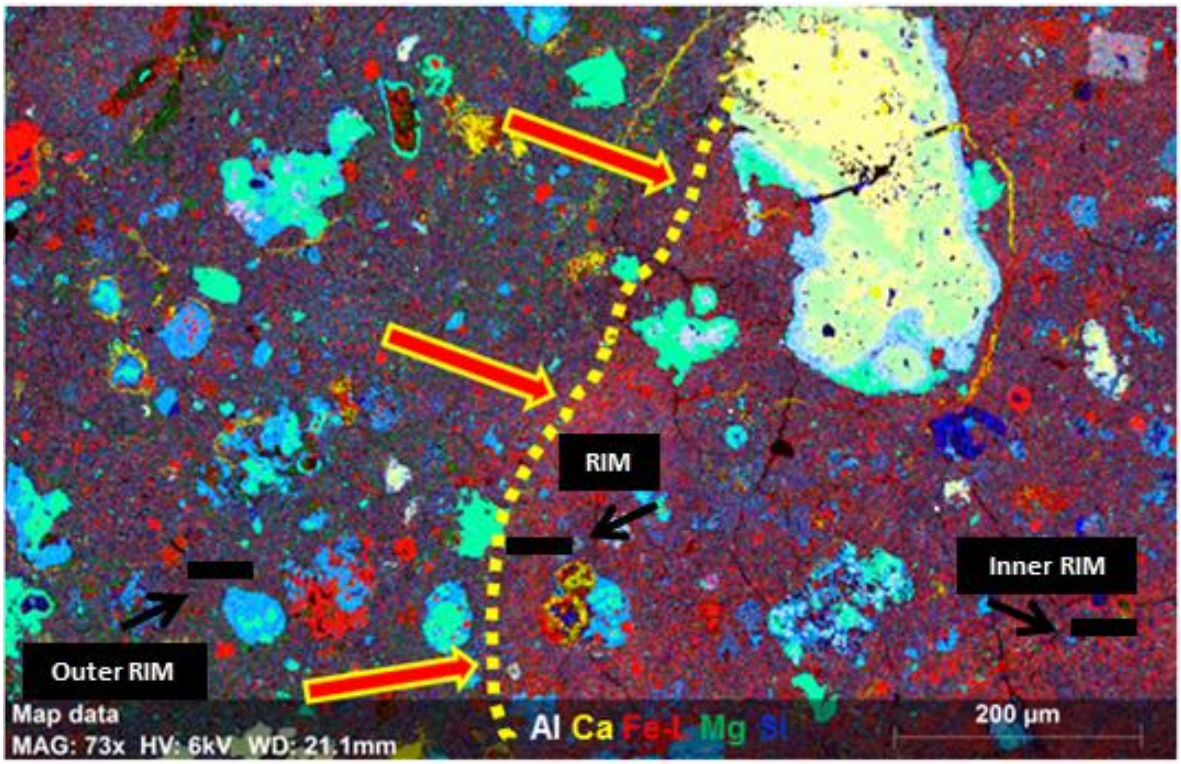

Fig. 3.2.17a - SEM element maps of matrix in sample MIL 07687 showing the different locations where the FIB sections were extracted.

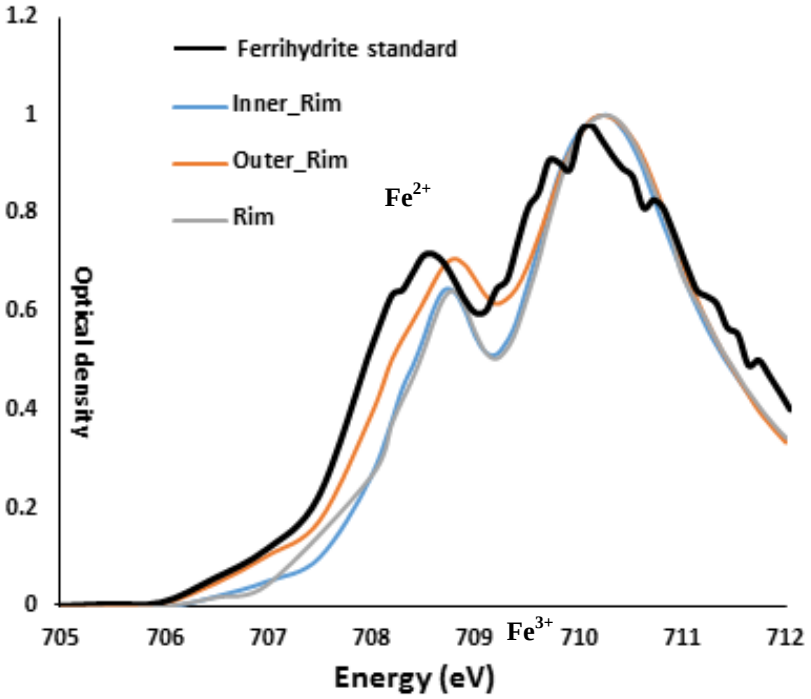

Fig. 3.2.17b – Bulk Spectra of the foils are consistent with Fe^{3+}.

The XANES spectra obtained within the FIB section extracted in the inner rim (Fig. 3.2.18) as well as the spectra obtained from the foil cut on the rim (Fig. 3.2.19) do not exhibit appreciable spatial variations in the Fe^{3+}/Σ Fe ratios. Based on features on the SEM images, contrast variation in the X–ray absorption images, and element distribution, three regions of interest within each foil were selected. All the spectra within these two foils are all consistent with Fe^{3+} as shown by the high intensity peaks relative to the Fe-L_3 absorption edge Fig. 3.2.18 & Fig. 3.2.19.

Contrary to spectra acquired on the inner rim and on the rim, the spectra acquired from the foil cut in the outer rim region where the matrix is characterised by a lower degree of aqueous alteration, and lower Fe-content, shows spatial variations in the Fe^{3+}/Σ Fe ratios. One of the ROIs within the foil is in fact characterised by a spectrum exhibiting a higher intensity for the Fe^{2+} peak Fig. 3.2.20. The XRF map shows this grain is enriched in Fe and O.

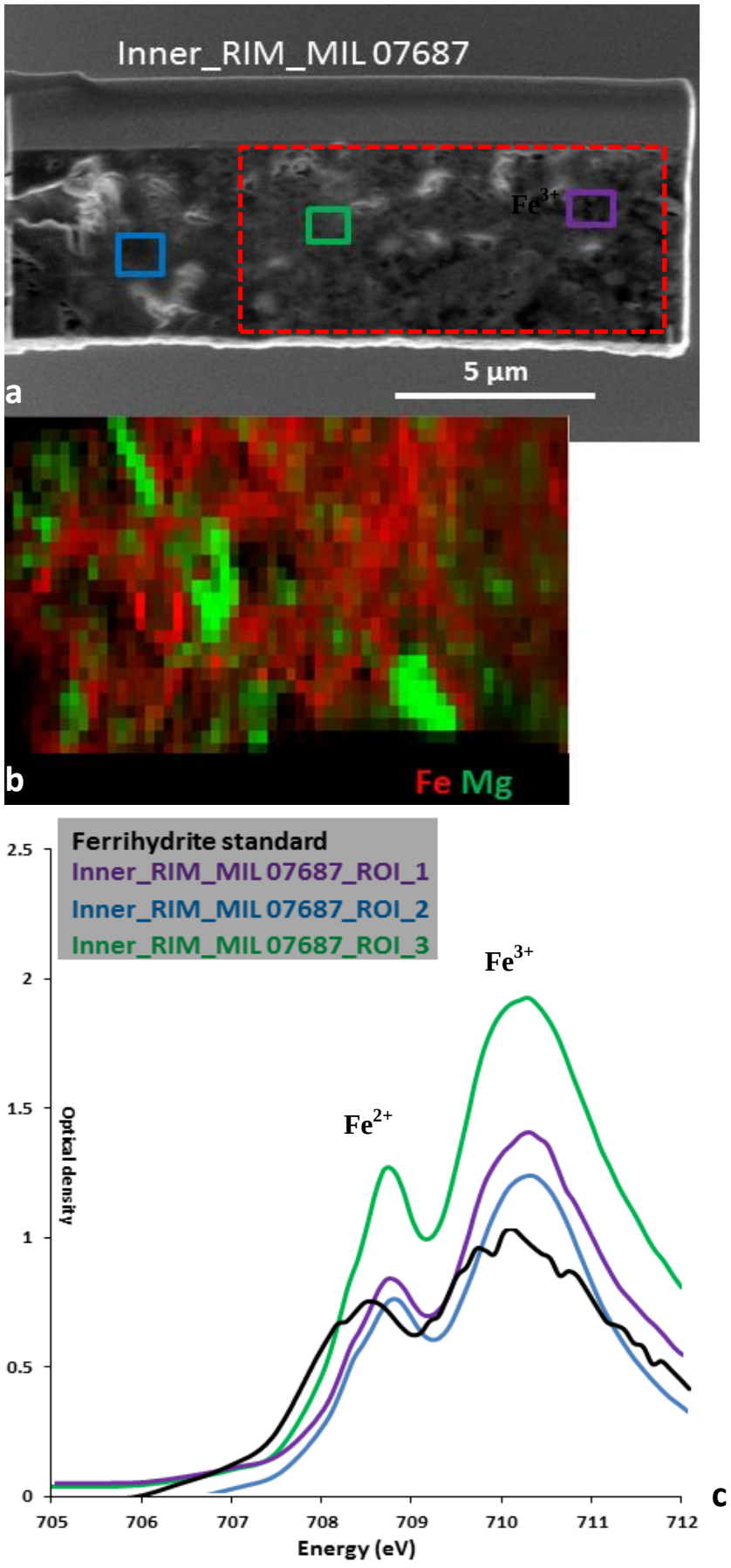

Fig. 3.2.18 – (a) SEM FIB section image of inner rim matrix in MIL 07687, (b) X-ray Fluorescence map of FIB section image (red dashed box in a) of inner rim matrix in MIL 07687, (c) Spectra of different ROIs within the same foil all characterised by Fe $^{3+}$ enrichments.

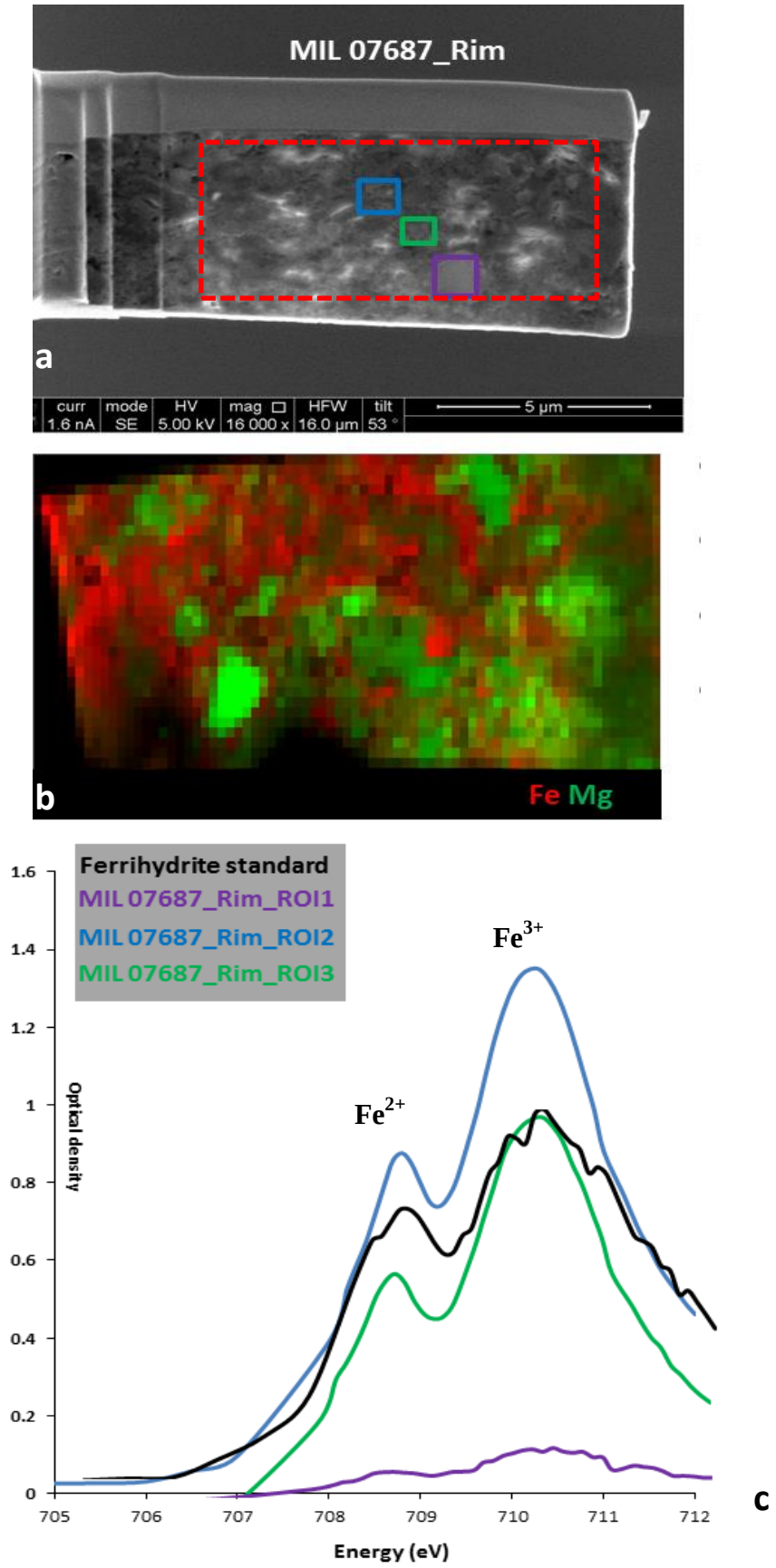

Fig. 3.2.19 – (a) SEM FIB section image of rim matrix in MIL 07687, (b) X-ray Fluorescence map of FIB section image (red dashed box in a) of inner rim matrix in MIL 07687, (c) Spectra of different ROIs within the same foil all characterised by Fe^{3+} enrichments.

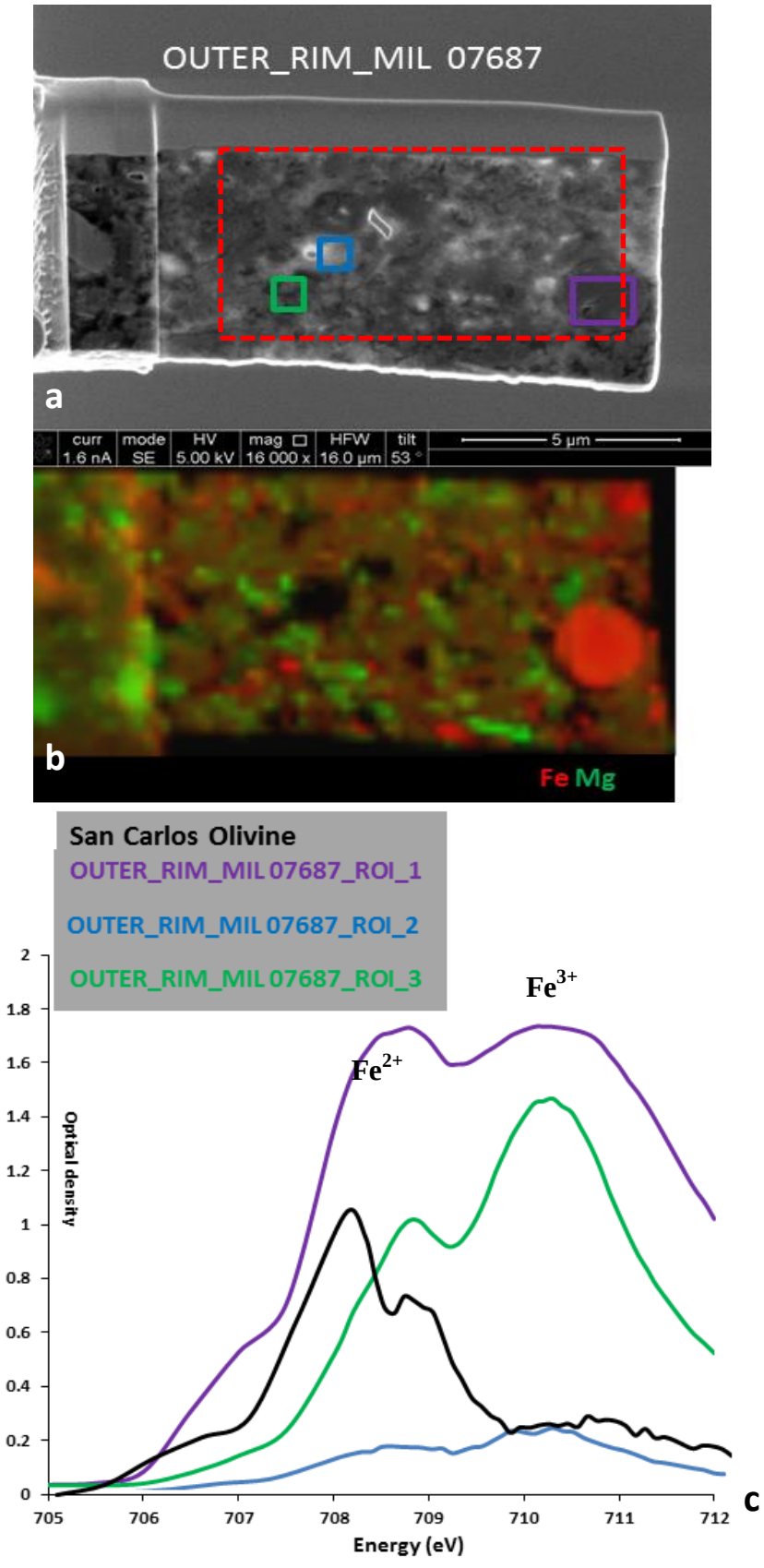

Fig. 3.2.20 – (a) SEM FIB section image of outer rim matrix in MIL 07687, (b) X-ray Fluorescence map of FIB section image (red dashed box in a) of inner rim matrix in MIL 07687, (c) Spectra of different ROIs within the same foil with one spectra from ROI 1 (purple) is characterised by Fe $^{2+}$ enrichments.

3.2.3 - Reactive transport during fluid flow

In the parent body subsurface, fluids play an important role by transporting dissolved minerals and precipitation processes. The chemical reactions taking place as a consequence of fluid percolating through the matrix leads to the distribution, in specific areas within the parent body, of the secondary mineralogical phases. In the case of MIL 07687 this has led to oxidation and deposition of the Fe-rich phases observed. The deposition of the secondary phases and the aqueous alteration is not uniform and rather localised. The complex geometries of pore spaces and fracture networks may make it very difficult to understand the direction of the fluid flow path. However, the distribution of the secondary mineralogical phases deposited can sometimes help to identify the direction of the fluid percolating and the source generating the fluid itself. In the sample MIL 07687 Fig.3.2.3.1 for instance the stalled front of alteration indicates a limited supply of fluid, and as a consequence the matrix outside the front of alteration has experience a less pronounced alteration. This area is therefore characterised by a less pronounced deposition of the secondary Fe-rich phases, and this has been confirmed by the XANES investigation.

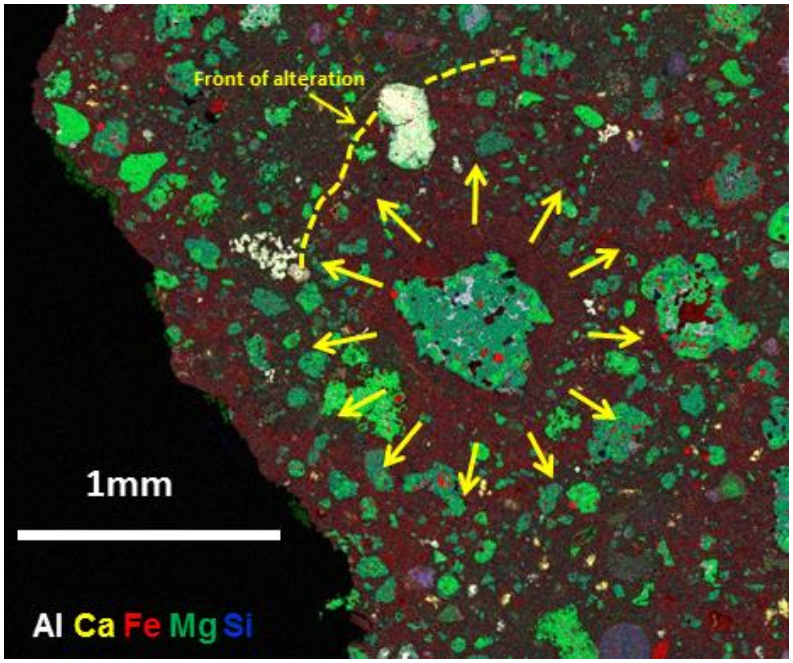

Fig.3.2.3.1 – Silicate grain in MIL 07687 surrounded by Fe-rich matrix suggesting that the source of water may have been the ice coating the grain and distributed outwards through capillary.

Observing closely the distribution of the Fe-rich phase in Fig. 3.2.3.1 it is noticeable that there is an enrichment of Fe (in red) around a large (~0.5 mm in diameter) silicate grain which is probably a chondrule fragment. The Fe-enrichment observed on the SEM Map appears to sharply terminate, producing a stalled front of alteration.

These observations can lead to the speculation that an ice layer coating the silicate grain may have been the source of the fluid percolating through this matrix region, and that the water generated by the ice melting distributed outwards through capillary action. The exhaustion of the water supply resulted in the stalled front of alteration and localised aqueous alteration observed in the matrix.

3.2.4 - Discussion of petrological results for ALHA77307 and MIL 07687

Each of the five matrix regions investigated in ALHA77307, according to the ternary Si-Fe-Mg (element wt %) diagram in Fig. 3.1.6, are characterised by a very narrow range of compositional variation where Mg and Si values are constant across the different areas. Fe exhibits slight variations across the sample which is also reflected in the micro-XRD analysis where crystalline Fe-sulfide phases are only present in Area 2, and in agreement with the high resolution image maps that show variable abundances of Fe-rich phases (white and pale-grey). The similarity in the chemical composition between the different matrix regions observed is consistent with previous work and suggests that different matrix regions within the same sample share a common origin (Brearley, 1993).

From Fig. 3.1.7 it appears evident that most major elements are fractionated relative to the solar values and in particular Ca and Al are fractionated relative to one another with a Ca/Al ratio that varies from 0.12 to 0.30, with an average of 0.23. These values are comparable to Brearley (1993) whose Ca/Al ratios varied from 0.067 to 0.41. Both sets of data are also consistent with McSween and Richardson (1977) who reported Ca/Al ratios of 0.159 to 0.259 in CO3.0 falls. Ca/Al increases as a result of aqueous alteration (Brearley, 1993) and in CI is 1.067 (Lodders, 2003). Ca depletion in ALHA77307, considering the lack of pervasive aqueous alteration experienced by the sample, is thought to have been inherited from the solar nebular and not due to aqueous alteration (Brearley, 1993).

The high resolution image maps reveal that the grain porosity in ALHA77307 matrix (4±1.9%) is generally lower than the bulk porosity values (up to 30% Corrigan et al., 1997). The porosity measured in matrix is interstitial porosity and the low values suggest that chondrite porosity may occur mainly in fractures.

The abundance of metal and sulfides is low, and Fe-oxides which appear to be the product of alteration, are relatively abundant. The element map observations have revealed the enrichment of the groundmass in the cations Al, Si and Fe, which is consistent with

astronomical observations where Fe-bearing amorphous silicates are seen in the protoplanetary disks around young stars. The Fe distribution in the element maps is also consistent with Ultra Plus observations. From the micro-XRD a maximum value of ~50vol % abundance of amorphous silicate is identified alongside the presence of olivine and enstatite grains. The presence of this material is consistent with astronomical observations in protoplanetary disks around young stars (e.g. Natta & Testi, 2006), where they make up the disk's solid component. When amorphous silicates are present in the matrix this suggests that the meteorites hosting these remnants of the protoplanetary disk are very pristine. While olivine and enstatite grains observed in the matrix could be chondrule fragments, they could also be dust grains which are part of the solid component of the protoplanetary disk. The phyllosilicates in the matrix seen in TEM observations and the ubiquitous presence of magnetite seen in the micro-XRD data is indicative of a minor degree of aqueous alteration (e.g. Tomeoka et al., 1988). The low abundance of Fe-sulfide and Fe-metal along with the presence of an amorphous Fe-oxide phase is, however, an indication of a certain degree of aqueous alteration or/and terrestrial weathering.

MIL 07687 analyses reported in the ternary Si-Fe-Mg (element wt %) diagram in Fig. 3.2.6 shows how all the matrix regions investigated are characterised by a narrow range of compositions with constant Mg and Si values whereas the Fe exhibits a more variable distribution in agreement with SEM observations. Major elements in MIL 07687 exhibit general fractionation relative to CI Fig. 3.2.7, Fe in particular exhibits a slight enrichment especially Areas 3 and 4, and Ca, Cr, and Na show the heaviest depletion. Similar to ALHA77307, each area of MIL 07687 exhibits a comparable major elements distribution. This similarity in the chemical composition between the different matrix regions as observed in ALHA77307, suggests that different matrix regions within the same sample have common origin (Brearley, 1993). Calcium and Al are fractionated relative to one another with a Ca/Al ratio that varies from 0.49 to 0.92, and an average of 0.66. These

values are slightly higher compared to the Ca/Al ratios reported here for ALHA77307 which probably reflects the higher degree of aqueous alteration experienced by MIL 07687. However, there is no clear correlation in Ca/Al ratio between altered matrix regions and less altered areas. Brearley (2012) reported Ca-sulphate grains that have partially replaced Ca-carbonate grains to different degrees. Ca-sulphate reportedly also occurs as very thin veins (<3 μm in width) at the interface between some chondrules and the surrounding matrix and may be due to terrestrial weathering (Brearley, 2012). However, similar to ALHA77307 Ca/Al ratios are still in line with the McSween and Richardson (1977) data, and are lower than measured for the CIs (1.067, Lodders, 2003). It seems reasonable, therefore, to assume that Ca depletion in MIL 07687, despite the effects of possible terrestrial weathering, might have been inherited from the solar nebular and is not due to aqueous alteration.

The origin of the volatile depletion in CC relative to solar composition (Palme et al., 2014) is as yet unresolved (e.g. Pringle et al., 2017). Hypotheses for the volatile element depletion in bulk chondrites include incomplete condensation from the solar nebula (Wasson and Chou, 1974), volatile loss by evaporation during accretion (Ringwood, 1966), or mixing of distinct primordial reservoirs consisting of a volatile-rich CI-like component and a volatile-poor refractory component (Larimer and Anders, 1967; Clayton and Mayeda, 1999; Luck et al., 2003).

Element maps reveal the Fe variability of the different matrix regions which is consistent with Ultra Plus observations. The matrix of MIL 07687 in the areas characterised by lower abundance of Fe has a fine-grained, heterogeneous texture, that closely resembles matrix in unaltered pristine chondrites such as ALHA77307 (Brearley 1993, 2012), and the presence of amorphous silicate also indicates that despite the evident alteration experienced by MIL 0767, it is a pristine chondrite that preserves remnants of the protoplanetary disk in the matrix. Porosity measured on high resolution image maps is interstitial and appears to be

low also in MIL 07687 (5%). As observed for ALHA77307, the abundance of Fe + FeS is low, and secondary Fe-oxides are relatively abundant (18%). Micro-XRD observations have surprisingly shown that even matrix regions characterised by lower Fe content have the same diffraction pattern as Fe-rich matrix regions. This might be due to the fact that even the least altered regions also experienced some aqueous alteration. MIL 07687 exhibits an evident localised aqueous alteration with an uneven Fe distribution in the matrix of the sample, which could explain the low abundance of Fe-sulfide and Fe-metal.

The XANES observations gathered on MIL 07687 suggest a slightly more complex scenario where the effects of parent body processing prevail, but the original reducing conditions of the environment where some grains constituting the matrix formed still remains. The foils cut in the inner rim and on the rim matrix regions do not show differences in the Fe^{3+}/Σ Fe ratios, which is consistent with the micro-XRD and SEM observation which reveal a considerable degree of aqueous alteration experienced by the sample. These results show a high abundance of Fe and, according to the XANES measurements, appear to be enriched in Fe^{3+}. These enrichments in the most oxidised state of the Fe observed appear to be associated to high oxygen fugacity fO_2 produced by parent body processes in the presence of water where Fe-O bearing minerals become stable.

Although the micro-XRD analyses acquired on the matrix regions have not highlighted significant differences the XANES investigation has revealed some subtle differences not appreciable with other techniques. From the observation of the three bulk spectra acquired it was noticed that the bulk spectra of the outer rim region in MIL 07687 shows a slightly higher intensity for the Fe^{2+} peak compared to the Fe^{3+} indicating that there are some differences with the inner rim and the outer rim regions. These differences suggest that the outer rim matrix region is characterised by less oxidizing conditions, which is consistent with SEM observations revealing a lower abundance of Fe in this matrix region indicating a lower degree of aqueous alteration. Even though the matrix in the outer part of the rim

appears less altered the micro-XRD data revealed that to some degree parent body processes have also affected this matrix region. The XANES study of the area has also revealed an almost totally pervasive effect of aqueous alteration resulting in a very fine scale Fe^{3+} enrichment, but one region of interest within the foils shows clear enrichments in Fe^{2+}. Therefore, reducing conditions were likely in place during the formation of this Fe^{2+} grain and that parent body processes have to be considered responsible for the oxidising conditions widely displayed by the rest of the matrix constituents.

Observations of the crystal shapes using the SEM element maps, in both ALHA77307 and MIL07687, have given indications about the environmental conditions prevailing during accretion. Collisional processes were likely operating, producing anhedral silicate crystals. However, reaction with gaseous fluids could have been also in place, causing partial removal of crystalline material producing poorly developed external crystal faces.

3.2.5 - Enstatite whisker in ALHA77307 and MIL07687

Enstatite whiskers occur in chondritic-porous interplanetary dust particles (CP IDPs) (Bradley et al., 1983), Antarctic micrometeorites (Noguchi et al., 2008) and in comet 81P/Wild-2 samples (Ishii et al., 2008). Their size is typically <10 μm in length and <0.2 μm in width (Bradley et al., 1983). Whiskers observed in this work in the matrix of ALHA77307 are ~2.5μm in length and ~0.2 μm in width, whilst in the matrix of MIL 07687 are ~3.5μm in length and ~0.3 μm in width, and therefore comparable in size to those reported in literature. Their abundance, in both ALHA77307 and MIL07687, accounts for <1% out of the total area observed.

Bradley et al., (1983) described the whiskers as, typically elongated along the [100] axis and contain axial screw dislocations, while non-whisker enstatite crystals in terrestrial rocks are elongated along [001]. The unique crystal morphologies and microstructures are consistent with the enstatite whiskers condensing above ~1300 K in a low-pressure nebular

or circumstellar gas (Bradley et al., 1983). Nakamura-Messenger et al., (2009) in order to constrain the site of enstatite whisker formation, have carried out coordinated mineralogical, chemical and oxygen isotope measurements on enstatite whiskers in a CP IDP, reporting the oxygen isotopic composition of the whisker falls within the range of Solar System materials. However, the whiskers display a ^{16}O-enrichment (δ^{18}O -117±37‰) suggesting that like refractory inclusions in meteorites and comet Wild-2 samples (McKeegan et al., 2006), may have also formed in the inner Solar System. Nakamura-Messenger et al., (2009) explained their absence in meteorites likely due to destruction during parent body thermal/ aqueous alteration.

Both, crystal morphologies and oxygen isotopic compositions are consistent with the enstatite whiskers forming in the inner Solar System (e.g. Bradley et al., 1983, Messenger et al., 2009). Since they are present in CP IDPs and Stardust material, both from the outer Solar System, this requires radial transport from the hot part of the disk to the cold comet forming region. Based on the morphology of these crystals (very small width compared to the length) they appear to be very fragile, therefore to survive the journey to the outmost part of the Solar System it is likely that they were protected by dust accreted during the transport to the comets forming regions.

3.3 - CR3.0 carbonaceous chondrite QUE 99177

3.3.1 - Previous studies

Sample QUE 99177 is a very low petrologic type 3 CR chondrite that has escaped the effects of aqueous alteration. The petrologic properties of QUE 99177 show that it is one of the most primitive members of the CR chondrite group. Its matrix is characterised by amorphous silicate material formed in the solar nebula by rapid condensation of material following high-temperature events (Abreu and Brearley, 2010). Such amorphous material is absent or significantly diminished in abundance in petrologic types higher than 3.1 chondrites. This observation has led to the hypothesis that even mild thermal metamorphism drives recrystallization of amorphous silicates to produce the FeO-rich olivine (Brearley, 1993, 2003b; Scott and Krot, 2005; Nuth et al., 2005). The degree of graphitization of carbonaceous material in the matrix correlates with thermal metamorphism (e.g., Brearley, 1999; Kitajima et al., 2002; Quirico et al., 2006; Bonal et al., 2006). Carbon in the QUE 99177 meteorite is either amorphous or poorly graphitised suggesting that QUE 99177 has experienced essentially no thermal metamorphism (Abreu and Brearley, 2010). The high abundances (220 ppm) of O-anomalous presolar grains present in QUE 99177 further emphasises the extremely pristine nature of this meteorite (Floss and Stadermann 2008 a, b).

3.3.1.1 – Anhydrous Crystalline Phases in the Matrix

Matrix in QUE 99177 is characterised by significant FeO-enrichments with respect to other CR chondrite matrices. The mineralogy is dominated by amorphous silicate material acting as groundmass within which occur Fe,Ni sulfides such as: troilite, pyrrhotite, and pentlandite. Those sulfides appear to be coated with a thin layer of carbonaceous material, often as either amorphous C or very poorly graphitized C (PGC) (Abreu & Brearley, 2010). Fine-grained, crystalline silicate phases such as olivine and pyroxene appear to be

extremely rare. Secondary alteration minerals that are characteristic of other CR chondrites (e.g., Renazzo and Al Rais), such as phyllosilicates, magnetite, and calcite are also rare. The texture and mineralogy of QUE 99177 appear to be similar to matrices in the primitive carbonaceous chondrites ALH A77307 (CO3.0) and Acfer 094 (unique).

3.3.1.2 - Amorphous Phases in Matrix

Amorphous silicates are also present in the matrix of QUE99177, and have compositions that are consistently Fe-rich, and generally host iron sulfides, which are found dispersed throughout. Phyllosilicates are also intimately associated with the amorphous silicates. (Abreu and Brearley, 2010).

3.3.1.3 - Phyllosilicates in the Matrix

Rare phyllosilicates occur as nanocrystals within the amorphous silicates. These phyllosilicates are disordered intergrowths of serpentine and smectite as identified from their characteristic lattice spaces (0.7 nm for serpentine and 1.1 nm for smectite) (Abreu and Brearley, 2010). The close relationship between the amorphous material and the phyllosilicates suggests a replacement relationship between the two. (Abreu and Brearley, 2010). Crystalline anhydrous silicates are essentially completely absent in QUE99177 (Abreu and Brearley, 2010).

3.3.2- Study carried out in this project

3.3.2a - Matrix abundance

Using the same approach as described for the other samples, the matrix abundance in QUE 99177 was estimated using Image J® which accounted for 23 vol%. This value of matrix abundance is comparable with the value obtained by Abreu & Brearley 2010 (20-30 vol%) and is the lowest matrix abundance value seen among the four meteorites studied in this project. In Fig. 3.3.1 & 3.3.2 is shown the element map of the sample which was then binarised to calculate the sample area total.

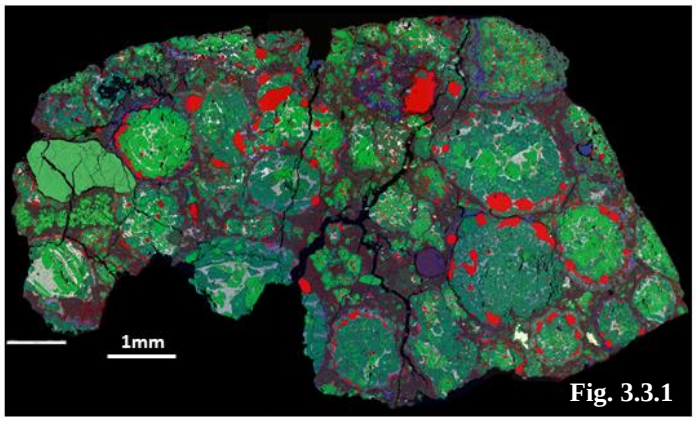

Fig. 3.3.1

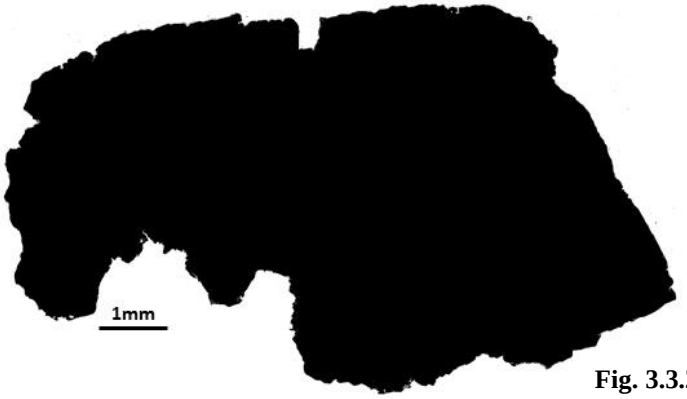

Fig. 3.3.2

Fig. 3.3.1 - Element map of sample QUE 99177
Fig. 3.3.2 - Binarised image of sample QUE 99177 element map

The surface area occupied by the micro fractures (Fig. 3.3.3) was calculated, and accounts for < 4 % vol., while chondrules and CAIs accounts for 73% vol. (Fig. 3.3.4).

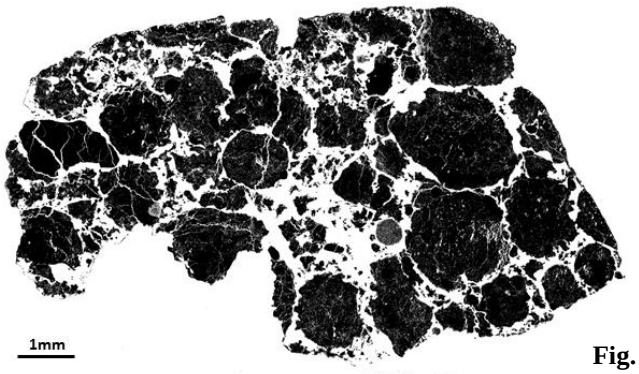

Fig. 3.3.3

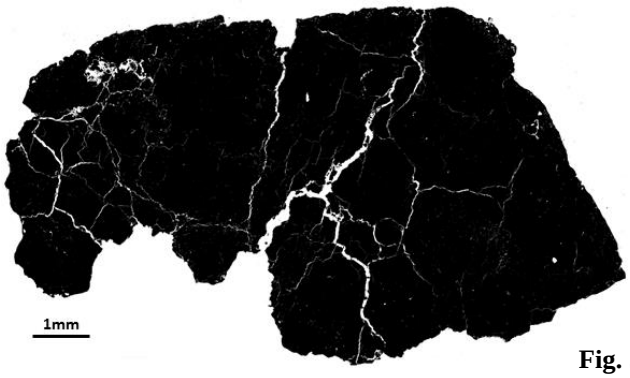

Fig. 3.3.4

Fig. 3.3.3- Binarised image of QUE 99177 element map showing micro fractures.
Fig. 3.3.4 - Binarised image of QUE 99177 element map showing chondrules and CAIs.

3.3.2b – Bulk Chemical Composition of the Matrix

Spectra extracted from the sample QUE 99177 montage map acquired using the EVO 15L SEM are reported in Table 3.3.1. Five different matrix regions across the sample (Fig. 3.3.5) of approximately 100 μm^2 each, were used to extract data, and results are plotted on a ternary Si-Fe-Mg (element wt %) diagram in Fig. 3.3.5. Compared to the other samples, QUE 99177 matrix exhibits the widest range of Fe abundance, and Areas 4 and 5, despite being next to each other, represent the extreme ends of the data set. However, Fe maintains the negative trend with Si and Mg observed in all other samples which would intercept the Si-Mg axis at approximately Mg/(Si + Mg) = 40.

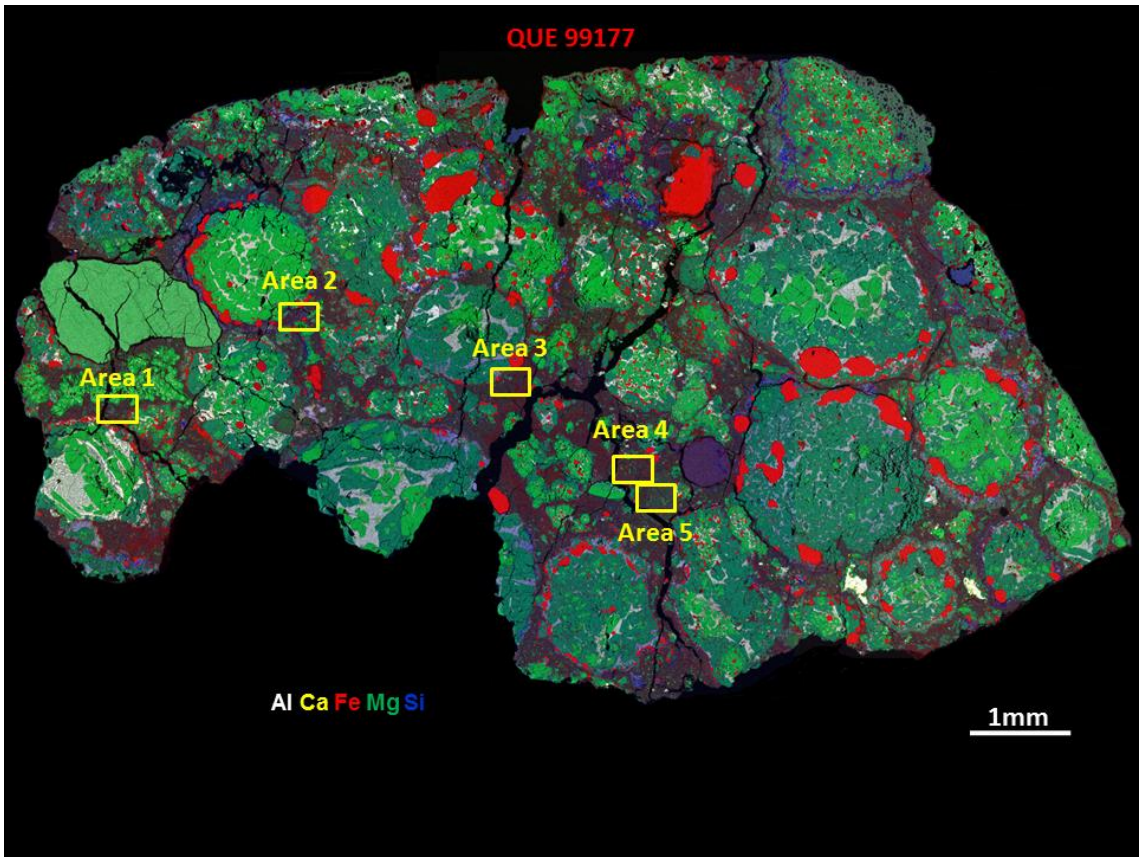

Fig. 3.3.5 – QUE 99177 Element map showing the 5 matrix Areas investigated.

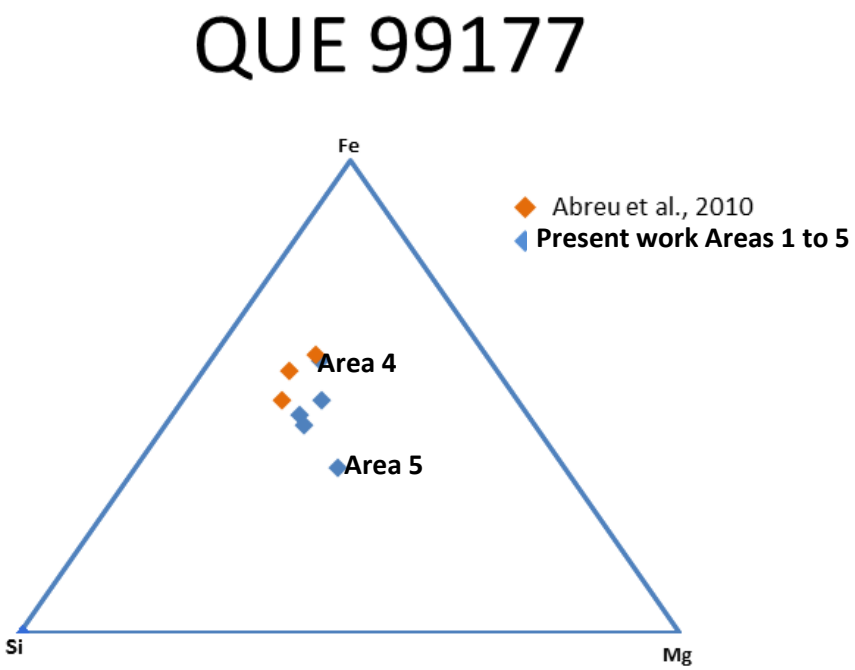

Fig. 3.3.6 – Plot showing the Fe:Mg:Si ratio of matrix regions in QUE 99177 plotted in a ternary (element wt %) diagram. Although there is a narrow range of compositions a trend of changing Fe content at constant Si; Mg ratio is apparent. Data are consistent with Abreu and Brearley, 2010. Area 5 shows a slightly different composition compared to the other areas

QUE99177 (wt%)	AREA 1	AREA 2	AREA 3	AREA 4	AREA 5
O	41.7	41.6	35.7	39.1	42.4
Na	0.5	0.4	0.2	0.2	0.0
Mg	8.4	9.2	9.3	7.6	13.8
Al	0.7	1.1	0.7	0.9	0.8
Si	14.8	15.1	12.8	11.5	15.3
S	1.6	2.4	3.8	3.4	1.2
K	0.0	0.1	0.1	0.1	0.0
Ca	0.9	1.1	0.4	0.5	1.1
Ti	0.1	0.1	0.0	0.1	0.1
Cr	0.4	0.4	0.2	0.2	0.4
Mn	0.5	0.1	0.2	0.2	0.1
Fe	19.8	19.0	21.2	25.9	15.5
Co	0.0	0.0	0.2	0.2	0.3
Ni	2.1	1.3	1.7	1.3	1.1
Total	91.4	92.0	86.4	91.2	91.8

Table 3.3.1 – Chemical compositions (element %) determined by the Evo 15L on selected matrix regions in QUE 99177

Major elements from the five different matrix regions are shown in Fig. 3.3.7, normalized to CI chondrite values and Si (from Anders & Grevesse, 1989). Similar to the observations related to other samples discussed earlier in this work (ALHA77307, MIL 07687), the matrix regions appear to be significantly fractionated in almost all the major elements relative to CI abundances.

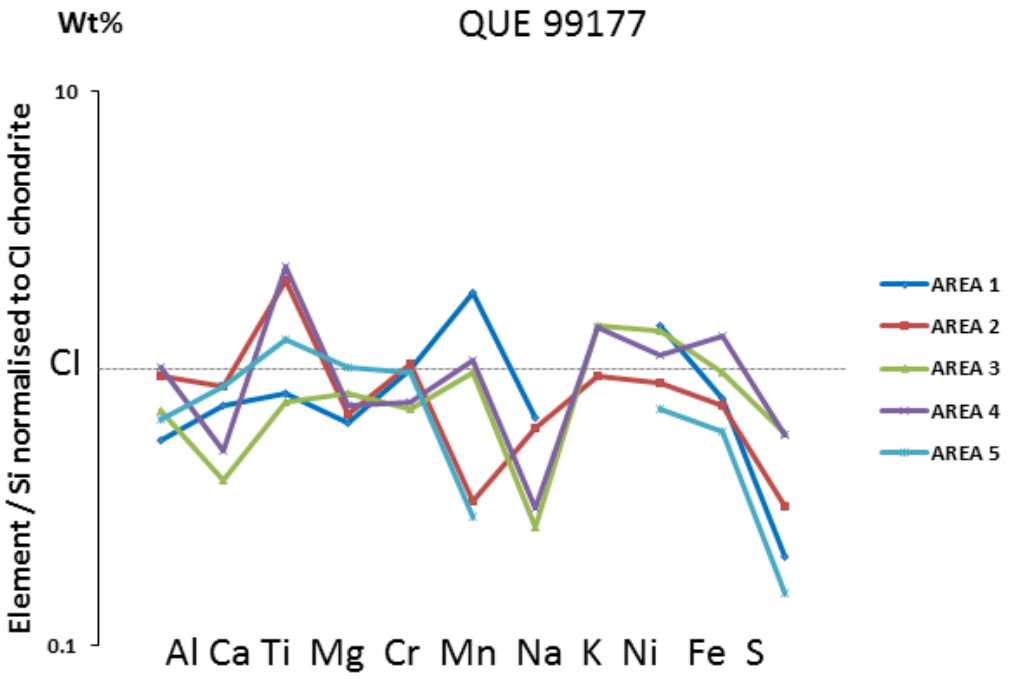

Fig. 3.3.7 - Normalised element ratio diagram showing data of five different matrix regions in QUE 99177. The data are normalised to Si and CI chondrite values from (Anders & Grevesse, 1989). All the different regions do not show differences in composition. X-ray detection limit ~ 0.1- 0.3 wt % depending on the element

However, contrary to the observations related to the samples ALHA77307 (see Section 3.1.2b), MIL 07687 (see Section 3.2.2b) and Acfer 094 (see Section 3.4.2b) the matrix areas in QUE 99177 seems to show some differences. In particular Area 5 shows the heaviest depletion in Mn compared to all the other areas which also exhibit depletion (except Area 2) and also displays chondritic abundance for Mg. Concentrations of K and Ca in Area 5 are found to be below the detection limit.

3.3.2c – Modal Mineralogy of the Matrix

Using the high definition EsB Images maps acquired using the FEG SEM Ultra Plus, and acquired on the same matrix regions of sample QUE99177 previously investigated the percentage abundance of the different matrix constituent was estimated on the basis of their different grey scale value using Image J® and reported in table 3.3.2; values are also reported in pie charts in Fig. 3.3.8

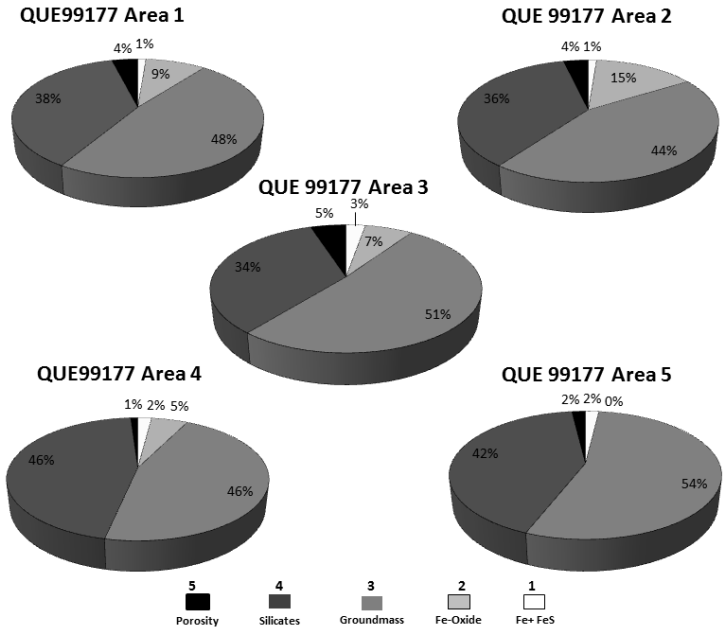

Fig. 3.3.8 - Pie Charts of the different sample areas in QUE 99177 showing abundances of the grayscale components present in the matrix

The five images maps, each map having an area of ~ 20 × 15 μm were thresholded and the abundances of the constituents are as follow: the average abundance of metal grains is 2±1%, the average porosity is 3±2%, and the average abundance of crystalline silicates is

22±7%. The light grey phase is a Fe-rich phase, most likely Fe-oxides, and accounts for 9±5% and the groundmass accounts for 46±3%. Thesholding values and average values are reported in Tables 3.3.2. & 3.3.3.

QUE99177		Threshold	%Area
Area 1	Fe+ FeS	255-205	1
Area 1	Fe-Oxide	204-170	9
Area 1	Groundmass	169-140	48
Area 1	Silicates	139-81	38
Area 1	Porosity	80-0	4
			100

QUE99177		Threshold	%Area
Area 3	Fe+ FeS	255-200	3
Area 3	Fe-Oxide	199-160	7
Area 3	Groundmass	159-120	51
Area 3	Silicates	119-55	34
Area 3	Porosity	54-0	5
			100

QUE99177		Threshold	%Area
Area 2	Fe+ FeS	255-210	1
Area 2	Fe-Oxide	209-140	15
Area 2	Groundmass	139-114	44
Area 2	Silicates	113-60	36
Area 2	Porosity	59-0	4
			100

QUE99177		Threshold	%Area
Area 4	Fe+ FeS	255-215	2
Area 4	Fe-Oxide	214-191	5
Area 4	Groundmass	190-140	46
Area 4	Silicates	139-30	46
Area 4	Porosity	29-0	1
			100

QUE99177		Threshold	%Area
Area 5	White	255-160	2
Area 5	light grey	---	---
Area 5	Dark grey	159-120	54
Area 5	Darkest Grey	119-75	42
Area 5	Black	74-0	2
			100

Table 3.3.2 - Table showing thresholding values of the different matrix regions in QUE 99177

QUE 99177	Porosity	Silicates	Groundmass	Opaques	Fe-Oxides
Area 1	4	38	48	1	9
Area 2	4	36	44	1	15
Area 3	5	34	51	3	7
Area 4	1	46	46	2	5
Area 5	2	54	42	2	
Average	3	42	46	2	9
STD(1σ)	1.6	8.3	3.5	0.8	4.3

Table 3.3.3 - Table showing abundances and average values of each individual grey scale units and in different matrix regions in QUE 99177

Area 4 and Area 5 Fig. 3.3.9 & Fig. 3.3.10 despite being close to each other show remarkable differences in their textural characteristics. Area 5 is in fact characterised by

the complete lack of pale grey phase and of any anhydrous silicates component, displaying instead a rather uniform platy texture. The two textures do not grade into one another and show a rather sharp edge.

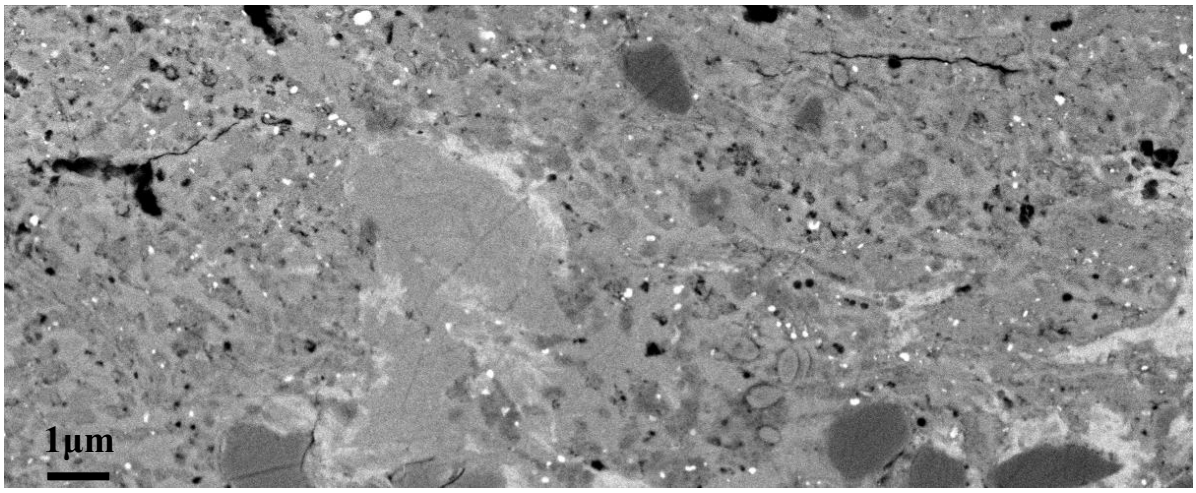

Fig. 3.3.9 - BSE of Area 4 in QUE 99177 showing a completely different texture to neighbour Area 5, characterised by a rather complex clastic texture

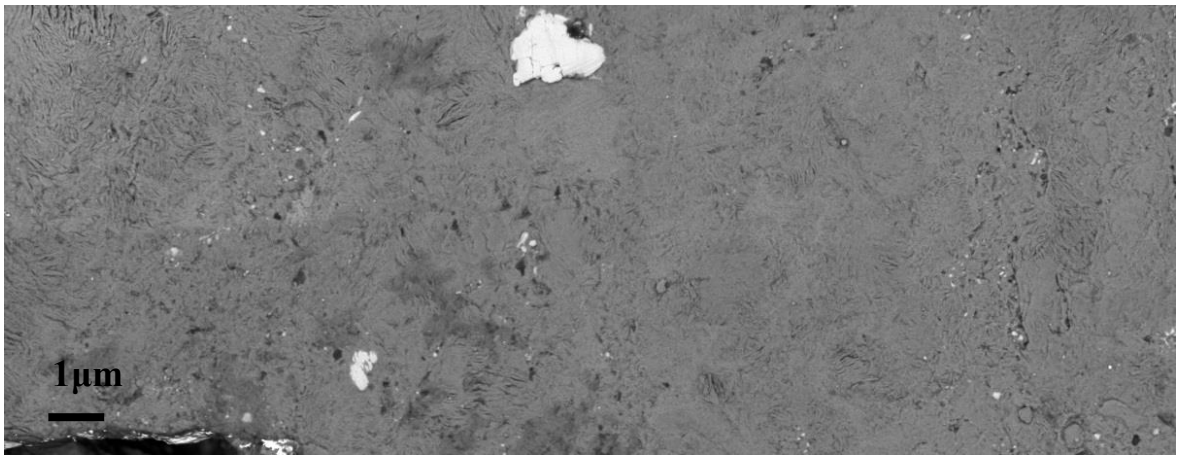

Fig. 3.3.10 - BSE of Area 5 in QUE 99177 showing a completely different texture to neighbour Area 4, characterised by platy uniform texture

3.3.2d – High Resolution Element Maps of Matrix

Element maps acquired at 6kV using a FEI Quanta 650 SEM have confirmed the textural heterogeneity and complexity of the different matrix regions in QUE 99177 previously revealed by the image maps acquired using the Ultra Plus FEG SEM. Area 5 shows an unusual enrichment in Mg compared to the surrounding matrix (Fig. 3.3.11), and based on the CI normalised values this area is the only one with CI like Mg abundances.

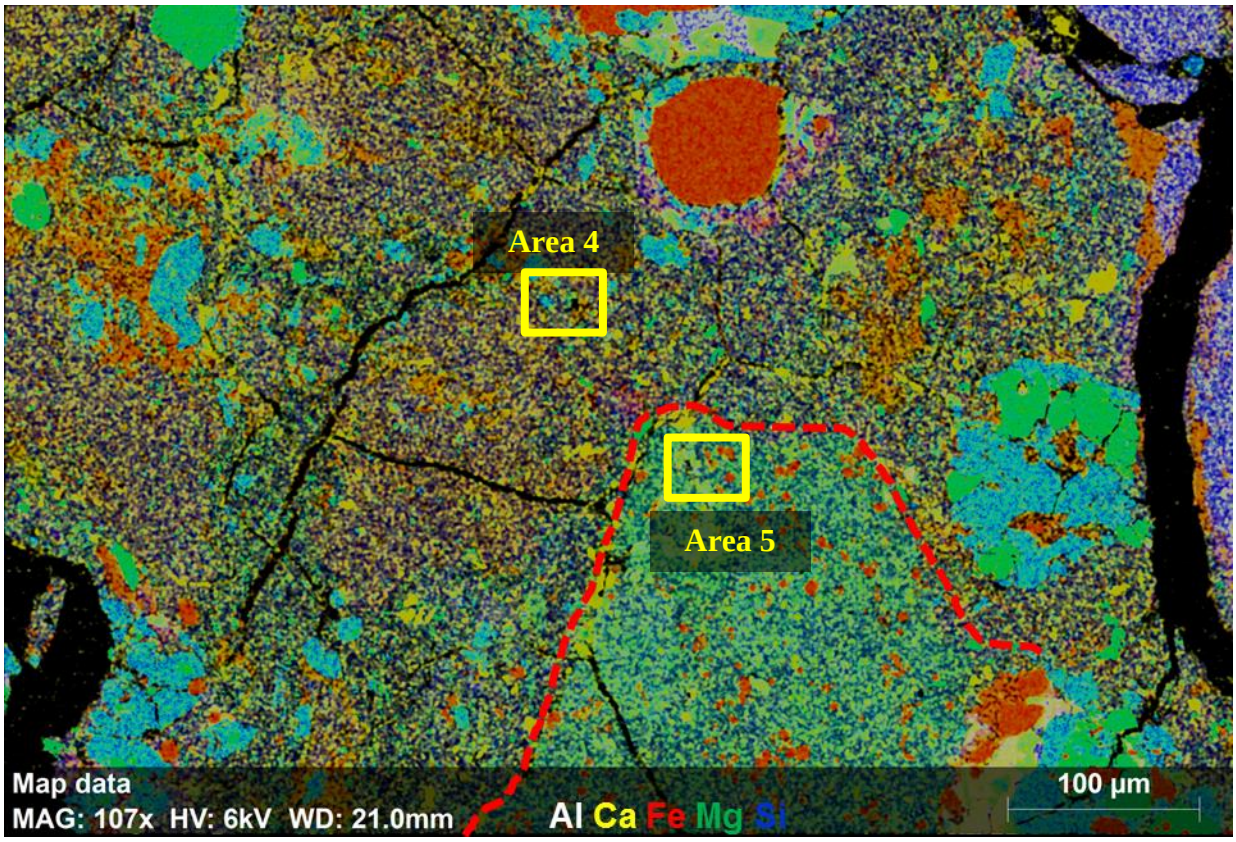

Fig. 3.3.11 - Element map of matrix Areas 4-5 in QUE 99177 red dotted line indicates the outline of the clast hosting Area 5, yellow boxes indicates Areas 4 & 5

The S in the matrix (Fig.3.3.12) seems to show a different distribution between the Mg-rich and Mg-poor areas. The enrichments in S appear to be associated with fluid percolating within the fractures in Area 4, whereas Area 5 seems to have experienced a different alteration history exhibiting a more modest enrichment in the element.

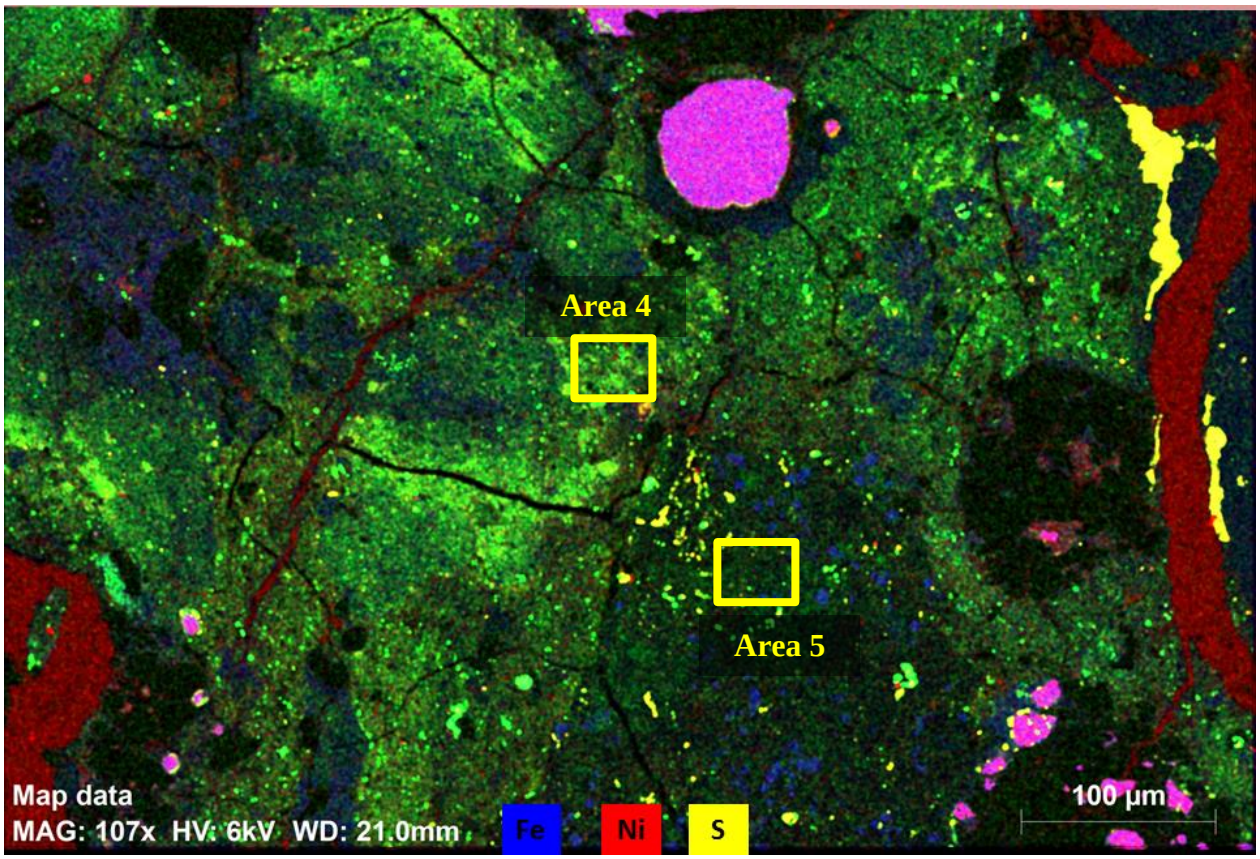

Fig. 3.3.12 - Element map of matrix Areas 4-5 in QUE 99177, pale green areas are enriched in S and Fe

3.3.2e – Mineralogy of the Matrix

From the micro-XRD patterns acquired on the matrix of sample QUE 99177 the following crystalline phases were identified: forsterite, enstatite, pyrrhotite, metal-iron and kamacite. Diffraction patterns look similar showing no significant differences between different areas (Fig. 3.3.13) with the exception of the pattern acquired in Area 5 where kamacite ($(Fe^{0+}_{0.9}Ni_{0.1})$ is not present, and magnetite ($Fe^{2+}Fe^{3+}_2O_4$), is considerably more abundant compared to the other areas .

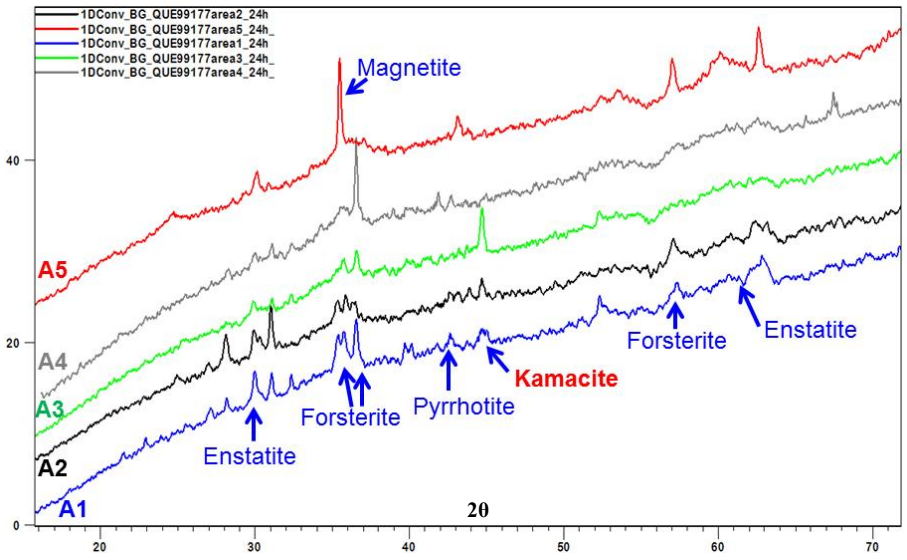

Fig. 3.3.13 - Diffraction pattern of the matrix areas investigated in QUE 99177

The average abundance volumes for QUE 99177 obtained using a profile-stripping method are: 27% olivine $(Mg, Fe)_2SiO_4$, 32% enstatite ($MgSiO_3$), 5% magnetite ($Fe^{2+}Fe^{3+}{}_2O_4$), 15% pyrrhotite ($Fe_{1-x}S$ (x = 0 to 0.2)) and iron metal 8%. Phase quantification values for each individual area are reported in Table 3.3.4 and (Fig. 3.3.14).

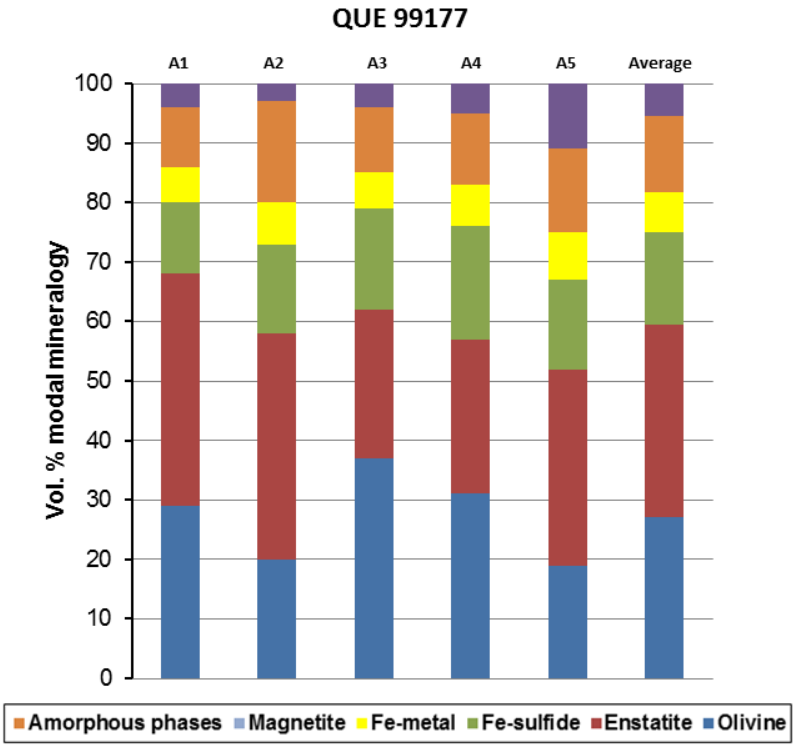

Fig. 3.3.14 – Bar chart reporting abundances of mineral phases present in each individual area and QUE 99177 average values

Kamacite ($Fe^{0+}_{0.9}Ni_{0.1}$) has been identified in the diffraction patterns of 4 areas (1, 2, 3 and 4), however the lack of standard for this phase make it difficult to quantify its abundance. The remaining 14% contribution which is not accounted for is likely to be the poorly crystalline phases e.g. amorphous silicates and a contribution of ferrihydrite, which most likely are also contributing to the overall pattern background.

QUE 99177	A1	A2	A3	A4	A5	Average
Olivine	29	20	37	31	19	27
Enstatite	39	38	25	26	33	32
Magnetite	4	3	4	5	11	5
Pyrrhotite	12	15	17	19	15	16
Fe-metal	6	7	6	7	8	7
Amorphous phase	10	17	11	12	14	13

Table 3.3.4 - Table showing abundances of the mineral phases calculated in each area and QUE 99177 average values

3.4 - Ungrouped carbonaceous chondrite Acfer 094

3.4.1 - Previous studies

The Saharan meteorite Acfer 094 is a unique carbonaceous chondrite. Chemical, mineralogical, and isotopic characteristics are unable to distinguish between a CO3 vs. CM2 classification (Newton et al., 1995). Whilst the matrix mineralogy and oxygen isotopic compositions imply affinities between Acfer 094 and the CO3 group (Bischoff et al., 1991), trace element concentrations suggest a close relationship of Acfer 094 with CM meteorites (Wlotzka, 1991; Spettel et al., 1992). Bischoff and Geiger (1994) suggested that Acfer 094 may be the first CM3 chondrite. However, this is excluded by measured C (1.00 ± 0.19 wt %) and N (682 ppm) abundance (Newton et al., 1995), which demonstrate that Acfer 094 is, in fact, a unique and primitive chondrite. Acfer 094 contains more interstellar SiC than any other meteorite studied (Newton et al., 1995; Gao et al., 1996). Additionally, its diamond concentration (732 ± 188 ppm) is second only to Orgueil (Gao et al., 1996). Although Orgueil experienced aqueous alteration, its diamond concentration is still high, suggesting that thermal metamorphism has the dominant effect in destroying presolar grains over aqueous alteration. Given the high diamond concentration of Acfer 094, this can be regarded as a good candidate to contain primitive materials, for example matrix components formed by processes in the early solar nebula.

3.4.1.1- Anhydrous Crystalline Phases in the Matrix

TEM observations and defocused beam microprobe analyses reveal totals of 93-96 wt% and indicate that the fine grained matrix mainly consists of anhydrous minerals (Newton et al., 1995). The matrix is clearly dominated by amorphous material which has been observed in all samples of the meteorite studied. The most abundant phases embedded in the amorphous material are tiny anhedral olivines (200-300 nm), pyroxenes (300-400 nm), and Fe,Ni-sulfides (100-300 nm). Some 15-80 nm sized olivines were found being rimmed

by material of unknown composition (Greshake, 1997). Sometimes olivine occurs as polycrystalline aggregates. Larger olivines and pyroxene grains up to 2 ~µm in size are rare. A few angular pyroxene and olivine fragments have been found. Serpentine and chlorite are present in small portions in the amorphous material. Serpentine occurring in cracks and ferrihydrite are the most common secondary minerals (Greshake, 1997).

3.4.1.2 Amorphous Phases in Matrix

Amorphous material is the most abundant phase of the inter-chondrule matrix in Acfer 094 and varies between 20 and 80 vol% (Greshake, 1997). This material acts as an intergranular groundmass to small olivine, pyroxene, and Fe-Ni sulfide grains.

The texture and chemical composition of this amorphous material suggests that it may be considered as a possible precursor of matrix materials in other types of chondrites. The fact that Acfer 094 is the meteorite containing the highest abundance of circumstellar SiC grains supports the view that at least parts of the amorphous material might be of circumstellar origin. Although Acfer 094 is essentially unique, there are some textural similarities with the matrix of the unequilibrated CO3 chondrite ALHA77307 (Greshake, 1997).

3.4.1.3 – Phyllosilicates in the Matrix

Phyllosilicates, which are most probably the product of hydrous alteration processes, have been found in a vein cross-cutting a large olivine grain. (They have a fibrous appearance and show lattice spacings of 0.7 nm corresponding to serpentine. Most of the phyllosilicates contain lattice defects and layer terminations.The serpentine most probably formed by aqueous alteration of the olivine grain (e.g., Keller and Buseck, 1990a). High resolution TEM shows that in some areas phyllosilicates are also present within the

amorphous component. The lattice spacings of 0.7 nm and 1.4 nm correspond to serpentine and chlorite. The abundance of these phases is probably <1 vol% (Greshake, 1997).

3.4.2 - Study carried out in this project

3.4.2a - Matrix abundance

In order to estimate the matrix percentage in our sample Acfer 094 the same approach as for samples ALHA77307 and MIL 07687 was followed. The element map acquired using EVO 50L was binarised and the total sample area was measured by thresholding (Fig. 3.4.1).

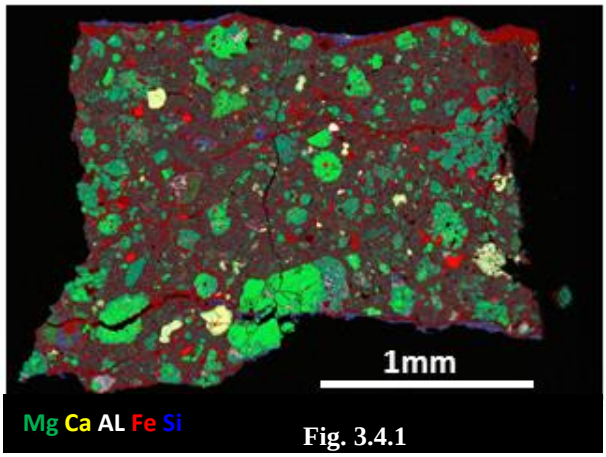

Fig. 3.4.1

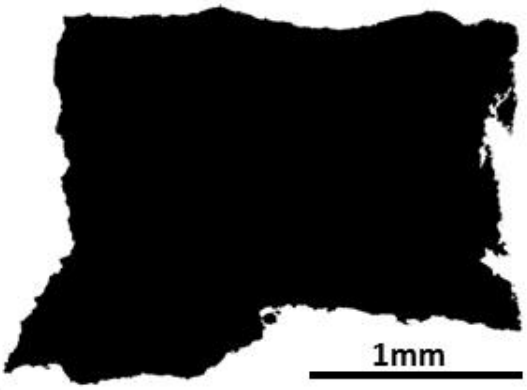

Fig. 3.4.2

Fig. 3.4.1 - Element map of Acfer 094
Fig. 3.4.2 - Binarised image of Acfer 094 element map

Major fractures occurring in the sample were estimated (Fig. 3.4.3) to account for 17% of the total area with the clastic component (Fig. 3.4.4) accounting for 33%. The matrix abundance in Acfer 094 was obtained subtracting from the total sample area the values for the clastic components and the fractures to provide a matrix abundance value of 50%. This is comparable to the value of 30-40% given by Newton et al. (1995), and similar to the matrix abundance value obtained for ALHA77307 of 47%. This is consistent with previous reports of similarities between the matrix of Acfer 094 and ALHA77307 (Greshake, 1997).

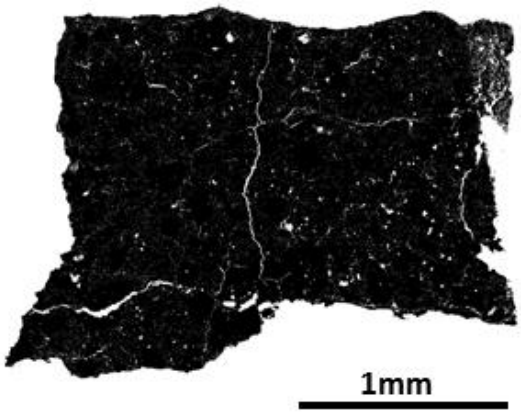

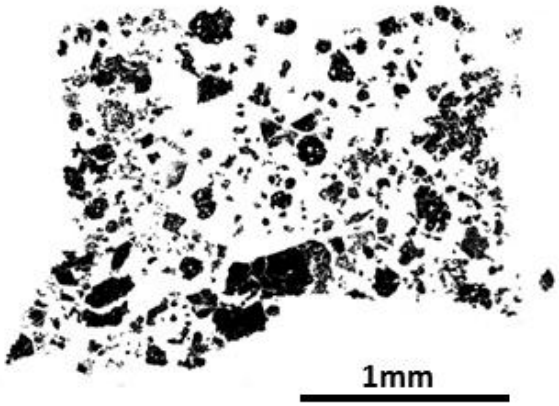

Fig. 3.4.3 **Fig. 3.4.4**

Fig. 3.4.3 - Binarised image of Acfer 094 element map showing micro fractures
Fig. 3.4.4 - Binarised image of Acfer 094 element map showing chondrules and CAI

3.4.2b – Bulk Chemical Composition of Matrix

Major element compositions of matrix Acfer 094 were extracted from the montage map acquired with EVO 15L SEM, from 5 different matrix regions of approximately 1 mm^2 in size (Fig. 3.4.5). Values of the extracted spectra are reported in Table 3.4.1 and plotted on a ternary Si-Fe-Mg (element wt %) diagram in Fig. 3.4.6. The negative correlation of the Fe with Si and Mg seems to be also true for Acfer 094 as previously observed for ALHA77307 and MIL 07687. Fe displays a rather narrow range of compositional variation, and it's trend from the Fe apex towards the Si-Mg join, while poorly defined, would define a line which would intercept this axis at approximately Mg/(Si + Mg) = 40%, remarkably similar to what has been observed for the samples ALHA77307 and MIL 07687 (e.g. Brearley et al., 1993).

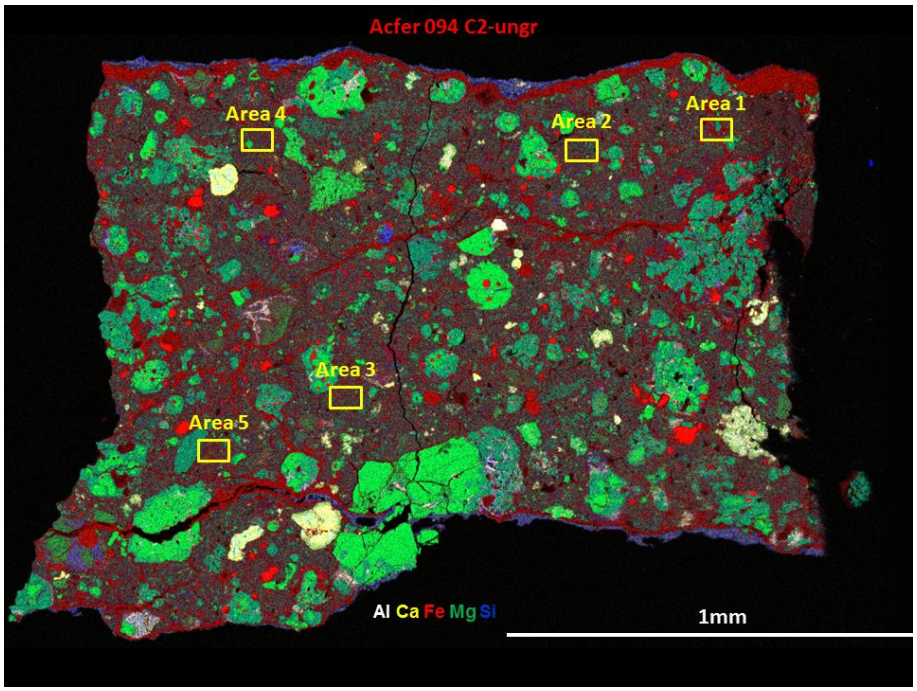

Fig. 3.4.5 – Acfer 094 Element map showing the 5 matrix Areas investigated

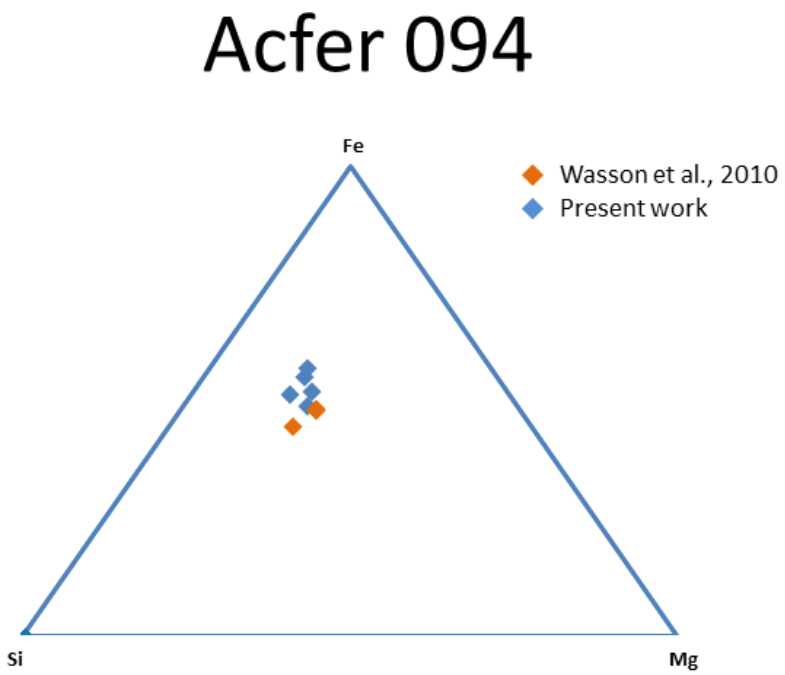

Fig. 3.4.6 – Compositional data from matrix regions of Acfer 094 plotted in a ternary Si-Fe- Mg (element wt %) diagram showing some indication of a negative correlation between Fe and Si+Mg

Acfer 094 (wt%)	AREA 1	AREA 2.2	AREA 3	AREA 4	AREA 5
O	38.9	38.9	38.0	37.8	37.4
Na	0.0	0.2	0.3	0.1	0.0
Mg	9.2	10.3	10.4	10.5	10.1
Al	1.1	1.1	0.9	1.1	0.9
Si	14.8	15.2	14.7	15.5	14.8
S	4.1	3.7	4.3	3.1	3.4
K	0.1	0.2	0.1	0.1	0.1
Ca	1.4	1.8	1.4	1.5	1.4
Ti	0.0	0.3	0.0	0.1	0.0
Cr	0.2	0.3	0.4	0.3	0.3
Mn	0.2	0.2	0.1	0.1	0.2
Fe	23.6	22.4	22.9	20.9	22.2
Co	0.4	0.1	0.1	0.0	0.4
Ni	1.6	1.5	1.3	1.0	1.4
Total	95.7	96.0	95.0	92.0	92.5

Table 3.4.1 - Evo 15L analyses of selected matrix regions in Acfer 094

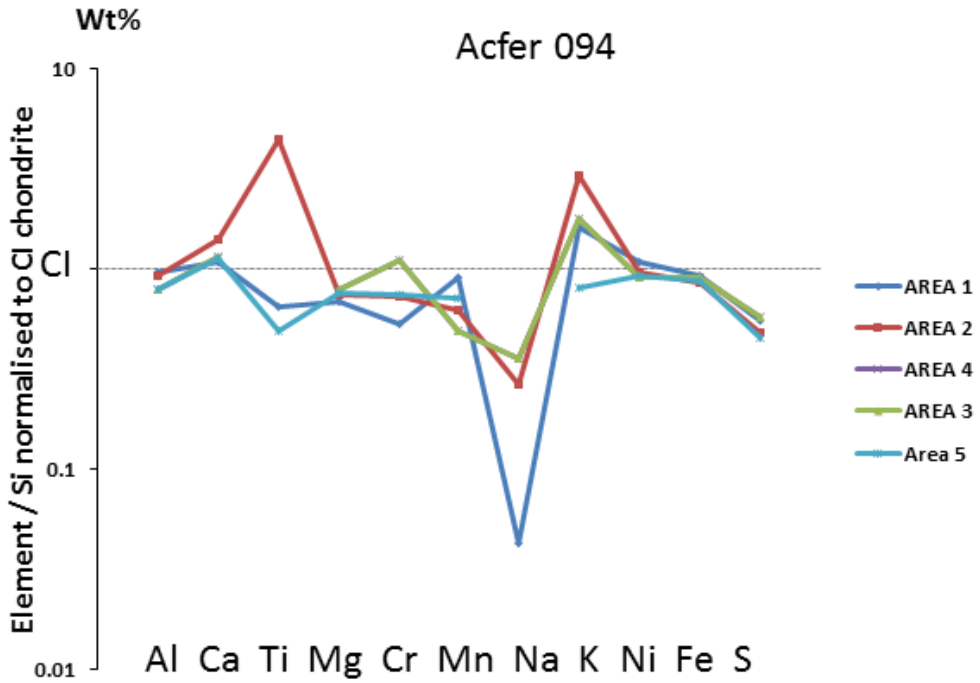

Fig. 3.4.7 - Normalised element ratio diagram showing data of five different matrix regions in Acfer 094. The data are normalised to Si and CI chondrite values from (Anders & Grevesse, 1989). The different regions do not show differences in composition. X-ray detection limit ~ 0.1- 0.3 mass % depending on the element

For Acfer 094 were also plotted the major elements from the five different matrix regions normalized to CI chondrite values and Si (from Anders & Grevesse, 1989) and results are shown in Fig. 3.4.7. The five different matrix regions analysed do not show appreciable differences suggesting a common origin. Consistent with previous observations for the other samples reported in this work, all matrix regions appear to be significantly fractionated in almost all the major elements relative to CI abundances. S and Na show the heaviest depletion in all the five regions analysed. In contrast to the observations for ALHA77307 and MIL 07687, sample Acfer 094 shows enhancement of Ca and K relative to solar values.

3.4.2c – Modal Mineralogy of Matrix

Based on high definition EsB images maps acquired using the FEG SEM Ultra Plus, the abundance of the matrix constituents have calculated based on the different grey scale displayed by the grains as for the other samples. The values obtained are reported in pie charts in Fig. 3.4.8 and the values of the thresholding and average values are reported in Table 3.4.2 The five images maps (each map having an area of ~ 20 x 20 μm) of the matrix regions investigated show the average abundance of metal grains as 5± 3%, an average porosity of 3±2%, and the average abundance of crystalline silicates of 46±14% while the groundmass accounts for 46±14%. The values are reported in Table 3.4.3. The light grey shades phase that was observed abundantly in the matrix of ALHA77307 and MIL 07687 characterised by relatively high intensity pixels suggestive of a Fe-rich phase, most likely Fe-oxides, is absent in the matrix of Acfer 094, but occurs in pre-existing micro-fractures. This phase was interpreted as a secondary mineral produced by terrestrial weathering (e.g. Wasson et al., 2010).

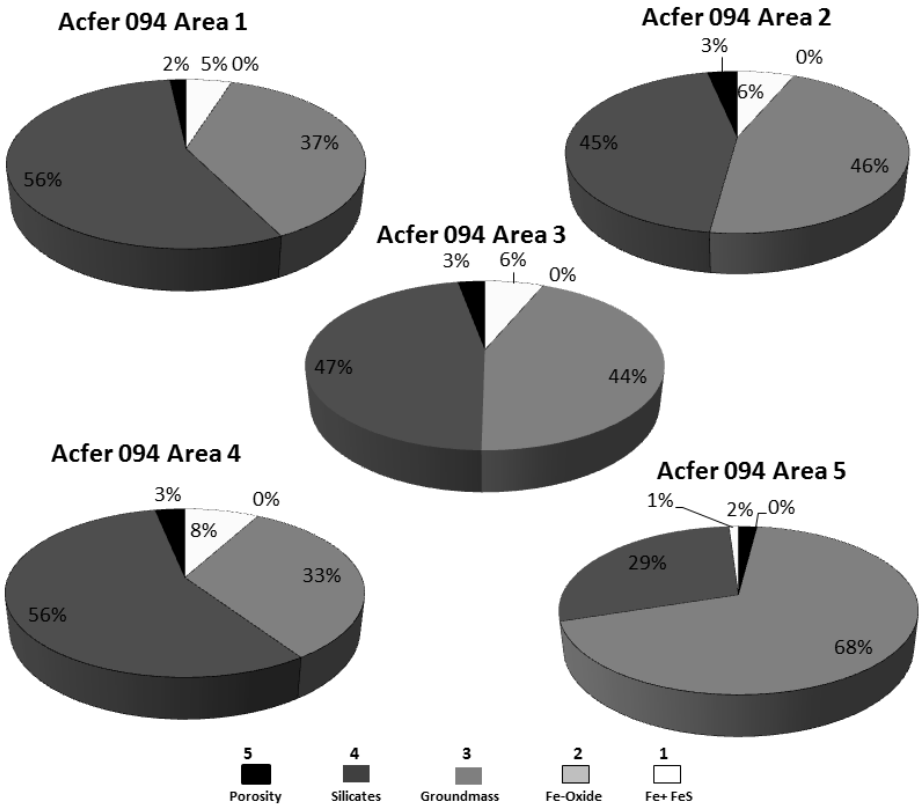

Fig. 3.4.8 - Pie Charts of the different sample areas in Acfer 094 showing abundances of the grayscale unities present in the matrix

Acfer094		Threshold	%Area
Area 1	Fe+ FeS	255-225	5
Area 1	Fe-Oxide	---	---
Area 1	Groundmass	224-165	37
Area 1	Silicates	164-55	56
Area 1	Porosity	54-0	2
			100

Acfer094		Threshold	%Area
Area 2	Fe+ FeS	255-205	6
Area 2	Fe-Oxide	---	---
Area 2	Groundmass	204-125	46
Area 2	Silicates	124-30	45
Area 3	Porosity	29-0	3
			100

Acfer094		Threshold	%Area
Area 3	Fe+ FeS	255-170	6
Area 3	Fe-Oxide	---	---
Area 3	Groundmass	169-90	44
Area 3	Silicates	89-20	47
Area 3	Porosity	19-0	3
			100

Acfer094		Threshold	%Area
Area 4	Fe+ FeS	255-165	8
Area 4	Fe-Oxide	---	---
Area 4	Groundmass	164-115	33
Area 4	Silicates	114-40	56
Area 4	Porosity	39-0	3
			100

Acfer094		Threshold	%Area
Area 5	Fe+ FeS	255-200	2
Area 5	Fe-Oxide	---	---
Area 5	Groundmass	199-95	68
Area 5	Silicates	94-30	29
Area 5	Porosity	29-0	1
			100

Table 3.4.2 - Table showing thresholding values of the different matrix regions in Acfer 094

Acfer 094	Porosity	Silicates	Groundmass	Opaques	Fe-Oxides
Area 1	2	56	37	5	---
Area 2	6	45	46	3	---
Area 3	3	47	44	6	---
Area 4	3	56	33	8	---
Area 5	2	29	68	1	---
Average	3	47	46	5	---
STDV (1σ)	1.6	11.1	13.6	2.7	---

Table 3.4.3 - Table showing abundances and average values of each individual grey scale unities and in different matrix regions in Acfer 094

3.4.2d – High Resolution Element Maps of Matrix

Element maps of the matrix regions previously mapped using the Ultra Plus were acquired at 6kV (Fig. 3.4.9 & 3.4.10) using the FEI Quanta 650 SEM. The element maps acquired show that the main cations of the amorphous groundmass are Mg, Si and Fe, consistent with previous work (e.g. Wasson & Rubin 2009). Rare ferrihydrite in the matrix (< 2 vol%) has been previously reported (Greshake, 1997), and the maps show a rather locally abundant poorly crystalline Fe–rich phase present within the major fractures (Fig. 3.4.10).

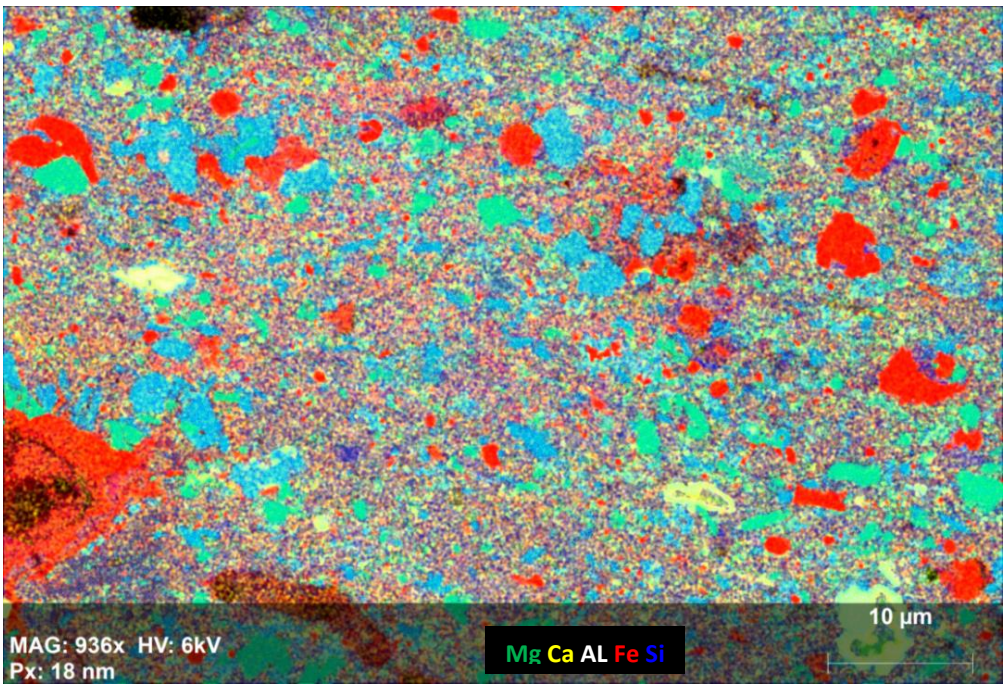

Fig. 3.4.9 - Element map of matrix Area 1

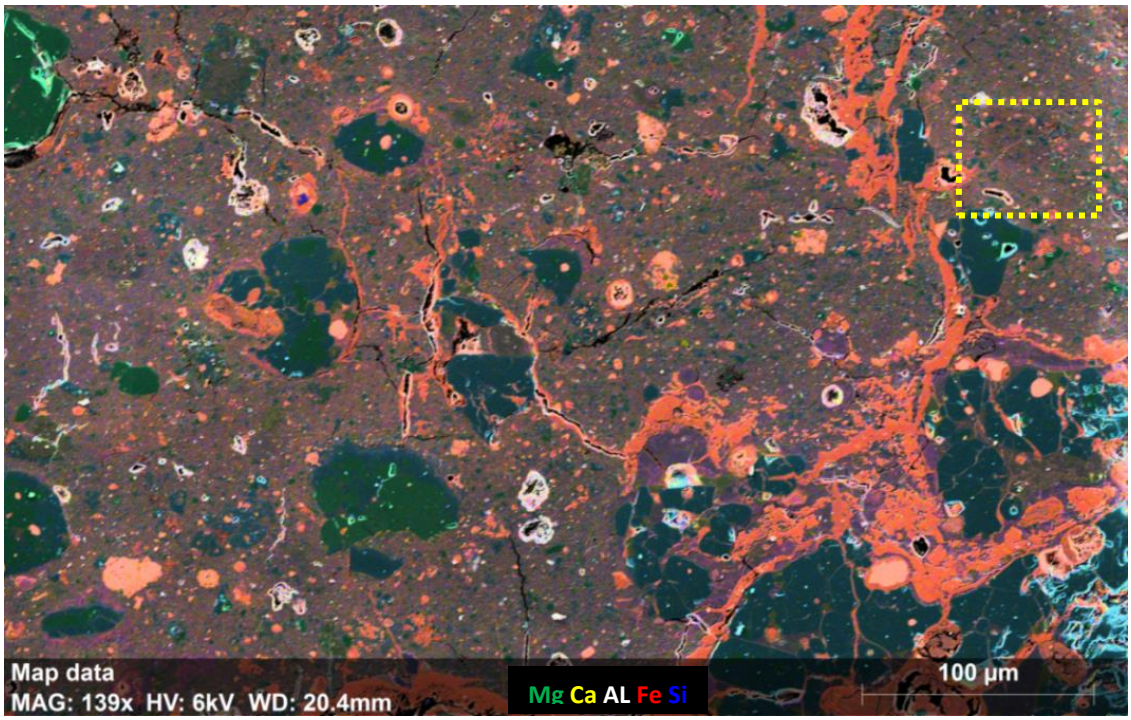

Fig. 3.4.10 - Element map of matrix showing Fe-rich poorly crystalline phases occurring in major fractures. Dotted yellow box outlines the Area 1in Fig. 3.4.9

3.4.2e- XANES Results

Quantification of the Fe^{3+} /Σ Fe ratio using STXM in the matrix of sample Acfer 094 reveals very little difference in the bulk measurements obtained from three FIB sections A, C and D (Fig. 3.4.11). Spectra were extracted from bulk of ~ 35µm^2 areas, and are similar to the Fe^{3+}-rich standard spectrum.

While the bulk compositions are broadly similar (Fig. 3.4.11) the texture and mineralogy in the FIB foils of Acfer 094 matrix exhibit some variations in the X–ray absorption images, and based on these variations three regions of interest were selected. The contrast variation exhibited by the three ROIs revealed variations in the Fe^{3+} /ΣFe ratio (Fig. 3.4.12), this is shown by the higher intensity of the Fe^{2+} peaks compared to the intensity of the Fe^{3+} peaks obtained for the bulk ROIs of the same foils observed in Fig. 3.4.11.

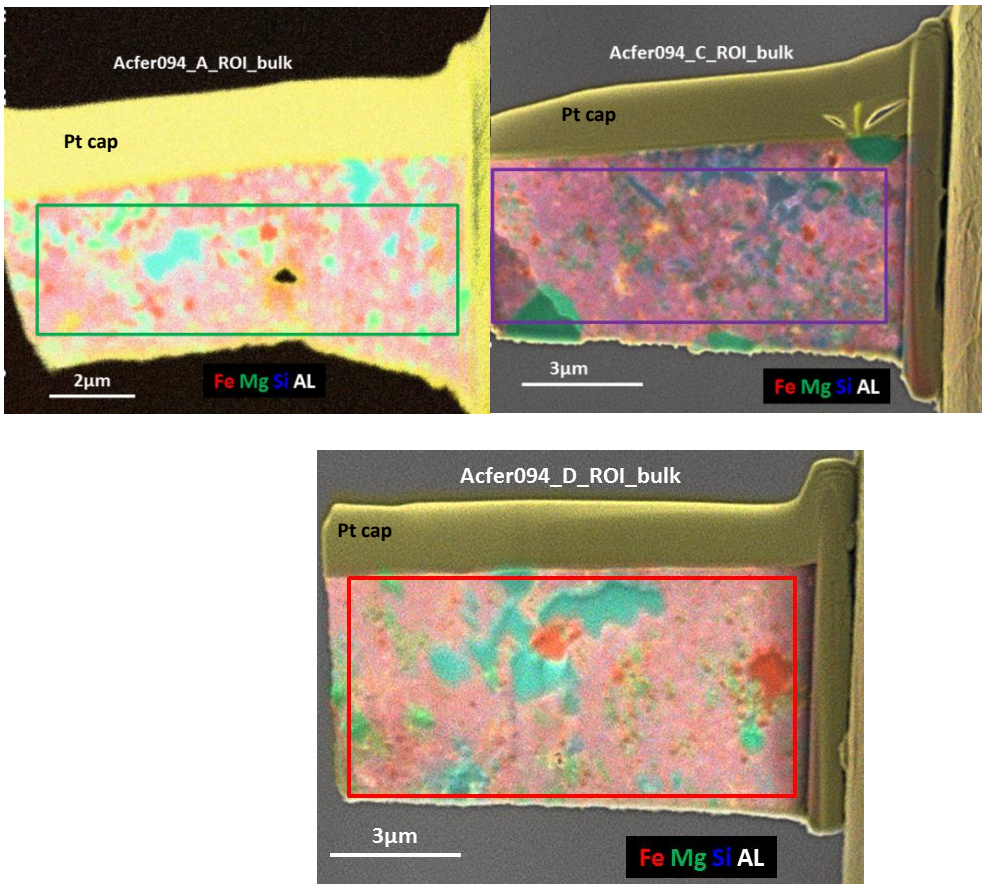

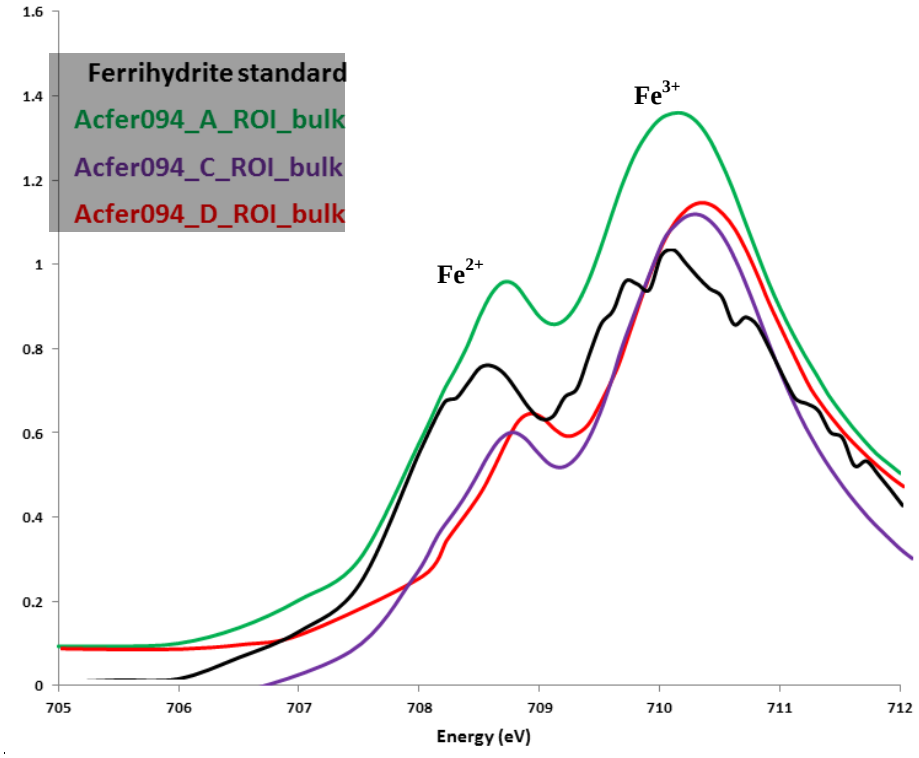

Fig. 3.4.11 - SEM element maps of FIB section A, C and D of Acfer 094 matrix showing bulk region (in boxes) were spectra were extracted to determine bulk values. All the bulk values show enrichment in Fe^{3+}. Spectra on foil B was not acquired as the foil was damaged

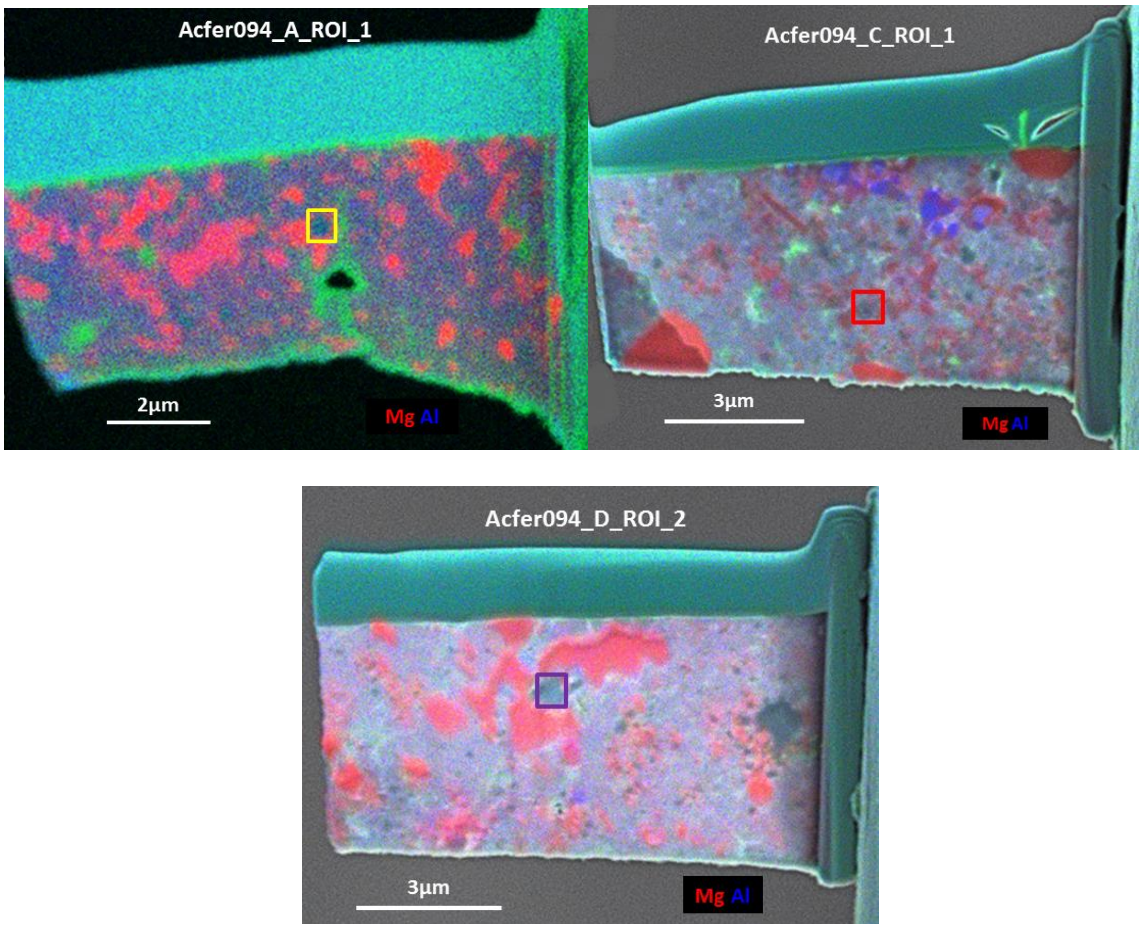

Fig. 3.4.12 - SEM element maps of FIB sections of Acfer 094 matrix showing ROIs (in boxes) within the foils and related spectra. All the ROIs value show more intense Fe^{2+} peaks compared to the bulk spectra

3.4.3 - Discussion of petrological results for QUE 99177 and Acfer 094

The results of the observations carried out in this work have highlighted aspects that can be summarised in two main categories: accretion and nebula processes versus parent body processes.

Accretion processes

Most of the matrix areas in QUE 99177 investigated in this work does not display major differences between them, with the exception of Areas 5 which appears to be different from the others, and considerably different from the contiguous Area 4. SEM analyses have highlighted some chemical differences between these two areas and in a ternary diagram (Fig. 3.3.6) they represent the extreme ends of the data range despite their proximity. High resolution image maps (e.g. Fig. 3.3.9 & Fig. 3.4.10) have revealed the textural difference between Area 4 and Area 5, which appears to have experienced some alteration resulting in a platy texture and lacking totally the clastic component and the Fe-rich pale grey phase that characterise the other areas. The micro-XRD analyses have also shown that Area 5 is the only area that does not contains kamacite. This suggests that this region might have been exposed to a microchemical environment with a high S activity, where kamacite altered to form tochilinite, and the Fe in kamacite is removed from the alteration region (Palmer & Lauretta, 2011). The S distribution highlighted by the SEM element map (Fig. 3.3.12) has shown how the element abundance seems to be related to fluid percolation. Its distribution is different between the two areas, probably due to the lower porosity and more uniform texture of the matrix in Area 5. This implies that Area 5 experienced a different alteration history compared to adjacent Area 4. An overview of the sample QUE 99177 displaying the two contiguous matrix regions Area4 and Area 5 is shown in Fig. 3.4.13, where the differences in the texture and the chemical composition of Areas 4 & 5 are clear.

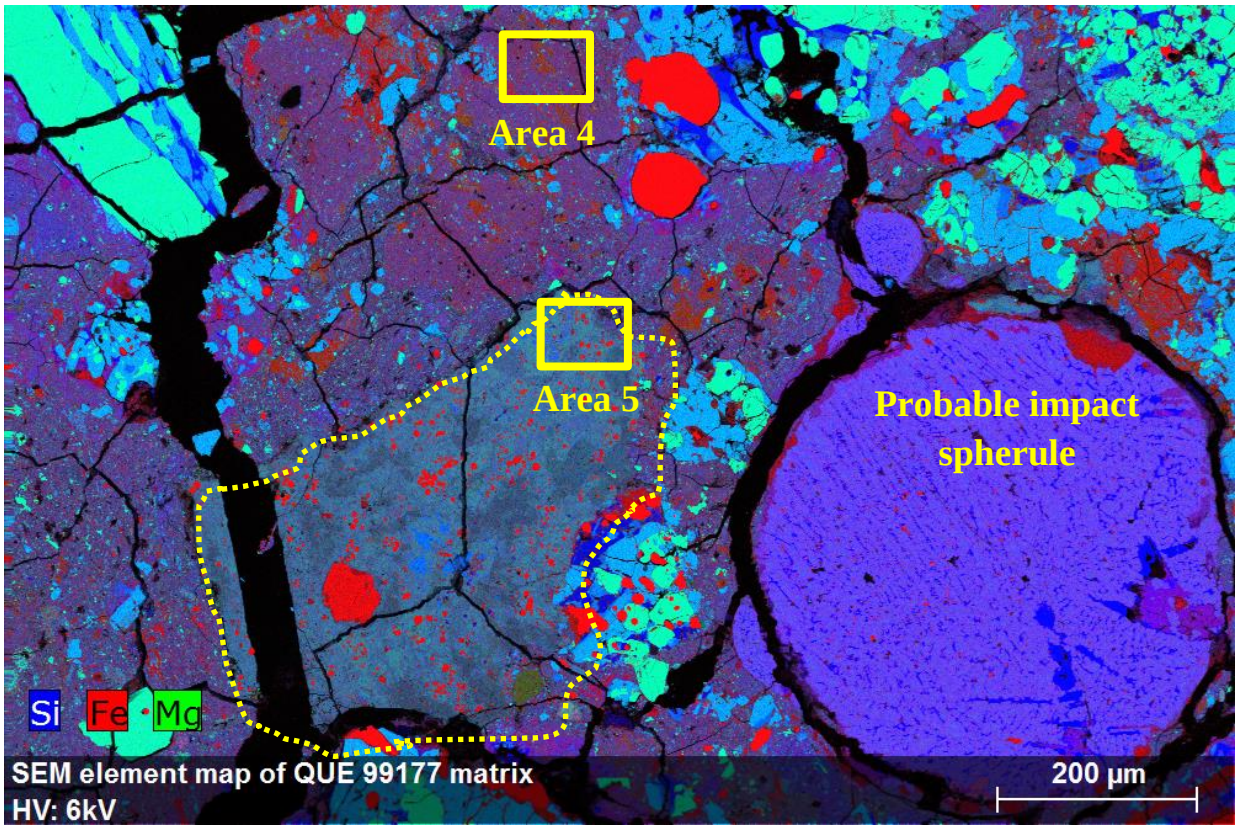

Fig. 3.4.13 - SE-element map of matrix Areas 4-5 (yellow boxes) in QUE 99177, dotted yellow line outlines the matrix clast hosting Area 5

The element map shows the presence of a round Si-rich object characterised by feathered texture which might be a glassy impact spherule. Glassy impact spherules with an Ir anomaly of likely asteroid belt provenance were found in in Ocean Drilling Hole in western Indian Ocean (e.g. Glass and Koeberl, 1999). They are thought to have formed by the condensation of vapour plumes ejected during impacts. Glassy spherules having a barred texture are also found in the S3 bed of the Barberton greenstone belt in South Africa and interpreted as distal fallout formed within an impact plume after a large impact event. The round object in Fig 3.3.13 shares textural and geochemical similarities to glassy impact spherules.

The barred texture presumably originated by quenching, in agreement with the impact spherules described Glass and Koeberl, (1999). The chemical composition is characterised

by high Si content (SiO_2 55.7 wt%) and low Mg (MgO 7.6 wt%). Fe (FeO 31.8 wt%) is the second most abundant element after Si, and occurs in small metal grains dispersed within the glass. The presence of Ni (1.12 wt%) is likely related to metal grains in agreement with the impact spherules described in impact spherules from howardites (Barrat et al., 2009).

The object is characterised by a general depletion in many alkalis (Na_2O 0.9 wt%, CaO 0.74 wt% and K_2O below detection limits) and it is important to note that the behavior of alkalis during impact melting is often complex, and that significant losses of these elements by evaporation can occur, which can explain their depletion in the object.

All these chemical and textural observation are pointing towards an impact origin for the spherule.

If the object is a glassy impact spherule, then this is another indication of impact event generating melt splash and clasts, pointing towards the model of chondrule redistribution in a carbonaceous chondrite parent body proposed by Tomeoka & Ohnishi (2011) (Fig. 3.4.14). This describes a highly hydrated clast in the Mokoia CV3 carbonaceous chondrite, and suggests that hydrated chondrules, inclusions, and the rims surrounding them in the host Mokoia chondrite are clasts produced by brecciation within a wet region of the parent body and that they were subsequently transported and incorporated into the dry matrix.

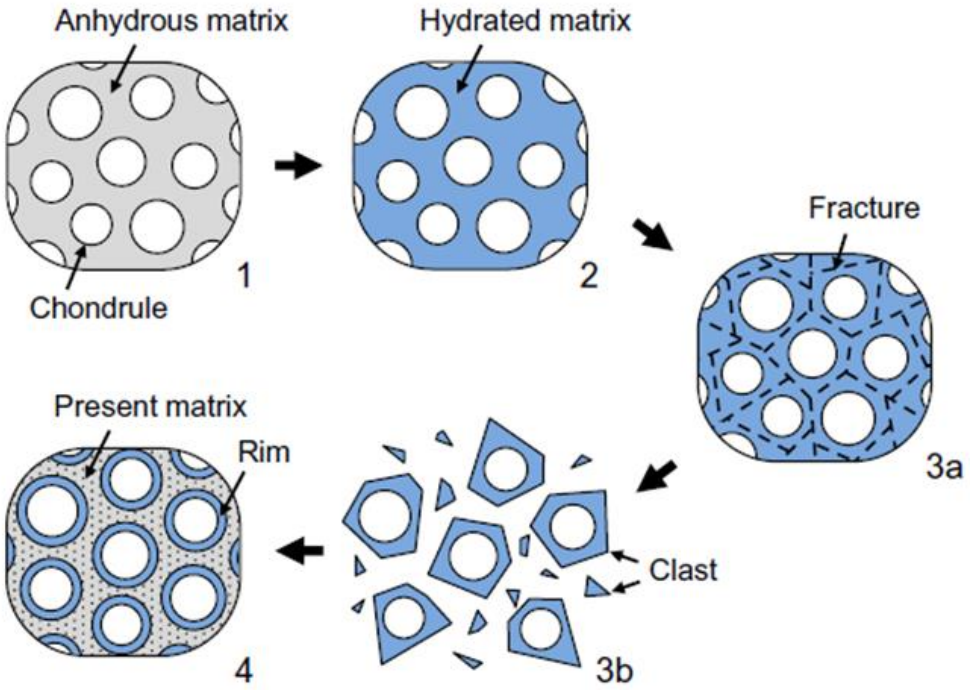

Fig. 3.4.14 - Cartoon of model of chondrules redistribution in carbonaceous chondrites parent body (Tomeoka et al., 2015)

Nebula versus parent body processes

Acfer 094 matrix analyses have shown enhancements in Ca and K relative to solar values. Enrichments in these particular elements can reflect terrestrial contamination during hot desert weathering. Terrestrial weathering is evident and occurs within pre-existing cracks depositing a microcrystalline Fe-oxide, but based on SEM observations there is no evidence of this weathering having significantly affected the matrix as was observed for ALHA77307 and MIL 07687. However, in previous work on the matrix of Acfer 094 Rubin et al. (2007) reported a low matrix bulk Na and a low Na/K characterised by Na depletion and relative enrichment in K. The anomalous concentration of these two alkalis was also reported and interpreted by Wasson & Rubin (2009) as an effect of terrestrial weathering where Na was extracted and K added during the process. Similar enrichment and depletions were observed in this study. Dreibus et al., (1995) also suggested that another effect of the terrestrial weathering visible in Acfer 094 was the S depletion due to the oxidation of S into SO_2(g), and SO_3(g), or $SO_4^{=}$, leached or lost as gas and replaced by

insoluble SeO_2. Based on SEM observations, considering the high abundances of Ni bearing opaque phases present in the matrix of Acfer 094 (see chapter 4) it is not surprising that there is a Ni enrichment relative to solar values.

The grain porosity values calculated from the high resolution image maps of the matrix regions are comparable to the porosity values obtained for ALHA77307 and MIL 07687, supporting another aspect of the similarity with the matrix of ALHA77307 reported by Greshake, 1997. This result is also compatible with the hypothesis that porosity measured in matrix is interstitial porosity and the low values suggest that chondrite porosity may occur mainly in fractures in fact, fractures were estimate and accounted for 17% of the total area, and they may have permitted the percolation of terrestrial fluids responsible for the observed weathering (e.g. Wasson et al., 2010). This also explains the lack of the pale-grey phase that was relatively abundant in ALHA77307 and MIL 07687, which appears to be the product of alteration of the opaque phases and is considerably higher in Acfer 094 compared to the other two samples.

The element map observations have revealed the enrichment of the groundmass in the cations Ca, Si and Fe. The presence of Ca is consistent with the enhancement also observed in the major elements analysis and attributed to the effects of terrestrial weathering. The Si and Fe is compatible with the Fe-bearing amorphous silicates characterising the matrix of pristine chondrites, which could be genetically linked to the amorphous silicates observed in protoplanetary disks. However, in the case of Acfer 094 it could have an impact related origin. Brearley and Rubie (1990) have shown that flash heating of fine hydrated silicates could be responsible for the formation of this amorphous material.

In terms of oxidation state of the matrix constituents of Acfer 094, the bulk values are Fe^{3+}-rich, indicating that the matrix constituents are highly oxidised. This could reflect the conditions of the solar nebula at the time of their formation, or exposure to such conditions

after formation, for example on the parent body or during terrestrial weathering. Detailed observations of the matrix constituents have revealed that the vast majority of the particles are oxidised and reflect the bulk values. However, some grains within the matrix are Fe^{2+}-rich indicating less oxidising conditions of the environment where they formed. Based on SEM observation these grains seem to be condensates from the solar nebula, and the element map indicates that are Al-rich (Fig. 3.4.12). If the nature of these grains is confirmed as CAI, this would indicate that they are exhibiting the oxidation state of the environment from where they condensed.

Owing to the fact that SEM based petrological observations of the matrix in Acfer 094 exhibits evidence of aqueous alteration affecting this sample, it is therefore proposed that the variations in the oxidation state exhibited by the matrix constituents are most likely reflecting aqueous alteration and/or terrestrial weathering. Fe^{2+}-rich grains clearly indicate that at the time of their formation there were regions of the solar nebula where reducing conditions were prevailing and that parent body processes and/or terrestrial weathering did not completely obliterate this reducing signature. It is very challenging to discriminate between oxidising conditions generated by aqueous alteration and Fe^{3+} caused by terrestrial weathering, without further NanoSIMS δD measurements, or TEM investigations. Post-accretionary processes are the most likely cause of the oxidation observed, however, the possibility that matrix constituents have sampled regions of the solar nebula characterised by oxidising conditions cannot be ruled out, and would be consistent with the observation of amorphous silicates as a nebular oxidation product of a fractionated solar gas component described by Hoppe et al., 2015. This would emphasise the small degree of homogenisation experienced by Acfer 094 parent body, but further investigations are required to confirm this hypothesis.

3.5 – Conclusions

The average values of mineral abundance in the matrix of the four samples studied in this work are summarised in Fig. 3.5.1. These values, estimated using the high resolution image maps acquired using the Ultra Plus, have revealed a similar abundance of opaque phases in ALHA77307 and MIL 07687 with an average value of around 2% . These phases are less abundant than the opaques present in Acfer 094 where they account for 5%. These observations are consistent with the results obtained in the grain size distribution study (see chapter 4) where a much higher abundance of opaque phases in Acfer 094 and QUE 99177 was observed, compared to ALHA77307 and MIL 0768. However, the abundance of Fe, FeNi+FeS in QUE 99177 estimated on the image maps, which accounts for 2%, is similar to the values reported for ALHA77307 and MIL 07687. In contrast the size distribution work suggests a much higher abundance for QUE99177 compared to ALHA77307 and MIL 07687.

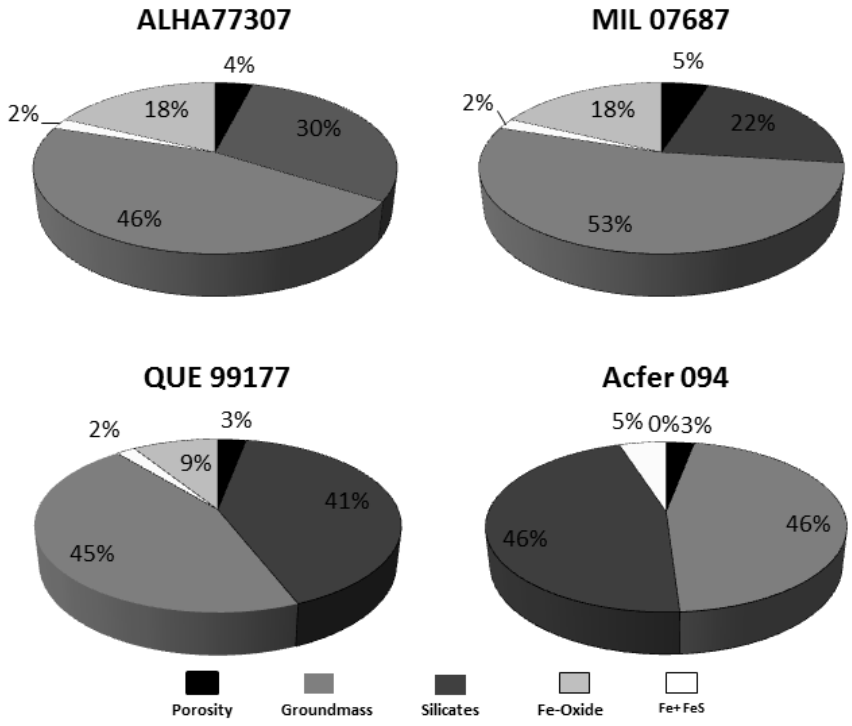

Fig. 3.5.1 - Pie Charts of ALHA77307, MIL 07687, QUE 99177 and Acfer 094 showing average values of mineral abundances present in the matrix

The discrepancy between grain size distribution results and image map estimates is likely due to the larger size displayed by the opaque phases in ALHA77307 and MIL 07687 compared to those in QUE 99177 where the opaques are smaller but numerically more abundant. This could be due to effects of mild thermal metamorphism experienced by ALHA77307 and MIL 07687, during which FeS increases its mobility and reduces its surface area resulting in coarser grains (Grossman and Brearley, 2005). Fig.3.5.1 also shows the similarities between QUE 99177 and Acfer 094, in the abundances of crystalline silicate phases compared to ALHA77307 and MIL 07687. The presence of Fe-oxide reflects the degree of alteration experienced by the meteorite but also highlights the type of terrestrial weathering associated with the location of the fall. Antarctic meteorites ALHA77307, MIL07687 and QUE 99177 all display the presence of Fe-oxide in the matrix where it is seen to replace the opaque phases (e.g. Fig. 4.4.1a, b, c). Acfer 094, which is a Saharan meteorite, is the only one that does not shown the presence of Fe-oxides in the matrix (see Fig. 3.5.1), although this phase is seen instead occurring in pre-existing cracks as displayed in Fig. 3.5.2.

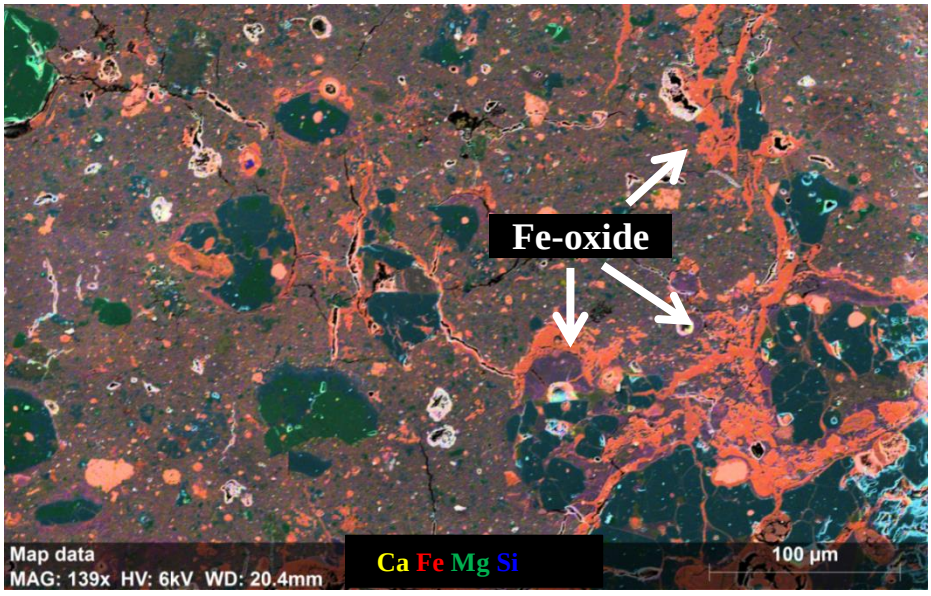

Fig. 3.5.2 - SE-element map of matrix in Acfer 094 showing the presence of Fe-oxide occurring in pre-existing cracks

This difference in the occurrence of the Fe-oxides appears to be associated with the different terrestrial environments and probably linked to the availability of liquid water percolating and interacting in different climatic conditions. Further TEM studies are required to confirm this.

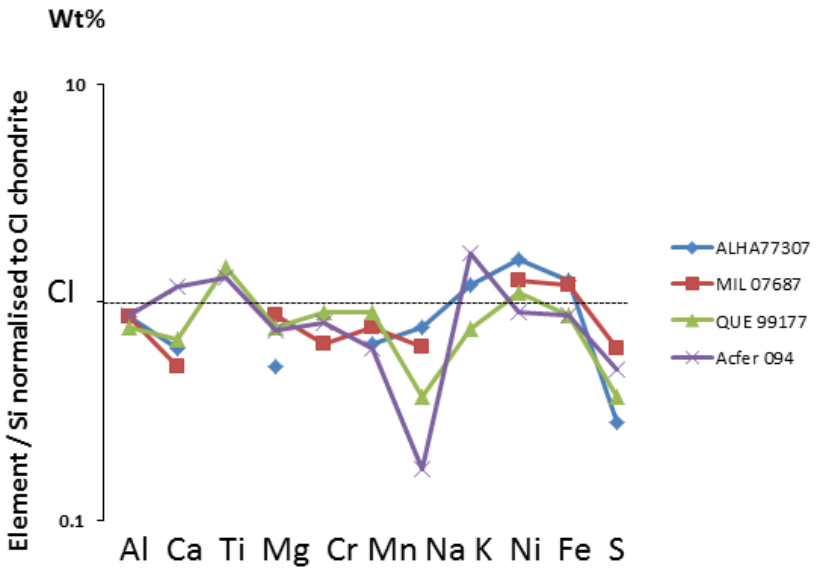

Fig. 3.5.3 - Normalised element ratio diagram showing averaged data of matrix regions in ALHA77307, MIL 07687, QUE 99177 and Acfer 094. The data are normalised to Si and CI chondrite values from (Anders & Grevesse, 1989). ALHA77307 is the only sample that shows evident compositional differences between the four different meteorites. The slight differences shown by the four samples are likely due to different terrestrial weathering. X-ray detection limit ~ 0.1- 0.3 mass % depending on the element

Averaged values of the five matrix regions analyses in each sample are reported in Fig. 3.5.3. The four meteorites seem to have a generally similar trend exhibiting depletion of most volatiles elements relative to the solar values, and a slight enrichment in siderophiles. ALHA77307 shows a slightly different trend, being the only meteorite to exhibit enrichment in Al and heavy depletion in Ti with respect to solar values.

ALHA77307, MIL 07687 and QUE 99177 show Ca depletion, likely inherited by the solar nebula (e.g. Brearley, 1993). Acfer 094 exhibits enrichment in Ca likely due to hot desert weathering (e.g. Greshake, 1997).

Micro-XRD patterns acquired on ALHA77307, MIL 07687 and QUE 99177 shown in Fig. 3.5.4, Fig. 3.5.5, and Fig. 3.5.6 have revealed that in terms of mineralogy the phases present in the matrix of the three meteorites are similar. However, QUE 99177 is

characterised by a more abundant clastic component, which is displayed by the peaks, high intensities of the XRD patterns. MIL 07687, on the other hand, is the sample exhibiting the least abundant clastic component in the matrix consistent, with the low intensity peaks of the mineral phases present. These results are in good agreement with the image map estimates reported in Fig. 3.5.1

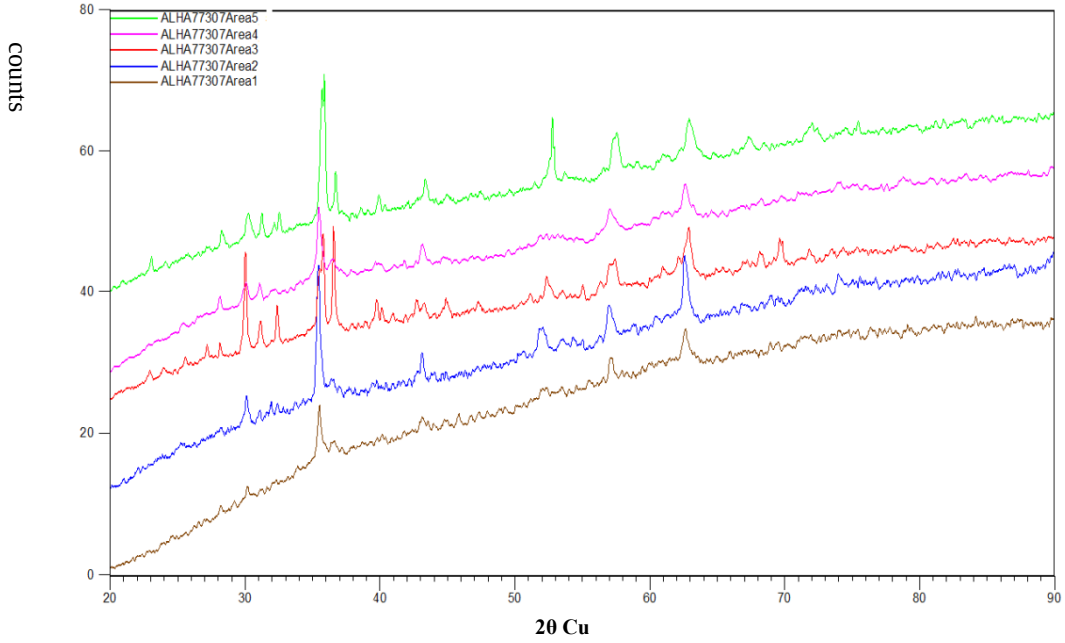

Fig. 3.5.4– X-ray diffraction pattern of the matrix areas investigated in ALHA77307

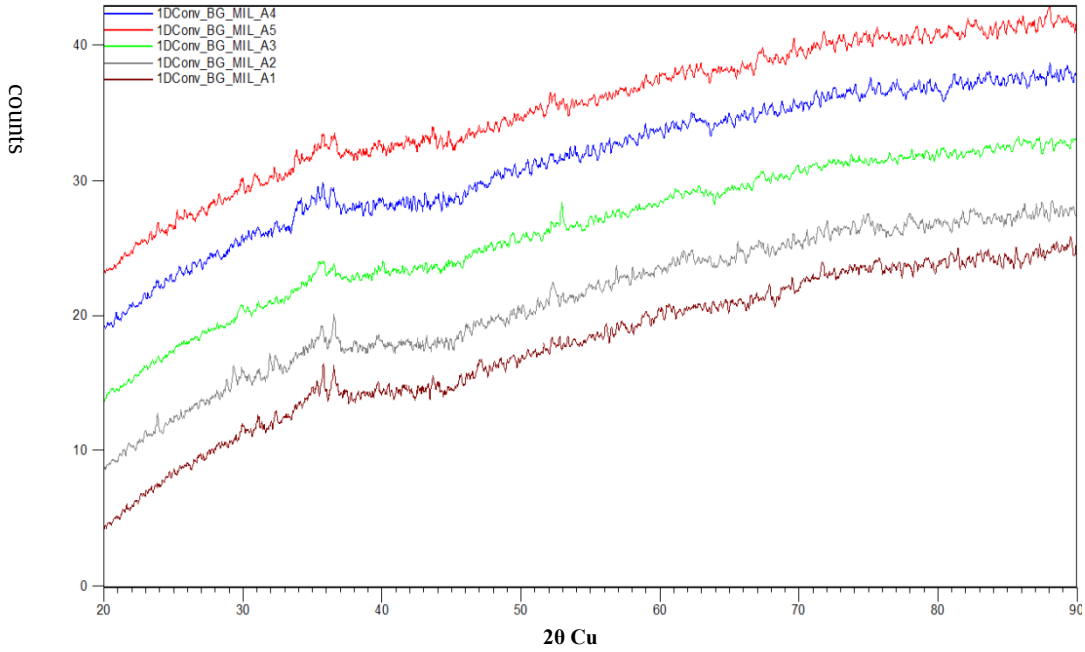

Fig. 3.5.5– X-ray diffraction pattern of the matrix areas investigated in MIL 07687

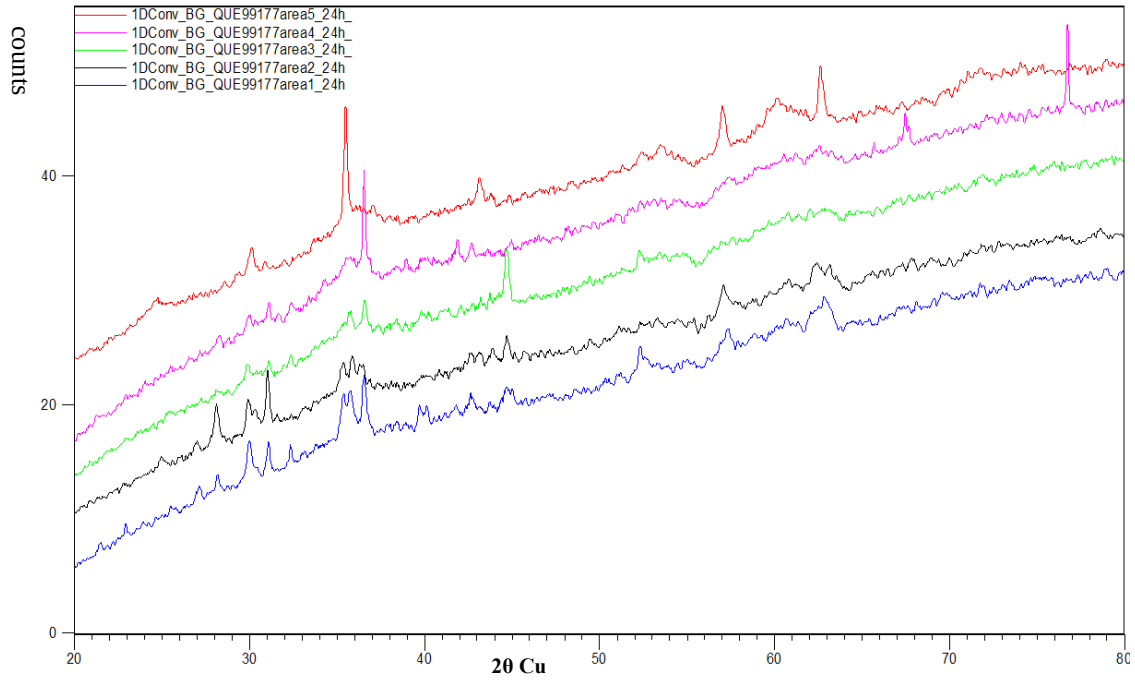

Fig. 3.5.6– X-ray diffraction pattern of the matrix areas investigated in QUE 99177

XANES data on MIL 07687 and Acfer 094 have shown the coexistence at the submicron scale of minerals displaying different redox conditions. This suggests that the matrix may have sampled different regions characterised by different redox conditions, and this scenario may indicate a rapid process of aggregation and accretion in order to preserve this heterogeneity. This indicates also that parent body processes and/or terrestrial weathering have not obliterated such nebula signature. Petrological evidence revealed by this work point towards matrix being affected by alteration. This appears to be related to the terrestrial environment but could also reflect different parent body processes; further TEM studies could help to understand better the relationship between minerals coexisting and distinguish parent bodies from terrestrial weathering effects. However, despite the evident effects of alteration to which matrix is very susceptible, this work has also revealed evidence of a pristine nebular signature that still persists in the matrix such as the presence of amorphous silicates, possible enstatite whiskers, and reducing conditions.

Chapter 4

4. Grain Size Distribution

4.1 – Introduction

The dynamics of dust grains is driven by protoplanetary disk winds and magneto-rotational turbulence, causing small dust grains which are strongly coupled to the gas to be dragged upward with the up-flowing gas, while large grains remain near the mid-plane of a disk (Miyake et al., 2016). These processes might be reflected in the matrix of primitive meteorites where the size sorting of the matrix constituent should be recorded, but other nebular or parent body processes could obliterate these effects causing grains to either grow or be reduced in size if not totally destroyed.

Crystalline grain size distributions in chondritic porous (CP) interplanetary dust particles (IDPs) to which the matrix of primitive meteorites is often compared, was investigated by Wozniakiewicz et al., 2012. These particles, based on their isotopic compositions such as anomalous bulk N compositions, are thought to be of cometary origin (e.g. Floss et al., 2004), and therefore believed that they accreted in the outermost regions of the solar nebula. The two most abundant phases in CP-IDPs (Mg-rich silicates and Fe-rich sulfides) were found to be predominantly <0.25 μm in radius with a mean grain size variable between IDPs. From the study of Wozniakiewicz et al. (2012) it appeared evident that there was a size–density relationship between the silicates and sulfides suggesting that the particles experienced sorting prior to accretion. Samples from the Stardust mission to comet 81P/Wild 2 and CP-IDPs contain micron and sub-micron grains (Scott & Krot 2003; Brownlee et al., 2006; Zolensky et al., 2006; Nakamura et al., 2008; Bradley et al., 1988, 1989) whose mineralogy is consistent with that observed in some protoplanetary disks. There appear to be variations in the size distribution of crystalline grains within these disks, and in particular, a reduction in size with distance from the star (Van Boekel et al., 2004).

Considering that CP-IDPs, share similarities with the matrix of primitive meteorites, and that CP-IDPs exhibit evidence of pre-accretionary sorting (Wozniakiewicz et al., 2012) the size distribution of matrix constituents was investigated. Results obtained from the matrix of the 4 primitive meteorites studied were compared to the data available in literature, looking for evidence of pre-accretionary sorting and of parent body processes preserved in these matrix grains. Here, is described the abundances and size distribution of discrete grains of different phases (silicate vs. opaque) from within the matrix of four primitive meteorites: Acfer 094 (C2-ung.), ALHA77307 (CO3), MIL 07687 (C3-ung.) and QUE 99177 (CR2).

4.2 – Methods

Element maps acquired using the Zeiss EVO 15LS SEM were primarily used to provide a preliminary survey of the four samples (ALHA77307, MIL 707687, Acfer 094, QUE 99177) in order to select the matrix regions of interest away from the most altered sample's areas. Using the latest generation of SEMs capable of achieving high resolution, therefore more suitable for the study of fine grained material such as the FEI Quanta 650 FEG SEM, high-resolution element map of the matrix regions (approx. $25\times10\mu m^2$) were then mapped to provide high resolution element maps of the matrix regions, revealing the major element (Al, Ca, Fe, Mg, Si,) distributions. These element maps were used as a base for tracing shapes, on a transparent layer using Photoshop©, around the crystalline silicates (green and blue) revealed by the element maps (Fig. 4.2.1a & b). Comparison with SE maps helped to discriminate between a single grain and a group of grains. The surface areas (A) in μm^2 of the shapes traced around the silicates was calculated using Image J. On the basis that the grains were be assumed to be spherical, the radii (r) of the silicates crystals were calculated using the following formula: $r = (A/\pi)^{1/2}$. Values are reported in appendix Table 4.1 to 4.22.

Considering that the grain population was greatly represented by rounded crystals, assuming them to be spherical was thought to have a negligible impact on the results.

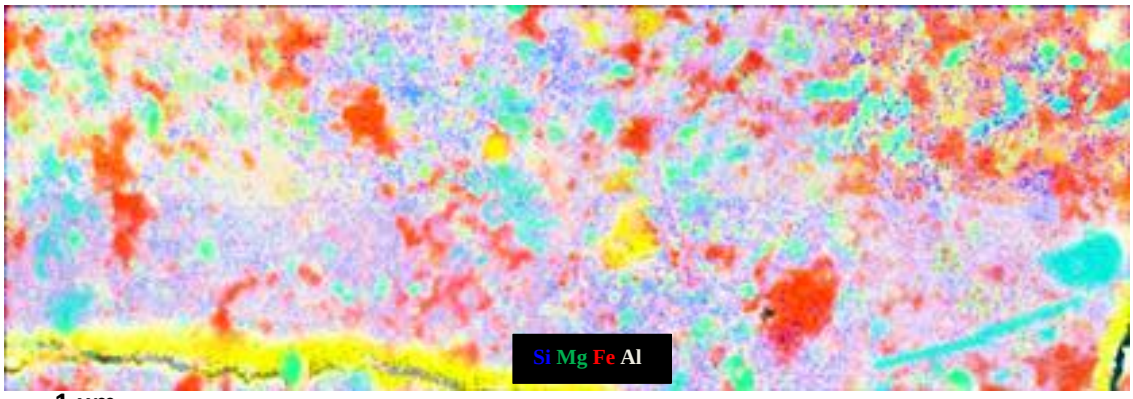

Fig. 4.2.1a

Fig. 4.2.1b

Fig. 4.2.1a - Element Map of ALHA 77307 Area 1 acquired with FEI Quanta Fig. 4.1b - Traced shapes around silicates phases (green and blue), revealed by element map, in sample ALHA77307 matrix area.

A slightly different approach was used to calculate the size of the opaque phases, using ultra-high resolution energy selective backscatter detector (EsB) images of matrix regions of interest using the FEG SEM Ultra Plus. The enhanced image quality that can be achieved with this instrument provides a good signal to noise ratio image and good contrast, making visible the fine contrast variations and enabling imaging at higher resolution. The portions of the image corresponding to the opaque phases are characterised by high intensity as the BSE intensity is a function of the average Z in the sample, i.e. larger atoms, with a greater atomic number, Z. The distribution of the grey scales values was examined

to select the range of values corresponding to the opaque phases (metal and sulfide, ranging from 255 to 160 depending on the area) see Fig. 4.2.2.

To improve accuracy the intensity histogram of the image was used to determinate the correct segmentation by isolating the region of the Gaussian to isolate (Fig. 4.2.2). The thresholded image that relates to the opaques phases was then used as a base for tracing shapes around the high intensity areas. Using Photoshop and applying the method described for the silicates the areas and radii of the opaque phases were calculated (Fig. 4.2.3b). The results are reported in appendix Table 4.23 to 4.71. The opaque phases did not show evidence of compositional grades or zonation within phases, therefore no bias is thought to be affecting the results due to the technique used.

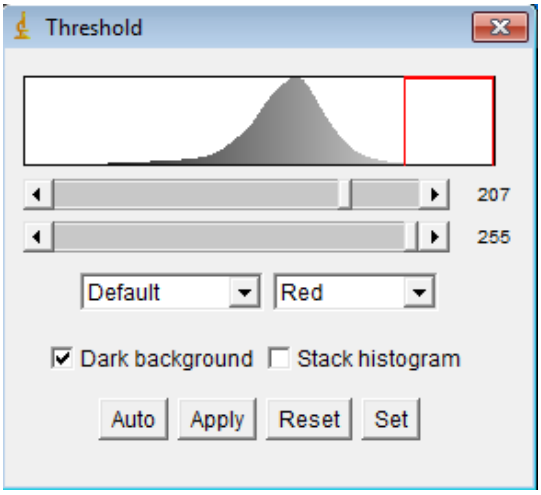

Fig. 4.2.2 - Threshold menu showing the Gaussian covering the whole range of pixels intensities, by moving the sliders were separated out the white pixels from the background.

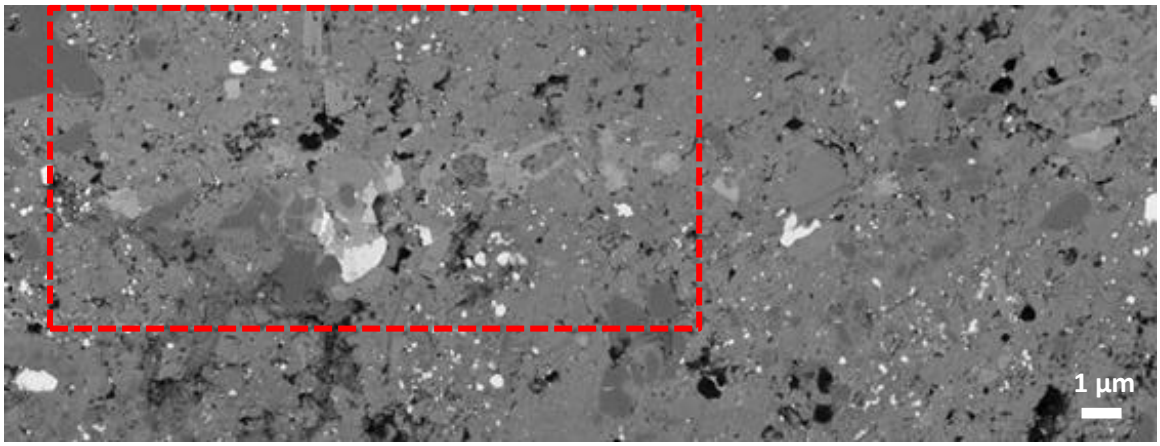

Fig. 4.2.3a

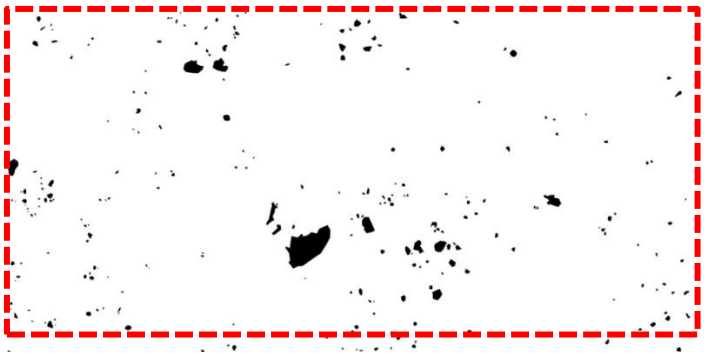

Fig. 4.2.3b

Fig. 4.2.3a - Image map of sample QUE99177 Area 2 acquired using the Ultra Plus.
Fig. 4.2.3b - Traced shapes around opaque phases thresholded within the dotted area of interest on Fig. 4.2.3a.

High definition EsB image maps acquired using the FEG SEM Ultra Plus were used to estimate the abundance of the opaques minerals present in the matrix on the basis of their different grey scale value using Image J (Fig. 4.2.3a&b).

The Ultra Plus scanning electron microscope is suitable for high-resolution imaging, as it features Energy selective Backscattered detector (EsB). This is capable of producing enhanced image quality, providing a good signal to noise ratio and good contrast. In order to obtain ultra-high resolution images maps of matrix regions, low accelerating voltage of 3.00 kV, and ~2.5mm working distance (WD) was used. These operating conditions, ideal for high resolution imaging, do not allow for the acquisition of analytical data, therefore the mineralogy based on the image map is uncertain. Each mineral phase displays a different intensity of EsB that depends on the average atomic density in the sample. The brighter phases in the EsB image contain the highest mass atoms and these generally relate to the most Fe-rich. On this basis, it is not possible to discern metal grains from iron-

sulfides, thus, mineralogical phases are given in grayscales, with the white phases, often referred to as opaque.

4.2a - Cumulative Frequencies, Geometric Mean and Standard Deviations

Kolmogorov–Smirnov (K-S) tests comparing the grain size distribution of CP-IDs has shown a statistically significant difference in the population of the silicate and sulfide. In order to quantify these differences Wozniakiewicz et al. (2012) have determined the mean and standard deviations of each data set and compared the data sets against cumulative distribution functions of possible fits.

In order to provide direct comparison to the IDP work of Wozniakiewicz et al., (2012), a similar approach was applied to the meteorite matrix grain-size data reported in this study. The cumulative frequency of the grains' radii was calculated and plotted against the natural log of the radius (Fig. 4.2.4).

Owing to the fact that size distribution profiles in the CP IDPs were best described by log-normal distributions, the geometric mean and standard deviation was used. Calculation of the mean radii (*Mr* in nm) and standard deviations (+σ and –σ in nm) were determined graphically from cumulative frequency distributions plotted as a function of ln(*r*), using the modified geometric Folk & Ward (1957) equations of Blott & Pye.

$$M_r = exp\left[\frac{lnP_{16}+lnP_{50}+lnP_{84}}{3}\right] \quad (4.1)$$

$$+\sigma = \exp\left[\ln M_r + \left(\frac{\ln P_{84}-\ln P_{16}}{4} + \frac{\ln P_{95}-\ln P_5}{6.6}\right)\right] - M_r \quad (4.2)$$

$$-\sigma = M_r - \exp\left[\ln M_r - \left(\frac{\ln P_{84}-\ln P_{16}}{4} + \frac{\ln P_{95}-\ln P_5}{6.6}\right)\right] \quad (4.3)$$

The values: P5, P16, P50, P84, and P95 are the grain sizes referring to the 5th, 16th, 50th, 84th, and 95th percentiles, respectively. The original geometric Folk & Ward equations were expressed logarithmically (in ϕ units) where phi (ϕ) values were ϕ= -log 2d, and d is the grain diameter in millimetres, a unit commonly employed in the field of sedimentology. Blott & Pye (2001) preferred statistics to be expressed geometrically (in metric units), and used equations 4.1, 4.2 & 4.3 to convert geometric mean and the standard deviation in nm units. The graphical method is commonly used in sedimentology and has also been applied previously to extra-terrestrial samples (e.g. chondrule measurements by Kuebler et al., 1999).

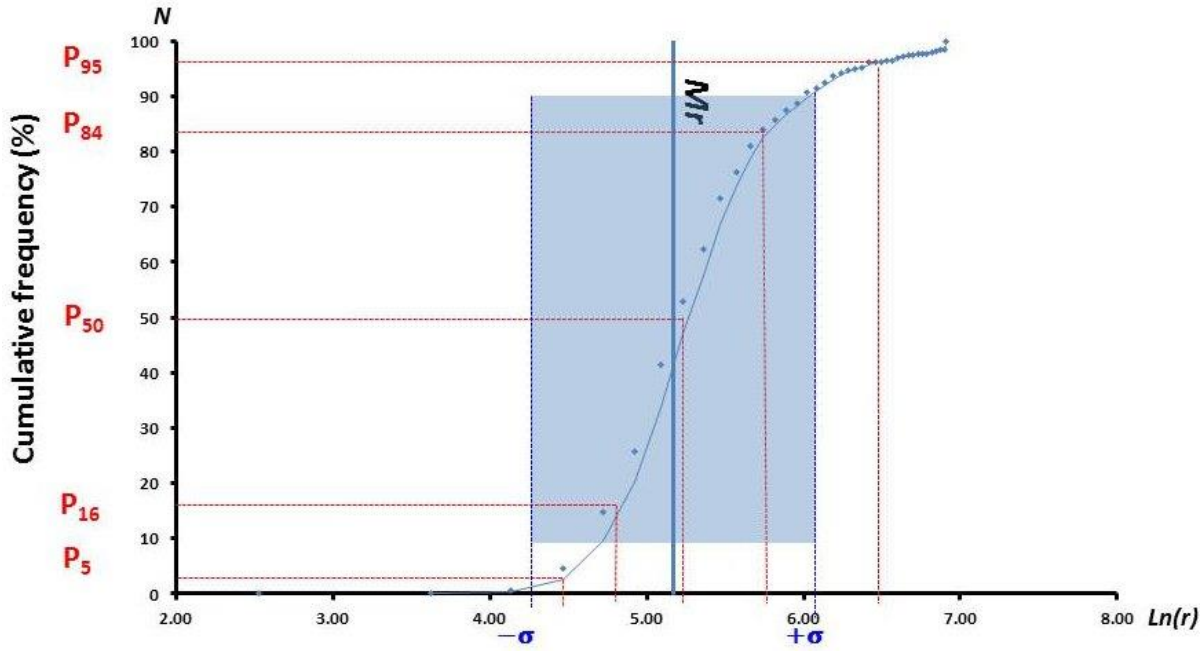

Fig. 4.2.4 –Example of cumulative frequency plotted as a function of ln(*r*), using the modified geometric Folk & Ward (1957) equations of Blott & Pye. This curve is only an example of the method used, and does not show results of data obtained in this work.

The solid line in Fig. 4.2.4 indicates the geometric mean radius which refers to the measure of the central tendency of a the radii's variability characterised by that distribution, while the shaded area surrounding represent the standard deviation about each mean, a quantity that expresses by how much the members of the group differ from the mean value for the group.

4.2b - 2D-3D correction

The grain size measured in the four thin sections and their distribution of observed random grain diameters might not closely reflect the size distribution of the hypothetical non-sectioned and polished grain of the un-prepared meteorite. Friedman (1958) determined that a fixed relationship existed between sieved and thin-section grain-size parameters and has expressed such relationship graphically. A correlation between sieve and thin-section grain-size analyses was established to enable the derivation from thin-section data the cumulative frequency curve which would have been obtained by sieving. It was found that the equation that expresses the correlation between sectioned and sieved grains was:

$$\mathbf{M_r\,(calc.) = 0.3815+0.9027M_r\,(thin\text{-}section)\ (4.4)}$$

We have applied the equation (4.4) to our data and calculated the corrected value for the M_r. Both corrected and uncorrected values were then plotted on a $M_{r\text{-}opaques}$ versus $M_{r\text{-}silicates}$ diagram (Fig. 4.2.5). The correction applied does not seem to significantly affect the position where our samples plot in the diagram.

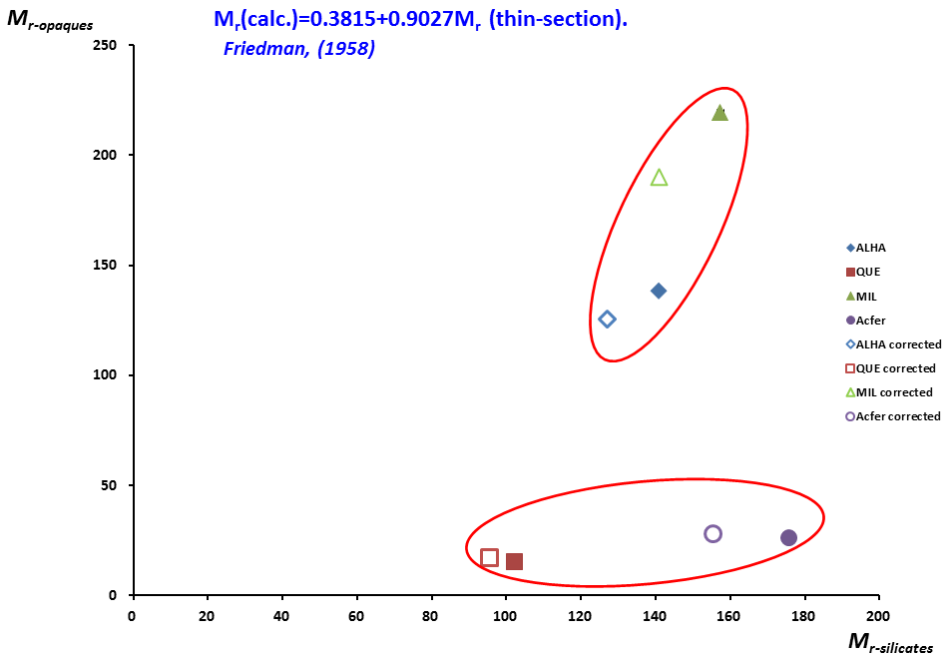

Fig. 4.2.5 - Diagram showing $M_{r\text{-}opaques}$ versus $M_{r\text{-}silicates}$ to consider the potential effects of sectioning bias. Plotted are uncorrected values obtained from five areas on each of the four samples (solid symbols) and corrected values (open symbols).

Owing to the fact that the grains making up the matrix of our meteorites are < 1µm and that Friedman's equation was determined on grain sizes several order of magnitude larger than the size of the matrix grains, it seems unlikely that grains of such a size are sectioned during the sample preparation. As a consequence most likely the conditions on which equation (3.4) was determined do not apply to the grains studied in this work. In addition, the correction applied did not produce a significant variation in the results obtained. For these two reasons this correction will not be applied to the results presented below.

4.3 - Result

In order to investigate whether the matrix components display differences in grain size distributions in the products of the metal + sulfide size-density consistent with grain sorting, the geometric mean radii (4.1) of the silicates are plotted against the geometric mean radii of the sulfides for samples ALHA77307, MIL 07687, QUE 99177, Acfer 094 and compared with CP-IDPs and comet 81P/Wild 2 (from Wozniakiewicz et al., 2013) (Fig. 4.3.1)

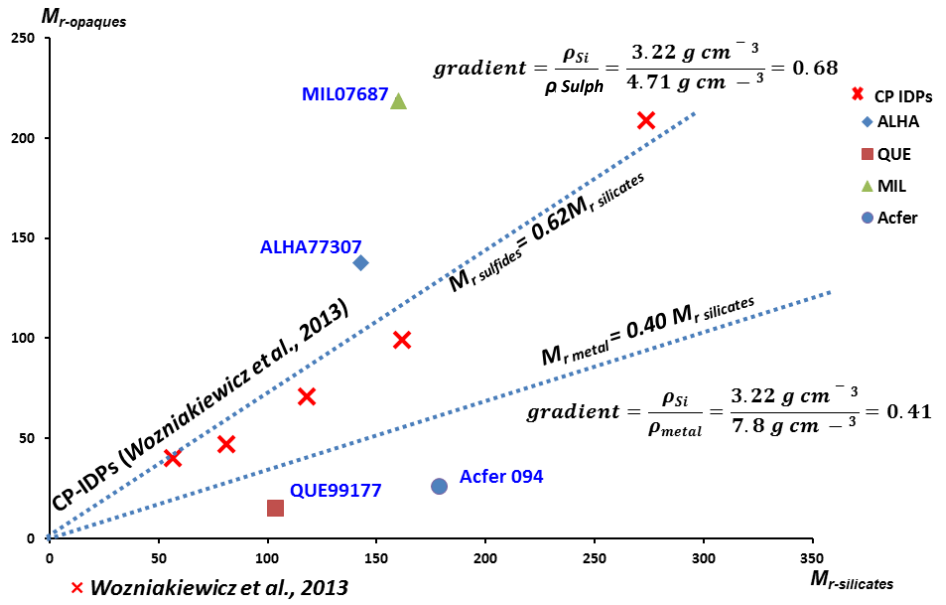

Fig. 4.3.1 - Diagram $M_{r\text{-}opaques}$ versus $M_{r\text{-}silicates}$ showing meteorite matrix data compared with that from CP-IDPs and Stardust grains (red crosses) reported by from Wozniakiewicz et al., 2013.

The geometric mean radii of matrix grains display a similar range of values for $M_{r\text{-silicates}}$ compared with that reported for IDPs. However, the matrix samples display a much larger range of values for $M_{r\text{-opaques.}}$ ALHA77307 and MIL07687 have $M_{r\text{-opaques}}$ values greater than the CP-IDPs while QUE 99177 and Acfer 094 have much lower $M_{r\text{-opaques}}$ values. While only based on two data points, the two grouping of matrix meteorites appear to define trends that are steeper (ALHA77307 and MIL07687) and shallower (QUE 99177 and Acfer 094) than that defined by the CP-IDPs (slope 0.6, equation 4.5) that may indicate two distinct populations.

Cumulative frequency (%) curve data

Despite the fact that the matrix components show considerably different means in the opaques size-density, which is not consistent with grain sorting, silicates and sulfides making up the matrix show significant differences in grain size distributions. Cumulative frequency distributions of silicate and sulfide grain sizes in the matrix of meteorites studied in this work are shown in Fig. 4.3.2a, b, c & d. Values are reported in appendix Table 4.72 to 4.80. Values of the mean radii (*Mr* in nm) and standard deviations ($+\sigma$ and $-\sigma$ in nm) are reported in Table 4.1. What appears obvious from the cumulative frequency curves is that the geometric mean radii of the grains (marked with solid lines) are similar for both silicates and sulfides grains in ALHA77307, and MIL 07687. For Acfer 094 and QUE 99177, while the geometric mean for the silicates is comparable to that in ALHA77307 and MIL 707687, the opaque phases have geometric mean values that are markedly smaller than the silicates. The standard deviations about the mean values, are indicated by shaded regions around each cumulative curve in Fig. 4.3.2a, b, c & d. The observed differences between the means of the opaque phases in the pair (ALHA77307 – MIL 707687) and the pair (Acfer 094 - QUE 99177) are very significant so that, each pair is distinguishable by the mean radii of its opaque phase populations.

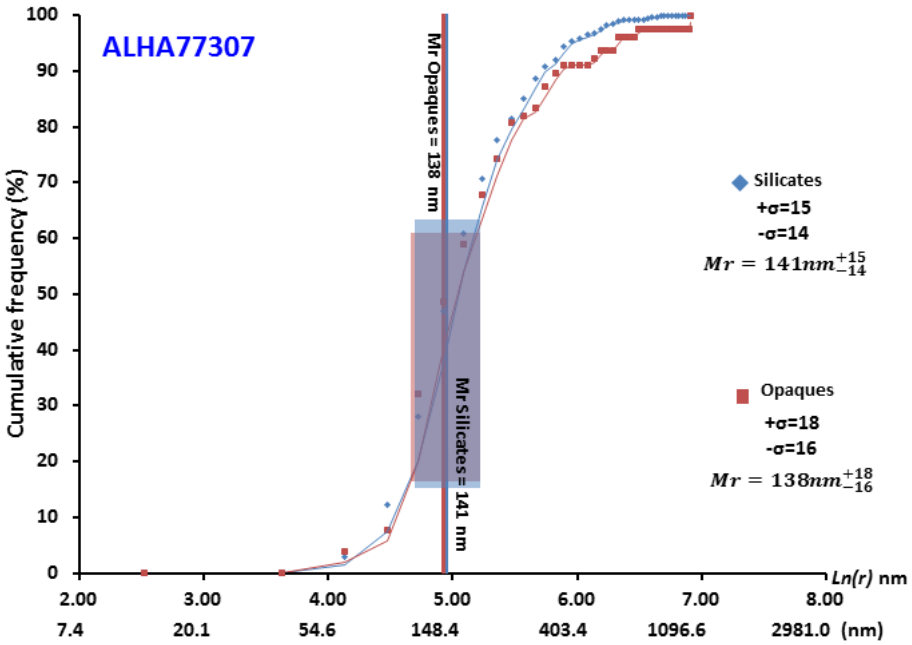

Fig. 4.3.2a

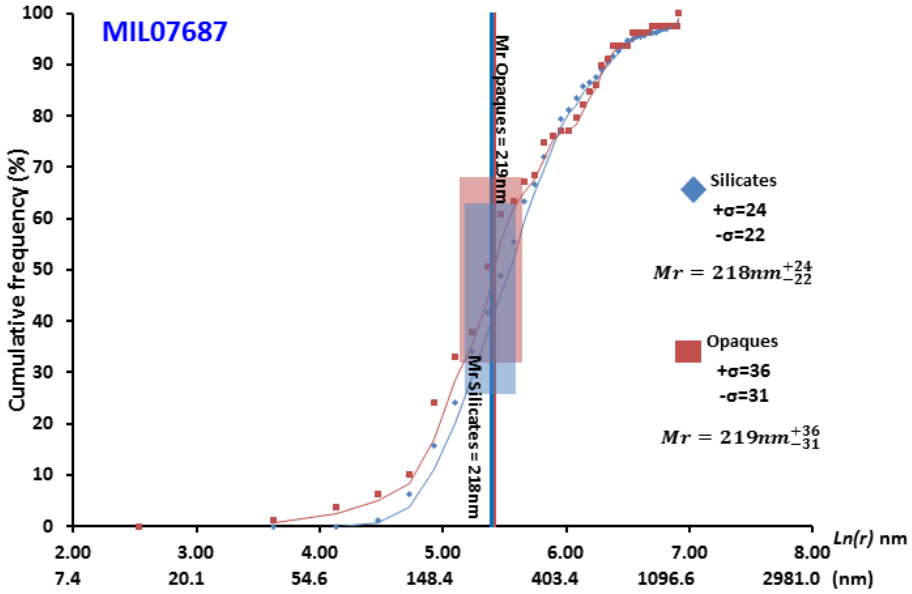

Fig. 4.3.2b

Fig. 4.3.2a - Cumulative frequency curves plotted as a function of ln(*r*) and fitted with a moving average of sample ALHA77307 using the modified geometric Folk & Ward (1957) equations of Blott & Pye. Cumulative frequency curves values are given in appendix Table 4.72 & 4.73 for the silicates phases, and in appendix Table 4.72 & 4.74 for the opaques. Geometric mean radii, and standard error on the mean values for all the samples are given in Table 4.1

Fig. 4.3.2b - Cumulative frequency curves plotted as a function of ln(*r*) and fitted with a moving average of samples MIL 07687 using the modified geometric Folk & Ward (1957) equations of Blott & Pye. Cumulative frequency curves data, are given in appendix Table 4.72 & 4.75 for the silicates phases, and in appendix Table 4.72 & 4.76 for the opaques.

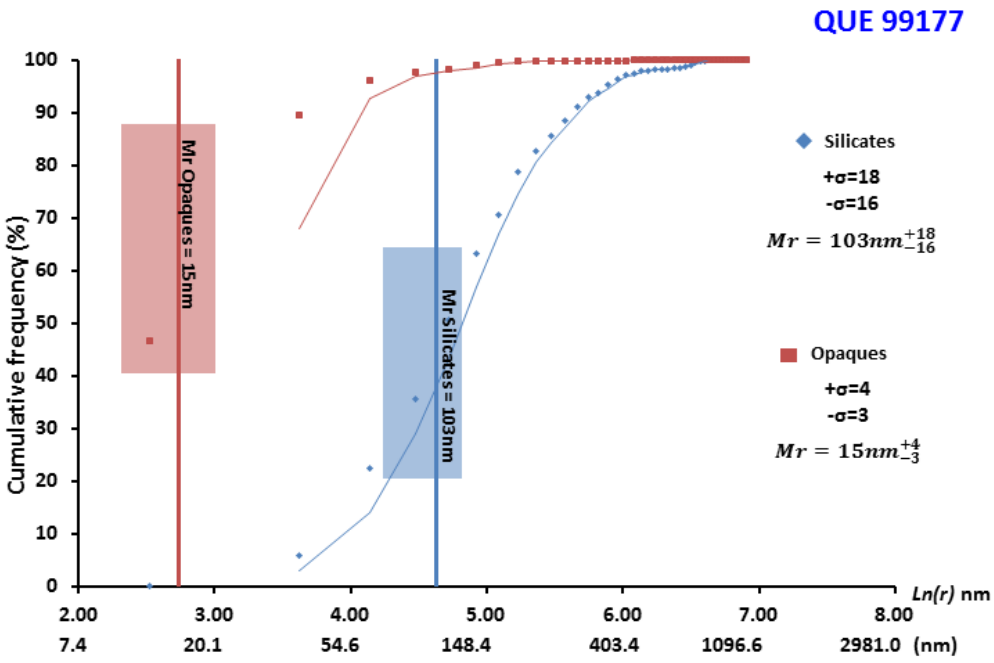

Fig. 4.3.2c

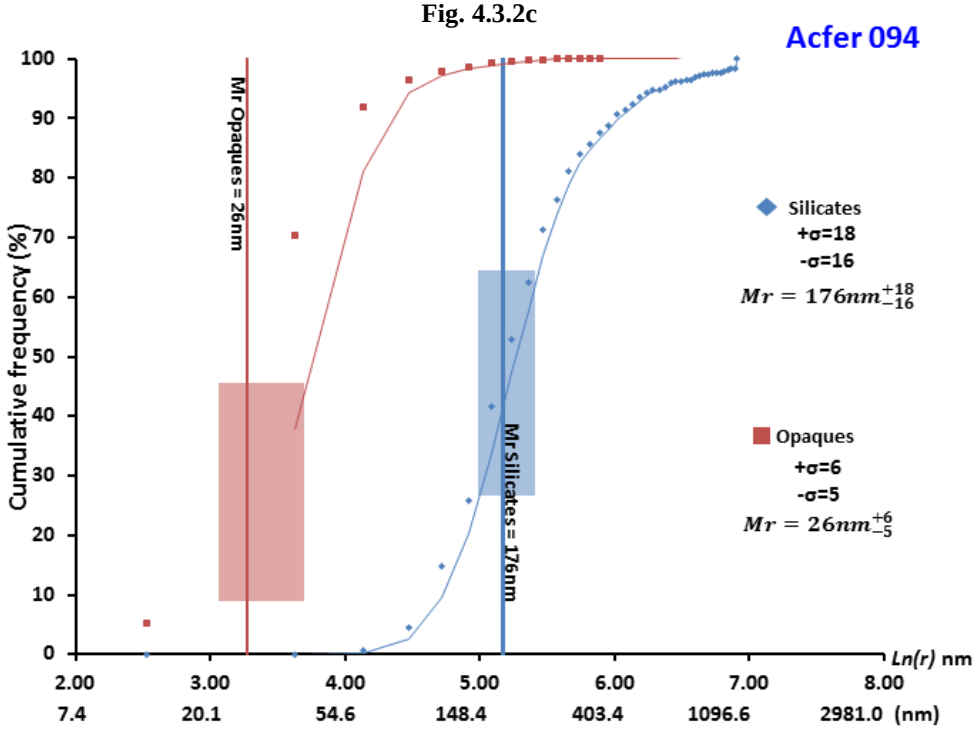

Fig. 4.3.2d

Fig. 4.3.2c - Cumulative frequency curves plotted as a function of ln(*r*) and fitted with a moving average of sample QUE 99177 using the modified geometric Folk & Ward (1957) equations of Blott & Pye. Cumulative frequency curves data are given in appendix Table 4.72 & 4.77 for the silicates phases, and in appendix Table 4.72 & 4.78 for the opaques. . Geometric mean radii, and standard error on the mean values for all the samples are given in Table 4.1

Fig. 4.3.2d - Cumulative frequency curves plotted as a function of ln(*r*) and fitted with a moving average of sample Acfer 094 using the modified geometric Folk & Ward (1957) equations of Blott & Pye. Cumulative frequency curves data are given in appendix Table 4.72 & 4.79 for the silicates phases, and in appendix Table 4.72 & 4.80 for the opaques.

ALHA77307	Silicates	Opaques
P95 (ln)	5.82	6.03
P84 (ln)	5.47	5.55
P50 (ln)	4.92	4.90
P16 (ln)	4.45	4.34
P5 (ln)	4.16	4.05
Mr (nm)	**141**	**138**
(+σ)	**15**	**18**
(-σ)	**14**	**16**

MIL 07687	Silicates	Opaques
P95 (ln)	6.42	6.40
P84 (ln)	5.93	6.29
P50 (ln)	5.41	5.26
P16 (ln)	4.82	4.63
P5 (ln)	4.54	3.86
Mr (nm)	**218**	**219**
(+σ)	**24**	**36**
(-σ)	**22**	**31**

QUE 99177	Silicates	Opaques
P95 (ln)	5.83	4.06
P84 (ln)	5.36	3.43
P50 (ln)	4.67	2.54
P16 (ln)	3.86	2.23
P5 (ln)	3.36	2.11
Mr (nm)	**103**	**15**
(+σ)	**18**	**4**
(-σ)	**16**	**3**

Acfer 094	Silicates	Opaques
P95 (ln)	6.14	4.41
P84 (ln)	5.66	3.91
P50 (ln)	5.14	3.25
P16 (ln)	4.71	2.65
P5 (ln)	4.37	2.38
Mr (nm)	**176**	**26**
(+σ)	**18**	**6**
(-σ)	**16**	**5**

Table 4.1 - Geometric mean radii, standard deviation values on the mean for silicates and opaque phases for samples ALHA77307, MIL 07687, QUE 99177 and Acfer 094.

Grain size distribution - histograms

In order to better investigate the differences observed in the geometric mean radii described in the preceding paragraph, graphical representations of the distribution of the radii for both the silicate and the opaque phases for the four meteorites are shown in Fig. 4.3.3 a, b, c & d. The radii were binned into a series of consecutive, non-overlapping intervals of 25nm, showing how many values fall into each interval. This provides a better understanding of the density of the underlying distribution of the radii of the particles. Values are reported in appendix Table 4.73 to 4.80. Similarly to what it was described for the geometric means from the cumulative frequency curves, it can be observed that ALHA77307 and MIL 07687 exhibit similarities between them. In the histogram this is reflected in the distribution of the radii for both the silicate and the opaque phases, with the number of silicates being considerably higher than the number of the opaques.

The geometric means of the pair Acfer 094 - QUE 99177 also, shows similarities, and in these histograms this is expressed by a much narrower distribution profile of the opaque phases compared to the distribution of the accompanying silicates phases. The geometric

means in this pair also show how the opaques are shifted towards smaller size compared to the opaque present in matrix of the pair ALHA77307 – MIL 07687.

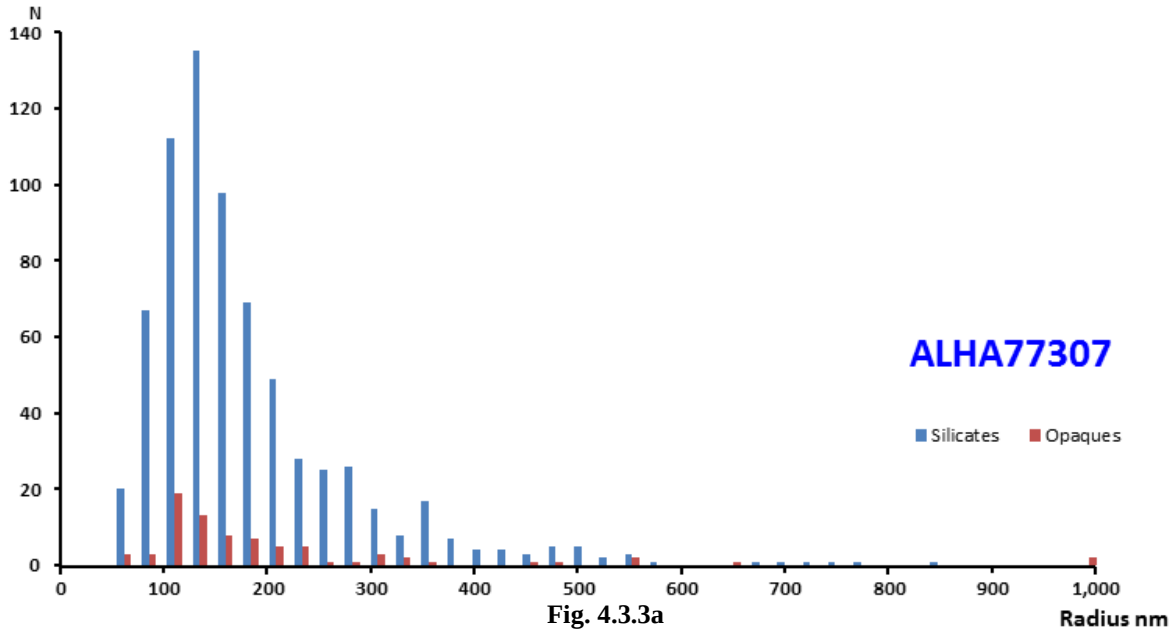

Fig. 4.3.3a

Fig. 4.3.3a - Histogram showing distribution of the radii for both the silicate and opaque phases for sample ALHA77307.

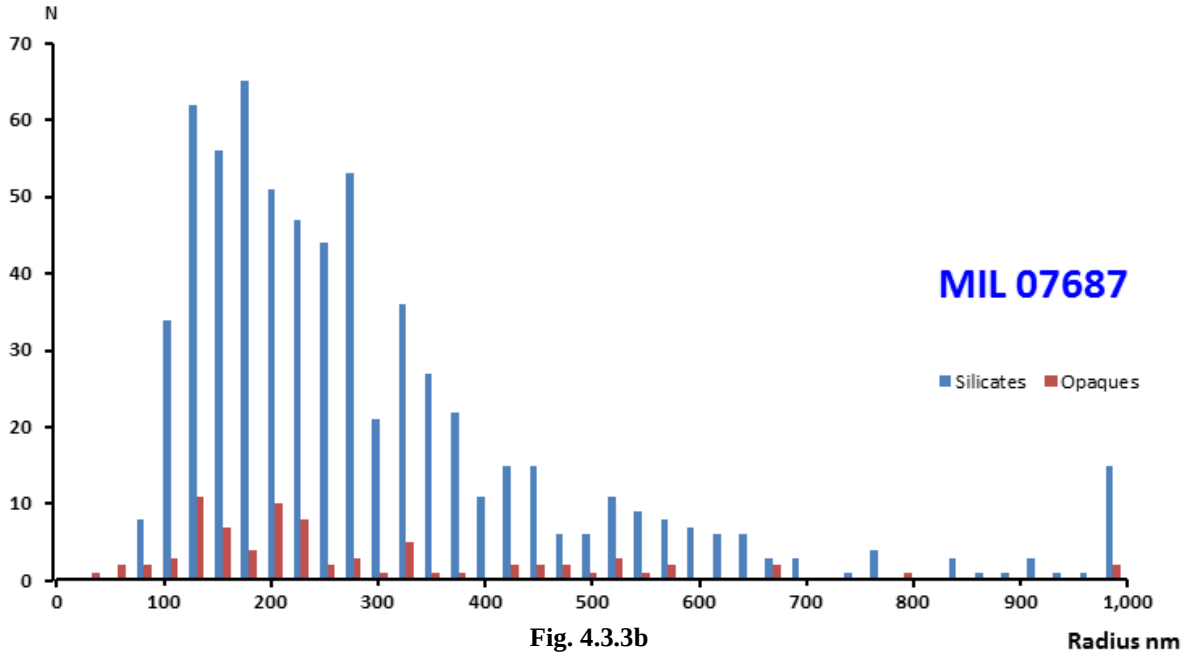

Fig. 4.3.3b

Fig. 4.3.3b - Histograms showing distribution of the radii for both the silicate and opaque phases for sample MIL 07687.

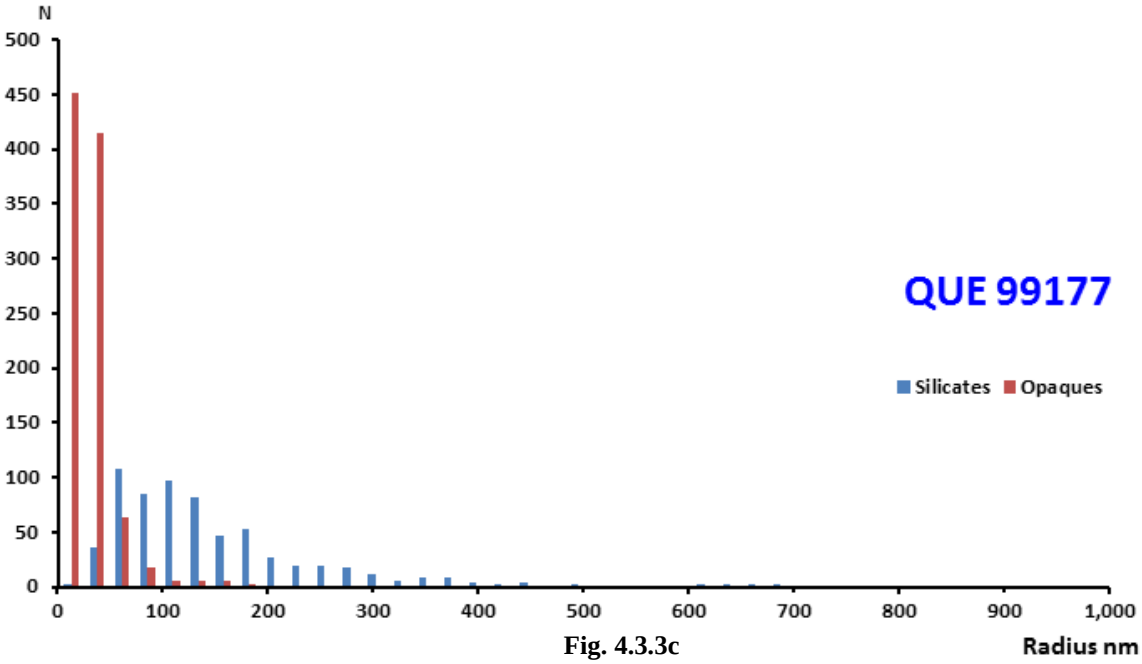

Fig. 4.3.3c

Fig. 4.3.3c - Histograms showing distribution of the radii for both the silicate and opaque phases for sample QUE 99177.

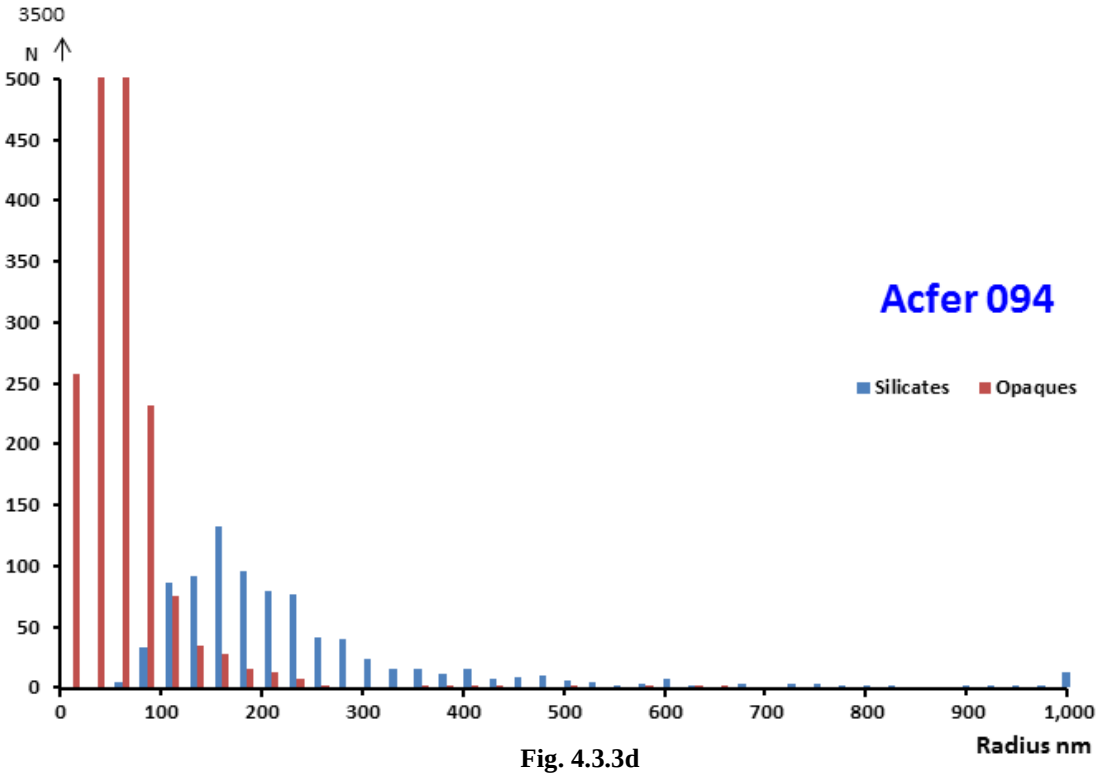

Fig. 4.3.3d

Fig. 4.3.3d - Histograms showing distribution of the radii for both the silicate and opaque phases for sample Acfer 094.

4.4 - Discussion

Aerodynamic sorting and Comparison with IDPs

Previous studies, now generally accepted, have shown that the constituents of chondritic meteorites such as silicates, sulfides, and metal grains that were aerodynamically equivalent have the same mean size–density product, as a consequence of a sorting mechanism that took place prior to accretion (Kuebler et al., 1999). The gas dynamics model is one of several natural processes evoked to explain the aerodynamic sorting of the large grains in chondritic meteorites proposed by Clayton (1980). According to this model particles travelling in a medium of gas, owing to the force resisting the relative motion of solid surfaces, experience a reduction in the speed as they penetrate the medium. This resisting force and the consequential speed reduction, depends on the size and density of the particles. Therefore chondritic meteorite constituents moving in a turbulent medium, bonding to the gas due to the particle's density, settle at different speeds. Turbulence in the disk could also be responsible for the segregation of grains of a certain size, comparable to the size of the matrix constituents, and density in areas of the disk characterised by low-vorticity as proposed by Cuzzi et al. (2008). These chondritic constituents then could have been accreted in rocky bodies in the asteroid belt region of the protoplanetary disk, between 2 and 4 AU, preserving the characteristic sorted size that is observed in the chondritic meteorites.

Shu et al. (1997) proposed another mechanism of aerodynamic sorting activated by the bipolar outflows, where grains settle onto the accretionary disk after being transported in a medium having negligible opposition to the flow above the plane of the protoplanetary disk. Smaller and/or less dense grains settle at larger heliocentric distances (Liffman 2005). CP-IDPs and comet 81P/Wild 2 studied by Wozniakiewicz et al. (2013) have shown significant differences in grain size distributions of the sulfides, which does not contain any logical contradiction with grain sorting. However, these aerodynamic sorting models

only apply to grains several orders of magnitude larger than CP IDPs, and only appear to be applicable to chondrules and other similarly sized components in chondritic meteorites and at heliocentric distances comparable with the region where the asteroids accreted. The size difference between CP-IDPs and chondritic components is considerable and, therefore, if the grains in CP-IDPs or comet 81P/Wild 2 had experienced the same sorting mechanism as chondritic components they would have been tightly bound to the gas, prohibiting any sorting. For these reasons it appears unlikely that the fine grains in CP-IDPs were subjected to the same sorting mechanism as that experienced by chondrules and other larger chondritic components.

The overall mineralogy of CP-IDPs indicates that they are likely cometary in origin, and therefore that the grain sorting they experienced occurred in the comet-forming region where lower gas density would have made the gas-particle bonding less effective. However, the conditions operating at the early stage of formation of the Solar System in the protoplanetary disk are poorly understood, and whether these sorting mechanisms could have been effective enough to produce these effects on such small sized grains is not clear yet (Wozniakiewicz et al., 2012). Wozniakiewicz et al. (2012) reported that the geometric mean radii (formula 4.1) of the CP-IDPs and comet 81P/Wild 2 silicate grains plotted against the geometric mean radii of the sulfides for each sample in Fig. (4.3.1) plot along a trend line that satisfies the equation:

$$\mathbf{M_{r\ sulfide} = 0.62 M_{r\ silicate}} \quad \mathbf{(4.5)}$$

The slope of this trend line is approximately equal to the ratio of the average silicate to sulfide densities. The most common silicates observed in CP-IDPs are low-Fe (Fe <5 atomic %) enstatite ($MgSiO_3$) and forsterite (Mg_2SiO_4), and sulfides are predominantly pyrrhotite (Bradley, 2003). A similar mineralogy is reported for comet 81P/Wild 2 (Zolensky et al., 2006). Assuming densities of 3.22 g cm^{-3} for the silicates (mid-point of forsterite and enstatite densities; Deer et al. 1992) and 4.71 g cm^{-3} for the sulfides (mid-

point of range of possible Ni-free pyrrhotite ($Fe_{1-x}S$) densities; Deer et al., 1992), the ratio of silicate to sulfide densities is approximately 0.68 (within 10% of the observed weighted trend). Thus, Wozniakiewicz et al. (2012), concluded that the product of the radius and density of the grains was approximately equivalent between silicates and sulfides in all of these cometary samples. The meteorite matrix samples reported here in contrast plot away from the line defined by the CP-IDPs (equation 4.5).

In terms of chemical composition, the silicate grains of the matrix constituents are similar to CP IDPs and comet 81P/Wild 2, enstatite ($MgSiO_3$), forsterite (Mg_2SiO_4), and chondrules in the same meteorite. In contrast, the opaque components of the matrix, show differences from the sulfides observed in the cometary particles, which are characterised by the presence of only Ni-free pyrrhotite, as the opaque component of the matrix of the four meteorites are primarily metal and Ni-bearing sulfides (e.g. see Fig. 4.5.3). The density of the opaques in the matrix is therefore different from the density of the Ni-free sulfides present in CP-IDPs, and the response of the particles to the sorting mechanism could potentially be different. Any difference could be expressed by a different trend line in the diagram $M_{r\text{-opaques}}$ versus $M_{r\text{-silicates}}$. If the opaque components in the matrix of the meteorites were only represented by the presence of metal, assuming densities of 7.8 g cm^{-3} , while the silicates were 3.22 g cm^{-3} (mid-point of forsterite and enstatite densities; Deer et al., 1992) the ratio densities of silicate to metal is approximately 0.41, that can be expressed as the equation

$$\mathbf{M_{r\ metal} = 0.40 M_{r\ silicate}} \quad \mathbf{(4.6)}$$

Equation 4.6 could describe the expected trend line of the sets of point where the meteorites matrix results would plot if the grain size distribution were the result of grain sorting. However, the matrix of the meteorites investigated, here actually contains opaque phases that are a mixture of metal grains and Ni-bearing sulfides. If the matrix grains were showing evidence of aerodynamic sorting taking place prior to accretion, it would be

expected that the meteorites matrix samples, should plot somewhere in between the two trend lines expressed by equations (5) and (6). Owing to the fact that none of the four meteorites matrix samples plot within the region defined by the equations suggests that the size distribution of the matrix constituents are not the result of pre-accretionary sorting. However, meteorites parent bodies experienced considerably more heating and/or alteration processes as a result of liquid water than are likely to have occurred on the cometary parent bodies of CP-IDPs and therefore it may be that the size distributions observed in the meteorite matrix have been modified on the parent asteroid(s) and that evidence for sorting in the disk has been destroyed.

Evidence of alteration

It appears evident from the geometric means on the frequency curves and from the graphical representations of the particle radii distributions that the main distinctive feature distinguishing the two meteorite pairs is given by the different distribution of the grain size and different geometric means of the opaque phases. In an attempt to understand the dissimilarities shown by the matrix, in the form of different opaque present, the high resolution image maps acquired using the Ultra Plus (see chap. 2) were carefully examined. These reveal that the matrix of samples ALHA77307 and MIL 07687 have experienced more pronounced alteration than QUE 99177 and Acfer 094.

ALHA77307 – The image map of the matrix of this meteorite (Fig. 4.4.1a, b) shows a limited presence of opaques (white Phases in EsB images) and these are of relatively large size, whereas nano-sized opaque grains are not visible. The matrix is also characterised by the abundant presence of another relatively high Z (pale grey) phase (Fig. 4.4.1b, c) which seems to be the product of alteration of the opaques. The element maps acquired by the FEI Quanta (see chap.2) (Fig. 4.4.1d) is a Fe-rich phase, consistent with an origin as alteration of the opaque phase, and is probably an iron oxide.

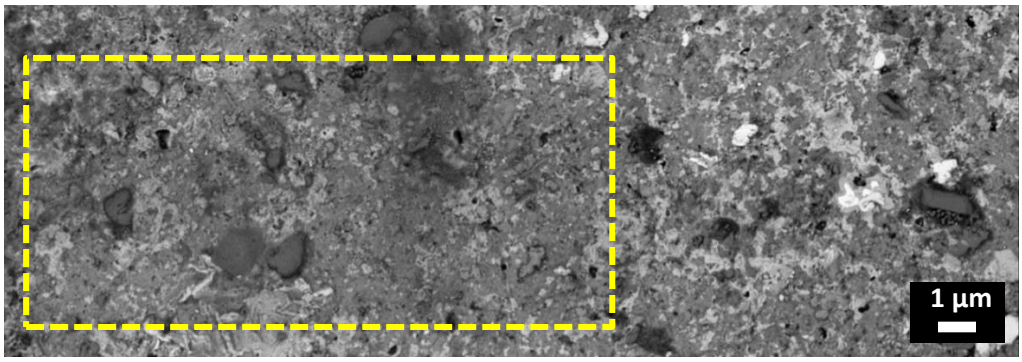

Fig. 4.4.1a

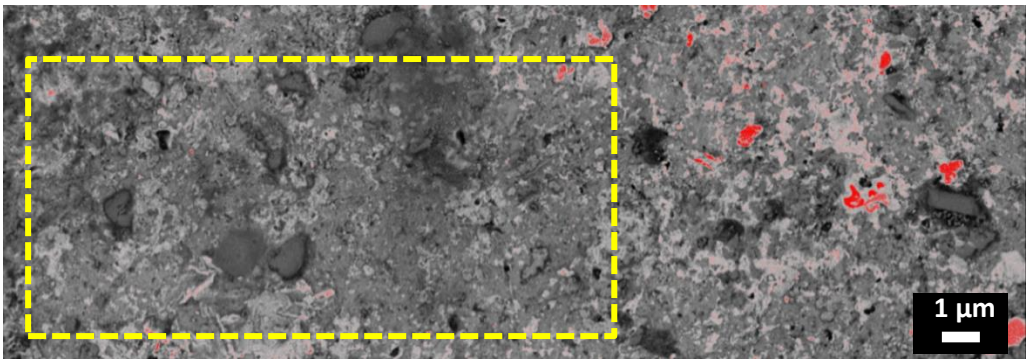

Fig. 4.4.1b

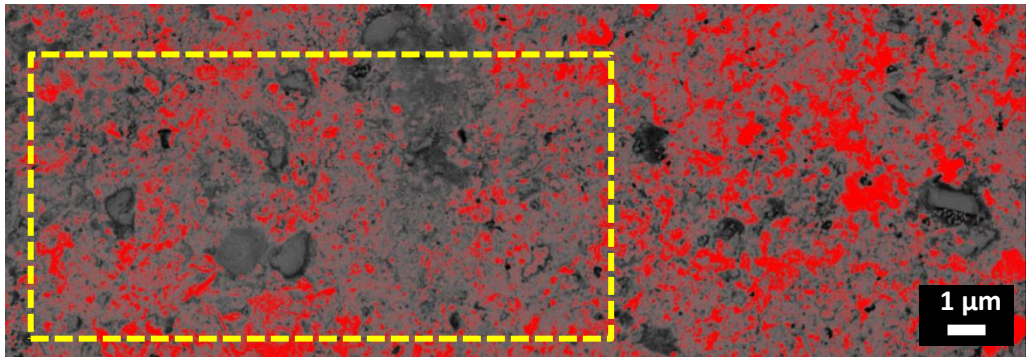

Fig. 4.4.1c

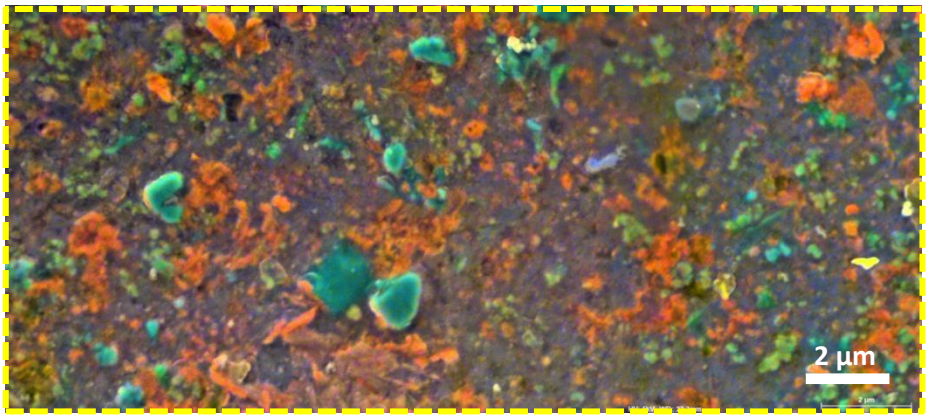

Fig. 4.4.1d

Fig. 4.1.1a - Image map of ALHA77307 Area 1 matrix acquired with the Ultra Plus, showing the limited presence and relatively large size of opaque phases (brightest features). Fig. 4.4.1b - Thresholding of the brightest phases using Image J emphasises the size and abundance of opaques. Fig. 4.4.1c - Thresholding of the pale grey phase using Image J emphasises the abundance of a Fe-rich phase that seems to be the product of alteration of the opaques. Fig. 4.4.1d - Element map of ALHA77307 Area 1 matrix acquired with the EI Quanta, showing the Fe-rich composition of the pale grey phase thresholded in Fig. 4.4.1c.

MIL 07687 - The matrix of the sample MIL 07687 shows evidence of partial and localized aqueous alteration characterised by a fibrous FeO-rich phase that electron diffraction data suggests is ferrihydrite or akaganeite (see chapter 3). The matrix of MIL 07687 is texturally complex and consists of highly irregular-shaped regions, with distinct contrast in EsB images (Fig. 4.4.1c). Brearley (2013) has shown that at TEM scale, the FeO-rich regions advance and encompass the FeO-poor regions "dendritically" with a high abundance of a fibrous phase randomly oriented. Based on the opaque grain morphology and the intimate association with the fibrous phases, it was also suggested that the FeO-rich matrix appears to be the result of alteration of precursor matrix by a percolating Fe-rich fluid, from which the fibrous phase deposited. The FeO-poor regions of the matrix on the other hand represent the original, relatively unaltered matrix (see chapter 3) which escaped the heavy aqueous alteration and appears now locally preserved. The boundary between the two different types of matrix is clearly defined by the high concentration of Fe oxides outlining a very distinctive alteration front (Fig. 4.4.1a & b,c) implying that the availability of water was highly localised, and not evenly distributed throughout the rock (Brearley, 2013). The EsB image maps of the matrix of this meteorite (Fig. 4.4.3a, b, c and Fig. 4.4.4a, b, c) similarly to ALHA77307, also show a limited abundance of opaques (white phases in EsB images) and dominance of relatively large size, and the lack of nano-sized opaque grains. The matrix in this sample is also characterised by the abundant presence of the ferrihydrite phase (the relatively high Z, pale grey phase).

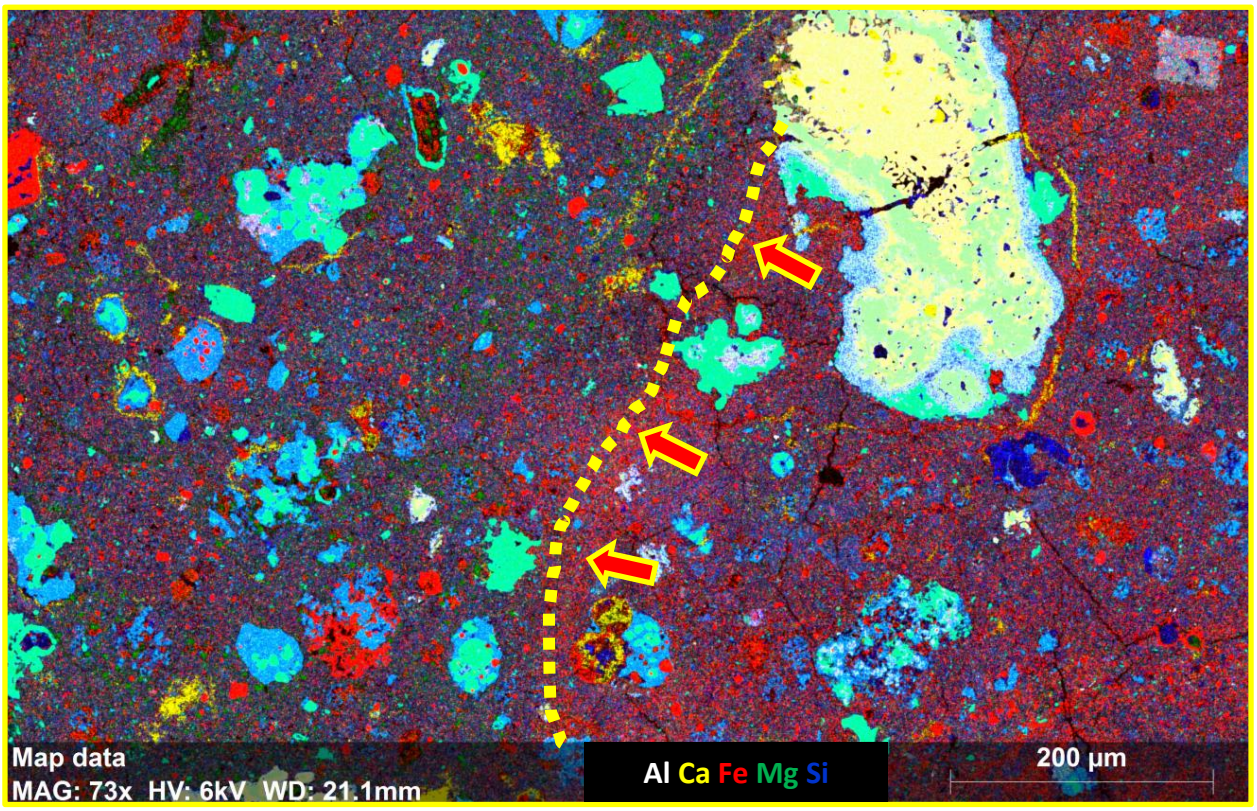

Fig. 4.4.2a

Fig. 4.4.2a - Element map of sample MIL 07687 acquired using FEI Quanta, showing a matrix region characterised by a clearly defined boundary between the two different types of matrix. Fig. 4.4.2b Element map of MIL 07687 acquired using the EVO. Fig. 4.4.2c BSE image map of sample MIL 07687 acquired using the EVO, showing the presence of Fe-rich (brighter), and Fe-poor (darker) matrix having different contrast.

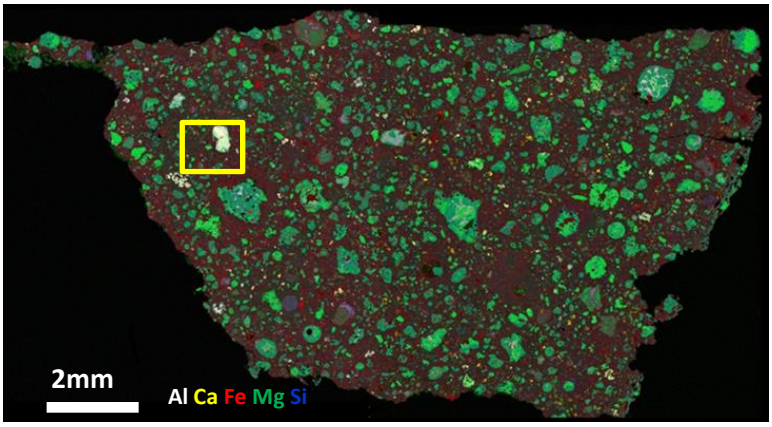

Fig. 4.4.2b

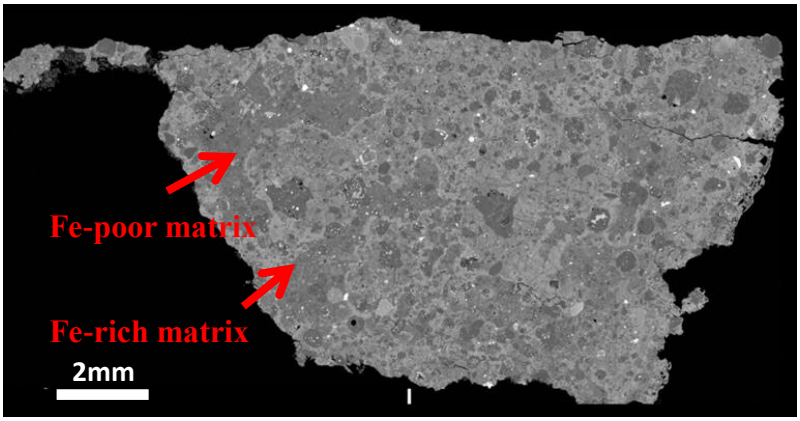

Fig. 4.4.2c

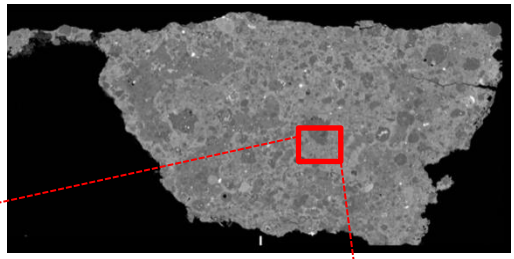

Fig. 4.4.3a

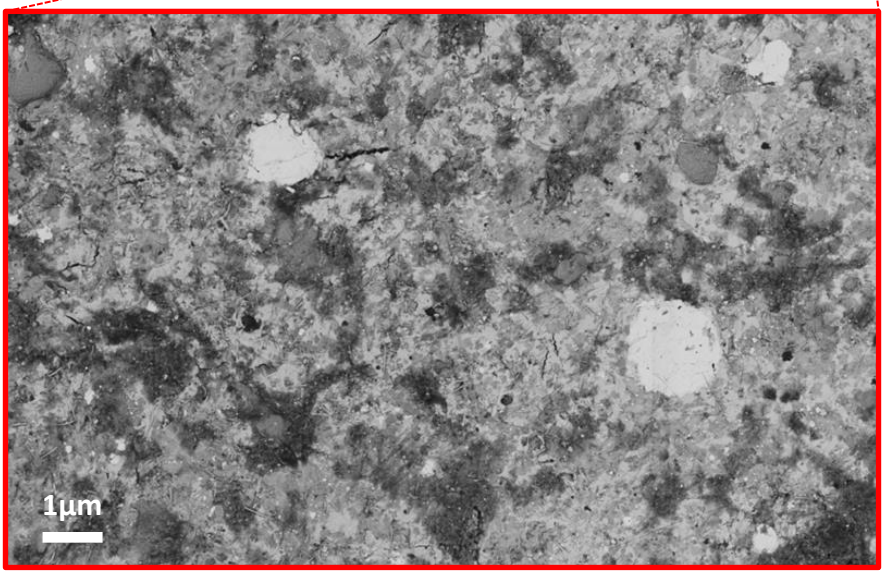

Fig. 4.4.3b

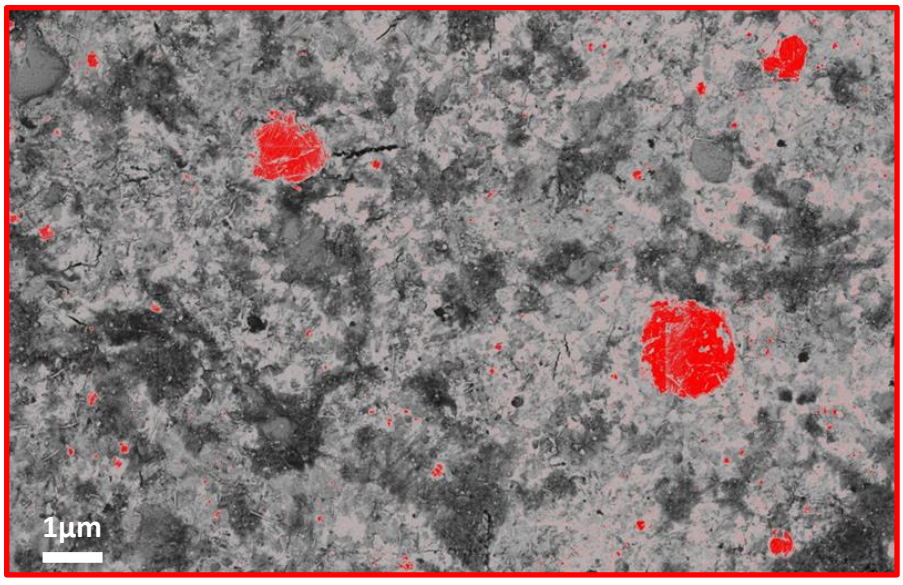

Fig. 4.4.3c

Fig. 4.4.3a - EsB image map of MIL 07687 acquired using the EVO. Fig. 4.4.3b Matrix image map of MIL 07687 Area 1 acquired with the Ultra Plus, showing evidence for aqueous alteration and limited presence and relatively large size of opaque phases. Fig. 4.4.3c Thresholding of the white phases of same area using Image J emphasizing the size and abundance of opaques

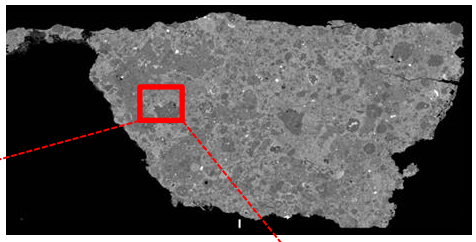

Fig. 4.4.4a

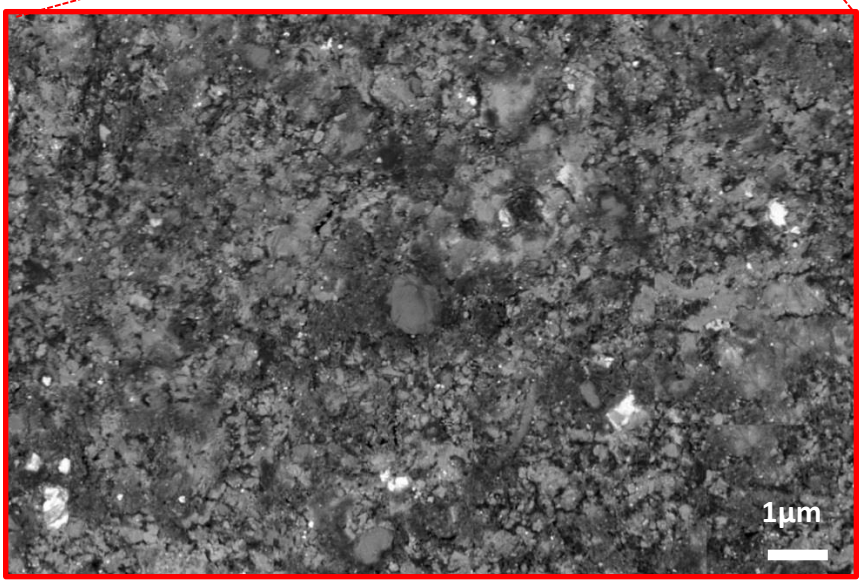

Fig. 4.4.4b

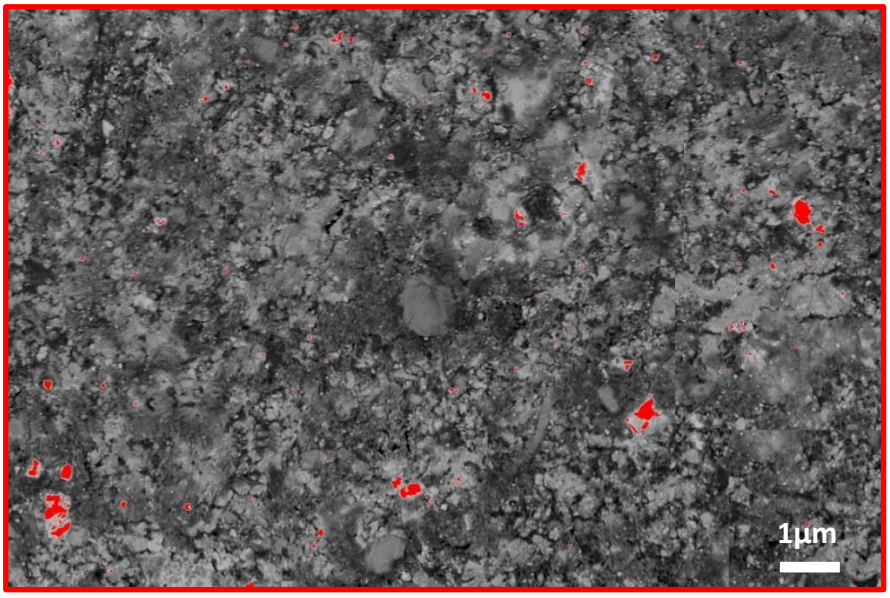

Fig. 4.4.4c

Fig. 4.4.4a - EsB image map of MIL 07687 acquired using the EVO. Fig. 4.4.4b Matrix image map of MIL 07687 Area 5 acquired with the Ultra Plus, showing little evidence of aqueous alteration and also limited presence and of relatively large size of opaque phases. Fig. 4.4.4c Thresholding of the white phases of same area using Image J emphasizing the size and abundance of opaques

In contrast to ALHA77307 and MIL 07687, where the matrix is characterised by a lack of nano-sized opaque phases, the matrix of QUE 99177 and Acfer 094 show a distinctive presence of opaque phases of nano-size as shown by Fig. 4.4.5a & b and, Fig. 4.4.6a & b. This considerably different occurrence of opaque phases in the matrix of the four samples, in terms of size and abundance, appears to be the main distinct feature responsible for producing, in the diagram $M_{r\text{-opaques}}$ versus $M_{r\text{-silicates}}$, the two pairs ALHA77307 – MIL 07687 and Acfer 094 – QUE 99177. Based on combined observations of the EsB and element maps that were acquired, it appears that the lack of nano-opaques that distinguish the matrix of the pair ALHA77307 - MIL 07687 is the result of more pronounced alteration that attacked the nano-phases and dissolved them into a secondary Fe-bearing oxide phase observed today in the matrix. The sample MIL 07687 shows obvious evidence of parent body aqueous alteration (Brearley, 2013). The XRD investigation (see chapter 3) of the Fe-poor region of the matrix described as relatively unaltered also shows evidence of alteration which might be attributed to terrestrial weathering. A parent body origin for the alteration observed in the sample ALHA77307 cannot be ruled out, yet is not as obvious as in MIL 07687, and an Antarctic weathering effect appears to be the likely source.

Although the samples for this work were selected on the basis of their pristinity, given the presence of amorphous silicates and presolar grains in the matrix indicating that they did not experienced major parent body processes, they obviously did not entirely escape aqueous alteration. Moreover, the matrix given its porous nature, that easily allows fluid percolation, is particularly susceptible to alteration which is present in every meteorite, even among the ones regarded as the most pristine. In addition to that, aqueous alteration and terrestrial weathering have affected different meteorites to different degrees, and the effects of these processes are reflected in the results of this study.

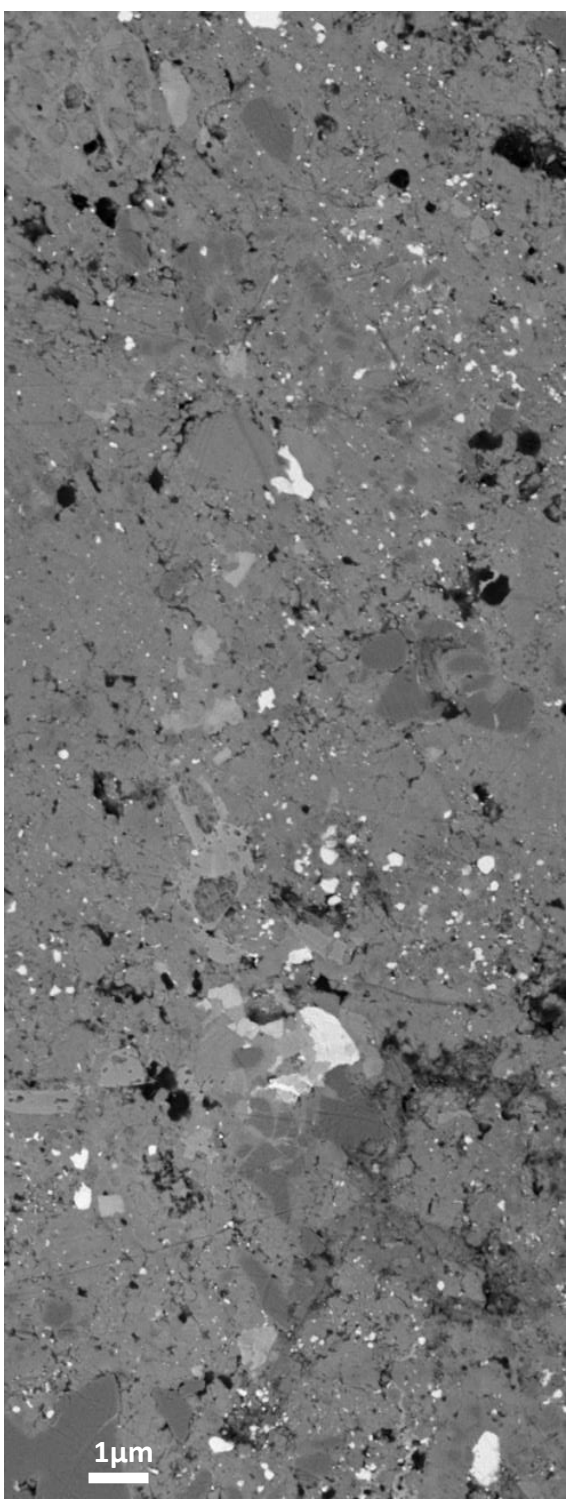

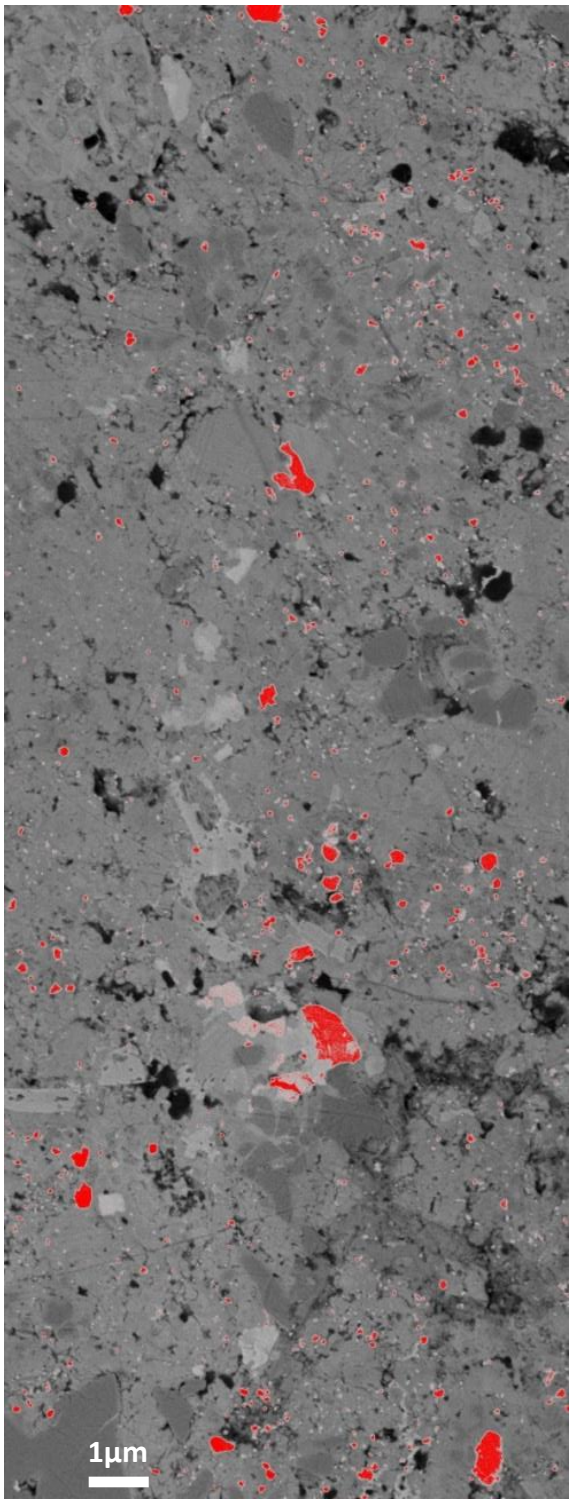

Fig. 4.4.5a **Fig. 4.4.5b**

Fig. 4.4.5a - Image map of QUE 99177 Area 2 acquired with the Ultra Plus, showing the presence of opaque phases of different size. Fig. 4.4.5b - Thresholding of the white phases of same area using Image J emphasizing the different size and abundance of opaque phases

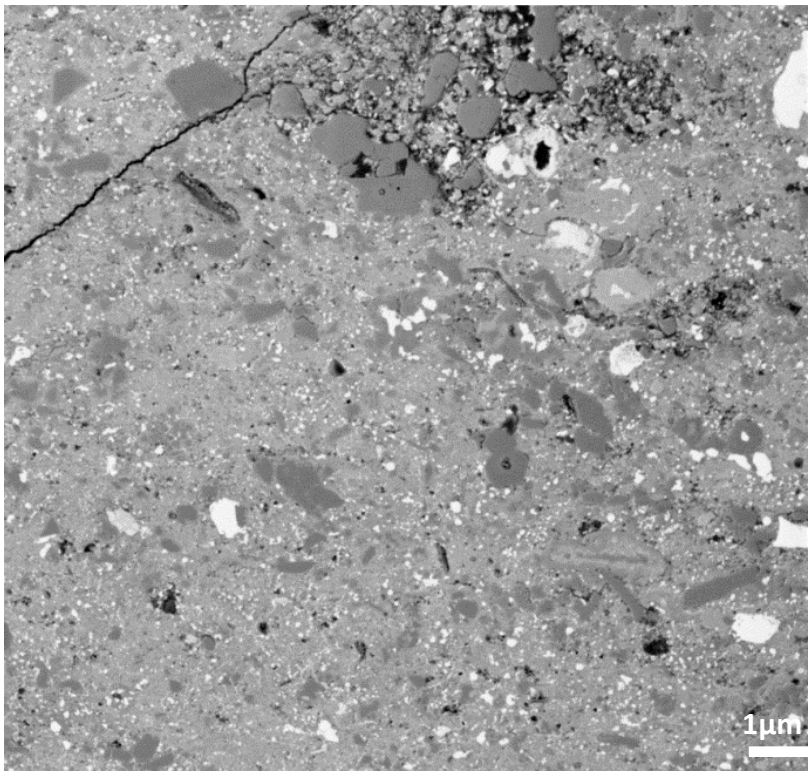

Fig. 4.4.6a

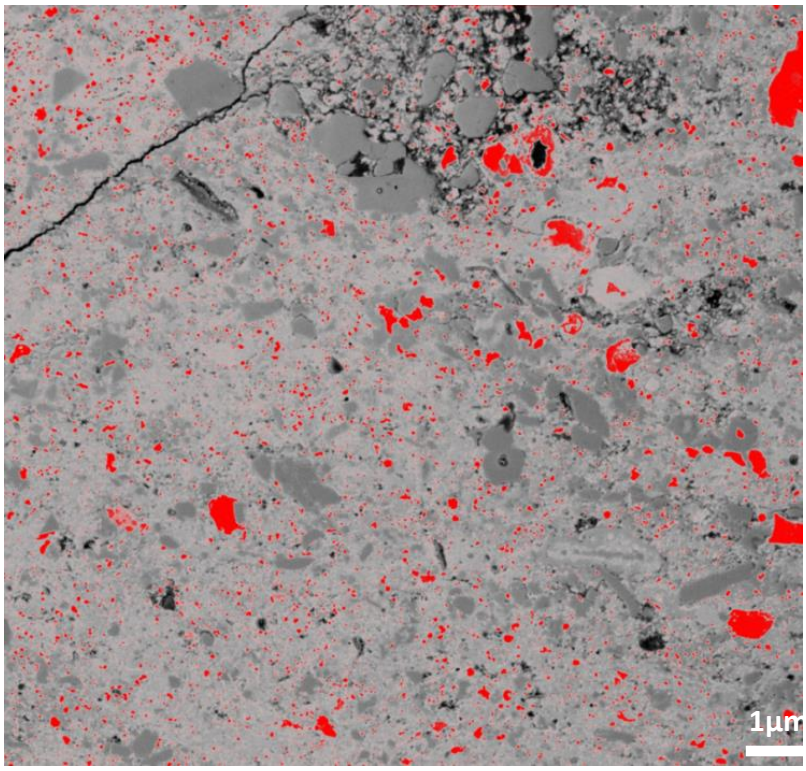

Fig. 4.4.6b

Fig. 4.4.6a - Image map of Acfer 094 Area 1 acquired with the Ultra Plus, showing the presence of opaque phases of different size. Fig. 4.4.6b - Thresholding of the white phases of same area using Image J emphasizing the different size and abundance of opaque phases

4.5 - Comparing Acfer 094 size distribution data to literature data

The mineralogical and chemical characteristics of the fine-grained matrix of the unique primitive carbonaceous chondrite Acfer 094 have been investigated by scanning electron microscopy (SEM) and analytical transmission electron microscopy (ATEM) by Greshake (1997) where he describes it as a highly unequilibrated assemblage of an amorphous material, reporting the sizes of the phases observed. The matrix is composed of small forsteritic olivines (100-150 nm in radius), low Ca-pyroxenes (150-200 nm), and Fe,Ni-sulfides (50-150 nm). Olivine is described as the most abundant phase in the fine-grained matrix, whereas sulfides are much less abundant than olivines and pyroxenes and occur within the amorphous matrix. EDX analyses and diffraction patterns carried out by Greshake show that most of the sulfides are Ni bearing (up to 6.4 wt% Ni) pyrrhotites ($Fe_{1-x}S$). Pentlandites [$(Fe,Ni)_9S_8$] (~200 nm) are rare. No troilites (FeS) have been found in the fine-grained matrix. The results reported by Greshake (1997) for the sample Acfer 094 are compared to grain size distributions determined from this study. The histogram in (Fig. 4.5.1 a, b) shows how there is a certain agreement with the data reported for the silicates in terms of sizes, yet there is a discrepancy between the data from this study and that from Greshake (1997) in terms of sizes and abundances of the opaque phases. In contrast to what Greshake reported, the most abundant minerals in the matrix are opaques rather than olivines and opaque phases ≤ 50nm in radius observed in this work were not reported in previous studies. ESB Image maps of Area 1 of Acfer 094 matrix acquired with Ultra Plus (Fig. 4.4.5a & b) shows the abundant presence of nano-sized opaque phases, estimated by thresholding to be 5%.

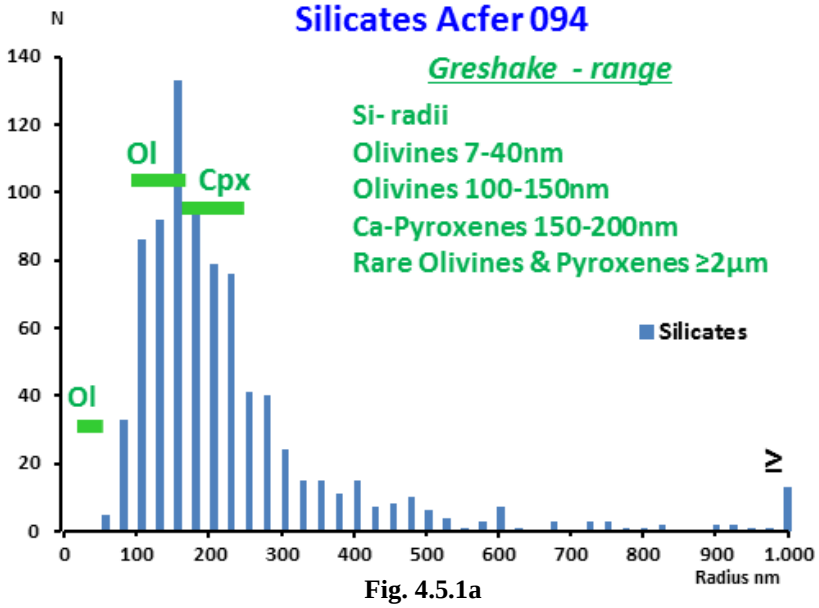

Fig. 4.5.1a

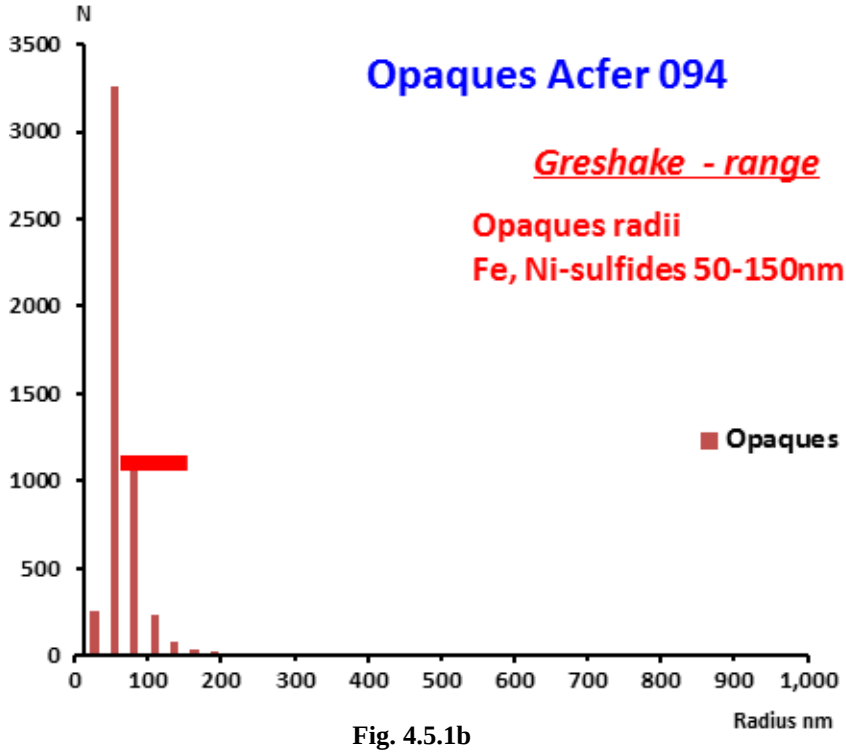

Fig. 4.5.1b

Fig. 4.5.1a - Histogram showing distribution of the radii for the silicate phases for Acfer 094, compared with data reported by Greshake, 1997

Fig. 4.5.1b - Histogram showing distribution of the radii for the opaque phases for Acfer 094, compared with data reported by Greshake, 1997

Element maps of the same area acquired using the FEI Quanta (e.g. Fig. 4.5.3) further emphasises the presence of nano-sized opaque phases with a range of different chemical compositions. The map shows also how unevenly the nano-phases are distributed throughout the matrix. Cutting out FIB foils from region of the matrix underpopulated by these nano-phases for ATEM investigations could lead to an inaccurate estimation of the size and abundances of the mineralogical phases present in the matrix, ultimately leading to possible misinterpretations of parent body and/or solar nebular process. This reinforces the advantages of using SEM high resolution images and element maps of wider regions of the matrix, compared to narrower areas investigated using TEM foils.

Another important feature worth noticing is the presence in the matrix of Acfer 094 of abundant iron-sulfide phases. In the false coloured element map (Fig. 4.5.3), the iron (Fe) coloured blue and Sulphur (S) green, there is evidence for the presence of cyan phases (Cyan produced by mixing blue and green Fig. 4.5.2) of variable size throughout the matrix area mapped. This raises the question of whether the absence of troilite (FeS) in the matrix of Acfer 094 reported by Greshake (1997) is due to heterogeneous distribution of mineralogical phase within the matrix or is real, and should be investigated further.

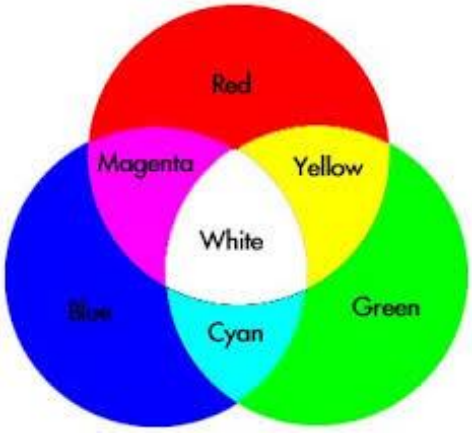

Fig. 4.5.2 - Additive colour mixtures diagram showing the mixing of blue and green to produce cyan.

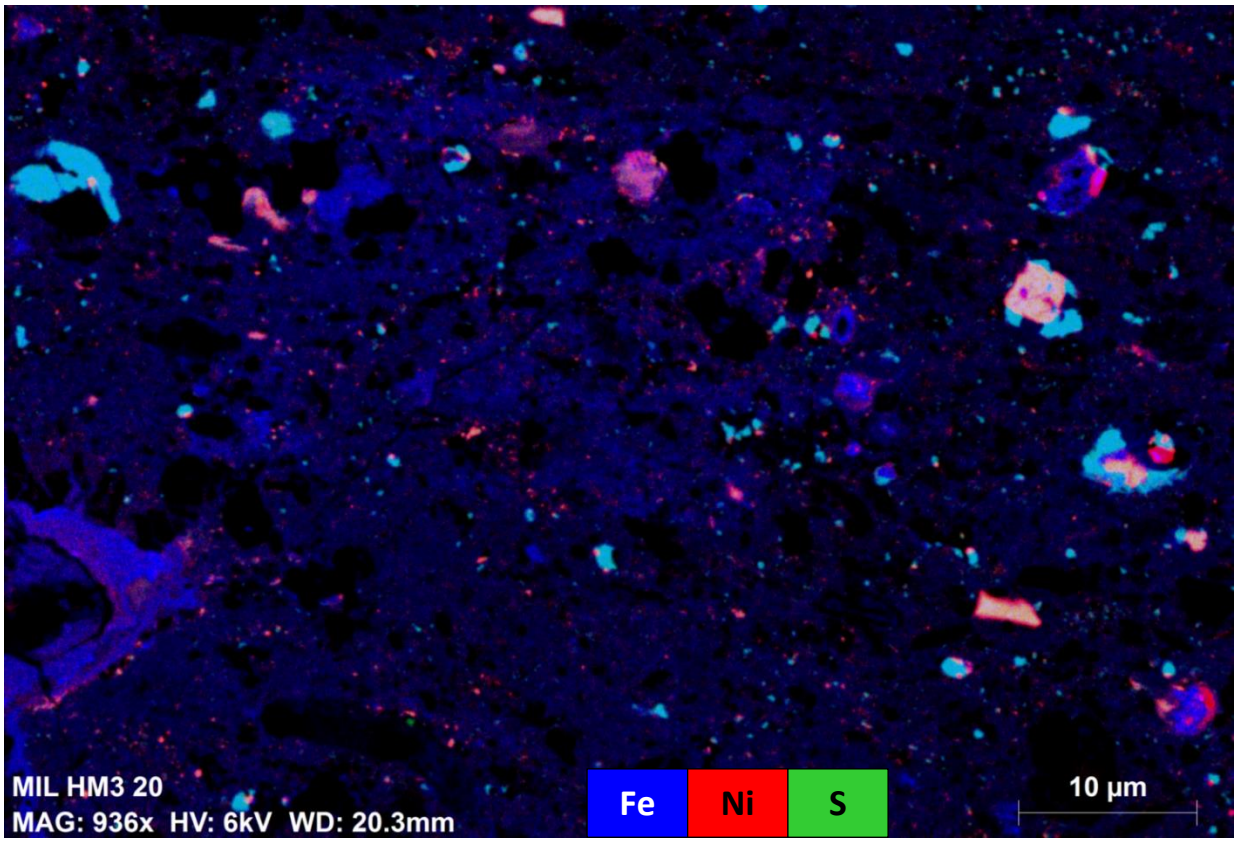

Fig. 4.5.3 - Element map of Acfer 094 Area 1 matrix acquired using the FEI Quanta, showing the presence on nano-sizes Ni bearing phases and Fe-S phases (in Cyan).

4.6 - Summary and conclusions

Pre-accretion processes operating in the protoplanetary disk such as disk winds and magneto-rotational turbulence dictate the dynamics of dust grains causing their size sorting (Miyake et al., 2016). Similar effects should be seen in the matrix constituents of primitive chondrites. CP-IDPs seem to show size distributions compatible with aerodynamic sorting prior to accretion. The results for the size distribution of discrete grains making up the crystalline components of the matrix, in contrast to what is observed for CP-IDPs, do not show evidence of aerodynamic sorting taking place prior to accretion. The lack of sorting

evidence might be due to a combination of processes varying from terrestrial weathering to parent body processes, such as aqueous alteration and/or mild thermal metamorphism. All these processes might cause the grain to coarsen or to produce a metasomatic transformation generating different mineral phases as products of chemical alteration of the starting mineral. Thus, the size of the metal sulfides occurring in the matrix of the samples investigated in this study appears to be controlled predominately by parent body processes. This has shed some light on the final question in the purpose of this study. Whether the parent body processes have made significant changes into the physical and chemical properties of the dust particles after accretion was a matter requiring resolution.

Moreover the origin of nano-sulfides is not clearly understood, their close association with amorphous silicates suggest a genetic relationship between the two materials and it has been proposed that the most plausible formation mechanism is annealing of an amorphous precursor either in the solar nebula or in the parent body (Abreu et al., 2010). If nano-sulfides are separating out from the amorphous silicates, thus never been loose as discrete grains, the disk winds and magneto-rotational turbulence in the protoplanetary disk might not have produced a sorting effect on them. Based on SEM observation it appears evident that nano-opaque phases are very sensitive to alteration, thus may be considered the most sensitive indication of alteration. These properties could be exploited in future work to quantify parent body processing. This study has also highlighted the importance of investigating wide surface areas by SEM compared to FIB sections. Given the extremely high heterogeneity of the matrix, and the non-uniform distribution in abundance of mineral phases, it becomes crucial to contextualise the observations to ensure the misrepresentation of mineral phase abundances is minimised.

4.6.1 - Mobility of sulfides and their coarsening during metamorphism

The effects of thermal metamorphism in meteorites were investigated by Grossman et al., in 2005, who found that the progressive coarsening of sulfide grains throughout the meteorite is caused by thermal metamorphism. They described the very high S content of matrix as a ubiquitous feature of very primitive chondrites such as in type 3.0 ordinary and CO chondrites. However, as the petrologic type increases towards type 6, meteorites were showing coarser FeS-rich grains. This was explained as a consequence of the temperature increase that caused FeS to become mobile and reduced its surface area. Thus, in fine-grained matrix, sulfides became redistributed and coarsen up during metamorphism.

Mobility of coarse troilite as well as μm-size grains in matrix during metamorphism of ordinary chondrites has also been suggested by Lauretta et al. (1996; 1997), who found experimental evidence for this process.

The presence of amorphous silicates and presolar grains in the matrix of the four meteorites studied in this project, indicates that the samples in question did not experience significant thermal metamorphism. Even a small increase in temperature would have caused the amorphous silicate to crystallise and the presolar grains to degas. This confirms that the samples investigated in this project are to be considered essentially unmetamorphosed, and the opaque coarsening observed in the matrix of ALHA 77307 and MIL 07687, compared to the opaques seen in Acfer 094 and QUE 99177 is likely to be caused by a different process.

4.6.2 - Crystal growth, during parent body aqueous alteration

Parent body aqueous alteration could be responsible for the general coarsening of the matrix grains, as it has been shown that precipitation of secondary phases, such as carbonates from percolating fluids, causes a general coarsening of the mineralogical phases. As a consequence, of the secondary phases grain growth, the interstitial pores close,

reducing the porosity (e. g. Lee et al., 2014). It is not clear whether aqueous alteration has a similar effect on the opaque phases causing crystal coarsening. However, based only on petrologic observation of the high resolution image maps, it appears that the brighter phases in the BSE image, almost certainly to be opaque phases, are intimately associated with the light grey phase. This is most likely Fe-oxides, probably originated by the alteration of the opaque phases. In addition to the opaque and Fe-oxides intimate association, suggesting a genetic relationship, the opaque phases in this context tend to be coarser than the usual nano-sized particles seen in the least altered portion of the investigated areas (Fig. 4.4.1a&b, 4.4.3b&c). These observations, suggest that aqueous alteration may play a role both in the oxidising and coarsening of the opaque phases, although more detailed investigations are needed to prove this hypothesis.

Chapter 5

5. Oxygen & Hydrogen Isotopes

Isotope abundance variations in meteorites are very useful to understand chemical and physical processes that took place during the formation of the Solar System (Clayton, 1993), and for tracking reservoirs that characterise the solar nebula (e.g. Starkey et al., 2014; Piani et al., 2015).

5.1 - Oxygen Isotopes in the Solar System

Oxygen is the most abundant element on Earth and the third most abundant element in the Universe. Oxygen has three stable isotopes occurring naturally: ^{16}O, ^{17}O, ^{18}O with ^{16}O being the most abundant on our planet and accounting for 99.762% followed by ^{18}O and ^{17}O accounting for 0.205% and 0.038% respectively. The high abundance of ^{16}O is due to the fact that is a major product of stellar evolution. Most of the ^{16}O is synthesized towards the end of the helium fusion process in stars, and it is also a primary isotope which means that it can be made by stars that originally were made of hydrogen only (e.g. Meyer, 2005). ^{17}O and ^{18}O are less abundant because there are secondary isotopes synthesized from seed nuclei in second generation stars (e.g. Emsley, 2001). Oxygen isotope abundance variations in extra-terrestrial materials have proved to be a very important tool to understand better the chemical and physical processes that took place in our Solar System. It is a convention to express variation in isotope abundances, indicated by the symbol δ, in the form of stable isotopic ratios relative to an arbitrary standard, in the case of oxygen known as SMOW (Standard Mean Oceanic Water), as follows:

$$\delta^{18}O = \left[\frac{(O^{18}/O^{16})sample}{(O^{18}/O^{16})SMOW} - 1\right] x1000$$

$$\delta^{17}O = \left[\frac{(O^{17}/O^{16})sample}{(O^{17}/O^{16})SMOW} - 1\right] x1000$$

When plotted on a 3 isotopes diagram of $\delta^{17}O$ versus $\delta^{18}O$ almost all terrestrial values plot along the TFL (Terrestrial Fractionation Line) (Fig. 5.1.1), which has a slope of ~0.52 (e.g. Clayton, 1993).

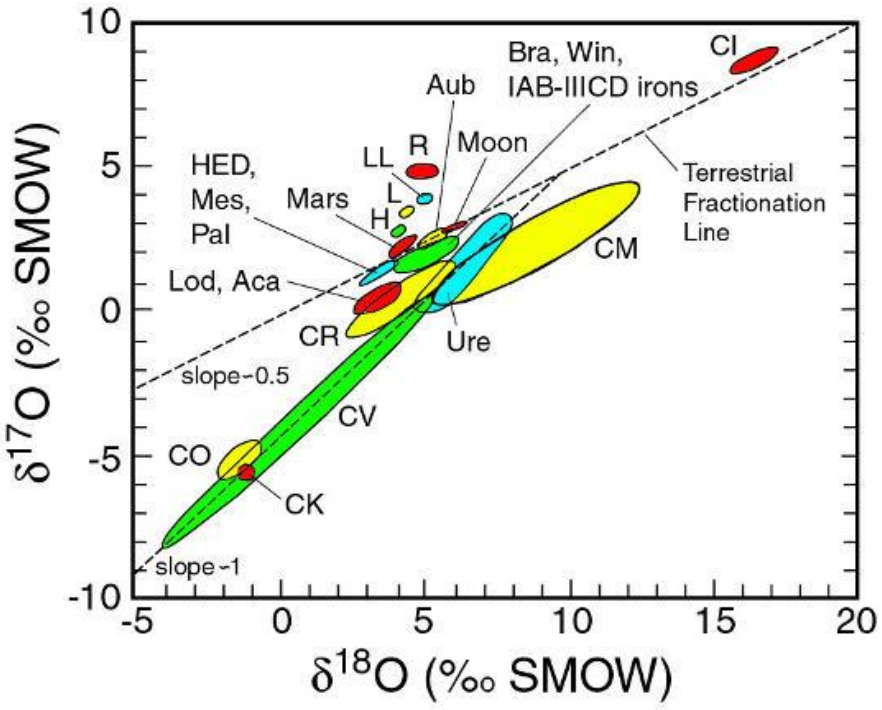

Fig. 5.1.1 - Meteorites of different classes plot in distinct fields on an oxygen isotope diagram. From Wittke (2008)

The slope of 0.52 is because for almost all processes the fractionation of the isotopes is related to the mass difference of the isotopes (i.e. mass dependent fractionation) such that the fractionation of $^{17}O/^{16}O$ to that of $^{18}O/^{16}O$ is 0.52.

The vast majority of extra-terrestrial materials do not plot on the terrestrial fractionation line, with the exception of some EH and EL meteorites, while rocks from the Moon have an isotopic compositions that plot very close to the TFL (Herwartz et al., 2014).

Meteorites display a wide range of isotopic compositions which do not fall on a single mass fractionation line (Fig. 5.1.1), implying that those meteorites have inherited heterogeneity from the very early Solar System. Most of the observed variation falls around a line approx. slope =1 (Fig. 5.1.1)

The deviations of extra-terrestrial samples from the TFL reflect evidence of two or more distinct isotopic reservoirs or mass independent fractionation processes that took place within the proto-stellar disk, or possibly even earlier (i.e. ISM) (Yurimoto et al., 2008).

5.2- Oxygen isotopic anomalies in the Solar System

Unequilibrated extra-terrestrial components display particularly large mass independent oxygen isotopic variations (e.g. Yurimoto et al., 2008, Clayton & Mayeda 1999).

In order to explain variations observed in chondritic components, different mechanisms have been proposed, the most common being:

- Nucleosynthetic effects
- Chemical mass-independent fractionation effects during solid formation
- Photochemical self-shielding effects

5.2.1 - Nucleosynthetic effects

It was proposed that the fractionation ratio of $^{17}O/^{16}O$ to that of $^{18}O/^{16}O$ close to 1, characterising the mass independent isotopic fractionation observed in chondritic components, reflects O-isotopic heterogeneity in solar nebula material. The observed ^{16}O-rich solids and gas enriched in ^{17}O and ^{18}O are a consequence of nucleosynthesis taking place in stars (Clayton et al., 1973) or alternatively a consequence of nuclear reaction

caused by energetic particles such as galactic cosmic rays or from the proto-sun (Lee, 1978). Since the variation of the other chemical elements are less significant, and uncorrelated to the oxygen isotopic anomalies observed, this mechanism appears to be not very likely (Clayton, 1993). The rarity of ^{16}O-rich presolar grains also suggests that these were not a major distinct contribution to early solar system (e.g. Lodders et al., 2005).

5.2.2 - Chemical mass-independent fractionation effect during solid formation

According to this hypothesis, the mass independent fractionation process inferred by the slope 1 line is the result of a chemical mass independent fractionation effect in the vapour phase precursor from which CAI minerals condense. Thiemens and Heidenreich, (1983) showed that when ozone is produced from molecular oxygen, it is equally enriched in ^{17}O and ^{18}O rather than showing a mass-dependant effect. Thus, chemical reactions are capable of producing material on a slope 1 line.

5.2.3 - Photochemical self-shielding effects

The photochemical self-shielding effect in CO is a phenomena that has been observed in astronomical environments (e.g. van Dishoeck 2004), and the same mechanism was suggested to explain the mass independent oxygen isotopic fractionation (e.g. Clayton, 2002; Lyons and Young, 2005; Yurimoto and Kuramoto, 2004).

Due to the absorption of UV radiation produced by the Sun or stars, CO molecules experience photolysis. The three different species: C^{16}O, C^{17}O, C^{18}O react chemically at different rates due to difference in column density. The much higher column density of C^{16}O means that the UV radiation at wavelengths required for photodissociation of this molecule becomes quickly attenuated in the outermost parts of the solar nebula or the molecular cloud so that in the innermost part of the cloud only the rare C^{17}O and C^{18}O are dissociated as their column densities are several orders of magnitude lower. The ^{17}O, ^{18}O-

rich atoms produced in the less distal parts of the disk can then react more readily to form solids that ultimately contribute to the planetary bodies. Although this is the most widely accepted model it lacks direct astronomical evidence of the oxygen isotopic heterogeneity within the disk. Photolytic decomposition of CO molecules by UV could also take place in the inner disk or in the molecular cloud prior to disk formation, however it remains unclear where this mechanism mostly occurred (e.g. Rumble et al., 2008).

5.3 – Bulk oxygen isotopes in meteorites

Ordinary chondrites (OCs) are the most abundant stony meteorites, with the H, L, and LL Fe-groups having rather restricted, similar but discernible oxygen isotopic compositions (Clayton et al., 1991) (Fig. 5.1.1). Carbonaceous chondrites on the other hand display oxygen isotopic compositions characterised by distinct and large variations in terms of isotopic composition compared to OCs (Fig. 5.1.1). These variations cannot be linked to a single process or event (e.g. Franchi et al., 2001). CAI data have shown gas-solid exchange, between the condensate enriched in ^{16}O and the surrounding gas enriched in ^{17}O and ^{18}O (e.g. Young and Russell, 1998). The large range of isotopic composition in CCs is also due to varying amounts of phyllosilicates and other hydrously formed minerals enriched in heavy isotopes, produced by mass dependent fractionation associated with varying degrees of low temperature aqueous alteration (e.g. Brearley and Jones, 1998; Clayton et al., 1999).

Despite the large range of oxygen isotopic variations in carbonaceous chondrites, some show characteristics implying genetic relations between the different groups. CR, CH, CB meteorites groups have a similar isotopic composition but different texture and different metal content (Weisberg et al., 2001). CKs, which show evidence of thermal metamorphism, plot into the CVs field implying that CKs are metamorphosed from CV precursors (Greenwood et al., 2010). The CV group displays a large isotopic range due to

the presence of refractory phases enriched in ^{16}O and the large size of components making representative sampling prohibitive.

In particular, CMs are characterised by hydrous clays rarely above 20% (Howard et al., 2011), which are believed to originate by the aqueous alteration of silicate phases.

These clays are enriched in the heavy isotopes of oxygen. Enrichments in ^{18}O reflects the effects of mass dependent fractionation associated with the formation of the clays at low temperature (e.g. Young et al., 1998 Clayton et al., 1999). However, the mixing line defined by the whole-rock CMs and matrix-rich fractions has a slope of ~0.7, indicating that the isotopic composition of the water reservoir was enriched in ^{17}O compared to the silicate reservoir (Clayton and Mayeda, 1999).

Considering that the matrix of CMs is enriched in heavy isotopes relative to the whole rock, the other constituents must be depleted in the corresponding amount of the same heavy isotopes in order to balance the mass. This places the oxygen isotopic composition of CMs within the range of the COs (Greenwood et al., 2014).

CRs chondrites are characterised by isotopic heterogeneity (Weisberg et al., 1995) similarly to CM's they have ^{16}O-rich anhydrous silicates and ^{16}O-poor phyllosilicates matrix and alteration products (Clayton and Mayeda, 1999). QUE 99177 is the isotopically lightest whole rock CR chondrite known, suggesting it is the least aqueously altered CR chondrite (Schrader et al., 2011).

5.3.1 - Oxygen Isotopic composition of chondrules and CAIs

During the chondrule formation process, the fluid droplet could have experienced interaction with the surrounding gas that led to isotopic exchange. Chondrules were formed from material isotopically distinct from Earth and hence do not plot on the TFL (Fig. 5.3.1). Although some have their own mass dependent fractionation line (Young et, al., 2001), they appear to have inherited the isotopic heterogeneity of the solar nebula and are generally ^{16}O depleted compared to the Sun (e.g. Yurimoto et. al., 2008).

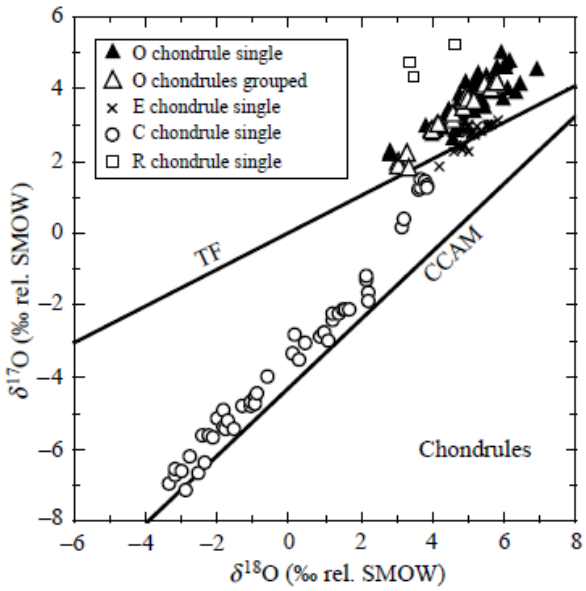

Fig. 5.3.1 - Oxygen isotopic composition of chondrules from all classes of chondritic meteorites. The TF line and carbonaceous chondrite anhydrous mineral (CCAM) line are shown for reference in this and many subsequent figures (Clayton et al., 2003)

Simon et al., (2008) reported data from a CAI with highly variable oxygen isotopic ratios in its Wark-Lovering rim, observing that different minerals within the same CAI appeared to have different isotopic composition. This implied that, in the early stages of Solar System formation, the region in the vicinity of the protosun was characterised by rapidly changing conditions, and that those variations were recorded in this object that rapidly condensed from the solar nebula (e.g. MacPherson et al., 2012). However, a subsequent study by Bodenan et al. (2014) of CAIs (Wark-Lovering rims and cores) from pristine meteorites that experienced only low degrees of aqueous alteration or metamorphism,

revealed only a uniform ^{16}O-rich composition. This study inferred that during the CAI and WL rim formation oxygen isotopic composition was constant in space and time and that the previously reported variations were the result of secondary processes that took place on the parent body.

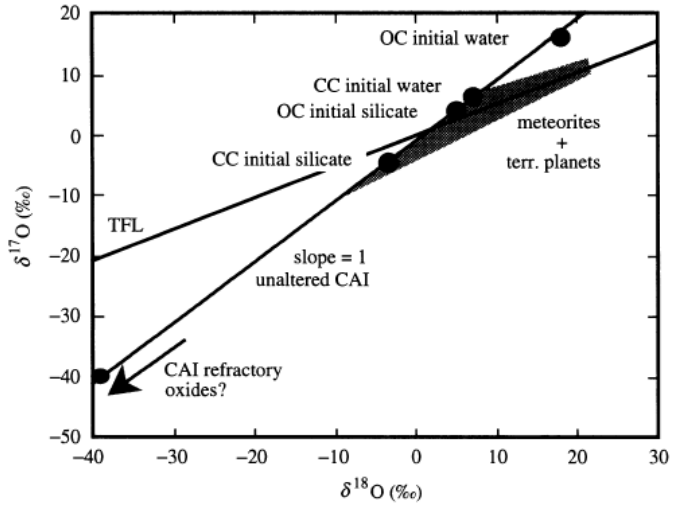

Fig. 5.3.2 - 3-isotopes diagram reporting meteorites and terrestrial planets data relative to the CAI slope=1 line (Young et.al., 1999, Franchi et.al., 2001). This diagram is an expanded scale diagram of Fig. 5.1.1

Given that all the meteorites groups, except for the R chondrites, plot to the right of the slope=1 line (Fig. 5.3.2), it is possible to attribute the oxygen isotopic composition of all the extra-terrestrial material of our Solar System to two different events that generated isotopic fractionations from an initially homogeneous reservoir. A process causing the mass independent fractionation (e.g. self- shielding and photo-dissociation of CO) could have been responsible for the spread along the slope~1 line, followed by a mass dependent fractionation associated with aqueous alteration effects and responsible for the shift to the right of the CAI line.

5.3.2 - Oxygen Isotopic composition of matrix

The study of CMs chondrite matrix by Clayton and Mayeda (1984, 1999) has revealed a ^{16}O-poor composition of the matrix minerals compared to the whole-rock, highlighting a two-component nature of CM isotopic compositions. Matrix in CV chondrites, consisting primarily of iron-rich olivine, fall on the anhydrous mineral mixing line. This implies that their isotopic composition is the result exchange interaction between a ^{16}O-rich and a ^{16}O-poor reservoir interpreted as dust and gas, respectively (Clayton and Mayeda, 1999).

Previous isotope studies of the matrix of the samples investigated in this work are very limited, and available only for QUE 99177 and Acfer 094. Schrader et al., (2011) have found that QUE 99177 is the isotopically lightest whole-rock CR chondrite known. They inferred that the anhydrous component of the CR chondrites is isotopically lighter than previously thought. The authors explained the enrichments in the light isotope of the whole-rock as possibly due to isotopically light unaltered matrix.

An oxygen isotopes study of the fine-grained matrix of meteorite Acfer 094 was carried out by Starkey et al., 2013, to test the effect of ^{16}OH on the determination of $\delta^{17}O$, and only available in the supplementary information. They have reported values ranging from $\delta^{17}O$, $\delta^{18}O$ = -1.3 (±0.2), 13.4 (±1.1) ‰ to 9.3 (±1.3), -0.8 (±1.1) ‰, and used them to test the effect of ^{16}OH on the determination of $\delta^{17}O$. Acfer 094 showed higher level of ^{16}OH compared to the IDPs, and the data scatter along the CCAM line suggested that the interference of ^{16}OH on ^{17}O measurements was adequately resolved.

5. 4 – Chondritic porous interplanetary dust particles (CP-IDPs)

Chondritic porous interplanetary dust particles (CP IDPs) are extra-terrestrial material whose properties are consistent with a cometary origin (e.g. Bradley, 2013). These particular IDPs do not show any significant evidence of alteration following accretion into a parent body and therefore can provide important information of the existing conditions and processes operating in the outer solar nebula. Some of the IDPs are characterised by the presence of enstatite whiskers that unlike rock-forming pyroxene, are elongated along the crystallographic axis [100], inferred to be a characteristic of condensation above 1300K in a low-pressure nebula or circumstellar gas (Bradley et al., 1983). The oxygen isotopic composition of such whiskers are comparable to ^{16}O-rich refractory inclusions found in meteorites, which suggest that they are condensates from the inner part of the Solar System (Nakamura- Messenger, 2009).

Oxygen isotopes studies of two IDPs, by Starkey et al. (2014), has revealed different compositions which provide important information in order to understand better the formation of the parent body of these particles. This study has revealed a grain with rare extreme ^{16}O depletion consistent with ^{16}O depletion due to self-shielding effects (Yurimoto and Kuramoto, 2004) and the rare extremity of the depletion allowed the authors to speculate that it formed close to where the O self-shielding effects were most intense and effective, and that the amorphous textural characteristic of this particle is consistent with that of silicates formed in the outer solar nebula where the extremely cold temperatures preserve these amorphous silicates. This evidence suggests that this material formed directly from a ^{16}O depleted reservoir in the comet forming region of our Solar System (Starkey et al., 2014).

Another important aspect revealed by this study is that the IDPs show isotopic variations at the micron-scale, thus sampling diverse isotopic reservoirs including inner and outer Solar System materials.

One region is characterised by a ^{16}O enrichment that, together with the blocky texture, suggests that it is a refractory grain originating in the inner Solar System. Conversely, the isotopic signature and fine-grained texture of a nearby area of the same particle seems to be similar to that of many carbonaceous chondrites, which likely originated in the inner part of the protoplanetary disk, and was subsequently transported, as consequence of the bipolar outflow, to the comet forming region (e.g. Nakamura et al., 2008). The third region of the Lumley IDP of this study revealed amorphous textures and high $\delta^{18}O$ values comparable with the oxygen composition of hydrated IDPs. The isotopic signature of the organic material in CP-IDPs also suggests they are from cometary sources (Robert, 2006) and that it is unlikely that the organics would have survived processing within the inner part of the protoplanetary disk or that they have experienced processing post accretion in a parent body, thus placing the origin of this material in the outer Solar System. These observations have led to the hypothesis that the parent body of this IDP has inherited the isotopic signature of at least three different reservoirs, from areas where different processes were in operation producing different textures, and was subsequently transported and mixed in the comet forming region in the outer Solar System (Starkey et al., 2014).

5. 5 - Oxygen composition of presolar grains

Circumstellar and/or interstellar O-rich dust is characterised by oxygen anomalies that are found in presolar silicates and oxides found in primitive Solar System materials (e. g. Amari 2014). Most silicate presolar grains are enriched in ^{17}O relative to the solar

composition (McKeegan et al., 2011) and show comparable variation in the $^{17}O/^{16}O$ $^{18}O/^{16}O$ ratios with that of presolar oxide grains that suggest they are likely to be products of the same types of stellar sources. Some other presolar grains are depleted in ^{17}O and ^{18}O and are linked to metal poor red giant or AGB stars (e.g. Lodders et al., 2005). ^{18}O rich presolar grains are thought to be produced by metal rich stars or supernovae (Yurimoto, 2006). The biggest contribution of oxygen rich dust to the ISM are AGB stars during the early stages of their evolution (Gail, Springer, 2002), and produce grains most of which (>70%) exhibit enrichments in^{17}O (e.g. Hoppe et al., 2008).

5.6 – D/H variations

The D/H ratio (deuterium/hydrogen) shows the largest variation of isotopic composition among the light elements (e.g. Füri, et al., 2015). D is preferentially transferred from the universal reservoir (H_2) by low-temperature reactions (10-100 K), and generally organic molecules and, to a lesser extent, water are characterised by D enrichments (e.g. Robert, 2006). Interplanetary dust particles show extremely large variations in their D/H ratios ranging from 90 to 4000 $\times 10^{-6}$ (McKeegan et al., 1985; Zinner et al., 1983; Messenger, 2000; Engrand et al., 1999). Much of the H in IDPs has a D/H ratio either close to chondritic values or close to cometary value for water (e.g. Robert, 2006). Cometary water have a D/H ratio of 300×10^{-6} (Meier et al., 1998a,b; Eberhardt et al., 1995; Bockelée-Morvan et al., 1988), and recently the direct in situ measurement of the D/H ratio in the Jupiter family comet 67P/Churyumov-Gerasimenko by the ROSINA mass spectrometer aboard the European Space Agency's Rosetta spacecraft, was found to be $(5.3 \pm 0.7) \times 10^{-4}$ - that is, approximately three times the terrestrial value (Altwegg et al., 2015).

Unequilibrated meteorites contain clay minerals and insoluble organic macromolecules, and ~90% of their bulk H is contained in water of the clays, whilst the remaining ~10% in

found in the Insoluble Organic Matter (IOM) (e.g. Robert, 2006). Insoluble organic matter generally shows D enrichments by a factor of 2 to 3 relative to the clays (Robert and Epstein, 1982; Kerridge et al., 1987; Epstein et al., 1987; Robert et al., 1987; Pizzarello et al., 1991).

The D enrichment of insoluble organic matter (IOM) present in ordinary chondrites and carbonaceous chondrites has been proposed to reflect isotope exchange of the molecular host with a D-rich component similar to gas phase molecules observed in dense clouds, and pre-stellar cores (Aléon, 2010).

Generally, clay minerals are depleted in D relative to the water from which they formed. Therefore, isotopic fractionation could occur during liquid water circulation in a warm parent body (Bunch and Chang, 1980; Sears et al., 1995). Mixing between water/OH in phyllosilicates and hydrogen in organics in CMs and CRs produces a linear trend that is reported in Fig. 5.6.1 a & b (Alexander et al., 2012).

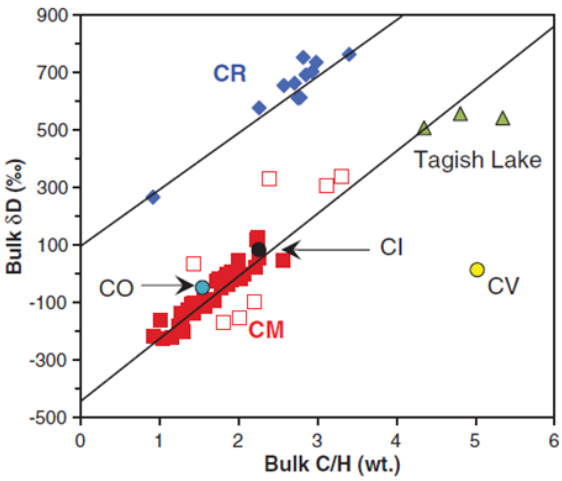

Fig 5.6.1a

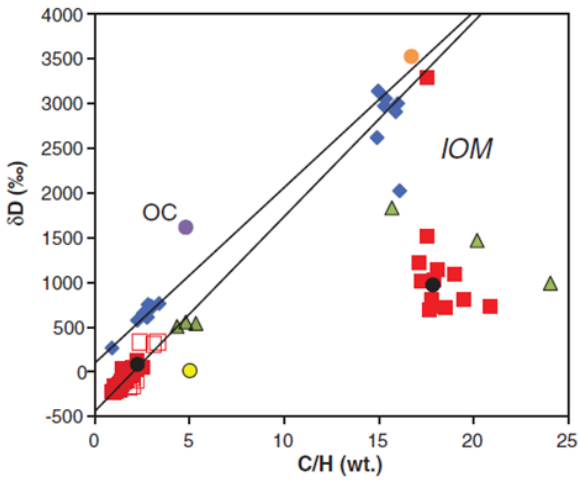

Fig 5.6.1b

Fig 5.6.1a – Bulk composition of carbonaceous chondrites plotting on subparallel lines
Fig 5.6.1b – Expanded scale of Fig 5.6.1a showing that CM and CR lines pass through the compositions of the most primitive chondritic IOM (data and figures from Alexander et al., 2012). Open red squares are CMs that were not included in the CM fit

CMs and CRs fall on lines which converge on the region where the most primitive insoluble organic material (IOM) plots implying that the CMs and CRs shared a common primitive organic component. The IOM in most chondrites is less deuterium-rich than that

in the most primitive meteorites, suggesting that there has been hydrogen isotope exchange between the water and the organics in closed systems (Alexander et al., 2012). Inner Solar System objects and comets show intermediate values, and possibly indicates an increase in the D/H ratio with heliocentric distance. This suggests that H_2 in the nebula was D depleted and exchanged isotopically with H_2O at low temperature, resulting in a preferential D-enrichment of the water. Deuterium-rich water then froze out onto grain surfaces and exchanged isotopically with organics and silicates as a result of turbulent transport and aqueous alteration on forming planetesimals (Jacquet et al., 2013).

5.7 - Oxygen isotopes results

5.7.1 – Bulk matrix oxygen isotope compositions

The oxygen isotopic composition of the matrix of samples ALHA77307, QUE 99177, and MIL 07687 were acquired in some of the matrix regions previously studied using SEMs and micro-XRD. Results of bulk matrix values obtained by integrating the entire area imaged are given in Table 5.7.1 and plotted in Fig. 5.7.1. Technical issues were experienced with the NanoSIMS at the Open University, resulting in it being unavailable for a considerable length of time. The number of samples investigated and the analyses acquired was therefore limited. Most of the areas analysed show depletions of ^{16}O relative to CAI and chondrules, plotting in the ^{16}O-poor region of the graph. The values range from $\delta^{17}O$, $\delta^{18}O$ = -5.0 (±3.8), -16.3 (±1.7) ‰ to 25.7 (±3.9), 25.0 (±1.7) ‰ and appear to exhibit a scattered distribution with a weak trend parallel to the slope 1 line enriched in ^{17}O. The matrix regions of ALHA77307 appear to display the most depleted ^{16}O values of all the three samples measured, ranging from $\delta^{17}O$, $\delta^{18}O$ = 7.5 (±3.5), 5.2 (±1.5) ‰ to 25.7 (±3.9), 19.4 (±1.7) ‰, whereas the sample QUE 99177 shows less ^{16}O depletion with values ranging from $\delta^{17}O$, $\delta^{18}O$ = -4.7 (±4.4), -13.6 (±1.9)‰ to 10.6 (±5.4), 5.6 (±2.4) ‰,

and MIL 07687 is the least ^{16}O depleted with values ranging from $\delta^{17}O$, $\delta^{18}O$ = -5.0 (±3.8), -16.3 (±1.7) ‰ to 5.2 (±3.8), -15.0 (±1.7) ‰.

ALHA77307	$\delta^{17}O$	$\delta^{17}O$ error	$\delta^{18}O$	$\delta^{18}O$ error
A_A1	20.7	3.9	25.0	1.7
A_A2	25.7	3.9	19.4	1.7
A_A3	8.7	3.7	12.5	1.6
A_A4	7.5	3.5	5.2	1.5
A_A5	12.6	3.8	17.6	1.7
QUE 99177				
Q_A2	-4.7	4.4	-13.6	1.9
Q_A3	4.5	4.7	-6.4	2.1
Q_A5	10.6	5.4	5.6	2.4
MIL 07687				
M_A3	-5.0	3.8	-16.3	1.7
M_A4	5.2	3.8	-15.0	1.7

Table 5.7.1 – Bulk oxygen isotope data for ALHA77307, MIL 07687, and QUE 99177 matrix.

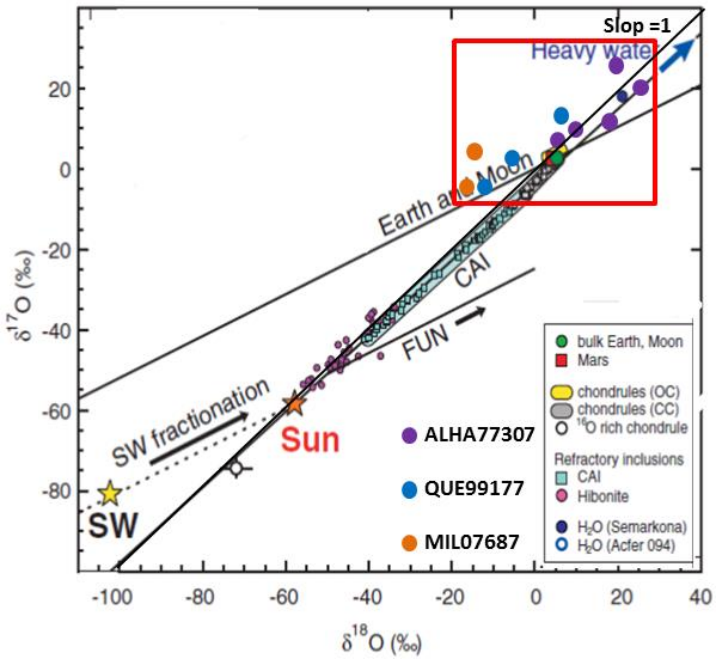

Fig. 5.7.1 - Oxygen three-isotope plot showing ALHA77307, MIL 07687, and QUE 99177 matrix date plotted with literature data for different compositions of major primary components of solar system matter, the solar wind (SW), and value for the Sun (Adapted from McKeegan et al., 2011)

5.8 – D/H isotope results

5.8.1 – Bulk D/H isotope compositions

D/H analyses were also acquired from the same regions of interest as the oxygen measurements on raster of 25×25 μm in size; due to varies technical difficulties the Nano SIMS at the Open University was not in operation for an extended period of time, therefore the number of analyses acquired was considerably limited.

The D/H ratios measured in the matrix of samples QUE 99177 and ALHA77307 are given in Table 5.8.1. D/H ratios for sample QUE 99177 range from 179 $\times 10^{-6}$ ($\delta D = 147$) to 321 $\times 10^{-6}$ ($\delta D = 1060$), whereas the value measured for the sample ALHA77307 is 142×10^{-6} ($\delta D = -90‰$).

Sample	δD	2 σ error	D/H × 10^6
QUE99177_A1	287	47	200
QUE 99177_A2	1060	47	321
QUE 99177_A3	601	37	249
QUE 99177_A4	147	33	179
ALHA77307_A1	-90	14	142

Table 5.8.1 – Showing bulk D/H ratios measured on samples QUE 99177 and ALHA77307.

5. 9 – Discussion

5.9.1 - Comparison oxygen isotopes with bulk meteorites

Data measured in this work of the matrix of samples ALHA77307, MIL 07687, and QUE 99177 are plotted alongside bulk values for carbonaceous chondrites measured by Clayton and Mayeda (1999), and Acfer 094 from Starkey et al., (2013) supplementary information and Fig. 5.9.1. Bulk rock values reflect the variability in oxygen isotopic composition of the carbonaceous chondrites and the matrix data reported here shows a wider range in

isotopic composition, which probably reflects the isotopic signature of different reservoirs sampled by the matrix in the nebula. The variability could also be the expression of parent body processes such as aqueous alteration that have stronger effects in the matrix than in the whole rock.

The effects of aqueous alteration are usually to drive the oxygen isotopic composition to the right on a three isotope plot along a mass fractionation line. However, in particular cases, isotope fractionation processes such as the formation of magnetite can shift values to lighter compositions (Choi et al., 1998). This is due to the negative fractionation with respect to water compared to the phyllosilicates. Micro–XRD analyses have revealed the presence of magnetite in the matrix of samples ALHA77307 and QUE 99177, with Area 2 in ALHA77307 and Area 5 in QUE 99177 being the most enhanced. Fig. 5.9.1 shows that matrix values are the areas exhibiting enhancement in magnetite are the heaviest, implying that the formation of magnetite did not shift values to lighter compositions.

The observed difference between whole-rock composition and matrix, but also between matrix results of previous works and the data presented here could be due to the different analytical procedure for their acquisition. Laser Fluorination analyses requires at least ~0.5 mm^2, many orders of magnitude larger than the areas analysed in this work. The regions of interest to be analysed using the NanoSIMS were accurately selected based on their petrological characteristics ensuring that the areas were representative of the matrix as much as possible through high resolution SEM observations.

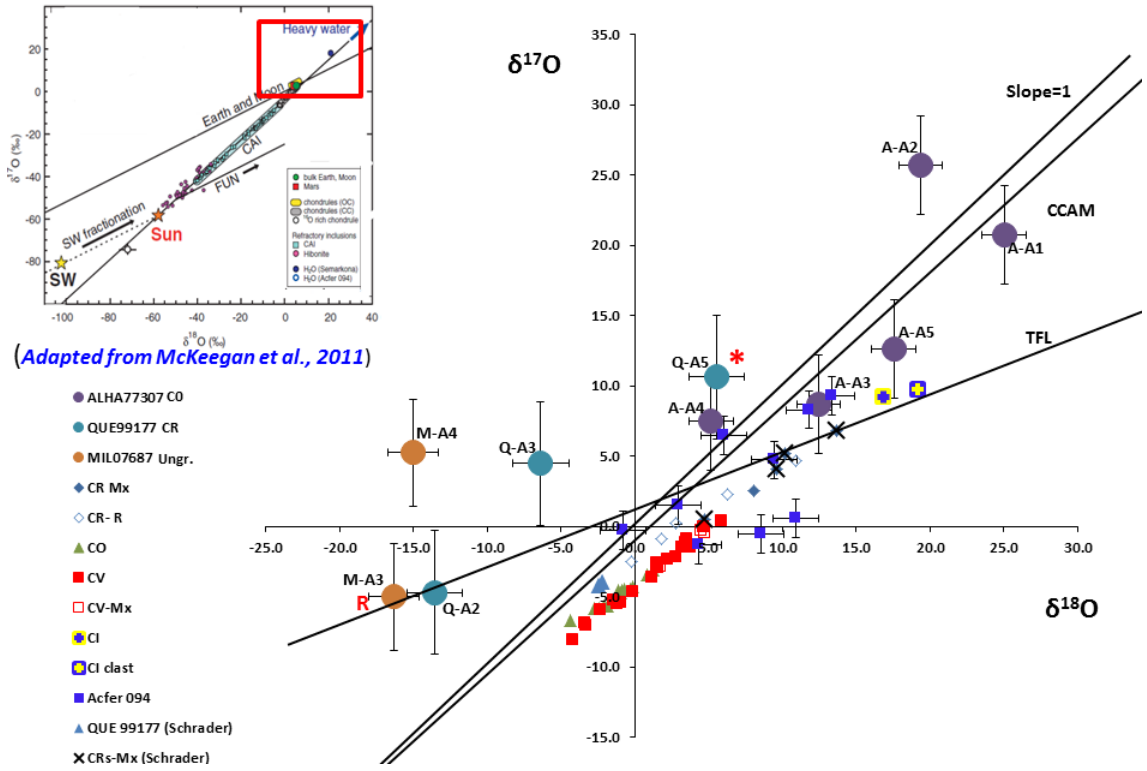

Fig. 5.9.1 - Oxygen three-isotope plot showing ALHA77307, MIL 07687, and QUE 99177 matrix data plotted with literature data for different groups of meteorites (Clayton & Mayeda, 1999), Acfer 094 from Starkey et al., (2013). Red * indicated QUE 99177 Area 5 characterised by aqueous alteration and red R (rim) indicated MIL 07687 Area 3 characterised by stalled front of alteration

Petrological evidence gathered from the SEM maps can help to decipher peculiar isotopic signatures, allowing us to understand better the different isotopic signature exhibited by a particular area. The sample QUE 99177 is a good example of a case where the petrological evidence can explain isotopic observations. Area 5 in the sample QUE 99177, marked with a star in Fig. 5.9.2, is more enriched in the heavy isotopes compared to values acquired on different areas in the sample, making the point shifted towards CI values compared to other analyses of these meteorites. This reflects increasing abundance of phyllosilicates that are usually enriched in heavier isotopes as a result of large positive equilibrium fractionation effects associated with their formation, and suggests that this particular area experienced more pronounced aqueous alteration. This is consistent with the petrological observations of Area 5 described in Chapter 4, which suggested a different history for that particular

matrix area, characterised by a heavy aqueous alteration and subsequent re-accretion into the QUE 99177 parent body.

Similar to sample QUE 99177, areas within the sample MIL 07687 show petrological and textural differences that are reflected in the isotopic heterogeneity exhibited by the different areas within the same sample. Area 3 in MIL 07687, marked with R (rim) in Fig. 5.9.1, is characterised by high concentration of Fe compared with adjacent areas (see SEM element map in Chapter 4.2.1.1d), which is interpreted as the termination of an alteration front. Despite the obvious alteration highlighted by the presence of enhanced Fe concentrations, the isotopic signature of this area is not dramatically different to the other MIL 07687 area analysed, that was from the more Fe-poor, more typical, unaltered regions. This could be due to the peculiar style of aqueous alteration that this particular sample experienced, resulting in lack of phyllosilicates, as reported by Brearley (2012). The stalled alteration front observed is indicative of limited water supply, and considering that the oxygen available from the water has been consumed, significant mass fractionation effects should not be visible; the process instead should produce a mixing line between starting silicates and water. Both MIL 07687 areas analysed are characterised by lighter values compared to other samples, possibly reflecting the fact that the ^{16}O-enrichments are due to the final water composition having exchanged with ^{16}O-rich silicates. However, further investigations and different areas are required to understand better these observations.

5.9.2 - Comparison oxygen isotopes with IDPs

The matrix data are plotted in Fig. 5.9.2 along with literature data reported for IDPs (Aléon et al., 2009, Nakashima et al., 2012, Starkey et al., 2014).

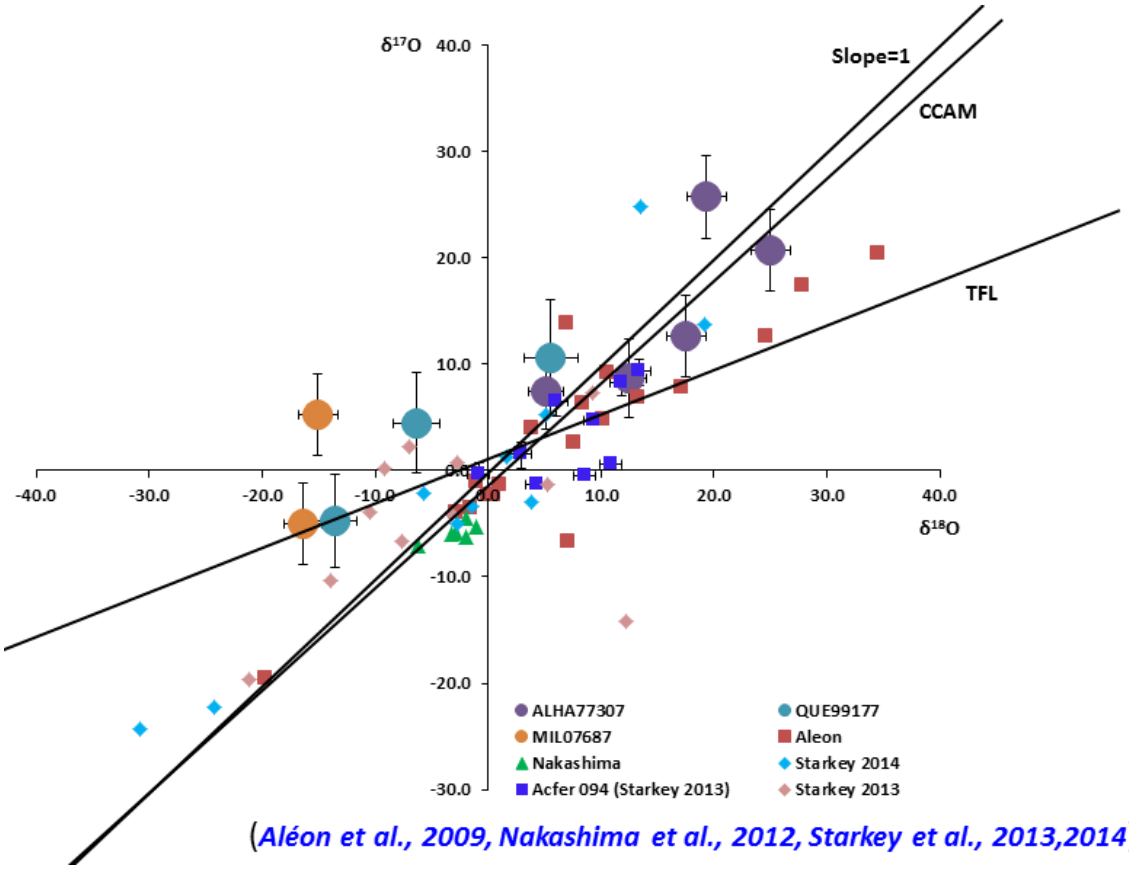

Fig. 5.9.2 - Oxygen three-isotope plot showing ALHA77307, MIL 07687, and QUE 99177 matrix date plotted with CP-IDPs literature data from (Aléon et al. 2009, Nakashima et al. 2012, Starkey et al. 2014) Acfer 094 from Starkey et al., 2013

The results are comparable to interplanetary dust particles values with the exception of some particles studied by Starkey et al., (2013) that show sub-regions of fine-grained material with extreme ^{16}O depletion. Matrix data measured in this study share more similarities with IDP values than meteorite whole-rock or bulk matrix values; these similarities between the matrix and IDPs are also emphasised by the petrological observation of possible enstatite whiskers in the matrix of carbonaceous chondrites previously reported only for ordinary chondrites (Alexander, 1987, Barberd & Hutchisonr, 1986, Leroux, et al., 2012), bridging the gaps between the different types of extra-terrestrial materials. It is important to notice that the matrix samples and the IDPs all plot above the slope=1 line to more ^{17}O-rich values. Starkey et al., (2013) discussed that the enrichments observed in the IDPs could be potentially related to poor control of the ^{16}OH interference on ^{17}O peak on samples, producing anomalous high $\delta^{17}O$ values, however no

correlation with OH abundance was seen. They also discussed the possibility that the ^{17}O enrichments could be due to an increased abundance of presolar silicates, and the authors suggested this could reflect late accretion of molecular cloud material on to the protoplanetary disk and the late accretion of theses IDPs. If this is the case, these observations can be applicable also to the matrix considering their similarity of their isotopic signature. This suggests a late accretion of the matrix constituent, from the molecular cloud into the protoplanetary disk, and consequent late accretion of this material into their parent body.

5.9.3 - Presolar grains

Despite the evidence of parent body processes affecting the matrix of the meteorites studied in this work, four presolar grains were identified by isotopic anomalies. The selection criteria for the presolar grains identification was that their isotopic composition had to be at least > 3σ compared to the average composition of the matrix.

Their oxygen isotopes ratios, size, and abundances, shown in Table 5.9.1, are comparable to results reported in previous works (e.g. Davidson et al., 2014). However, abundances of presolar grains previously reported (ALHA77307 (11^{+4}_{-3} ppm), QUE 99177 (44^{+24}_{-17} ppm), Davidson et al., 2014) are statistically more accurate than abundances reported here due to the much smaller matrix areas investigated in this work.

The presence of such grains in the matrix indicates that the sample, despite experiencing processing, preserves material of the ISM and from the protoplanetary disk, and can therefore be considered among the most pristine samples. Three of the presolar grains (two identified in the matrix of sample ALHA77307 and one identified in the matrix of sample QUE 99177) plot in the Group 1 field of an oxygen three-isotope plot (Fig. 5.9.3); this group is characterised by ^{17}O excess and ^{18}O deficiency relative to SMOW O-isotopic

composition. These grains are believed to have formed in winds of low-to intermediate-mass AGB stars (Nitter et al., 1997).

Sample	$^{17}O/^{16}O$ ($\times10^{-4}$)	$^{18}O/^{16}O$ ($\times10^{-3}$)	size (nm)	abun. per sample (ppm)
ALHA77307_Area 2	9.39	2.03	220×173	39±6
ALHA77307_Area 4	6.3	2.03	326×256	
QUE 99177_Area 2	7.22	2.08	220×173	26±9
QUE 99177_Area 3	3.42	2.63	191×150	

Table 5.9.1- Showing $^{17}O/^{16}O$ and $^{18}O/^{16}O$ ratios, size, and abundances of presolar grains in QUE 99177 and ALHA77307

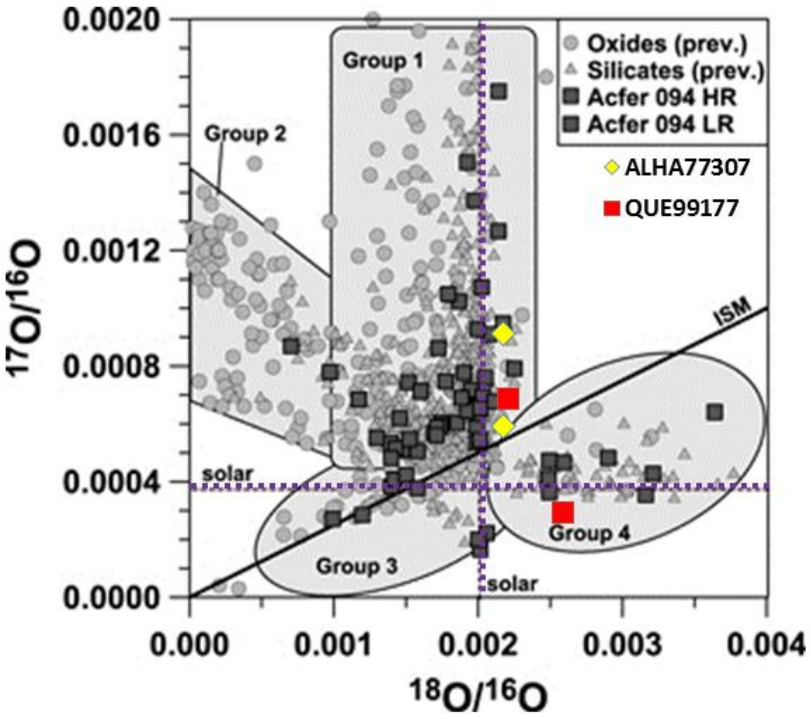

Fig. 5.9.3 - Oxygen three-isotope plot of oxygen-rich presolar grain identified in ALHA77307 and QUE 99177 (Adapted from Hoppe et al., 2015). Red and yellow points are data from this work

Another presolar grain was identified in the matrix of sample QUE 99177 and plots in the Group 4 field of an oxygen three-isotope plot. This group is ^{18}O-rich, and it is likely to have originated in supernova outflows (Nguyen, 2010). The presence of presolar grains in matrix of QUE 99177 and belonging to Group 4 is also consistent with previous works (Nguyen et al., 2008).

5.9.4 –D/H discussion

D/H ratios of matrix areas in QUE 99177 and ALHA77307 were compared with D/H values for chondrites and IDPs, and plotted in Fig. 5.9.4. The histogram shows how CR meteorites are D-enriched relative to CIs and CMs, ranging from D/H=145×10^{-6} to 314×10^{-6} (Robert, 2002) and 197×10^{-6} to 275×10^{-6} (Alexander et al., 2012) respectively. D/H values obtained in this work for sample QUE 99177 (CR2) show a wider isotopic variation compared to other CR values extending to lower D/H ratios than previously reported. While the lower values could be the result of terrestial contamination not entirely removed from the areas analysed, this is unlikely because of the pre-sputtering protocol. It is more likely due to the presence of small amounts of a component not previously reported for CR values. Alternatively, the variation in D/H could reflect greater isotopic exchange between the hydrous fluids, generally depleted in D (e.g. Alexander et al., 2012) and the D-rich organic matter during aqueous alteration, similar to that previously observed in chondrite matrix (Piani et al., 2015).

The D/H value measured in this work for sample ALHA77307 plots close to the terrestrial value and is consistent with previous bulk measurements ($\delta D = -48‰ \pm 4$ Alexander et al., 2012). Furthermore, the sample plots within the CI, CV, CM values indicating common reservoirs and processes for these groups.

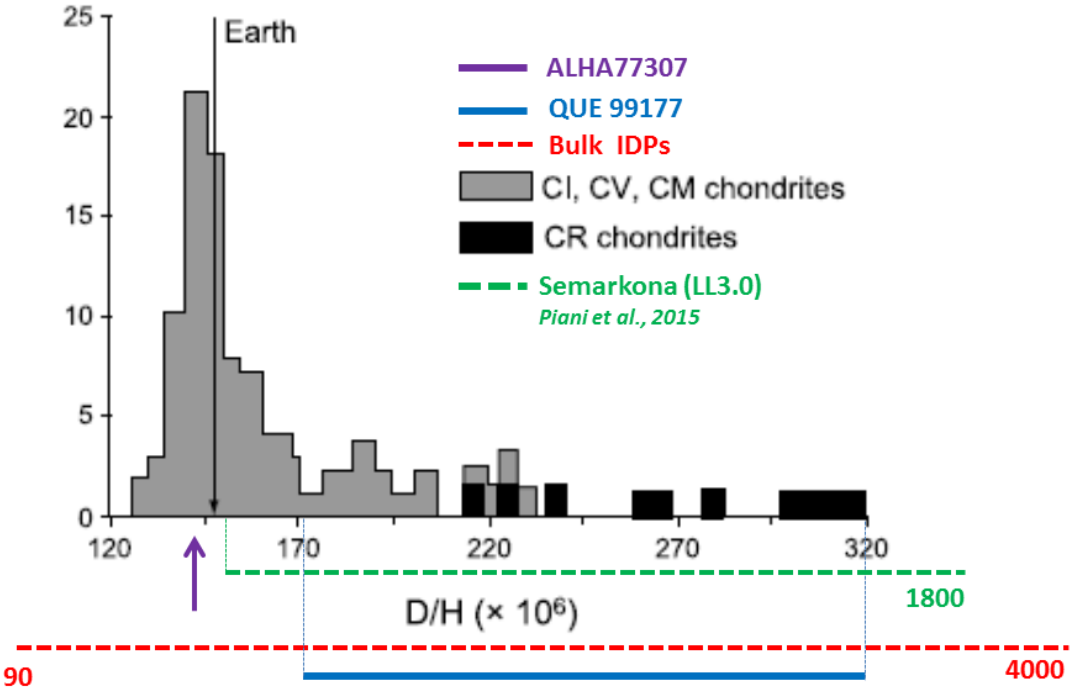

Fig. 5.9.4 - Histogram showing comparison between D/H ratios of QUE 99177, ALHA77307 matrices (values from this study) and distribution of D/H ratio in IDPs and carbonaceous chondrites (N=106) (Adapted from Robert, 2006). ALHA77307 (purple) and QUE 99177(blue) are data from this work

From Fig. 5.9.4, it is also evident that the bulk values for IDPs show extremely large variations in their D/H ratios ranging from 90 to 4000 $\times 10^{-6}$ (Robert, 2006).

Messenger (2000) also reported H isotopic anomalies in IDPs with D/H ratios that reach the values of interstellar molecules, suggesting that molecular cloud material survived in some IDPs. Semarkona's clay minerals also shows highly heteogeneous D/H ratios, whilst the IOM in the same sample does not show such large variation. This was interprteted as a result of limited isotopic exchange between the two phases during aqueous alteration (Piani et al., 2015). Considering that there are indications of an increase in the D/H ratio with heliocentric distance (Jacquet et al., 2013), the extreme variations exhibited by IDPs might reflect the fact that these particles are sampling different reservoirs within the protoplanetary disk, at different heliocentric distances. Values of the matrix measured in this work in QUE 99177 and ALHA77307 plot within these IDPs values, showing a more restricted range of isotopic variations and indicating that matrix in these samples is perhaps sampling material from a relatively restricted region of the protoplanetary disk or is better

mixed. Interpretations of these data are made with consideration of the limited areas analysed and the bias that this may impose. Ideally more reference points are required to better represent sources and processes involved.

5.10 – Conclusions

In contrast to whole rock observations, the oxygen isotopic signature of matrix regions appears to show similarities with IDPs. The ^{17}O enrichment observed could be due to the presence of presolar grains (e.g. Starkey et al., 2013). This hypothesis is supported by our observations of Group I presolar grains in ALHA77307, and QUE 99177. Enrichment of ^{17}O in IDPs observed both in this work, and that of Starkey et al. (2013), is thought to be the result of late accretion of molecular cloud material on to the protoplanetary disk (Starkey et al., 2013). Therefore, isotopic analyses of matrix regions within meteorites provide supporting evidence that cometary-like material is present within asteroids. Similarities between the matrix and IDPs are also emphasised by the petrological observation of probable condensate from the solar nebula allowing us to establish a genetic correlation between the matrix of carbonaceous chondrites and IDPs.

The matrix of carbonaceous chondrites is characterised by an heterogeneous mixture of intimately mixed D-rich organic matter and hydrous silicates (e.g. Piani et al., 2015), and this heterogeneity could be responsible for the wider D/H isotopic variation observed in this study within the matrix of sample CR2 QUE 99177 compared to other CR values. Limited isotopic exchange between hydrous silicates and D-rich organic matter during aqueous alteration previously observed in the matrix of other chondrites could also play a role and contribute to these variation observed. However, variations in the D/H ratios in the samples measured show a much narrower range compared to the bulk value measured for IDPs and this could reflect the fact that matrix sampled dust from a much narrower region of the protoplanetary disk or might be indicative of a more pronounced homogenisation.

The petrological observations correlates to isotope variations, however further studies are required to explore this further. The matrix of sample studied in this work shows similarities to IDPs suggesting they originate from a similar source, suggesting that fine grained material is ubiquitus in the protoplanetary disk, sampling both inner and outer Solar System.

Chapter 6

6. Conclusions and Future work

The aim of this work was to investigate the fine grained matrix material found among the coarser part of primitive chondrites, such as chondrules and CAI that hold the whole rock together. Meteorites that did not undergo important parent body process and remained relatively pristine since their accretion were selected. They did not experience significant changes and, therefore, the matrix preserves the closest physical and chemical properties of the protoplanetary disk solid component. This precursor material was once surrounding our young Sun, and at the very early stages of formation of our Solar System accreted into celestial bodies some of which eventually evolved into planets. Therefore, it holds the secrets of the accretion processes.

The aim was achieved by studying the matrix of samples ALHA77307, MIL 07687, Acfer 094 and QUE 99177 regarded among the most pristine primitive chondrites, focussing on the most pristine matrix areas.

6.1 - Enstatite whisker and grain transport in the protoplanetary disk

This study has reported the first discovery of enstatite whiskers in carbonaceous meteorites. Nakamura-Messenger et al., (2009) explained their absence in meteorites as likely due to destruction during parent body thermal/ aqueous alteration. This work has demonstrated that even the samples regarded as the most pristine have experienced some aqueous alteration and despite these effects, enstatite whiskers have survived.

The main reason why this work was successful in reporting the first presence of enstatite whiskers in the matrix on meteorite, although the matrix of these samples has been

extensively studied before, lies in the facts that a novel investigation method was used to carry out this investigation using the latest generation of scanning electron microscopes. This reinforces the advantages of using SEM high resolution images and element maps of wider regions of the matrix, compared to narrower areas investigated using TEM foils. Cutting out FIB foils from region of the matrix narrows down considerably the field of view, as a consequence, vital information can be missed.

The unique crystal morphologies and microstructures of the enstatite whiskers are consistent with them condensing above ~1300 K in a low-pressure nebular or circumstellar gas (Bradley et al., 1983). To constrain the site of enstatite whisker formation Nakamura-Messenger et al., (2009) have performed chemical and oxygen isotope measurements on enstatite whiskers in a CP IDP, and based on the oxygen isotopic composition of the whisker have concluded they may have formed in the inner Solar System.

These results have important implications on the whiskers outwards transport to the comet forming region. Since they are found in CP IDPs and Stardust material, both from the outer Solar System, this requires a considerable radial mixing to transport material from the hot parts of the disk to the cold parts of the comet forming region.

These crystals have a very peculiar morphology and are characterised by a very small width compared to their length. This makes them too fragile to survive the journey to the outmost part of the Solar System. These observations have resulted in speculation, that they were shielded by dust accreted during the transport to the comets forming regions.

6.2 - Size distribution

Pre-accretionary processes operating in the protoplanetary disk such as disk winds and magneto-rotational turbulence dictate the dynamics of dust grains, and these effects should be seen in the matrix constituent of primitive chondrites. The size distribution study, of discrete grains making up the crystalline components of the matrix, studied in this work, do not show evidence of aerodynamic sorting taking place prior to accretion. This work has identified that the lack of sorting evidence might be due to a combination of processes varying from terrestrial weathering to parent body processes such as aqueous alteration and/or mild thermal metamorphism. All these processes might cause the grain to coarsen or to produce a metasomatic transformation generating different mineral phases as product of chemical alteration of the starting mineral. Thus, the metals and sulfides size appear to be controlled prevalently by parent body processes, either thermal or aqueous processes.

The presence of amorphous silicates and presolar grains in the matrix of the four meteorites studied in this project, indicated that the samples in question did not experience significant thermal metamorphism. Even a small increase in temperature would have caused the amorphous silicate to crystallise and the presolar grains to degas. This confirms that the samples investigated in this project are to be considered unmetamorphosed, and the opaque coarsening observed in the matrix of ALHA77307 and MIL 07687, compared to the opaques seen in Acfer 094 and QUE 99177 is likely to be not caused by thermal metamorphism.

It is not clear whether aqueous alteration has a similar effect on the opaque phases causing crystal coarsening. However, based only on petrologic observation of the high resolution image maps, it appears that the brighter phases in the EsB image, almost certainly to be opaque phases, are intimately associated with the light grey phase. This is most likely Fe-oxides, probably originated by the alteration of the opaque phases. In addition to the

opaque and Fe-oxides intimate association, suggesting a genetic relationship, the opaque phases in this context tend to be coarser than the usual nano-sized particles seen in the least altered portion of the investigated areas (Fig. 4.4.1a&b, 4.4.3b&c); the samples ALHA77307 and MIL 07687 are more affected by these processes. These observations suggest that aqueous alteration may play a role both in the oxidising and coarsening of the opaque phases, although more detailed investigations are needed to prove this hypothesis.

6.3 - Matrix similarities with IDPs and protoplanetary dust

This work has highlighted some similarities between matrix constituents, astronomical dust and IDPs, bridging the gaps between these different types of extra-terrestrial material which have been suspected to have genetic links. The infrared and mid-infrared Space Observations of protoplanetary disks surrounding pre-main-sequence stars have revealed the presence of amorphous silicates and other dust species whose emission bands match well those of Mg-rich and Fe-poor crystalline silicates of the olivine in particular their Mg-rich end members forsterite and enstatite respectively (Natta and Testi, 2006). Also evidence for FeS and SiO_2 was found (Keller et al., 2002), similar to observation of astronomers, these investigations have revealed in the matrix of our samples the presence of these components. For instance micro-XRD investigations have revealed the presence of abundant amorphous silicates along with the presence of olivine and enstatite grains; element map observations have supported these observations revealing the enrichment of the cations Si and Fe in the groundmass (presumably amorphous material). This is consistent with astronomical observations, where Fe-bearing amorphous silicates are observed. Furthermore, evidence of primordial dust preserved within the matrix on samples ALHA77307 and MIL 0767 is given by the presence of crystals whose features are compatible with enstatite whiskers, typical solar nebula condensates found usually in

IDPs and occasionally reported in the matrix of ordinary chondrites (Alexander et al., 1989a, b; Leroux H. 2012) but never described in the matrix of carbonaceous chondrites.

The heterogeneity observed in chondrite matrix shows similarities to IDPs. Both sample types include materials from different parts of the protoplanetary disk, implying efficient horizontal transport mechanisms in the disk. Oxygen isotopic measurements carried out in this work have revealed dissimilarities with the oxygen isotopic signatures of bulk meteorites previously measured by Clayton and Mayeda (1998). This may be because the matrix has sampled different reservoirs within the protoplanetary disk. In contrast to whole rock observations, the oxygen isotopic signature of matrix regions appears to show similarities to IDPs. Enrichments in ^{17}O observed both in matrix and IDPs, possibly because of the presence of presolar grains, from the late accretion of molecular cloud material onto the protoplanetary disk. Therefore, isotopic analyses of matrix regions within meteorites provide supporting evidence for less than complete mixing in the protoplanetary disk prior to accretion.

Similarities between the matrix and IDPs are also emphasised by the petrological observation of probable condensates from the solar nebula allowing a genetic correlation between the matrix of carbonaceous chondrites and IDPs to be established. D/H isotopic variation within the matrix of sample CR2 QUE 99177 compared to other CR values was also revealed by this study. These variations in the D/H ratios in the samples measured show a narrower range compared to the bulk value measured for IDPs and this could be indicative of a more pronounced homogenisation.

6.4 - Parent body versus nebula processes

XANES investigations of the matrix on samples MIL 07687 and Acfer 094 have revealed that the bulk values of the oxidation state of the matrix constituents for both samples are Fe^{3+}-rich indicating that the matrix constituents are highly oxidised. Detailed observations of the matrix constituents have revealed that the vast majority of the particles are oxidised and reflect the bulk values. However, some grains within the matrix are Fe^{2+}-rich indicating less oxidising conditions of the environment where they formed.

Based on SEM observation these Fe^{2+}-rich grains in Acfer 094 seem to be condensates from the solar nebula, and the element map indicates that are Al-rich (Fig. 3.4.12). If the nature of these grains is confirmed as CAI, this would indicate that they are exhibiting the oxidation state of the environment from where they condensed. Similarly, a Fe-rich grain the matrix of MIL 07687 shares same less oxidising conditions. Therefore reducing conditions were likely in place during the formation of this Fe^{2+} grain. Aqueous alteration processes have to be considered responsible for the oxidising conditions widely displayed by the rest of the matrix constituents. That matrix constituents have sampled regions of the solar nebula characterised by oxidizing conditions cannot be ruled out, and for Acfer 094 this would be consistent with the finding of amorphous silicates as a nebular oxidation product of a fractionated solar gas component described by Hoppe et al., 2015.

In general, it is very challenging to discriminate between oxidising conditions generated by aqueous alteration and Fe^{3+} caused by terrestrial weathering. However, post-accretionary processes are the most likely cause of the oxidation observed, and as for MIL 07687 the petrological evidence of reactive transport during fluid flow are pointing towards a parent body origin of these oxidizing conditions. The distribution of the Fe-rich phase in Fig. 3.2.21 has led, in fact, to the speculation that an ice layer coating the silicate grain may have been the source of the fluid percolating through this matrix region. The water

generated by the ice melting distributed outwards through capillary action, and the exhaustion of the water supply resulted in the stalled front of alteration and localised aqueous alteration observed in the matrix.

6.5 - Accretion processes

The observations carried out in this work, on the matrix of QUE 99177, have highlighted some interesting accretionary processes. These are linkable to the model of chondrule redistribution in the carbonaceous chondrite parent body proposed by Tomeoka & Ohnishi (2011). According to this model highly hydrated clasts in the Mokoia CV3 carbonaceous chondrite, including hydrated chondrules, inclusions, and the rims surrounding them, are produced by brecciation within a wet region of the parent body. These were subsequently transported and incorporated into the dry matrix. Similarly, in the matrix of QUE 99177 it has been observed in this work a region exhibiting substantial differences in degree of aqueous alteration compared to other areas. These textural differences suggest the region experienced heavy alteration processes and it may be a clast. The absence of kamacite in the clast, also suggests that this region might have been exposed to a micro-chemical environment where kamacite altered perhaps to form tochilinite, therefore confirming the heavy alteration experienced by the clast. Finally, the presence in the clast's neighbourhood, of a Si-rich object characterised by feathered texture which might be a glassy impact spherule, also points towards an impact event that generated splash melt and clasts.

6.6 - Future work

While this project has provided some constraints on the pre-accretionary and post-accretionary history of chondritic matrix, further work is required to fully understand the origins and evolution of this material. The outcome of this research is paramount for our understanding of primitive asteroids, which will be the target of the asteroid return missions JAXA Hayabusa 2 returning in 2020 and NASA OSIRIS-REx returning in 2023, and therefore interest in this topic is likely to be high.

In particular it is important to address the following questions:

What is the 3D structure of meteorite matrix and what is the relationship of opaque grains to amorphous material?

The study in this thesis looked only at the 2D structure of this material. Further to the study of matrix in primitive chondrites in this work, the samples Acfer 094 and QUE 99177 have been selected for analysis of the 3D distribution of metal grains embedded in the amorphous silicates. The selection criteria leading to the choice of these two particular samples were based on the abundances of the opaque phases revealed by the size distribution study of the grains constituting the matrix.

Some of amorphous silicates present in the matrix may have an interstellar origin, since these silicates are ubiquitous through the interstellar space (Bradley, 2005). However, these amorphous grains are mainly considered of nebular origin and thought to have formed from disequilibrium condensation (e.g. Brearley, 1992) and are intimately associated with sulfides and Fe, Ni metal. The origin of nanosulfides is not clearly understood, their close association with amorphous silicates suggest a genetic relationship between the two materials and it has been proposed that the most plausible formation mechanism is annealing of an amorphous precursor either in the solar nebula or in the parent body

(Abreu et al., 2009), and further study of these matrix constituents and their relationships are needed. Studying the relationship between the discrete grains of sulfides and Fe, Ni metal occurring in the amorphous silicates could elucidate the mechanism process for their formation.

How did the amorphous material form? Condensation experiments will complement the investigation carried out on the meteorites. This further research project aims to construct a robust model for solid formation and evolution in space by combining the 3D structure analysis of GEMS and matrix material. To gain a better understanding of dust evolution processes linked to space weathering conditions 3D structure analysis of space-weathered samples with ion-beam irradiation experiments will be combined. Understanding the mechanism of solid formation of the amorphous silicates and opaque grains associated can lead to a better understanding of the accretionary processes. This future experiment will be carried out in collaboration with Kyoto University in Japan where we will have access to SR micro and nano-XCT (resolution: >~100 μm) at the Japanese SPring-8 synchrotron facilities SPring-8. Prior to the synchrotron experiments samples almost cube in shape, of approximately 30×30×30 μm in size, will be extracted using FIB technique at Kyoto University. The results obtained will then be then compared with nano-CT investigations that will be carried out at the Natural History Museum in London, using the Gatan X-ray Ultra Microscope (XUM) which is a scanning electron microscope-hosted system capable of sub-micron voxel resolution (theoretical resolution of 500nm).

Did the whisker shaped crystals observed in the matrix form by condensation? FIB sections of the Mg silicate whiskers observed in the matrix of samples ALHA77307 and MIL 07687 will be FIB-ed at Hawaii University where accurate TEM investigation will be carried out in order to identify the mineralogical phase of these acicular shaped crystals

and reveal their axis of elongation. Crystals formed by nebular or circumstellar gas condensation at low-pressure environment and temperatures are characterised by axial screw dislocations and are elongated along the axis of elongation [100] which should be identifiable by TEM.

What are the oxygen and hydrogen isotope systematics of primitive matrix? We only had the opportunity to make preliminary measurements on oxygen and very little for D/H. Further characterisation of oxygen and hydrogen isotopes in the matrix is required to better constrain the different isotopic reservoirs in the protoplanetary disk and the effects of the aqueous alteration. For oxygen analyses, in order to compare bulk matrix to bulk meteorite and IDPs better, higher probe currents in spot mode should be used as opposed to mapping. This would provide much higher precision results to explore variability observed better although this would cause the loss of any isotopic heterogeneity information within each area analysed.

What was the pre-accretionary oxidation state of matrix material? The investigation of the oxidation state of the minerals in the matrix was carried out to on two samples (Acfer 094 and MIL 07687) only, and therefore should be applied to the other two samples (QUE99177 and ALHA77307). These minerals in the matrix of these samples may preserve the oxidation state of the environments where they formed as it was confirmed during the course of this work that they also preserve matrix constituents of nebular origin such as whiskers in ALHA77307, or presolar grains in both samples. Further investigations such as detailed TEM observations are required to establish the nature of the variation in the minerals oxidation state observed. The aim of the carrying out more detailed investigations would be to assess whether these variations are due to the sampling of diverse reservoir in the protoplanetary disk or whether these are due to the effects of parent

body processes and/or terrestrial contamination. Investigating the relationship between different matrix constituents would allow the discrimination between parent bodies processes effects from terrestrial weathering.

References

Abreu M., & Brearley A., J. 2006. *Meteoritics & Planetary Science.* (41): 5372.

Abreu N., M., & Brearley A., J. 2009. *Geochimica et Cosmochimica Acta*. (74): 1146–1171.

Abreu N., M., Brearley A., J. 2010. *Geochimica et Cosmochimica Acta* (74): 1146-1171.

Abreu N., M., & Brearley A., J. 2010. *Meteoritics & Planetary Science*. (46): 252–274.

Aléon J. *Astrophys. J* . 2010. (722): 1342–1351.

Aléon J., Engrand C., Leshin L., A., McKeegan K., D. *Geochimica et Cosmochimica Acta* .2009. (73): 4558–4575.

Allen A. 2004. *Astrophysics and Space Science* (292): 361–364.

Alexander C., M.,O' D., Bowden, R., Fogel, M., L., Howard , K., T., Herd, C.,D.,K., Nittler L., R., 2012 *Science* (337): 721-723.

Alexander C., M., O., Hutchison R., & Barber D., J. 1989a. . *Earth Planet. Sci. Lett.* (95): 187-207.

Alexander C., M., O'D., Barber D., J., & Hutchison R. 1989b. *Geochimica et Cosmochimica Acta* (5): 3045-3057.

Alexander C., M., O'D., Bowden R., Fogel M., L., Herd C., D., K., & Nittler L., R. 2012. *Science*. (337): 721–723.

Alexander C., M., O., Bowden R., Fogel M., L., Howard K., T., Herd C., D., K., Nittler L., R.2012. *Science.* (337): 721–723.

Alexander C., M., O'D. 2005. *Meteoritics & Planetary Science*. (40): 943–965.

Alexander C., M.,O'D., 2004. *Geochimica et Cosmochimica Acta. (68*): 3943-3969.

Altwegg K. et al. 2015. *Science.* (347): 1261952-1.

Amari S. 2014. *The Mass Spectrometry Society of Japan.* (3):1-6.

Amari S., Anders E., Virag A., & Zinner E. 1990. *Nature.* (345): 238–240.

Amari S., Lewis R., S., & Anders E. 1995. *Geochimica et Cosmochimica. Acta.* (59): 1411–1426.

Anders E., & Grevesse N. 1989. *Geochimica et Cosmochimica Acta.* (53): 197-2 14.

Anders E., & Zinner E. 1993. *Meteoritics* (28): 490–514.

Anders E. 1964. *Space Science Review*. (3): 583–714.

Apai D., Pascucci I., Bouwman J., Natta A., Henning T., & Dullemond C., P. 2005. *Science* .(310): 834-836.

Arce H., G, Sargent A., I. 2006. *Astrophys. J.* (646): 1070.

Ashworth J., R. 1977. *Earth Planet. Sci. Lett.* (35): 25-34.

Balbus S.A., Hawley J.F. 1991. *Astrophys. J*. (376): 214

Benisty M., Juhasz A., Boccaletti A. 2015. *Astronomy and Astrphysics*. (578): L6.

Bland P., A., Alard O., Benedix G., K., Kearsley A., T., Menzies O., N., Watt L., E., & Rogers N., W. 2005. *PNAS*. (102): 13755–13760.

Blum J., & Wurm G. 2000. *Icarus*. (143): 138.
Boccaletti A., Pantin E., Lagrange A., M., Augereau J.,C., Meheut H., & Quanz S., P. 2013. *Astronomy and Astrphysics*.(560): A20.
Bockelee-Morvan D., Gautier D., Hersant F., Hure' J., M., & Robert F. 2002. *Astronomy and Astrophysics*. (384): 1107-1118.

Bockelée-Morvan D., Gautier D., Lis D., C., Young K., Keene J., Phillips T., Owen T., Crovisier J., Goldsmith P., F., Bergin E., A., Despois D., & Wooten A. 1998. *Icarus.* (193): 147–162.

Bouvier A., & Wadhwa M. 2010. *Nature Geoscience*. (3): 637-641.

Brogan C., L., et al., 2015. *The Astrophysical Journal Letters.* (808): 1-10.

Bunch T., E., & Chang S. 1980. *Geochimica et Cosmochimica Acta*. (44): 1543–1577.

Bell J., F., Davis D., R., Hartmann W., K., & Gaffey M., J. 1989. *In Asteroids II University of Arizona Press, Tucson* : 921–945.

Berger M., 1963. *Methods in computational physics I*. (Academics, New York).

Bernatowicz T., Fraundorf G., Tang M., Anders E., Wopenka B., Zinner E., & Fraundorf P. 1987. *Nature.* (330): 728–730.

Bernatowicz T., J., Akande O., W., Croat T., K., & Cowsik R. 2005. *Astrophys. J*. (631): 988–1000.

Bernatowicz T., J., Amari S., Zinner E., K., & Lewis R., S. 1991. *Astrophys. J.* (373): 73–76.

Bernatowicz T., J., & Walker R., M.1997. *Physics Today*. (50): 26-32.

Bernatowicz T., J., & Zinner E. 1996. *AIP*, 750pp.

Bernatowicz T., J., Cowsik R., Gibbons P., C., Lodders K., Fegley B., Jr., Amari S., & Lewis R., S. 1996. *Ap. J.* (472): 760–782.

Bernatowicz T., J., Messenger S., Pravdivtseva O., Swan P., & Walker R., M. 2003. *Geochimica et Cosmochimica. Acta*. (67): 4679–4691.

Bischoff A., & Geiger T. 1994. 25th *Lunar and Planet. Sci.* 115-116.

Bischoff A., Palme H., Clayton R.,N., Mayeda T.,K.., Grund T., Spettel B., Geiger T., Endreß M., Beckerling W., & Metzler K. 1991. *Meteoritics.* (260): 318-319.

Bizzarro M., Baker J.,A., Haack H., Lundgaard K., L. 2005. *Astrophys. J*. (632): 41–44.

Bland P., A., Alard O., Benedix G., K., Kearsley A., T., Menzies O., N., Watt L., E., & Rogers N., W. 2005. *Proc. Natl. Acad. Sci.* (102): 13755–13760.

Blott S., J., & Pye K. 2001. *Earth Surface Processes and Landforms.* (26): 1237–1248.

Bodénan J., D., N., A., Starkey, Russell S., S., Wright I., P., Franchi I., A. *Earth and Planetary Science Letters.* 2014 (401): 327–336.

Bonal L., Bourot-Denise M., Quirico E., Montagnac G., & Lewin E. 2007. *Geochimica et Cosmochimica Acta.* (71): 1605–1623

Bonal L., Quirico E., Bourot-Denise M., Montagnac G. 2006. *Geochimica et Cosmochimica Acta.* (70): 1849-1863.

Bourdelle F., Benzerara K., Beyssac O., Cosmidis J., Neuville D., Gordon R., Brown Jr., Paineau E. 2013. *Contrib Mineral Petrol*. (166): 423–434.

Bouwman J., Henning T., Hillenbrand L., Silverstone M., Meyer M., Carpenter J., Pascucci I., Wolf I., Hines D., & Kim J. 2006. *Astrophys. J.* (653): 57-60.

Bradley J., P., 1988. *Geochimica et Cosmochimica Acta. (*52): 889.

Bradley J.P. 2005. *Treatise on Geochemistry II*, (1): 689-737.

Bradley J., P., Brownlee D., E., & Veblen D., R. 1983. *Nature.* (301): 473.

Bernatowicz T., J., Messenger S., Pravdivtseva O., Swan P., & Walker R., M. 2003. *Geochimica et Cosmochimica. Acta*. (67): 4679–4691.

Bradley J., P., Germani M., S., & Brownlee D., E. 1989. *Earth Planet. Sci. Lett.* (1): 93.

Bradley J., P., Davis A., M. 2003. *Meteorites, Comets and Planets, Treatise on Geochemistry.* (Oxford: Elsevier) (1): 689.

Brearley A., J., & Jones R., H. 1998. *In Planetary Materials* (ed. J. J. Papike). (36): 3-1–3-398.

Brearley A., J. 2012. *43*rd *Lunar and Planet. Sci.* 1233.

Brearley A., J. 2003b. 66th *Annual Meteoritical Society Meeting*.5262.

Brearley A., J. 1992. *Geochimica et Cosmochimica Acta.* (57): 1521-1550.

Brearley A., J. 1993. *Geochimica et Cosmochimica Acta* (57): 1521–1550.

Brearley A., J. 1997. 28th *Lunar and Planet. Sci.* 153–154.

Brearley A., J. 2013. *76th Annual Meteoritical Society Meeting. 5206.*

Brearley A., J., Krot A., N. 2013 *Notes in Earth System Sciences*.659–789.

Brearley A., J., & Rubie D.,C. 1990. *Journal of Petrology*. (31): 925–956.

Brotton S., J., Shapiro R., van der Laan G., Guo J., Glans P., A., Ajello J., M. 2007. *J Geophys Res Biogeosci*. (112):G3.

Brownlee D., E., Tsou P., Aléon J., et al. 2006. *Science.* (314): 1711.

Brucato J., Colangelo R., Mannella V., Palumbo P., & Bussoletti E. 1999. *Astron. Astrophys.* (3487): 1012-1019.

Burbidge E., M., Burbidge G., R., Fowler W., A., & Hoyle F. 1957. *Rev. Mod. Phys.* (29): 547–650.

Burbine T., H., McCoy T., J., Meibom A., Gladman B., & Keil K. 2002. *University of Arizona Press, Tucson.* 653–669.

Busemann H., Alexander C., M., O'D., Nitta L., R. 2007. *Meteor. Planet. Sci.* (42): 1387–1416.

Busemann H., Young A., F., Alexander C., M., O'D., Hoppe P., Mukhopadhyay S., Nittler L., R. 2006. *Science.* (312): 727–30.

Cameron A., G., W. 1957. *AELC (Atomic Energy Canada),* CRL: 41.

Cameron A., G., W. 1962. *Icarus.* (1): 13–69.

Campbell A., J., Zanda B., Perron C., Meibom A., Petaev M., I. 2005. *In Chondrites and the protoplanetary disk.* 407–31.

Carballido A., Fromang S., & Papaloizou J. 2006. *Montly Notices of the Royal Astronomical Society*. (373): 1633–1640.

Chen C.,T., Idzerda Y., U., Lin H., J., Smith N., V., Meigs G., Chaban E., Ho G., H., Pellegrin E., Sette F. 1995. *Phys Rev Lett 75.* (1):152–155.

Choi B., McKeegan K., Krot A., & Wasson J. 1998. *Nature* (392): 577-579.

Ciesla F., J., Lauretta D., S., Cohen B., A., Hood L., L. 2003. *Science.* (299): 549–52.

Clayton R., N., & Mayeda T., K. 1984. *Earth and Planetary Science Letters*. (67): 151–161.

Clayton R., N., & Mayeda T., K. 1963. *Geochimica et Cosmochiica Acta.* (27): 43–52.

Clayton R., N., & Mayeda T., K. 1983. *Earth Planet. Sci. Lett. (*62):1–6.
Clayton R., N., & Mayeda T., K. 1996. *Geochimica et Cosmochimica Acta*. (60): 1999–2017.

Clayton D., D. 1980. *Earth Planet. Sci. Lett.* (47): 199.

Clayton D., D.2003. *Astrophys. J.* (598): 313–324.

Clayton R., N. 2002. *Nature.* (415): 860–861.

Clayton R., N., Mayeda T., K., Goswami J., N., & Olsen E., J. 1991. *Geochimica et Cosmochimica. Acta*. (55): 2317–2337.

Clayton R., N., 1993. Annual Review of Earth & Planetary Sciences (21): 115–149.

Clayton R., N., & Mayeda T., K 1999. *Geochimimica et Cosmochimica Acta*. (63): 2089–2104.

Clayton R., N., Grossman L., & Mayeda T., K. 1973. *Science.* (182): 485–488.

Connelly J., N., Bizzarro M., Krot A., N., Nordlund Å., Wielandt D., Ivanova M., A. 2012. *Science.* (338): 651.

Corrigani C., M., Zolensky M., E., Dahl J., Long M., L., Weir J., Sapp C., & Burket P., J.1997.*Meteoritics & Planetay Science.* (32): 509-5 15.

Cressey G., & Schofield P., F. 1996. *Powder Diffr.* (11): 35–39.

Croat T., K., Bernatowicz T., Amari S., Messenger S., & Stadermann F., J. 2003. *Geochimica et Cosmochimica. Acta*. (67): 4705–4725.

Croat T., K., Stadermann F., J., & Bernatowicz T., J. 2005a. *36th Lunar and Planet. Sci.* 1507.

Cuzzi J., N. 2004. *Icarus.* (168): 484–97.
Cuzzi J., N., Hogan R., C., & Bottke W., F. 2010. *Icarus*. (208): 518–538.

Cuzzi J., N., Hogan R., C., Paque J., M., Dobrovolskis A., R. 2001. *Astrophys. J.* (546): 496–508.

Cuzzi J., N., Hogan, R., C., & Shariff, K. 2008. *Astrophys. J.* (687): 1432.

Davidson J., Nittler L., R., Stroud R., M., Takigawa A., Alexander C., M., O'D., Kilcoyne A., L., D., & Cody G., D. 2015. *46th Lunar and Planet. Sci.* 1609.

Deer W., A., Howie, R., A., & Zussman J. 1992. Longman Scientific & *Technical, Harlow*.

Desch S., J ., Connolly H.,C., Jr. 2002. *Meteor. Planet. Sci.* (37): 183–207.

Dominik C., & Tielens A., G., G., M. 1997. *Astrophysical J.* (480): 647.

Draine B., T. 2003 *Ann. Rev. Astron. Astrophys.* (41): 241-289.
Dreibus G., Palme H., Spettel B., & Wänke H. 1995. *Meteorit. Planet. Sci.* (30): 439-445.

Eberhardt P., Reber M., Krankowsky D., & Hodges R., R. 1995. *Astron. Astrophys*. (302): 301–316.

Elmegreen D., M. 1980. *Astrophys. J* .(242): 528.

Emsley J. 2001. *Oxford University Press*. (1): 297- 304.

Engrand C., Deloule E., Robert F., Maurette M., & Kurat G.1999. *Meteoritics & Planetary Science*. (34): 773–786.

Epstein S., Krishnamuty R., V., Cronin J., R., Pizzarello S., & Yuen G., U. 1987. *Nature.* (326): 477–479.

Evans Analytical Group (EAG). http://www.eag.com/mc/sims-ion-beam-sputtering.html.

Fegley B., Jr., & Palme H. 1985. *Earth Planet. Sci. Lett.* (72):311–326.

Floss C., Stadermann F. J., Bradley J. P., Dai Z. R., Bajt S., & Graham G. 2004. *Science*. (303): 1355.

Floss C., & Stadermann F., J. 2007. *Meteorit. Planet. Sci.* (42): 5060.

Floss C., & Stadermann F., J. 2008a. 39th *Lunar and Planet. Sci.*1280.

Floss C., & Stadermann F., J. 2008b. *Geochimica et Cosmochimica Acta.* (73): 2415–2440.

Floss C., Brearley A., J. 2014. *77th Annual Meteoritical Society Meeting.* 5183.

Folk R., L., & Ward, W., C. 1957. *J. Sed. Pet*. (3): 27.

Franchi A., Baker L., Bridges J., C., Wright P., & Pillinger C., T. 2001. *Phil. Trans. Royal Soc. London* (359): 2019-2035.
Fromang S., Papaloizou J. 2006. *Astronomy and Astrophysics*. (452): 751.
Fukagawa et al. 2013. *Publications of the Astronomical Society of Japan*.

Füri E., Marty B. 2015. *Nature Geoscience*. (8): 515–522.

Gail H., P. 1998. *Astronomy and Astrophysics*. (332): 1099.

Gail H., P. 2002. *Astromineralogy.* (1): 55.

Gail H., P. 2004. *Astronomy and Astrophysics*. (413): 571–591.

Gao X., Amari S., Messenger S., Nittler L., R., Swan P., D., & Walker R., M. 1996. *Meteoritics.* (31): A48.
Gilmour I., Heinrich D., H., & Karl K., T., 2003. *In Treatise on Geochemistry*. (1):269-290.

Goldreich P., Lithwick Y., & Sari R. 2004. *Annual Review of Astronomy and Astrophysics* (42): 549-601.

Goldreich P., Ward W., R. 1973. *Astrophys. J.* (183): 1051.

Goldstein J., I., Newbury D., E., Echlin P., Joy D., C., Roming A., D., Lyman C., E., Fiori C., Lifshin E. 1992. *Scanning electron Microscopy and X-ray Microanalysis.* (2):820.
Gómez G., C., Ostriker E., C. 2005. *Astrophys. J.* (630): 1093.

Goodman J., & Rafikov R., R. 2001. *Astrophys. J.* (552): 793.

Grady C., A., Muto T., Hashimoto J. 2013. *Astrophys. J.* (762): 48.

Greenwood R., C., Franchi I., A., Kearsley A., T., & Alard O. 2010. *Geochimica et Cosmochimica Acta*. (5) 1684–1705.

Greenwood R., C., Barrat J., A., Yamaguchi A., Franchi I., A., Scott E., R., D., Bottke W., F., & Gibson J., M. 2014. *Earth and Planetary Science Letters.* (390): 165–174.
Greenzweig Y. & Lissauer J., J. 1990. *Icarus.* (87): 40.

Greenzweig Y., & Lissauer J., J. 1992. *Icarus.* (100): 440.

Greshake A. 1997. *Geochimica et Cosmochimica Acta.* (61): 437–452.

Grossman J., N., & Brearley A., J. 2005. *Meteoritics & Planetary Science*. (40):87–122.

Grossman J., N., & Brearley A. J., 2005. *Annu. Rev. Astron. Astrophys*. (42): 119–67.

Grossman J., N., Rubin A., E., Nagahara H., & King E., A. 1988. In *Meteorites and the Early Solar System.* (ed. J.F. Kerridge & M. S. Matthews): 619-659.

Grossman, J., N., Alexander C., M., O'D., Wang, J. & Breadley A., J. 2000. *Meteoritic and Planetary Science* (35): 467-486.

Grossman J., N., & Wasson J. 1982. *Geochimica et Cosmochimica Acta* (46): 1081– 1099.

Grossman J., N., & Wasson J. 1983. *Geochimica et Cosmochimica Acta* (47): 759–771.

Haisch K., E., Lada Jr., E., A., & Lada C., J. 2001. *Astrophys. J.* (553): 153.

Hayashi C., Narita S., & Miyama S., M. 1982. *Progress of Theoretical Physic.* (68): 1949-1966.

Hat'nCoat. 2008. File:Tungsten-filament.svg,12.
https://en.wikipedia.org/wiki/Transmission_electron_microscopy#/media/File:Tungsten-filament.svg.

Heinrich K., F., J., & Newbury D., E. 1991. *Plenum New York.*

Heinrich K., F., J., Newbury D., E., & Yakowitz H. 1976. *National Bureau of Standards Special Publication.* 460.

Herwartz D., Pack A., Bjarne F., Bischoff A. 2014. (344): 1146- 1150.

Hezel D., C. & Palme H. 2010. *Earth and Planetary Science Letters.* (294): 85–93.

Higginbottom N., Proga D., Knigge C., & Long K., S. 2017. *Astrophysical J.* (836): 1.

Hiroi T., Zolensky M., E., & Pieters C., M. 2001. *Science.* (293): 2234–2236.

Hong Y., & Fegley B., Jr. 1998. *Meteoritics & Planetary Science.* (33): 1101-1112**.**

Hoppe P., Amari S., Zinner E., & Lewis R. S. 1995. *Geochim. Cosmochim. Acta*. (59):4029–4056.

Hoppe P., & Vollmer C. 2008. *AIP Conference Proceedings.* (1001): 254-261.

Hoppe P., & Zinner E. 2000. *J. Geophys. Res.* (105): 10371–10385.

Hoppe P., Leitner J., Kodolányi J. 2015. *46th Lunar and Planet. Sci.*1315.

Howard K., T., Benedix G., K., Bland P., A. & Cressey G. 2009. *Geochimica et Cosmochimica Acta.* (73): 4576–4589.

Howard K., T., Benedix G.,K.,. Bland P.,A., Cressey G.2011. *Geochimica et Cosmochimica Acta* (75): 2735–2751.

Hsu W., Wasserburg G. J., & Huss G. R. 2000. *Earth Planet. Sci. Lett.* (182): 15–29.

Huss G., R., Alexander C., M.,O'D., Palme H., Bland P.A., Wasson J.,T. 2005. (See Krot et al. 2005c): 701–3.

Huss G., R., & Lewis R., S. 1995. *Geochim. Cosmochim. Acta.* (59): 115–160.

Huss G., R., MacPherson G., J., Wasserburg G., J., Russell S., S., & Srinivasan G. 2001. *Meteorit. Planet. Sci.* (36): 975–997.

Hutchison D., J., Alexander M., O'D., Barberd J. 1987. *Geochimica et. Cosmochimica Acta.*(51):1875-1882.

Hynes K., M., Croat T., K., Amari S., & Bernatowicz T., J. 2006. *46th Lunar and Planet. Sci.* 2202.

Ida S., & Makino J., 1993. *Icarus.* (106): 210.

Ikeda Y.1983. *Proc. NIPR Svom. Ant. Meteor Memoirs NIPR (Spec* Issue.) (30): 93-108.
Inaba S., & Ikoma M. 2003. *Astronomy and Astrophysics*. (410): 711.
Jacquet E., & Robert F. *Icarus.* 2013. *(*223): 722–732.

Johansen A., & Youdin A., N. 2007. *Astrophysical J.* (662): 627.

Johansen A., Youdin A., & Mac Low M. 2009. *Astrophys. J. Lett.* (704): L75.

Jones R., H., Lee T., Connolly H., C., Jr., Love S., G., & Shang H. 2000a *Protostars and Planets IV* (eds. V. Mannings, A. P. Boss, & S. S. Russell): 927–962.

Jones T., D., Lebofsky L., A., Lewis J., S., & Marley M., S. 1990. *Icarus*. (88): 172–192.

Keil K., 1968. *J. Geophys. Res*. (73):6945–6976.

Keller L., P., & Buseck P., R. 1990a. *Geochimica et Cosmochimica Acta.* (54): 1155-1163.

Keller L., P., & Messenger S. 2011. *Geochimica et Cosmochimica Acta* (75): 5336.

Keller L., P., Hony S., Bradley J., P., Molster F., J., Waters L., B., F., M., et al. 2002. *Nature*. (417): 148-150.

Kemper F., Vriend W., J., & Tielens A., G., G., M. 2004. *Astrophys. J.* (609): 826–837.

Kerridge J., F., Chang S., & Shipp R. 1987. *Geochimica et Cosmochimica Acta*. (51): 2527–2540.

Kilburn M., R., & Wacey D. 2014. *Principles and Practice of Analytical Techniques in Geosciences* (4): 1-34.

King A., J., Schofield P., F., Howard K.,T., Russell S.,S. 2015. *Geochimica et Cosmochimica Acta.* (165): 148–160.

Kita N., T., Huss G., R., Tachibana S., Amelin Y., Nyquist L., E., & Hutcheon I., D. 2005. *In Chondrites and the Protoplanetary Disk* (eds. A. N. Krot, E. R. D. Scott, & B. Reipurth). (341): 558–587.

Kitajima F., Nakamura T., Takaoka N., & Murae T. 2002. *Geochimica et Cosmochimica Acta.* (66): 163–172.

Kleine T., Mezger K., Palme H., Scherer E., & Münker C. 2005.*Geochimica et Cosmochimica Acta*. (69): 5805–5818.

Klerner S., & Palme H. 2000. *Meteorit. Planet. Sci.* (35): A89.

Kokubo E., & Ida S. 1998. *Icarus*. (131): 171.

Krot A., N., Amelin Y., Cassen P., Meibom A. 2005a. *Nature.* (436): 989–92.

Krot A., N., Brearley A., J., Ulyanov A., A., Biryukov V., V., Swindle T., D., Keil K., Mittlefehldt D., W., Scott E., R., D., Clayton R., N., & Mayeda T., K., 1999. *Meteoritics & Planetary Science*. (34): 67-89.

Krot A., N., Fegley B., JR., Lodders K., & Palme H. 2000. *Protostars and planets* (IV):1019.

Krot A., N., Petaev M., I., Scott E., R., D., Choi, B.-G., Zolensky M., E., & Keil K. 1998c . *Meteorit. Planet. Sci.* (33): 1065–1085.

Krot A., N., Petaev M., I., Zolensky M., E., Keil K., Scott E., R., D., & Nakamura K. 1998d. *Meteorit. Planet. Sci.* (33): 623–645.

Krot A., N., Scott E., R., D., & Zolensky M., E. 1997. (32): 31–49.

Krot A., N., Scott, E., R., D., &, Zolensky M., E. 1995. *Meteoritics*. (30): 748–776.

Kuebler K., E., McSween, H., Y., Jr., Carlson W., D., & Hirsch D. 1999. *Icarus.* (96): 141.

Kwon W., Looney L., W., & Mundy L., G. 2011. *Astrophys. J.* (741): 3.

Larimer J., W., & Anders E. 1967. *Geochimica et Cosmochimica Acta* (31): 1239-1270.

Larimer J., W., & Anders E. 1970. *Geochimica et Cosmochimica Acta* (34): 367-387.

Lauretta D. S., Kremser D. T., and Fegley B. 1996. *Proceedings of the NIPR Symposium on Antarctic Meteorites.* (9): 97–110.

Lauretta D. S., Lodders K., Fegley B., & Kremser D. T. 1997. *Earth and Planetary Science Letters.* (151): 289–301.

La Vigne M., A., Vogel S., N., Ostriker E., C. 2006. *Astrophys. J.* (650): 818

Le Guillou C., Changela H., G., Brearley A., J. *Earth and Planetary Science Letters* .13117.

Lee T., Papanastassiou D., A., & Wasserburg G., J. 1978. *Astrophys. J. Lett*. (220): 21–25.

Leroux H.2012. *43rd Lunar and Planet. Sci.*1761.
Lewis R., S., Tang M., Wacker J., F., Anders E., & Steel E.1987. *Nature*. (326): 160–162.
Liffman K., 2005. *Meteorit. Planet. Sci.* (40): 123.

Liffman K., & Toscano M. 2000. *Icarus.* (143): 106–125.

Lodders K., & Osborne R. 1999. *Space Sci. Rev.* (90): 289–297.

Lodders K.2003. *Astrophys. J.* (591): 1220-1247.

Lodders K., Amari S. 2005. *Chemie der Erde Geochemistry.* (65): 93-166.

Lugaro M., Zinner E., Gallino R., & Amari S. 1999. *Astrophys. J.* (527): 369–394.

Lyons J., R., & Young E., D. 2005. *Nature*. (435): 317–320.

MacPherson G., J., Kita N.,T., Ushikubo T., Bullock E.,S., Davis A.,M. 2012. *Earth Planet. Sci. Lett.(*43–54): 331–332.

Marty B. *Earth Planet. Sci. Lett.* 2012. (56–66): 313–314.

Mathis J., A. 1993. *Rep. Prog. Phys.* (56): 605–652.

Mathis J., S. 1990. *Ann. Rev. Astron. Astrophys.* (28): 37–70.

Mayer L., Quinn T., Wadsley J., & Stadel J. 2004. *Astrophys. J.* (609): 1045–1064.

McKee C., F., Ostriker E., C. 2007. *Annual Review of Astronomy and Astrophysics*. (45): 565–687.

McKeegan K., D., Kallio A., P., A., Heber V., S., Jarzebinski G., Mao P., H., Coath C., D., Kunihiro T., Wiens R., C., Nordholt J., E., Moses R., W., Jr., Reisenfeld D., B., Jurewicz A., J., G., & Burnett D., S. 2011.*Science.* (332):1528–1532.

McKeegan K., D., Kudryavtsev A.,B., & Schopf J.,W. 2007. *Geology*. (35): 591–594.

McKeegan K., D., Walker R., M., & Zinner E. 1985. *Geochimica et Cosmochimica Acta*. (49): 1971–1987.

McSween H., Y., Jr. & Richardson S., M. 1977. *Geochimica et Cosmochimica Acta*. (41): 1145–1161.

McSween H., Y., Jr. 1979. Rev. *Geophys. Space Phys.* (17): 1059–1078.

Mcsween H., Y., JR. 1977. *Geochimica et Cosmochimica Acta*. (41): 477-491.

Meier R., Owen T., C., Jewitt D., C., Matthews H., M., Senay M., Biver N., Bockelée-Morvan D., Crovisier J., & Gautier D. 1998a. *Science*. (279): 1707–1710.

Meier R., Owen T., C., Matthews H., E., Jewitt D., C., Bockelée- Morvan D., Biver N., Crovisier J., & Gautier D. 1998b. *Science*. (279): 842–898.

Mendybaev R., A., Beckett J., R., Grossman L., Stolper E., Cooper R., F., & Bradley J., P. 2002. *Geochimica et Cosmochimica. Acta*.(66): 661–682.
Messenger S. 2000. *Nature.* (404): 968–971.

Messenger S., & Bernatowicz T., J. 2000.*Meteorit. Planet. Sci.* (35): 109.

Messenger S., Amari S., Gao X., Walker R., M., Clemett S., Chillier X., D., F., Zare R., N., & Lewis R. 1998. *Astrophys. J.* (502): 284–295.

Messenger S., Keller L., P., Stadermann F., J., Walker R., M., & Zinner E., 2003. *Science* (300): 105-108.

Metzler K., Bischoff A., & Stöffler D. 1992. *Geochimica et Cosmochimica Acta. (*56): 2873–2897.

Meyer B., S.2005. *In Chondrites and the Protoplanetary Disk, Astronomical Society of the Pacific Conference Series* (341): 515-526.

Miller M., F., Franchi I., A., Sexton A., S. & Pillinger C., T. 1999. *Rapid Commun. Mass Spectrom.* (13): 1211–1217.

Miyake T., Suzuki T., K., Inutsuka S. 2016. *astro-ph.EP* (3). Morfill G., E., Durisen R., H., & Turner G., W. 1998. *Icarus.* (134): 180–184.

Molster F., J., Yamamura I., Waters L., B., F., M. 1999. *Nature*. (401): 563.

Muto T., Grady C., A., Hashimoto J. 2012. *Astrophys. J. Lett.* (748): L22.

Nakamura K., Messenger S., Keller L., P., Robert F., Walker M. 2009. *72nd Annual Meteoritical Society Meeting.* 5330.

Nakamura T., Noguchi T., Tsuchiyama A., et al. 2008. *Science* (321): 1664.

Nakamura T., Noguchi T., Tsuchiyama A., Ushikubo T., Kita N., T., Valley J., W., Zolensky M., E., Kakazu Y., Sakamoto K., Mashio E., Uesugi K., & Nakano T. 2008. *Science*. (321): 1664–1667.

Nakashima D., Ushikubo T., Zolensky M., E., & Kita N., T. 2012.
Meteorit. Planet. Sci. (47): 197–208.

Natta A., & Testi L. 2006. *Astrophys. J.* (645): 69-72.

Newbury D., E., Joy D., C., Fiori C., Goldstein J., I. 1986. *Plenum New York.*

Newton J., Bishoff A., Arden J., W., Franchi I., A., Geiger T., Greshake A., & C.,T., Phillinger. 1995. *Meteoritics.* (30): 47-56.

Nguyen A., N., Alexander C., M., O'D., & Nittler L., R.2008. *71st Annual Meteoritical Society Meeting*. 5277.

Nguyen A., N., Nittler L., R., Stadermann F., J., Stroud R., M., & Alexander C., M., O'D. 2010. *Astrophys. J.* (719): 166–189.

Nittler L., R. 2003. *Earth Planet. Sci. Lett*. (209): 259–273.

Nittler L., R., Alexander C., M., O' D., Gao X., Walker R., M., & Zinner E. 1997. *Astrophys. J.(*483): 475–495.

Nuth Brearley A., J., & Scott E., R., D. 2005. *Astronomical Society of the Pacific, San Francisco.* (3): 675–700.

Ormel C., W., Dullemond C., P., & Spaans M., 2010. *Astrophys. J.* (714): L103.

Ormel C., W., & Klahr H., H. 2010. *Astronomy and Astrophysics*. (43): 520A.

Owen J., E., Ercolano B., Clarke C., J., & Alexander R., D. 2010. *Montly Notices of the Royal Astronomical Society*. (401): 1415–1428.

Owen J. 2016. *Publications of the Astronomical Society of Australia*. (33).
Padovani M., Galli D., Glassgold A., E. 2009. *Astronomy and Astrphysics*. (501): 619.
Palme H., & Wlotzka F. 1976. *Earth Planet. Sci. Lett.* (33): 45–60.

Palmer E., E., & Lauretta D., S. 2011. *Meteoritics & Planetary Science.* (46): 1587–1607.

Paque J., M. & Cuzzi J., N. 1997. 28th *Lunar and Planet. Sci.* 1071–1072.

Pecharsky V., K., & Zavalij P., Y. *Kluwer academic publishers*. 2003. (1):1-713.

Peck J., A., & Wood J., A. 1987. (51): 1503–1510.

Piani L., Robert F., Remusat L. 2015. *Earth and Planetary Science Letters.* (415): 154–164.

Pizzarello S., Krisnamurthy R., V., Epstein S., & Cronin J., R. 1991. *Geochimica et Cosmochimica Acta*. (55): 905–910.

Quirico E., Bonal L., Bourot-Denise M., & Montagnac G. 2006. *Meteorit. Planet. Sci.* (41): 5305.

Rafikov R., R. 2002, *Astrophys. J.* (569): 997.

Rafikov R., R. 2016. *Astrophys. J.* (831):122-133.

Raha N., Sellwood J., A., James R., A., & Kahn F., D. 1991. *Nature.* (352): 411.

Rivkin A., S., Campins H., Emery J., P., Howell E., S., Licantro J., Takir D., & Vilas F. 2015. *Asteroids IV.* (P.Michel et al., eds.): 65-87.

Robert F. 2006. *In Meteorites and the Early Solar System II*. (943): 341–351

Robert F. 2003. *Planet. Space Sci.* (50): 1227–1234.

Robert F., M., Javoy J., Halbout B., Dimon B., & Merlivat L. 1987. *Geochimica et Cosmochimica Acta*. (51): 1787–1806.

Robert F., & Epstein S. 1982. *Geochimica et Cosmochimica Acta*. (160): 81–95.

Rubin A., E., & Wasson J., T. 1986. *Geochimica et Cosmochimica Acta*. (50): 307–315.

Rubin A., E., Trigo-Rodríguez J.,M., Huber H., & Wasson J., T. 2007. *Geochimica et Cosmochimica Acta*. (71): 2361-2382.

Rumble D., Young E., D., Shahar A., & Guo W. 2008. *Elements magazine.* (7): 23-28.

Russell S., S., Arden J.,W., Pillinger C., T. 1991. *Science.* (254): 1188-1191.

Russell S., S., Srinivasan G., Huss G., R., Wasserburg G., J., & MacPherson G., J. 1996. *Science*. (273): 757–762.

Safronov V., S. 1969. *NASA Technical* Reports Server. F-677.

Sakamoto K., Okumura S.,K., Ishizuki S., Scoville N., Z. 1999. *Astrophys. J. Suppl.* (124): 403.

Sandford S., A. 1996. *Meteorit. Planet. Sci.* (31): 449–476.

Scalo J., M. 1977. *Astrophysical J.* (213): 705-711.

Scheller S., Berlin J.,& Terborg R. 2010. *Multi-Channel EDS Webinar*. Bruker Nano.

Scherstén A., Elliott T., Hawkesworth C., Russell S., & Masarik J. 2006. *Earth and Planetary Science Letters.* (241): 530–542.

Schneider D., M., Benoit P., H., Kracher A., & Sears D., W., G. 2003. *Geophys. Res. Lett.*(8): 1420.

Schrader D., L., Franchi I., A., Connolly H., C., Jr. Greenwood R., C., Lauretta D., S., Gibson M., J. 2011. *Geochimica et Cosmochimica Acta.* (75): 308–325.

Scott E., R., D. & Krot A., N. 2005 *Astrophys. J.*(623): 571–578.

Scott E., R., D., & Jones R., H. 1990. *Geochimica et Cosmochimica Acta.* (54): 2485-2502.

Scott E., R., D., & Krot A., N., 2003. *Meteorites, Comets and Planets, Treatise on Geochemistry.* (1): 143.

Scott E., R., D., & Krot A., N. 2005b. *In Chondrites and the Protoplanetary Disk (eds. A. N. Krot, E. R. D. Scott, & B. Reipurth). Astron. Soc. Pacific Conf. Ser*. (341): 15–53.

Scott E., R., D., & Krot A., N. 2007. *Meteorites, Comets and Planets (ed. A. M. Davis) Treatise on Geochemistry* (1): 1-72.

Scott E., R., D., Barber D., J., Alexander C., M., Hutchison R., & Peck J., A. 1988. *In Meteorites and the Early Solar System (eds. J. F. Kerridge & M. S. Matthews). University of Arizona Press*.718–745.

Scott E., R., D., Rubin A., E., Taylor G., J., & Keil K., Brearley A., J. 1984. *Geochimica et Cosmochimica Acta.* (48): 114 1- 1151.

Seab C., G., 1987. *In Interstellar Processes (eds. D. J. Hollenbach & H. A. Thronson).* 491.

Sears D., W., G., Morse A., D., Hutchison R., Guimon K., R., Kie L., Alexander C., M., O'D., Benoit P., H., Wright I., Pilinger C., Kie T., & Lipschutz M., E. 1995. *Meteoritics.* (30): 169–181.

Shimizu R., & Murata K.1971. *J. Appl. Phys.* (42): 387

Shu F., H., Adams F., C., Lizano S. 1987. *Annual Review of Astronomy and Astrophysics.* (25): 23-81.

Shu F., H., Shang H., Glassgold A., E., & Lee T. 1997. *Science.* (277): 1475.

Shu F., H., Shang H., & Lee T. 1996. *Science*. (271): 1545–1552.

Simon S., B., Joswiak D., J., Ishii H., A., Bradley J., P., Chi M., Grossman L., Aléon J., Brownlee D., E., Fallon S., Hutcheon I., D., Matrajt G., & McKeegan K., D. 2011. *Meteorit. Planet. Sci*. (43): 1861–1877.

Skinner W., R., & Leenhouts J., M. 1993. *24th Lunar and Planet. Sci.* 1315–1316.

Speakman S., A. *Basics of X-Ray Powder Diffraction.* http://prism.mit.edu/xray/oldsite/Basics%20of%20X- ay%20Powder%20Diffraction.pdf

Spettel B., Palme H., Wlotzka F., & Bischoff A. 1992. *Meteoritics.* (27): 290-291.

Starkey N., A., Franchi I., A., Lee M.,R. 2014. *Geochimica et Cosmochimica Acta.* (142): 115–131.

Stroud R., M., & Bernatowicz T., J., 2005. 36th *Lunar and Planet. Sci.* 2010.

Stroud R., M., Nittler L., R., Alexander C., M., O'D., Bernatowicz T., J., & Messenger S., R. 2003. 34th *Lunar and Planet. Sci.* 1755.

Stroud R., M., Nittler L., R., & Hoppe P. 2004b. *Meteorit. Planet. Sci.* (39): A101.

Symes S., J., K., Sears D., W., G., Huang S., X., & Benoit P., H. 1998. *Meteorit. Planet. Sci.* (33): 13–29.

Tang M., & Anders E. 1988a. *Astrophys. J.* (335): 31–34.

Tanigawa T., & Ohtsuki K., 2010. *Icarus*. (205): 658.

Taylor G., J. 2011. *PlanetaryScienceResearch Discoveries.* http://www.psrd.hawaii.edu/April11/amino_acids.html (date accessed).

Thiemens M., H., & Heidenreich III, J., E. 1983. *Science*. (219): 1073– 1075.

Tomeoka K. 2015. *Meteoritics.* (28): 450.

Tomeoka K., & Buseck P., R. 1988. *Geochimica et Cosmochimica Acta.* (52): 1627-1640.
Tomeoka K., & Ohnishi I. 2015. *Geochimica et Cosmochimica Acta.* (75): 6064–6079.

Tomeoka K., &Tanimura I. 2000. *Geochimica et Cosmochimica Acta.* (64): 1971–1988.

Tonks K., B., & Melosh H., J. 1992. I*carus*. (100): 326-46.

Toomre A. 1982. *Astrophys. J.* (259): 535.

Trigo-Rodriguez J., M., Rubin A., E., & Wasson J., T. 2006. *Geochimica et Cosmochimica. Acta.* (70): 1271–1290.
Turner N., J., Willacy K., Bryden G., Yorke H., W. 2006. *Astrophys. J.* (639): 121.

Vaccaro E., Lee M., R., Starkey N., A.,. Franchi I., A. Russell S., S. 2014 .77th *Annual Meteoritical Society Meeting.* 5348.

Van Aken P., A., Liebscher B. 2002. *Phys Chem Miner.*29. (3): 188–200.

Van Boekel R., Min M., Waters L., B., F., M., de Koter A., Dominik C., van den Ancker M., E., & Bouwman J. 2005. *Astron.Astrophys.* (437): 189-208.

Van Boekel R., Waters L., B., F., M., Dominik C., Dullemond C., P., Tielens A., G., G., M., & de Koter A. 2004b. *Astron. Astrophys.* (418): 177-184.

Van Boekel, R, Min, M., Leinert, Ch., et al. 2004. *Nature.* (432): 479.

Wänke H. 1981. *Philosoph. Trans. Roy. Soc. Lond.*(A303): 287–302.

Vogel S., N, Kulkarni S., R, Scoville N., Z. 1988. *Nature.* (334): 402.

Wasson J., T., & Rubin A., E. 2009. *Geochimimica. Cosmochimica Acta*. (73): 1436-1460.

Wagner K., Apai D., Kasper M., & Robberto, M. 2015, *Astrophys. J. Lett.* (813): L2.

Wasson T., J. 2008. *Icarus.* (195): 895-907.

Weisberg M., K., McCoy T., J., & Krot A., N. 2006. *In Meteorites and the Early Solar System* (II).

Weisberg M., K., Prinz M., Clayton R., N., Mayeda T., K., Sugiura N., Zashu S., & Ebihara M. 2001. *Meteorit. Planet. Sci.* (36): 401–418.

Wetherill G., W., & Stewart G., R. 1989. *Icarus.* (77): 330.

Williams J., P. 2012. *Meteoritics & Planetary Science* (47): 1915–1921.

Wiersema D. *Iconset: Solar System Icons*. http://www.iconarchive.com/artist/dan-wiersma.html

Wilner D., J., D'Alessio P., Calvet N., Claussen M., J., &Hartmann L. 2005. *Astrophys. J.* (626): 109-112.

Winson K., J., Stephen J., L. 2014. *Chem. Rev.*, (8): 4470–4495.

Wittke J. 2008. *Northern Arizona Meteorite Laboratory.* http://nau.edu/cefns/labs/meteorite/about/science-tools-and-jargon/

Wlotzka F. 1991. *Meteoritics*.(26): 255-262.

Wood J., A. 2000b. *Space Sci. Rev.* (92): 97–112.

Wood J., A. 2004. *Geochimica et Cosmochimica Acta.* (68): 4007–4021.

Wozniakiewicz P., J., Bradley J., P., Ishii H., A., Brownlee D., E., Kearsley A., T., Burchell M., J., & Price M., C. 2012. *Astrophys. J.* (60): L23.

Wozniakiewicz P., J., Bradley J., P., Ishii H., A., Price M., C., & Brownlee D., E. 2013. *Astrophys. J.* (779): 164.

Yang J., & Epstein S. 1985. *Geophys. Res. Lett.* (12): 73–76.

Young E., D., Ash R., D., England P., & Rumble, D. 1999. *Science*. (286): 1331–1335.

Young E., D. 2001. *Phil. Tran. R. Soc. Lond.* (359): 2095-2110.

Young E., D., &Russell S., S. 1998. *Science*. (282): 452– 455.

Yurimoto H., Krot A., N., Choi B.,G., Aléon J., Kunihiro T., & Brearley A., J. 2008. *In Oxygen in the Solar System.* (1): 141–186.

Yurimoto H., & Kuramoto K. 2002. *Meteorit. Planet. Sci. Suppl.* (A153): 37.

Yurimoto H., & Kuramoto K. 2004. *Science*. (305): 1763–1766.

Yurimoto H., Kuramoto K., Krot A., N., Scott E., R., D., Cuzzi J., N. 2006. *In Protostars and Planets.* (5): 849–62.

Zanda B., Hewins R., H., Bourot-Denise M., Bland P., A. & Albarède F. 2006. *Earth and Planetary Science Letters* (248): 650– 660.

Zinner E., McKeegan K., D., & Walker R., M. 1983. *Nature.* (305): 119–121.

Zolensky M., E., Bourcier W., L., & Gooding J., L. 1989. *Icarus.* (78): 411–425.

Zolensky M., E., Zega T., J., Yano H. et al. 2006. *Science.* (314): 1735.